Title
Radiative relativistic magnetohydrodynamic simulations of neutron star column accretion

Permalink
https://escholarship.org/uc/item/01f759vr

Author
Zhang, Lizhong

Publication Date
2023

Peer reviewed|Thesis/dissertation

University of California
Santa Barbara

Radiative relativistic magnetohydrodynamic simulations of neutron star column accretion

A dissertation submitted in partial satisfaction
of the requirements for the degree

Doctor of Philosophy
in
Physics

by

Lizhong Zhang (张力中)

Committee in charge:

Professor Omer Blaes, Chair
Professor Lars Bildsten
Professor Timothy Brandt

September 2023

The Dissertation of Lizhong Zhang is approved.

_____

Professor Lars Bildsten

_____

Professor Timothy Brandt

_____

Professor Omer Blaes, Committee Chair

July 2023

Radiative relativistic magnetohydrodynamic simulations of neutron star column
accretion

Acknowledgements

My six-year journey in Santa Barbara marks the closure of my checkered life and initiates a new chapter in my academic career. I consider myself fortunate to have maintained enthusiasm and drive, allowing me to persist in my scientific pursuits. Throughout these years, I have encountered numerous individuals who have played vital roles in shaping my trajectory and propelling me to this point.

I sincerely appreciate the support and guidance of my advisor, Omer Blaes, a humble and genuine human being who is always patient to my naive questions. I am consistently amazed by his dedication and deep engagement with every detail of our projects. I am grateful that our collaboration has ultimately evolved into a genuine friendship, partially enriched by countless wonderful spicy food experiences. Another mentor of mine, Yan-Fei Jiang (姜燕飞), has generously shared his expertise in computational astrophysics, reshaping my perception of scientific computation with his creative ideas and practical skills. His guidance has provided me with a valuable and insightful experience in numerical simulations. Chris White has been a lifesaver throughout my struggles with using ATHENA++. He patiently guided me through every aspect of the code and imparted invaluable hands-on experience. His dedication to science is both admirable and inspiring. Xin Sheng (盛昕) is one of the most talented undergraduates I have ever encountered. Together, we have overcome many challenges and frustrations involved in debugging simulations. Bryance Oyang, my debugging brother, has also shared in many painful debugging experiences. Each time I felt stuck, our comforting conversations helped me regain confidence and alleviate anxiety. Jason Kaufmann, the first senior graduate student I encountered, graciously shared his experiences as an early-stage PhD graduate student in theoretical astrophysics.

I would also like to express my gratitude to the other two members of my committee.

Lars Bildsten, thank you for helping me realize the importance of connecting theory to observation and for providing pratical suggestions on identifying valuable scientific problems from observational phenomena. Tim Brandt, thank you for engaging in the variable inversion problem with me and for sharing insightful perspectives on the application of machine learning in astrophysics.

I must mention the kindness I received from the Athena community as well. Jim Stone, thanks for your encouragement when we first succeeded in simulating accretion columns. You helped me realize that perfection is not a prerequisite for numerical simulations; instead, they offer valuable opportunities for learning and understanding the underlying physics. Patrick Mullen, thanks for generously sharing your code work in ATHENAK and providing sincere advice as a postdoctoral researcher in the field. Zhaohuan Zhu (朱照寰), thank you for providing me with many useful suggestions for my academic career, particularly from the perspective of someone from the same hometown.

I have been treated kindly by many other people in the field. I extend my appreciation to Matt Middleton for providing invaluable insights from an observer's perspective, as well as for allowing me to use your diagram, which beautifully shows the global picture of super-Eddington neutron star accretion. Your observational expertise has greatly broadened my understanding, escalating this project towards becoming a long-term career goal. Mitch Begelman, thank you for sharing your unpublished work with us and providing your point of view based on your analytical work, which greatly enhanced our understanding of the dynamics involved in neutron star accretion. Ruediger Staubert, thanks for your generosity in granting me permission to utilize your plot. It serves as a perfect illustration of how the observation and theory of neutron star accretion can be interconnected.

My previous undergraduate projects at the University of Illinois were an important starting point for everything that followed. I am indebted to Joaquin Vieira, my first

in my heart with her unwavering support in every aspect of my life. Her unconditional love has been a constant source of inspiration for me. My stepgrandfather, Gong Liang (梁恭), thank you for your companionship and support to my beloved grandmother and this family. My dad, Luxing Zhang (张露兴), thank you for training my mental strength, which has been essential in helping me overcome challenges throughout this journey. My aunt, Ya Nie (聂娅), thanks for being one of the few individuals who believed in and supported my academic journey in physics. Nanxing Tang (唐楠鑫) is my lifelong best friend. His support has consistently served as a source of motivation for me. Thank you, Buffy (肭肭), my beloved and silly cat, whose presence has never failed to bring me joy, particularly during moments of exhaustion. Finally, I must express my special gratitude to my partner, Fangyuan Dong (董方圆), who entered my life when I was at my lowest point. Her support and companionship have not only uplifted my spirit but also paved the way for a promising future. I am eternally grateful for the positive impact she has had on my life.

To anyone else who has contributed to my growth and the completion of this thesis, I offer my heartfelt thanks. Your support has made this achievement possible, and I am forever grateful.

Curriculum Vitæ
Lizhong Zhang (张力中)

Education

2023	Ph.D. in Physics (Expected), University of California, Santa Barbara
2020	M.A. in Physics, University of California, Santa Barbara
2016	B.S. in Physics and Astronomy, University of Illinois Urbana-Champaign

Academic Positions

2018 – 2023	Graduate student researcher, UCSB
2017 – 2019	Teaching assistant, UCSB and UIUC
2014 – 2017	Research assistant, UIUC

Publications

12. *Dynamical Effects of Magnetic Opacity in Neutron Star Accretion Columns*
Sheng X., **Zhang, L.**, Blaes, O., Jiang, Y.-F.
2023, MNRAS, 524, 2431

11. *An Extension of the Athena++ Code Framework for Radiation-Magnetohydrodynamics in General Relativity Using a Finite-Solid-Angle Discretization*
White, C.J., Mullen, P.D., Jiang, Y.-F., Davis, S.W., Stone, J.M., ..., **Zhang, L.**
2023, ApJ, 949, 103

10. *Evaluating the Microheterogeneous Distribution of Photochemically Generated Singlet Oxygen using Furfuryl Amine*
Cheng, K., **Zhang, L.**, McKay, G.
2023, ES&T, 57(19), 7568

9. *Simultaneous Millimeter-wave, Gamma-ray, and Optical Monitoring of the Blazar PKS 2326-502 During a Flaring State*
Hood II, J.C., Simpson, A., McDaniel, A., Foster A., Ade, P.A.R., ..., **Zhang, L.**
2023, ApJL, 945, L23

8. *The Nature of Blue Stars with Mid-infrared Excesses in the Large Magellanic Cloud*
Ishioka, R., Chu, Y.-H., Edmister, A., Gruendl, R.A., **Zhang, L.**, Zhu, J.
2023, ApJS, 265, 18

7. *Dynamics of Neutron Star Accretion Columns in Split-Monopole Magnetic Fields*
Zhang, L., Blaes, O., Jiang, Y.-F.
2023, MNRAS, 520, 1421

6. *New Identifications and Multi-wavelength Properties of Extragalactic Fermi Gamma-Ray Sources in the SPT-SZ Survey Field*
Zhang, L., Vieira, J.D., Ajello, M., Malkan, M.A., Archipley, M.A., et al.
2022, ApJ, 939, 117

5. *Radiative Relativistic Magnetohydrodynamic Simulations of Neutron Star Column Accretion in Cartesian Geometry*
Zhang, L., Blaes, O., Jiang, Y.-F.
2022, MNRAS, 515, 4371

4. *Radiative MHD Simulations of Photon Bubbles in Radiation-Supported Magnetized Atmospheres of Neutron Stars with Isotropic Thomson Scattering*
Zhang, L., Blaes, O., Jiang, Y.-F.
2021, MNRAS, 508, 617

3. *Detection of Galactic and Extragalactic Millimeter-wavelength Transient Sources with SPT-3G*
Guns, S., Foster, A., Daley, C., Rahlin, A., Whitehorn, N., ..., **Zhang, L.**
2021, ApJ, 916, 98

2. *Millimeter-wave Point Sources from the 2500 Square Degree SPT-SZ Survey: Catalog and Population Statistics*
Everett, W.B., **Zhang, L.**, Crawford, T.M., Vieira, J.D., Aravena, M., et al.
2020, ApJ, 900, 55

1. *Can CMB Surveys Help the AGN Community?*
Partridge, B., Bonavera, L., López-Caniego, M., Datta, R., ..., **Zhang, L.**
2017, Galaxies, 5(3), 47

Abstract

Radiative relativistic magnetohydrodynamic simulations of neutron star column accretion

by

Lizhong Zhang (张力中)

Accretion onto a strongly magnetized neutron star at a sufficiently high mass accretion rate results in the formation of a radiation pressure-supported columnar structure near the polar regions. In this region, the accretion inflow is magnetically constrained and shocked above the stellar surface. Below the shock, the accretion column liberates most of the accretion power through the sideways radiation emission in a so-called 'fan-beam' pattern, in contrast to the 'pencil-beam' emission where radiation leaves directly from the top of the column. The physics of the accretion column plays a defining role in understanding the observations of accretion-powered X-ray pulsars, including pulsating ultraluminous X-ray sources (ULXs). The observed pulsations arise from the misalignment between the anisotropic radiation emission and the spin axis of the rotating neutron star.

We perform radiative relativistic MHD simulations to study the nonlinear dynamics of the accretion column. The column structure is extremely dynamical and exhibits kHz quasi-periodic oscillations. The existence of the photon bubble instability is identified in simulated accretion columns but proved to be not responsible for triggering the oscillatory behaviors. Instead, the oscillations originate from the inability of the system to resupply heat and locally balance the sideways cooling. When the oscillation amplitude is sufficiently large, the emergent radiation can exhibit hybrid fan- and pencil-beam patterns. The column structure is very sensitive to the shock geometry, which directly

determines the cooling efficiency. A more diverging geometry of the accretion column can provide more heat support through PdV work. The time-averaged column structures from the simulations can be approximately reproduced by a 1D stationary model, given the correction for the actual 2D mound shape of the time-averaged column. The increase in magnetic opacity with temperature below the radiative shock may introduce an additional unstable mechanism in the dynamics of the accretion column. Pair production can boost the opacity above $\sim 4 \times 10^8$ K near the base of the column, which is likely to introduce further dynamical effects. To further investigate these problems, we propose an extension of the current numerical framework by incorporating magnetic polarization into the radiation module.

Contents

Chapter 1

Introduction

1.1 Observation of Accretion onto Strongly Magnetized Neutron Stars

In marked contrast to a black hole accretor in an X-ray binary, a strongly magnetized neutron star can truncate the accretion disk in the vicinity of the Alfvén radius. Within this truncation region, magnetic stresses become dominant and therefore guide the accreting matter through the magnetosphere toward the magnetic poles (Ghosh et al. 1977). At a low accretion rate, the infalling gas is shocked near the stellar surface and forms a hot spot (Basko & Sunyaev 1975). With sufficiently high accretion rates, a shock forms above the stellar surface, below which a radiation pressure dominated columnar structure is established (Inoue 1975; Basko & Sunyaev 1976). In either case, the misalignment of the anisotropic radiation-emitting polar regions with respect to the stellar rotation axis produces the observed pulsations.

These magnetized neutron star accretors widely exist in a variety of astronomical systems. Accretion-powered X-ray pulsars, most of which are in high mass X-ray binaries,

have been known since the early days of X-ray astronomy (see e.g. Caballero & Wilms 2012, Walter et al. 2015, and Mushtukov & Tsygankov 2022 for recent reviews). Accreting millisecond pulsars in low mass X-ray binaries were discovered much later (Wijnands & van der Klis 1998; see Burderi & Di Salvo 2013 for recent review). Beginning with the discovery by Bachetti et al. (2014), some ultraluminous X-ray sources (ULXs, see e.g. Kaaret et al. 2017 and King et al. 2023 for recent reviews) are now known to exhibit coherent pulsations and are therefore clearly accreting, magnetized, rotating neutron stars. These make up a sizable fraction ($\sim 25\%$) of all ULX populations (Rodríguez Castillo et al. 2020).

1.1.1   X-ray Pulsars and Pulsating ULXs

An accretion-powered X-ray pulsar refers to a binary system characterized by a strongly magnetized, rotating neutron star that accretes material from its donor star. In this system, the accretion matter falls into the deep gravitational well of the accretor, liberating its mechanical energy through X-ray radiation emission. According to the nature of the binary companion stars, X-ray pulsars can have different accretion types and a wide range of accretion rates. High-mass X-ray pulsars generally consist of strongly magnetized neutron star accretors ($B \gtrsim 10^{12}$ G) and massive donor stars ($\gtrsim 8M_\odot$; O-type or B-type). These young, massive optical companions enable the neutron stars to directly accrete at high mass rates from their strong stellar winds (e.g. Vela X-1, Nagase et al. 1986). Low-mass X-ray pulsars are rare and typically older systems, where the surface magnetic fields of neutron stars tend to have relatively weaker $B \sim 10^9$ G and the donor stars are less massive ($\lesssim 2M_\odot$). These systems usually undergo the disk accretion at relatively lower rates via the Roche lobe overflow (e.g. SAX J1808.4-3658, Wijnands & van der Klis 1998). However, it is worth noting that some low-mass X-ray

pulsars are also observed to exhibit strong magnetic fields near $B \sim 10^{12}$ G (e.g. Her X-1, Tananbaum et al. 1972).

Ultraluminous X-ray sources are classified as non-nuclear X-ray sources with their assumed isotropic, apparent X-ray luminosity $L_X \geq 10^{39}$ erg s^{-1}, which roughly corresponds to the Eddington luminosity for a $10 M_\odot$ black hole. Therefore, ULXs were generally thought to be powered by accretion onto an intermediate-mass black hole or a stellar-mass black hole with strongly beamed radiation. However, recent observations have discovered some ULXs with coherent pulsations, which also make the super-Eddington accreting neutron star a promising candidates. There are two effects that enable the accreting neutron star ($\sim 1.4 M_\odot$) to achieve such high Eddington ratio (ranging from 1 to 500): 1. a strong beaming effect resulting from anisotropic accretion, and 2. significant opacity reduction in strong magnetic fields, enabling very high mass accretion rates. Nevertheless, the geometric beaming effects might result in the smearing out of the observed neutron star spin pulsations (Mushtukov et al. 2017, 2021), and the reduction in magnetic opacity ceases when pair production occurrs at magnetic fields $B \gtrsim 10^{14}$ G (Suleimanov et al. 2022). Therefore, how a neutron star can accrete in the super-Eddington regime is still not well understood.

1.1.2   Magnetic Field

What distinguishes neutron star accretion from other accretion systems is the presence of strong magnetic fields. These magnetic fields give rise to various observational effects, greatly enriching the phenomenology of accreting neutron star systems. Firstly, the geometric configuration of the magnetic field plays a defining role in determining the accretion geometry by confining the gas motion near the neutron star (Basko & Sunyaev 1975, 1976; Ghosh et al. 1977). Secondly, the strength of the magnetic field can modify

the scattering opacity, thus influencing the interaction between the gas and radiation (Arons et al. 1987; Mushtukov et al. 2016). Both of these factors significantly contribute to determining the beam pattern of radiation emission, which ultimately manifests in the shape of observed pulse profiles. In addition, the anisotropy of magnetic fields can introduce strong polarization in the emergent radiation (Caiazzo & Heyl 2021). The occurrence of anisotropic scattering, resulting from strong magnetic fields, makes neutron star accretion a rare case where polarization can directly impact the dynamics of the accretion system.

The magnetic field strength of an accreting neutron star can be directly measured from the cyclotron absorption lines, produced by the resonant scattering of photons by electrons or even protons. Since the geometry of the radiation-emitting region strongly depends on local magnetic fields and accretion rates, different variations of observed cyclotron lines can serve to constrain the existing theoretical model and enhance our understanding of the underlying physics. For instance, in Figure 1.1 (reproduction of Fig. 9 in Staubert et al. 2019), the two most luminous X-ray pulsars, V 0332+53 and SMC X-2, demonstrate a negative correlation between cyclotron energy and X-ray luminosity. This relationship is likely to be directly elucidated by the accretion column model. When the accretion onto a neutron star is supercritical (i.e. capable of forming an accretion column structure), higher luminosities/accretion rates lead to an increase in the effective column height. This height increase, in diverging magnetic fields, then results in a reduction of the field strength and consequently a decrease in the emergent cyclotron energy. An alternative explanation involves the reprocessing of X-ray radiation by the atmosphere of the neutron star (for details see the review by Mushtukov & Tsygankov 2022). Furthermore, the variation of cyclotron lines in pulse phase can provide an extra constraint for tracking the height of line-forming region, which however, might be confused by light bending near the neutron star (Staubert et al. 2019). Hence, it is necessary to employ a
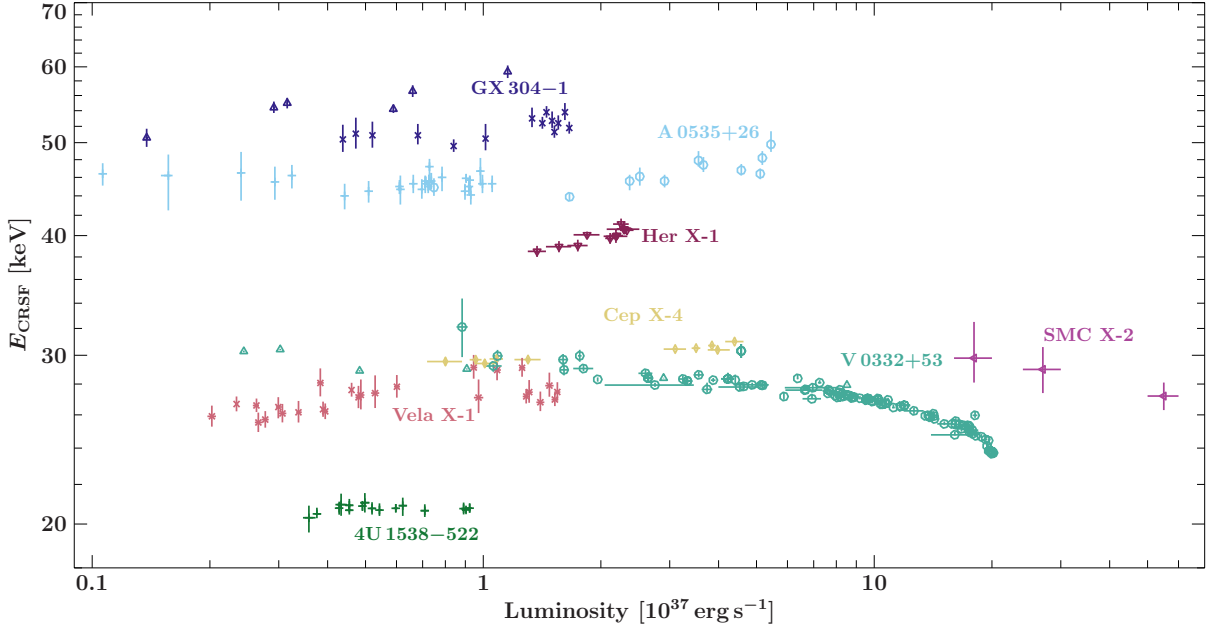
Figure 1.1: Reproduction of Fig. 9 in Staubert et al. (2019). Correlation between cyclotron energy (E_{CRSF}) and X-ray luminosity for eight accretion-powered X-ray pulsars. The two most luminous sources exhibit a clear negative correlation, which can be interpreted as an increase in height of the accretion column with higher accretion rates in diverging magnetic fields.

ray tracing model that incorporates general relativistic effects and even birefringence, to ensure accurate quantifications.

1.1.3   Pulse Profile

The coherent pulse profile is perhaps the most prominent observational characteristic that sets apart neutron star accretors from black holes in X-ray binaries. Its shape directly reflects the manifestation of the beamed radiation emitted by the X-ray pulsar. Moreover, the variations in pulse profiles, dependent on observables such as luminosity and photon energy, provide valuable insights that may help resolve some long-standing theoretical challenges in the neutron star accretion. These challenges, including the transition from the hot spot to the accretion column and the radiation dynamical feedback

on the surrounding accreting material (e.g. accretion curtain), have not been fully understood.

In X-ray transient sources powered by the accretion onto neutron stars, the light curves display distinct shapes in different luminosity states (e.g. 4U 1901+03, Ji et al. 2020), indicating significant variations in radiation beam patterns across subcritical to supercritical accretion regimes. Although stationary 1D models for neutron star accretion tend to favor distinct beam patterns, with pencil beams representing surface hot spots and fan beams corresponding to the accretion column, a mixture of pencil and fan-beam emission geometries is frequently required to accurately interpret observed pulse profile shapes (e.g. Klochkov et al. 2008; Becker et al. 2012; Iwakiri et al. 2019). This might be simply explained by the oscillating structure of the accretion column (for details see chapter 4). Furthermore, pulse profiles can significantly vary with the observed photon energy in the intermediate luminosity regime (e.g. 4U 1626-67, Iwakiri et al. 2019), but display only slight differences in the ULX regime (e.g. SMC X-3, Tsygankov et al. 2017). These distinctions indicate the intrinsic differences between the sub- and super-Eddington accretion process onto a strongly magnetized neutron star.

1.1.4   Polarization

The X-ray polarization is another observable that directly arises from the inherent anisotropic nature of accretion-powered X-ray pulsars. Recent unprecedented observations conducted by the Imaging X-ray Polarimetry Explorer (IXPE) have successfully detected polarizations in three X-ray pulsars, Cyg X-2, Her X-1, and Cen X-3 (Farinelli et al. 2023; Doroshenko et al. 2022; Tsygankov et al. 2022), which span the regime from low- to high-mass optical companions and weakly to strongly magnetized neutron star accretors. However, the observed polarizations are far below the predictions of the clas-

sical theoretical model. Multiple physical scenarios have been proposed to address this unexpected result, such as the intrinsic low polarization degree of the pencil-beam radiation from surface hot spots and radiation reprocessing in different regions, particularly reflection from the stellar surface. Therefore, to confirm the underlying reason of the low polarization degree, we need to further investigate the time-dependent accretion structure near the neutron star accretor and its nonlinear dynamics, which is significantly influenced by the radiation feedback.

1.2 Neutron Star Accretion Column

1.2.1 Analytical Models and Numerical Simulations

When the accretion rate is supercritical and the magnetic confinement is sufficiently strong, the accretion flow can be shocked above the stellar surface, resulting in the formation of a radiation pressure dominated columnar structure below. Above the shock, the inflow free falls directly onto the shock front (known as the 'free-fall zone'), where a substantial fraction of its kinetic energy is converted into heat. Below the shock, the material is in approximate hydrostatic equilibrium between outward radiation pressure and gravity, thereby subsonically settling down (known as the 'sinking zone') and liberating the remaining gravitational energy through the sideways emission (Inoue 1975; Basko & Sunyaev 1976).

The accretion column model is widely preferred for achieving a high Eddington ratio by generating beamed radiation due to the anisotropic nature of strongly magnetized neutron stars. An early analytical solution of the accretion column was proposed by Basko & Sunyaev (1976) and assumed a simplified 1D geometry of a stationary columnar structure with a constant scattering opacity. Following this work, a series of 1D station-

ary models were developed by using more careful treatments of radiative transfer and magnetic opacities (e.g. Becker 1998; Becker & Wolff 2007; Mushtukov et al. 2015; West et al. 2017a,b). More recent work done by Abolmasov & Lipunova (2022) has further relaxed the time dependence in the 1D accretion column model.

Nevertheless, the accretion column is generally thought to be inherently unstable due to the growth of entropy waves, a phenomenon which is also known as the 'photon bubble instability' (Arons 1992; Begelman 2006). The pioneering numerical simulations conducted by Klein & Arons (1989) and Klein et al. (1996) revealed that the accretion column structure is not stationary but highly dynamical. These simulations displayed evidence of oscillatory behavior in the nonlinear development of accretion columns, and predicted that these might be observable as 'photon bubble oscillations' at frequencies ranging from $\sim 10^2 - 10^4$ Hz. Unfortunately, those simulations were poorly resolved and did not run long enough due to the limited computational resources in the past. However,
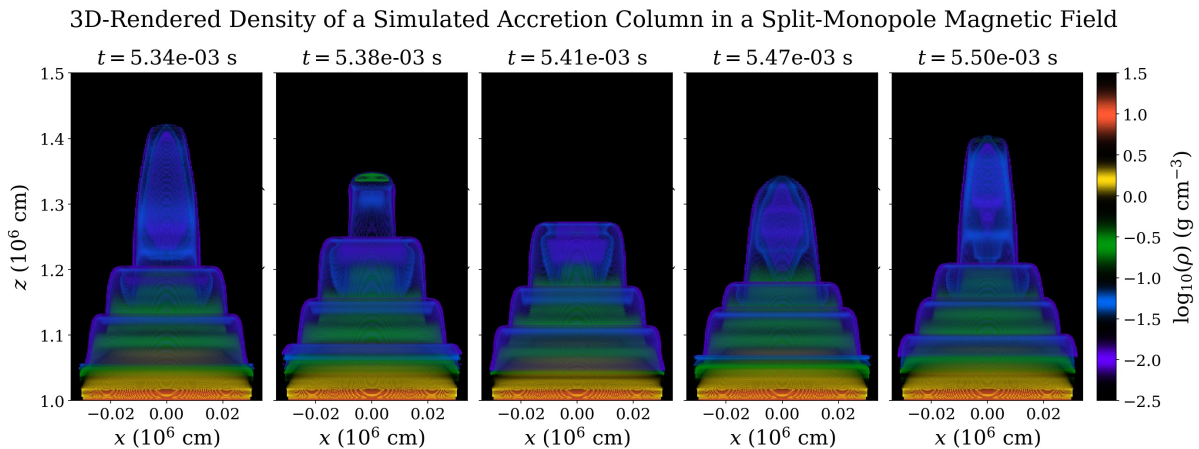
Figure 1.2: 3D-rendered structures of density snapshots of the accretion column in a split-monopole magnetic field over one full oscillation period. The fountain-shaped 3D structures result from the propagation of the entropy waves that are associated with the slow-diffusion photon bubble instability. However, the oscillation is not driven the photon bubbles but the thermal imbalance between heating and cooling.

in more recent simulations conducted by Zhang et al. (2022, 2023) as shown in Figure 1.2, the results suggest that the photon bubbles add additional spatial complexity to the

column structure but do not appear to be directly responsible for the high-frequency oscillatory behavior. Instead, it is caused by the instantaneous imbalance between global heating and cooling due to inefficient vertical energy transport (for details see chapter 3 and chapter 5).

1.2.2   Photon Bubble Instability

A linear analysis of the growth of infinitesimal fluctuations due to the photon bubble instability was first explored by Arons (1992) and Gammie (1998), and then extended to shorter length scales by Blaes & Socrates (2003). The instability grows exponentially in time at a rate that is faster for shorter length scales, presumably until the fluctuations are large enough that nonlinear effects come into play. However, at the shortest length scales, radiative diffusion eventually becomes fast enough to smooth out fluctuations in radiation pressure (the rapid diffusion regime). There the growth rate levels off at length scales of order the gas pressure scale height, and the instability becomes a radiatively amplified slow magnetosonic mode in the gas alone. Even before this linear behavior was understood, Begelman (2001) analytically predicted that the nonlinear development of the instability in the rapid diffusion regime would result in trains of shock waves, and this was confirmed in detail by radiation MHD simulations of Turner et al. (2005). The rapid diffusion limit of the instability can even exist in regimes where gas pressure is comparable to radiation pressure or magnetic pressure (Blaes & Socrates 2003), and its nonlinear outcome has been simulated by Fernández & Socrates (2013).

Deep inside a neutron star accretion column, the optical depths are so high that the rapid diffusion regime is only achieved on wavelengths much smaller than the scale height of the column. It is here that the slow diffusion regime version of the photon bubble instability first studied by Arons (1992) is most relevant, and where the instability

takes on the character of a diffusion entropy mode. The first numerical simulations that studied the development of this instability were conducted by Hsu et al. (1997). These simulations were 2D, and assumed 1D gas motion along prescribed rigid magnetic field lines. Radiation transport was treated within the flux-limited diffusion approximation, and accounted for nonzero chemical potential effects in a Bose-Einstein spectrum. The linear growth of the instability agreed well with the Arons (1992) dispersion relation and photon bubbles were found to transport energy efficiently. More recent simulations of photon bubbles in the slow diffusion regime, conducted by Zhang et al. (2021), have employed a state-of-the-art numerical algorithm that solves both the angle-dependent radiation transfer and relativistic magnetohydrodynamics. The simulation results are highly consistent with the linear solution and also confirm, for the first time, that radiation viscosity sets the smallest length scale of the photon bubbles. In addition, a new instability driven by the temperature-dependent magnetic opacity can take place in the strong magnetic field regime, where the temperature width of the opacity peak can be resolved in the accretion column structure (for details see chapter 4 and section A.4).

1.3   Permissions and Attributions

1. Figure 1.1 is a reproduction of Fig. 9 in Staubert et al. (2019) with permission by Ruediger Staubert. The introductory text in section 1.2 is partially adapted from the introduction section of Zhang, Blaes & Jiang (2021).

2. The content of chapter 2 is the result of a collaboration with Omer Blaes and Yan-Fei Jiang, and was published in the *Monthly Notices of the Royal Astronomical Society* as Zhang et al. (2021).

3. The content of chapter 3 is the result of a collaboration with Omer Blaes and Yan-

Fei Jiang, and was published in the *Monthly Notices of the Royal Astronomical Society* as Zhang, Blaes & Jiang (2022).

4. The content of chapter 4 is the result of a collaboration with Xin Sheng, Omer Blaes and Yan-Fei Jiang, and was published in the *Monthly Notices of the Royal Astronomical Society* as Sheng, Zhang, Blaes & Jiang (2023).

5. The content of chapter 5 is the result of a collaboration with Omer Blaes and Yan-Fei Jiang, and was published in the *Monthly Notices of the Royal Astronomical Society* as Zhang, Blaes & Jiang (2023).

6. The content of chapter 6 is original work conducted by Lizhong Zhang, Omer Blaes and Yan-Fei Jiang. Figure 6.1, created by Matthew Middleton, is used with his permission.

7. The first three sections of Appendix A is adapted from the appendix A of Zhang et al. (2021). The last section of Appendix A is adapted from the appendix B of Sheng et al. (2023).

8. The content of Appendix B is adapted from the appendix B of Zhang et al. (2021).

9. The calculations and numerical tests in Appendix C were performed by Lizhong Zhang.

10. The content of Appendix D is original work conducted by Lizhong Zhang.

11. The first two sections of Appendix E is original work conducted by Lizhong Zhang and Omer Blaes. The last section is adapted from the appendix A of Sheng et al. (2023).

Chapter 2

Simulations of Slow-Diffusion Photon Bubble Instability

This chapter is adapted from our research work published as Zhang, Blaes & Jiang (2021). In this chapter, we establish a numerical framework and simulate the photon bubble dynamics in static non-accreting columns. This chapter is organized as follows. In section 2.1, we give a brief explanation of the photon bubble physics. In section 2.2, we introduce the numerical approaches and model configurations behind the simulations. In section 2.3, we present and explain the simulation results, compare the simulation with linear theory, and study the behavior of the photon bubble simulations at different resolutions. In section 2.4, we discuss the significance of the simulation results and summarize our conclusions.

2.1   Overview of Photon Bubble Instability

The linear analysis of the photon bubble instability in the slow diffusion regime was explored by Arons (1992) and Gammie (1998), although both of these studies also in-

cluded aspects of the shorter wavelength rapid diffusion regime behavior. We begin by briefly describing the physics of the slow diffusion mode. More details can be found in Appendix A, where we present a detailed derivation of our version of the instability dispersion relation that includes the effects of radiation viscosity. We assume a constant opacity and use this dispersion relation to compare with our numerical simulations.

Consider a static column at one of the magnetic poles of the neutron star, and assume for simplicity that its vertical extent is much smaller than the radius of the star, so that the magnetic field can be treated as purely vertical and the gravitational acceleration g can be assumed constant. For the purposes of this physics discussion, imagine the magnetic field to be so strong as to be perfectly rigid, although we will allow for the field to be dynamic in our numerical simulations below. Because no fluid can then move horizontally, and radiation pressure completely dominates gas pressure, hydrostatic equilibrium in the column states simply that the vertical radiation flux is $F_{r,z} = cg/\kappa$. Taking the opacity κ to be constant[1] this then implies that the vertical radiation flux is constant. Assuming radiative diffusion, $F_{r,z} = -(c/3\kappa\rho)dE_r/dz$ then relates the vertical gradient in radiation energy density E_r to the density ρ.

A key reason why the column is vulnerable to instability is that such an equilibrium is completely unchanged if we add arbitrary vertical fluctuations in density, provided we maintain a vertically constant flux $F_{r,z} = cg/\kappa$ by adjusting the radiation energy density gradient to be such that $dE_r/dz \propto \rho$. Because such fluctuations necessarily involve fluctuations in radiation entropy, this static mode is an entropy mode. However, the finite horizontal extent of the accretion column means that such fluctuations must themselves have horizontal variations, and the resulting horizontal radiative diffusion then causes time dependence in the density and radiation energy density. Provided this

---

[1]Throughout this chapter we assume that the opacity is simply that of non-magnetic Thomson scattering, neglecting the angle and polarization dependence that is in fact important for neutron star accretion columns. We intend to incorporate these effects in future work.

time-dependence is slow enough that the gas inertia is truly negligible, then vertical hydrostatic equilibrium would still be maintained, and of course horizontal equilibrium is maintained by the strong vertical magnetic field.

However, the gas inertia, while small, is still finite in the slow diffusion regime, and cannot in fact be neglected. As first shown by Arons (1992) (see also section A.3), the inertia introduces a finite perturbed vertical flux, which provides extra radiation support to balance the perturbed net force. This response of the force balancing has a 90° phase delay with respect to the density perturbation ((A.21), (A.22) and Figure A.2), which causes a small amount of radiation to flow from high-density regions to low-density regions. Although this unstable effect is small, this tendency would eventually evacuate the perturbed low-density regions by feeding in radiation and leading to an increasing amplitude of density perturbation.

In section A.2, we derive a short-wavelength (WKB) linear dispersion relation that fully includes the effects of radiation viscosity for the first time (A.7). Numerical solutions of this dispersion relation using constant opacity for the instability growth rate are shown in Figure A.1. Smaller length scale modes generally grow faster until reaching a maximum growth rate at a length scale l_{vis} (A.10) set by radiation viscosity. The purpose of our simulations below will be to test our numerics against the predictions of this linear dispersion relation, and to explore the nonlinear outcome of the instability.

2.2 Numerical Method

2.2.1 Equations

Accreting neutron stars in high mass X-ray binary systems have strong surface fields $\sim 10^{12-13}$ G (e.g. Bellm et al. 2014; Dall'Osso et al. 2015) that may in some cases even

extend up to magnetar field strengths (10^{14} G, Tsygankov et al. 2016). Because of this, the Alfvén speed in Newtonian MHD can easily exceed the speed of light in low density regions, which slows down the numerical simulation because of the CFL condition on the time step. On the other hand, the Alfvén speed in relativistic MHD is intrinsically limited to the speed of light. Therefore, we couple special relativistic MHD (RMHD, Beckwith & Stone 2011) and the radiative transfer equation (Jiang et al. 2014) in the ATHENA++ code (Stone et al. 2020), and solve them together for the radiation pressure dominated static column on the neutron star. We provide details of our modifications to the ATHENA++ algorithms in the appendix C of Zhang et al. (2021).

The primitive variables (ρ, v^i, P_g, B^i) in RMHD are defined in the fluid rest frame, where ρ is the gas density, P_g is the gas pressure, v^i is the fluid three-velocity, and B^i is the magnetic field three-vector. Hereafter, we use Latin indices in italics to denote spatial components of three-vectors (from 1 to 3) and Greek indices to denote components of four-vectors (from 0 to 3), where 0 represents the time component. We adopt velocity units with $c = 1$ and Minkowski metric $\eta_{\mu\nu} = \mathrm{diag}(-1, 1, 1, 1)$ for flat spacetime. Given a Lorentz factor defined as $\Gamma = (1 - v_j v^j)^{-1/2}$, the fluid four-velocity components are $u_0 = \Gamma$ and $u^i = \Gamma v^i$. The magnetic field four-vector b^μ and the total enthalpy w are defined as follows for convenience

$$b^0 = u_j B^j, \quad b^i = \frac{1}{\Gamma}(B^i + b^0 u^i) \quad , \tag{2.1}$$

$$w = \rho + \frac{\gamma}{\gamma - 1} P_g + b_\nu b^\nu \quad , \tag{2.2}$$

where the equation of state for ideal gas is adopted in (2.2) with the gas adiabatic index γ. The system is governed by the gas conservation laws and the radiative transfer equation. We summarize these equations below in the sequence of particle number conservation,

momentum conservation, energy conservation and radiative transfer.

$$\partial_0(\rho u^0) + \partial_j(\rho u^j) = S_{\text{gr1}} \quad , \tag{2.3a}$$

$$\partial_0(wu^0u^i - b^0b^i) + \partial_j\left(wu^iu^j + \left(P_g + \frac{1}{2}b_\nu b^\nu\right)\delta^{ij} - b^ib^j\right) = S^i_{\text{gr2}} - S^i_{r2} \quad , \tag{2.3b}$$

$$\partial_0\left[wu^0u^0 - \left(P_g + \frac{1}{2}b_\nu b^\nu\right) - b^0b^0\right] + \partial_j(wu^0u^j - b^0b^j) = S_{\text{gr3}} - S_{r3} \quad , \tag{2.3c}$$

$$\partial_0 I + n^j\partial_j I = \mathcal{L}^{-1}(\bar{S}_r) \quad , \tag{2.3d}$$

where S_{gr1}, S^i_{gr2} and S_{gr3} are the gravitational source terms that mock up the gravity in special relativity. I is the frequency-integrated intensity and the unit vector n^i is the direction of the intensity. $\mathcal{L}$ is the Lorentz boost operator from the lab frame to the fluid frame and $\mathcal{L}^{-1}$ vice versa. S^i_{r2} and S_{r3} are the momentum and energy exchange between gas and radiation. The radiative transport term $\bar{S}_r$ is defined in the fluid frame including the processes of elastic scattering, absorption and Compton scattering. Note that the coordinates and radiation variables are defined in the lab frame and we denote these quantities in the fluid frame with overbars.

When the plasma is radiation pressure dominated and the Lorentz factor is near unity or varies slowly in spacetime, we can treat the gravitational field near the neutron star surface by using the following approximate source terms in RMHD (see derivations in Appendix B).

$$S_{\text{gr1}} = (2\Gamma^2 + 1)\rho u^j\partial_j\phi \quad , \tag{2.4a}$$

$$S^i_{\text{gr2}} = 2(2\Gamma^2 + 1)w_g u^i u^j\partial_j\phi - (2\Gamma^2 - 1)w_g\partial_i\phi \quad , \tag{2.4b}$$

$$S_{\text{gr3}} = 2\Gamma(2\Gamma^2 - 1)w_g u^j\partial_j\phi \quad , \tag{2.4c}$$

where $\phi = -GMr^{-1}$ is the Newtonian gravitational potential and $w_g = \rho + \gamma(\gamma - 1)^{-1}P_g$

is the gas enthalpy.

The radiative transfer equation is solved in the mixed frame by operator splitting the advection and source term steps. The source term $\bar{S}_r$ is used to update the intensity in the fluid frame. Then we Lorentz transform back to the lab frame and compute the momentum (S_{r2}^i) and energy exchange (S_{r3}) between gas and radiation to update the gas primitive variables. The momentum and energy exchange between gas and radiation are

$$S_{r2}^i = \oint \mathcal{L}^{-1}(\bar{S}_r) n^i d\Omega \quad , \tag{2.5a}$$

$$S_{r3} = \oint \mathcal{L}^{-1}(\bar{S}_r) d\Omega \quad , \tag{2.5b}$$

where Ω is the solid angle of the radiation field. The radiative transport source term in the fluid frame is

$$\begin{aligned} \bar{S}_r = \Gamma(1 - v_j n^j) \Bigg[&\rho \kappa_s (\bar{J} - \bar{I}) \\ &+ \rho \kappa_R \left(\frac{a_r T_g^4}{4\pi} - \bar{I} \right) + \rho(\kappa_P - \kappa_R) \left(\frac{a_r T_g^4}{4\pi} - \bar{J} \right) \\ &+ \rho \kappa_s \frac{4(T_g - \bar{T}_r)}{T_e} \bar{J} \Bigg] \quad , \end{aligned} \tag{2.6}$$

where $\kappa_s = 0.34$ cm^2 g^{-1} is the electron scattering opacity for a fully ionized plasma. κ_R and κ_P are the Rosseland and Planck mean thermal absorption opacities, which can be numerically computed following the approximations in Hirose et al. (2009).[2] Other quantities are the radiation density constant a_r, the fluid frame zeroth angular moment of intensity $\bar{J} = (4\pi)^{-1} \oint \bar{I} d\bar{\Omega}$, and the effective temperature of the radiation $\bar{T}_r = (4\pi \bar{J}/a_r)^{1/4}$, and the electron rest mass energy expressed as a temperature T_e. The

---

[2]It turns out that our results are not sensitive to these approximations, as electron scattering dominates over the Rosseland absorption opacity, and Compton scattering dominates over the Planck mean, producing enough gas-radiation energy exchange that no significant departures from LTE occur.

gas temperature is $T_g = P_g(\rho R)^{-1}$, where R is the ideal gas constant assuming solar abundance. Note that the factor $\Gamma(1 - \boldsymbol{v} \cdot \boldsymbol{n})$ outside the square brackets comes from the frame transformation. The first term in the square brackets refers to the elastic scattering. The second and third terms represent absorption or emission process. The last term is an approximation for the gas-radiation heat exchange via Compton scattering (Blaes & Socrates 2003; Hirose et al. 2009).

In the appendix C of Zhang et al. (2021), we briefly describe how to solve radiation transport numerically and how we modify it for special relativity based on the work done by Jiang et al. (2014). Note that we assume isotropic opacities and neglect the angle and polarization dependence. We use a frequency-averaged treatment of radiation transfer with an assumed blackbody spectrum and neglect photon chemical potential and Bose-Einstein effects. We also neglect QED effects and electron-positron pair production, as we never achieve temperatures here where pair production will be important. This can be an important effect for high magnetic field strengths and/or higher temperatures in real accretion columns in ultraluminous X-ray sources, and will likely have a strong effect on photon bubble dynamics simply by reducing the Eddington limit (Mushtukov et al. 2019). On the other hand, photon bubbles might enhance radiation escape and lower the temperature inside the accretion column.

2.2.2   Simulation Domain, Initial and Boundary Conditions

We adopt a Cartesian geometry in a plane-parallel atmosphere on the neutron star surface near a magnetic pole. We initialize the simulation with a vertical magnetic field and the fluid in vertical hydrostatic equilibrium. Although our simulation uses RMHD, we neglect this and also assume a constant Newtonian gravitational acceleration for our initial condition. For the purposes of setting up the initial condition only, we assume

local thermal equilibrium (LTE) between the gas temperature and radiation effective temperature $T_g = T_r \equiv T$, and a standard Eddington closure scheme between the zeroth and second angular moments of the radiation field. We can then integrate the zeroth and first moments of the radiative transport equation to obtain the energy and momentum equations for the radiation. Meanwhile, the equations of conservation of particle number (2.3a) and energy (2.3c) become trivial because of $v^i = 0$ and LTE. Then hydrostatic equilibrium can be described by the following equations

$$\partial_z P_g = -\rho \left(g - \kappa_F \frac{F_{r,z}}{c} \right) \quad , \tag{2.7a}$$

$$\partial_z F_{r,z} = 0, \ E_r = a_r T^4 \quad , \tag{2.7b}$$

$$\partial_z P_r = -\rho \kappa_F \frac{F_{r,z}}{c} \quad , \tag{2.7c}$$

where E_r, $F_{r,z}$ and P_r are the radiation energy density, radiation flux and radiation pressure respectively. The gravitational acceleration $g = 1.86 \times 10^{14}$ cm s^{-2} is for the surface of neutron star. The flux mean opacity $\kappa_F = \kappa_s + \kappa_R$ is the effective opacity for gas-radiation momentum coupling. In order to close the system in hydrostatic equilibrium and obtain the smooth transition near the photosphere, we initialize the radiation field by the two-stream approximation as follows

$$E_r \equiv a_0^+ I^+ + a_0^- I^- \quad , \tag{2.8a}$$

$$F_{r,z}/c \equiv a_1^+ I^+ + a_1^- I^- \quad , \tag{2.8b}$$

$$P_r \equiv a_2^+ I^+ + a_2^- I^- \quad , \tag{2.8c}$$

where I^+ refers to the direction $n_z > 0$ and I^- refers to the direction $n_z < 0$. Here $n_z = \cos\theta_r$ and θ_r is the polar angle. The coefficients $a_0^\pm$, $a_1^\pm$ and $a_2^\pm$ are constants and

depend on the numerical setup of the discrete solid angles of the intensity field.

$$a_0^+ = \sum w^+ \quad, \qquad\qquad a_0^- = \sum w^- \quad, \tag{2.9a}$$

$$a_1^+ = \sum w^+ n_z^+ \quad, \qquad\qquad a_1^- = \sum w^- n_z^- \quad, \tag{2.9b}$$

$$a_2^+ = \sum w^+ n_z^+ n_z^+ \quad, \qquad\qquad a_2^- = \sum w^- n_z^- n_z^- \quad, \tag{2.9c}$$

where n_z^+ and n_z^- correspond to the direction with $n_z > 0$ and $n_z < 0$, respectively. The quantities $w^\pm$ are the weights corresponding to the directions $n_z^\pm$. Therefore, we can rewrite the hydrostatic equilibrium for the numerical purpose as follows

$$\partial_z \rho = -\frac{(1-\epsilon)\rho g}{RT} - \left(\frac{a_0^- a_1^+}{a_1^- a_2^+ - a_1^+ a_2^-} + \frac{a_0^+ a_1^-}{a_1^+ a_2^- - a_1^- a_2^+} \right) \frac{\epsilon \rho g}{4 a_r T^4} \quad, \tag{2.10a}$$

$$\partial_z T = \left(\frac{a_0^- a_1^+}{a_1^- a_2^+ - a_1^+ a_2^-} + \frac{a_0^+ a_1^-}{a_1^+ a_2^- - a_1^- a_2^+} \right) \frac{\epsilon \rho g}{4 a_r T^3} \quad, \tag{2.10b}$$

$$\partial_z I^+ = \left(\frac{a_1^+}{a_1^-} a_2^- - a_2^+ \right)^{-1} \epsilon \rho g \quad, \tag{2.10c}$$

$$\partial_z I^- = \left(\frac{a_1^-}{a_1^+} a_2^+ - a_2^- \right)^{-1} \epsilon \rho g \quad, \tag{2.10d}$$

where ϵ is the local Eddington ratio, which indicates the fraction of the gravity supported by the radiation support. Then the system can be integrated from the top given

$$\rho|_{z_\infty} = 0 \quad, \tag{2.11a}$$

$$T|_{z_\infty} = \left(\frac{a_0^+}{a_1^+} \frac{\epsilon g}{a_r \kappa_F} \right)^{\frac{1}{4}} \quad, \tag{2.11b}$$

$$I^+|_{z_\infty} = \frac{\epsilon g}{a_1^+ \kappa_F} \quad, \tag{2.11c}$$

$$I^-|_{z_\infty} = 0 \quad, \tag{2.11d}$$

where we adopt $z_\infty = 0.12 R_\star$ and $\epsilon = 0.994$, with a neutron star radius $R_\star = 10$ km.

The initial conditions are numerically integrated as shown in Figure 2.1. In order to
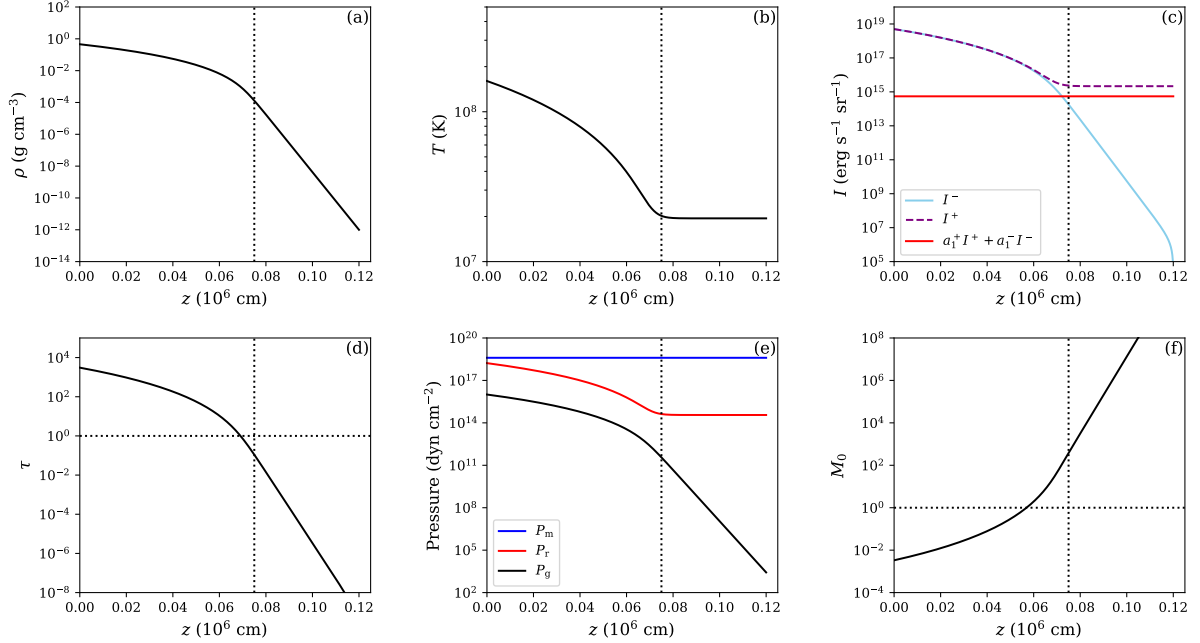
Figure 2.1: The vertical profiles of various quantities in the initial condition of the atmosphere: (a) density; (b) gas temperature, which equals the radiation effective temperature as the initial condition is assumed to be in LTE; (c) upward (I^+) and downward (I^-) two-stream intensities along with vertical radiation flux divided by the speed of light ($F_{r,z}/c = a_1^+ I^+ + a_1^- I^-$); (d) vertical Rosseland mean optical depth; (e) magnetic (P_{m}), radiation (P_{r}), and gas (P_{g}) pressures; and (f) the radiation diffusion Mach number (A.4). The vertical dotted line in all panels indicates the location where the vertical Rosseland mean optical depth $\tau = 0.1$. Horizontal dotted lines in panels (d) and (e) indicate where $\tau = 1$ and $M_0 = 1$, respectively.

resolve the gas pressure in the simulation, we want to keep the ratio of the gas pressure to the magnetic pressure ($P_m = b_\nu b^\nu/2$) as large as possible. Therefore, we adopt the magnetic field $B = 10^{10}$ Gauss and then select the top of the domain to be where the optical depth is 0.1, which is shown as the vertical dotted line in Figure 2.1. This selection guarantees that the atmosphere would be well confined by the magnetic field from $z/R_\star = 0.02$ to the top of the domain. Moreover, it covers a range of vertical optical depths from slow to rapid radiative diffusion.

We use periodic boundary conditions for the gas and radiation at the two sides. At

the top, we use an outflow boundary condition for the gas, which zeros the gradient of primitive variables at the top. However, we forbid the gas to flow into the domain from the top ghost zones:

$$\rho_{(\mathrm{k_{max}}+\mathrm{k'})} = \rho_{(\mathrm{k_{max}})} \quad , \tag{2.12a}$$

$$v_{x(\mathrm{k_{max}}+\mathrm{k'})} = v_{x(\mathrm{k_{max}})} \quad , \tag{2.12b}$$

$$v_{z(\mathrm{k_{max}}+\mathrm{k'})} = \begin{cases} v_{z(\mathrm{k_{max}})} & , \text{ if } v_{z(\mathrm{k_{max}})} \geq 0 \\ 0 & , \text{ if } v_{z(\mathrm{k_{max}})} < 0 \end{cases} \quad , \tag{2.12c}$$

$$P_{g(\mathrm{k_{max}}+\mathrm{k'})} = P_{g(\mathrm{k_{max}})} \quad , \tag{2.12d}$$

where the subscript $(\mathrm{k_{max}})$ refers to the index of z that corresponds to the highest grid cell in the active zone and $(\mathrm{k'})$ starts from the first to the last grid cell in the ghost zone. We use a vacuum boundary condition for the radiation at the top, which zeros the inward intensity at the top. This is a decent condition for the optical depths near the top, where the intensity is mostly outwards:

$$I_{(\mathrm{k_{max}}+\mathrm{k'})} = \begin{cases} I_{(\mathrm{k_{max}})} & , \text{ if } n_z \geq 0 \\ 0 & , \text{ if } n_z < 0 \end{cases} . \tag{2.13}$$

At the bottom, we use a reflecting boundary condition for the gas.

$$\rho_{(\mathrm{k_{min}}-\mathrm{k'})} = \rho_{(\mathrm{k_{min}}+\mathrm{k'}-1)} \quad , \tag{2.14a}$$

$$v_{x(\mathrm{k_{min}}-\mathrm{k'})} = v_{x(\mathrm{k_{min}}+\mathrm{k'}-1)} \quad , \tag{2.14b}$$

$$v_{z(\mathrm{k_{min}}-\mathrm{k'})} = -v_{z(\mathrm{k_{min}}+\mathrm{k'}-1)} \quad , \tag{2.14c}$$

$$P_{g(\mathrm{k_{min}}-\mathrm{k'})} = P_{g(\mathrm{k_{min}}+\mathrm{k'}-1)} \quad , \tag{2.14d}$$

where the subscript $(\mathrm{k_{min}})$ refers to the index of z that corresponds to the lowest grid cell in the active zone. The radiation boundary condition at the bottom is determined by enforcing hydrostatic equilibrium there in the two-stream approximation.

$$I_{(\mathrm{k_{min}}-\mathrm{k'})} = I_{(\mathrm{k_{min}}-\mathrm{k'}+1)} + \begin{cases} \left(a_2^+ - \dfrac{a_1^+}{a_1^-}a_2^-\right)^{-1} \epsilon\rho_{(\mathrm{k_{min}}-\mathrm{k'}+1)}g\Delta z, & \text{if } n_z \geq 0 \\[3mm] \left(a_2^- - \dfrac{a_1^-}{a_1^+}a_2^+\right)^{-1} \epsilon\rho_{(\mathrm{k_{min}}-\mathrm{k'}+1)}g\Delta z, & \text{if } n_z < 0 \end{cases} . \tag{2.15}$$

In the initial condition, this leads to an upward constant radiation flux, which arises from the assumed constant Eddington ratio ϵ. Then with the local primitive variables, we can compute the $I^\pm$ in the bottom ghost zones with first-order accuracy as follows

$$I_{(\mathrm{k}-1)}^+ = I_{(\mathrm{k})}^+ + \left(a_2^+ - \frac{a_1^+}{a_1^-}a_2^-\right)^{-1} \epsilon\rho_{(\mathrm{k})}g\Delta z \quad, \tag{2.16}$$

$$I_{(\mathrm{k}-1)}^- = I_{(\mathrm{k})}^- + \left(a_2^- - \frac{a_1^-}{a_1^+}a_2^+\right)^{-1} \epsilon\rho_{(\mathrm{k})}g\Delta z \quad, \tag{2.17}$$

where subscript (k) refers to the index of z in the active zone.

We set up five simulations with different domain sizes, resolutions and durations as shown in Table 2.1. All simulations evolve toward collapse of the atmosphere, but we

Version	Name	Mesh	Width $(R_\star)$	Height $(R_\star)$	Resolution $(\mathrm{cm^2/grid\,cell})$	Duration (t_{sim})
0	LR	340×512	0.0500	0.075	147×146	1000
1	MR	680×1024	0.0500	0.075	74×73	1000
2	HR	680×3072	0.0167	0.075	25×24	300
3	SHR	1280×9472	0.0100	0.075	8×8	200
4	UHR	2560×18944	0.0100	0.075	4×4	200

Table 2.1: Domain size, resolution, and duration of all the simulations.

are only able to investigate this in detail in the nonlinear regime in the low-resolution (LR) and medium-resolution (MR) simulations, which we run for $1000t_{\mathrm{sim}}$. Here $t_{\mathrm{sim}} = 2.8 \times 10^{-7}$ s is the simulation time unit in this chapter, roughly corresponding to the

(vacuum) light crossing time across a radiation pressure scale height. The three higher resolution simulations provide a resolution study. Therefore, we only evolve the instability within the linear regime and run high-resolution (HR), super-high-resolution (SHR) and ultra-high-resolution (UHR) simulations for $300t_{\mathrm{sim}}$, $200t_{\mathrm{sim}}$ and $200t_{\mathrm{sim}}$, respectively, given limited computational resources. All simulations are launched by applying cell-to-cell random perturbations on the initial profile in all variables with a fractional amplitude 10^{-3}.

There are two reasons that we prefer to apply random perturbations rather than excite one single mode: 1. the simulation is initialized by using the approximate hydrostatic equilibrium, which deviates from the true solution. Such deviation and the numerical error from the discretization of simulation grids would both contribute to the actual initial perturbation. So the linear instability would be dominated by a particular short-wavelength mode from this systematic perturbation. Therefore, we apply the cell-to-cell random perturbation to broaden the spectrum of initial perturbations. 2. in the neutron star column accretion problem, the perturbations are intrinsically random. So studying the instability in the random perturbation would provide more insight to understand the multi-mode behavior of in such system.

2.3   Results

In the following sections, we present and evaluate the simulation results. In section 2.3.1, we adopt the MR simulation as our fiducial simulation to give an overall description and explanation of the evolution of photon bubble instability. In section 2.3.2, we use both the MR and UHR simulations to evaluate the consistency between the simulation results and the analytical dispersion relation. In section 2.3.3, we compare the simulations at different resolutions and discuss the discrepancies introduced by finite res-

olution. Note that the resolution dependence is studied in the linear regime with all five simulations but in the nonlinear regime with only the LR and MR simulations.

The photon bubble instabilities appear in all five simulations. Animations are available online[3]. Note that in section 2.3.1 and section 2.3.2, we only focus on the MR simulation and use it to study the photon bubble instability for the following reasons: 1. only the LR and MR simulations are evolved long enough for the atmosphere to collapse due to the photon bubble instability. 2. compared with the LR simulation, the MR simulation is less noisy and has better numerical performance. 3. the MR simulation can resolve shorter wavelengths than the LR simulation, where the photon bubble instability grows faster.

2.3.1 Overview of Evolution

We track the fluctuations in terms of characteristic variables at each snapshot to study the evolution of the photon bubble instability. In the simulation, the instability patterns gradually appear from the top to the bottom because the instability growth rate is different at each height. The instability grows faster and first becomes nonlinear towards the top, since the radiation diffuses more rapidly as the gas density decreases. As the instability grows, gas and radiation are gradually spatially decoupled. Such decoupling eventually makes the gas lose the radiation support and sink down due to the gravity. Then the whole atmosphere collapses and the radiation freely leaves the domain at the top.

Before the nonlinear phase of the instability starts to dominate the system, we select four different heights ($z/R_\star = 0.02, 0.03, 0.04$ and 0.05, where the magnetic field continues to be strong enough to constrain the gas to move vertically) to study the linear growth of the instability by monitoring the horizontally averaged perturbations in density, velocity

---

[3]https://youtube.com/playlist?list=PLbQOoEYOCFpW276rfp1Wuzc0uoE6726cO

Perturbation Measurement (MR, v1)
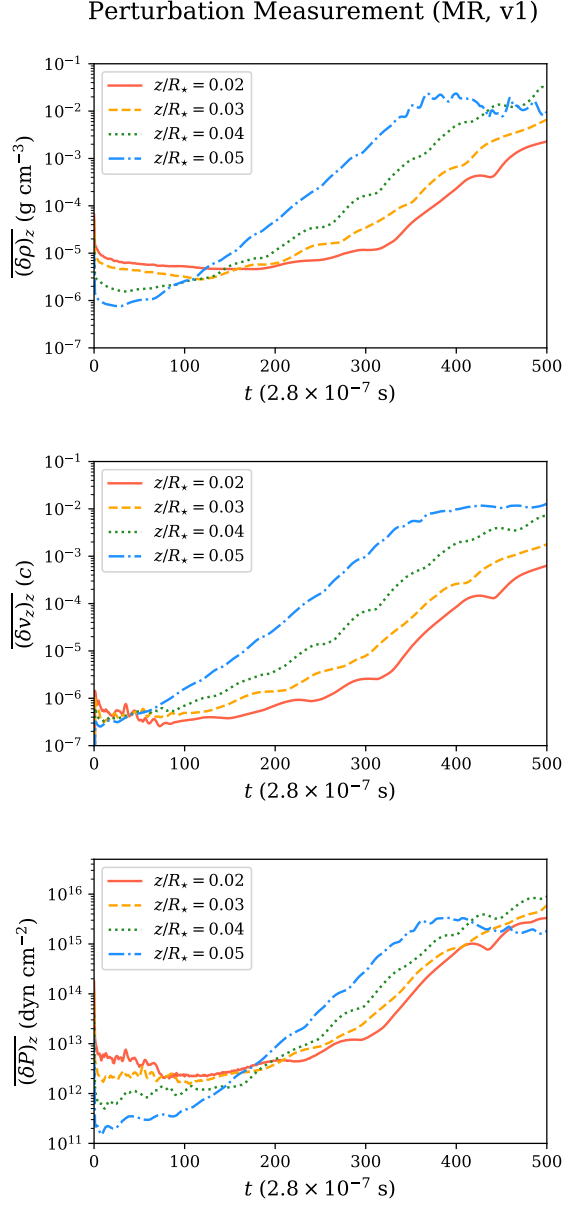
Figure 2.2:   Horizontal average of the absolute value of perturbations with respect to the unperturbed initial profile in density (top), vertical velocity (middle) and thermal pressure (bottom) as a function of time and for various altitudes in the simulation as indicated.

and pressure.   Specifically, we use v_z and P to denote the velocity in z-direction and the total pressure of the gas and radiation respectively. Note that $P \simeq P_r$ because the regime is radiation-dominated. As shown in the Figure 2.2, in the beginning, the initial

perturbations at each height are relaxed by the system since the initial condition is not in the perfect hydrostatic equilibrium. After the system is relaxed close to the hydrostatic equilibrium, the linear instability starts to grow independently at each height, growing fastest in the highest altitude regions. As the linear instability grows, the fluctuations at different heights propagate and interfere with each other. During such interference, one region would be dominated by another. In our case, fluctuations in higher regions always dominate lower regions because of the higher instability growth rate. Therefore, we can approximately identify when the interference happens by tracing the time that growth rates at two adjacent heights start to synchronize (Table 2.2), where we denote such time as t_{syn}. As the simulation continues, the photon bubble instability becomes nonlinear and thus we stop tracking the perturbations.

$z/R_\star$	$0.05 \to 0.04$	$0.04 \to 0.03$	$0.03 \to 0.02$
$t_{\mathrm{syn}}/t_{\mathrm{sim}}$	~ 310	~ 330	~ 350

Table 2.2: The approximate times when the linear growth rates synchronize between two adjacent heights in the MR simulation.

We pick three snapshots at $t/t_{\mathrm{sim}} = 200$, 400 and 800 from the MR simulation. The format of each snapshot is the same, where the upper-left panel refers to the gas density; lower-left refers to the gas density variation; upper-middle refers to the fluid velocity; lower-middle refers to the vertical velocity variation; upper-right refers to the gas-radiation pressure; lower-right refers to the gas-radiation pressure variation. Note that in the upper-middle panel, the color represents the magnitude of the velocity and the black arrows indicates the directions of the velocity. As shown in Figure 2.3, the system is at the early stage of the linear instability at $t/t_{\mathrm{sim}} = 200$ before the first synchronization time and the instability grows independently at each height. Although the density profile is rather smooth, the instability patterns are already clear and roughly consistent in the variation (lower) panels. Moreover, we can find that the tilted angles of

27

$t = 200 \times (2.8 \times 10^{-7} \text{ s})$ (MR, v1)

Figure 2.3: Snapshot at $t = 200 \times (2.8 \times 10^{-7} \text{ s})$ in the MR simulation.

$t = 400 \times (2.8 \times 10^{-7} \text{ s})$ (MR, v1)

Figure 2.4: Snapshot at $t = 400 \times (2.8 \times 10^{-7} \text{ s})$ in the MR simulation.
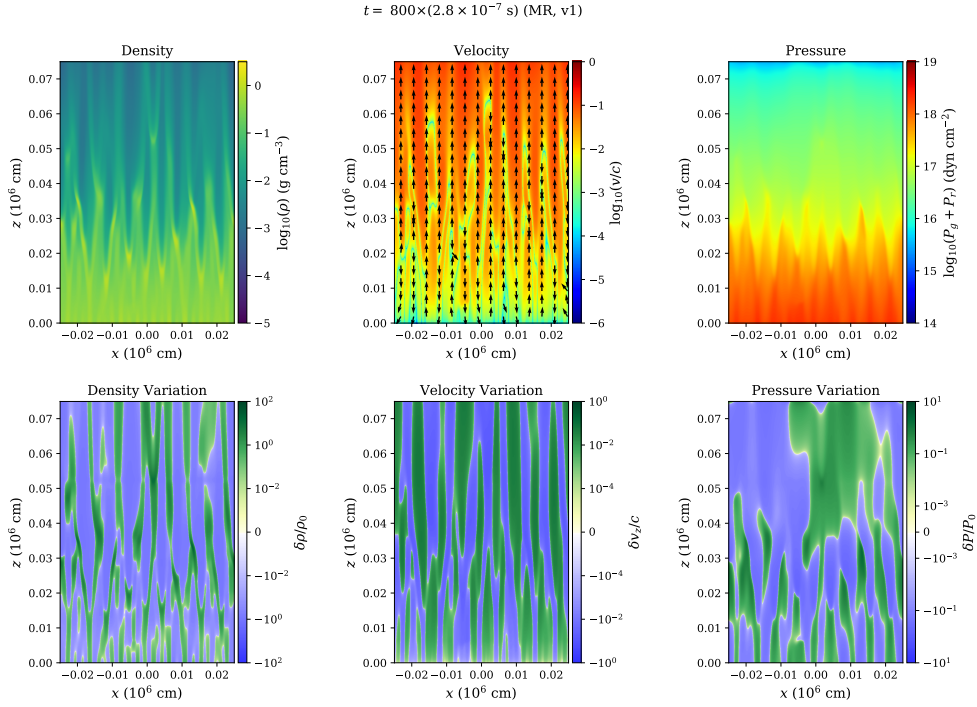
Figure 2.5: Snapshot at $t = 800 \times (2.8 \times 10^{-7} \text{ s})$ in the MR simulation.

the instability patterns become more vertical towards the bottom. This agrees with our analytical solution that the maximum growth rate peaks at more vertically tilted angles as the diffusion regime becomes slower (i.e. $M_0 \to 0$) and we will discuss details in the section 2.3.2. As shown in Figure 2.4, the contrast in density profile at the top is large enough to see the pattern. Meanwhile, the instability patterns become more irregular at $t/t_{\text{sim}} = 400$. The instabilities at higher regions clearly step into the nonlinear phase, which would gradually propagate down and interfere the regions below. Furthermore, the gas is sinking after losing the radiation support because of the spatial decoupling between gas and radiation. Eventually, the whole atmosphere collapses at $t/t_{\text{sim}} = 800$ as shown in Figure 2.5. At this stage, the gas and radiation are driven into different channels by the instabilities, where the gas sinks downwards and the radiation escapes upwards. Now we can zoom in to these selected snapshots to track the gas-radiation
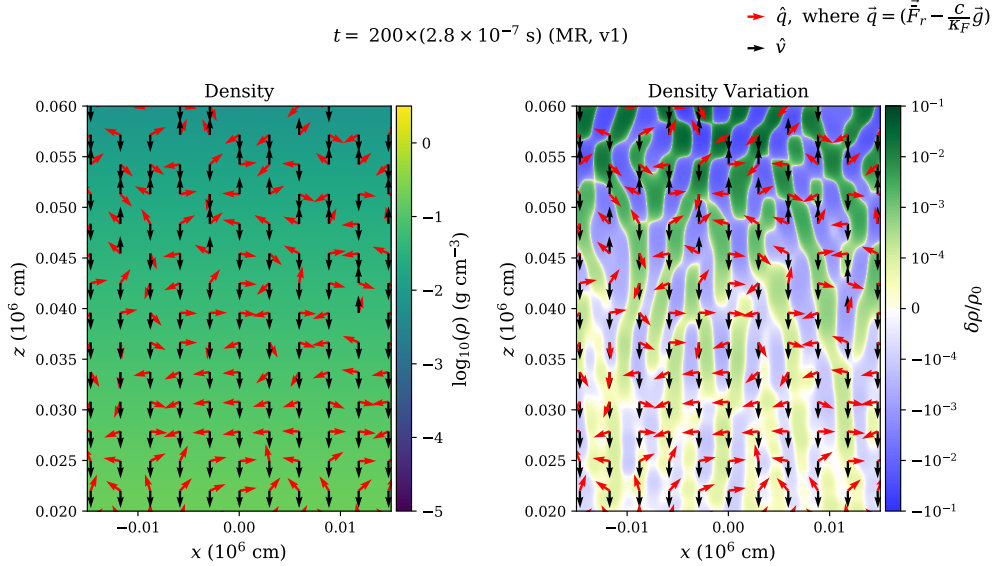
Figure 2.6: Zoom-in profiles at $t = 200 \times (2.8 \times 10^{-7}$ s) in the MR simulation. Black arrows indicate unit vectors in the direction of the local velocity, and red arrows indicate unit vectors in the direction of the portion of the radiation flux that is not providing hydrostatic support.

decoupling via gas velocity and heat flow. Figure 2.6 shows the density distribution (left) and density variation (right) at time $t/t_{\text{sim}} = 200$, when we are still in the linear regime. Arrows show the directions of velocity (black) and the portion of the radiation flux (red) that is not providing hydrostatic support. As we discussed in section 2.1, the vertical component of this portion is what drives the linear photon bubble instability, and indeed we find that this heat predominantly flows from regions of high perturbed density to the regions of low perturbed density (see red arrows in Figure 2.6). This is a clear indication of photon bubble instability in the slow diffusion regime. Since the heat flow is mostly in the form of radiation, the radiation further evacuates the low perturbed density regions and eventually causes spatial decoupling from the gas. Meanwhile, the gas in high perturbed density regions is gradually sinking because of loss of radiation pressure support (see black arrows in Figure 2.6). This decoupling process becomes more intense as the instability grows. As shown in Figure 2.7 at $t/t_{\text{sim}} = 400$, the instability in
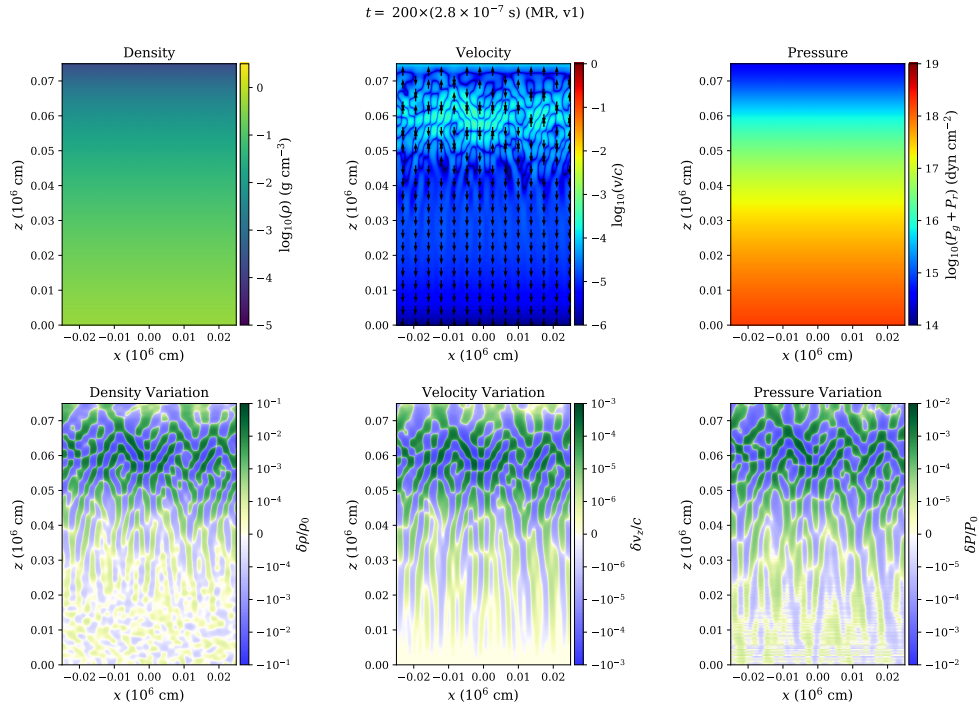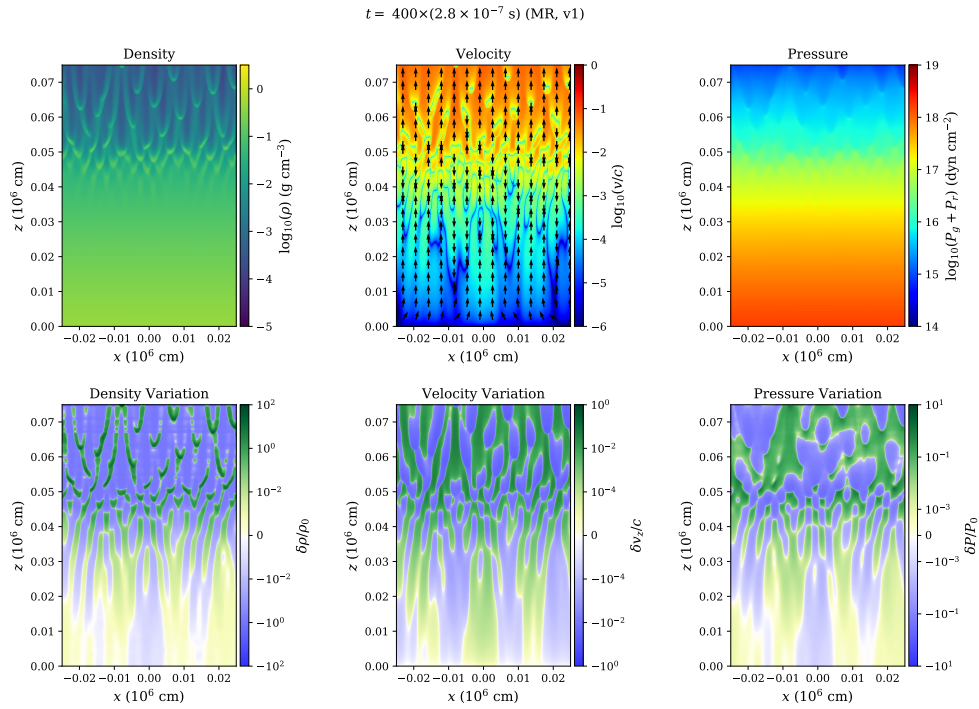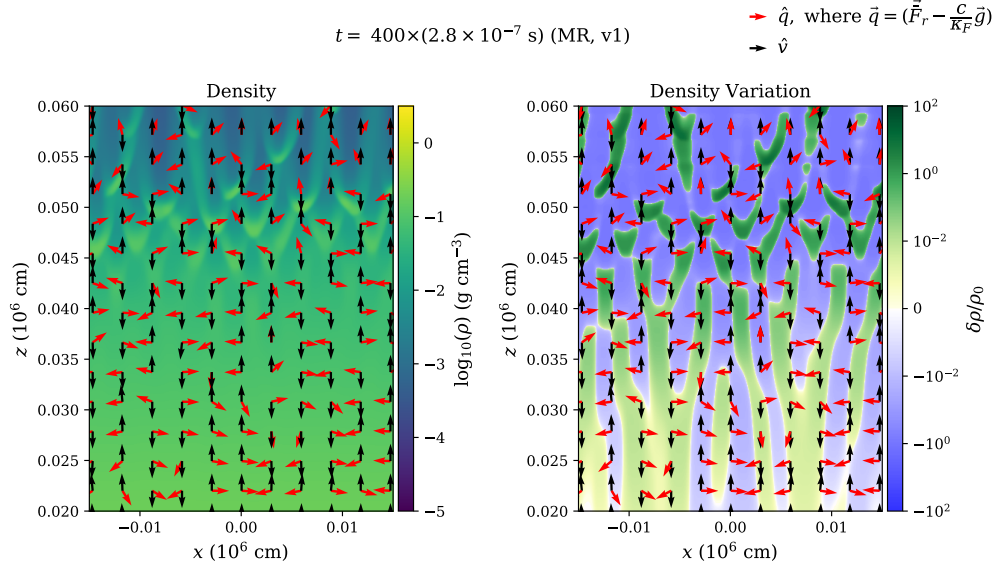
Figure 2.7: Zoom-in profiles at $t = 400 \times (2.8 \times 10^{-7} \text{ s})$ in the MR simulation.
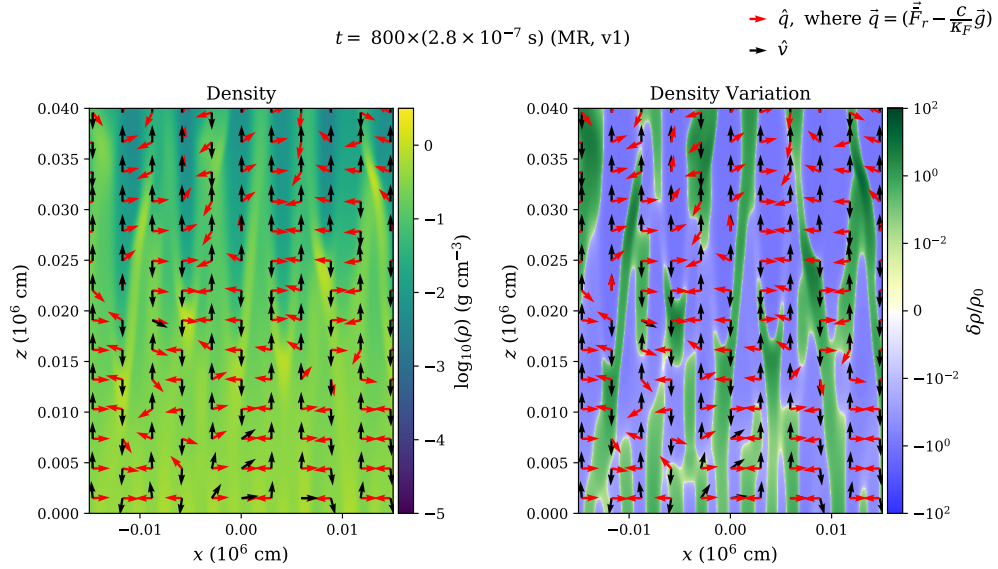
Figure 2.8: Zoom-in profiles at $t = 800 \times (2.8 \times 10^{-7} \text{ s})$ in the MR simulation.

upper region grows into nonlinear phase and the density contract become more clear. The gas in high density regions keeps sinking, while the radiation in low density regions escapes upwards and blows the gas away. Finally, the whole system become nonlinear at $t/t_{\text{sim}} = 800$ as shown in Figure 2.8, where the gas and radiation are clearly separated

in different channels by the effects of photon bubble physics. Note that by this time the fluid velocity is no longer entirely vertical at the base, indicating significant bending of the magnetic field lines there.

2.3.2   Comparison with Linear Theory

At each wavelength, there is a specific angle θ_{max} between the wave vector direction and the vertical that maximizes the linear growth rate of the instability (see Figure A.1). This is essential for understanding the instability pattern. Therefore, we solve for θ_{max} at each selected height as a function of wavelength, and show the results in Figure 2.9. The stars indicate the maximum growth rate by numerically solving the dispersion re-
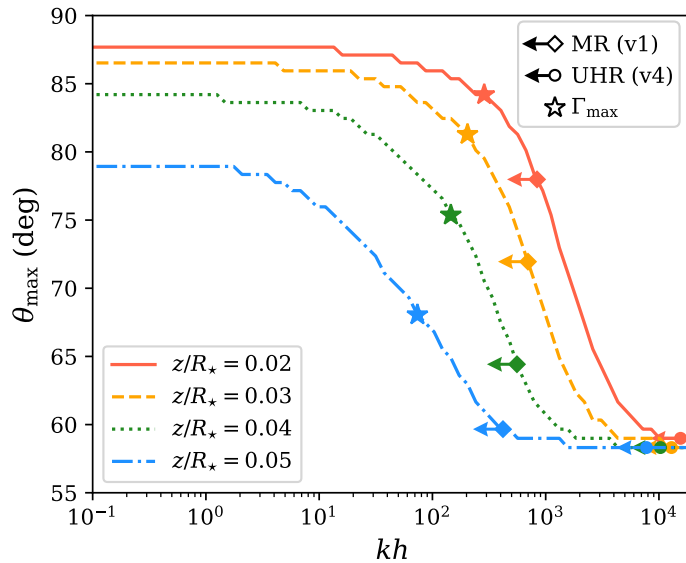
Figure 2.9: The analytical dependence of the angle corresponding to the maximum growth rate (θ_{max}) as a function of wavenumber. The stars indicate the theoretical maximum growth rate at each height. The diamonds and dots with arrows refer to the minimum resolved wavelength (2 grid zones) in the MR and UHR simulations, respectively.

lation (A.11) with the constant opacity given the profile at each height. The shortest wavelengths that can be resolved (2 grid zones for a crest and a trough) are marked

with diamonds for the MR simulation and dots for the UHR simulation, where the arrow indicates the longer wavelengths that can be resolved. Short wavelengths generally grow fastest until the viscous length scale is reached (Figure A.1), and therefore tend to dominate the instability pattern. High altitudes have the smallest $\theta_{\max}$, and $\theta_{\max}$ approaches 90° as the height decreases. This is consistent with the overall instability patterns becoming less tilted with decreasing height as shown in Figure 2.3. In Figure 2.9, we also notice the wider range of $\theta_{\max}$ in higher altitude regions. This suggests the 'block structure' along these tilted patterns from the mixing modes because some less dominant modes tweak the substructure of the tilted pattern to be more vertical, which can also be seen directly in the variation (lower) panels of Figure 2.3.

To test the analytical expectation of the instability growth rate and the tilted angles, we first need to measure the wavelength from the fluctuations in the linear growth phase. Since the modes are mixed, we distinguish the wavelengths in Fourier space. Here, we briefly describe how we obtain the dominant wavelength from the simulation data. At each selected height, we first analyze the horizontal profile to obtain the perturbation with respect to the unperturbed initial condition (e.g. $\delta\rho$, δv_z or δP) as a function of horizontal distance x. Next, we project these variables into Fourier space, in order to identify the dominant mode from the peak in the power spectrum. We then pick the measured wavelength of the dominant mode and calculate the corresponding $\theta_{\max}$. Note that here the horizontal wavelength $\lambda_\perp = \lambda/\sin\theta_{\max}$ (where '⊥' means perpendicular to the magnetic field) is the horizontal projection of the real wavelength (λ). Therefore, we need to correct it with the angle by iterating the value of $\theta_{\max}$ until it converges within some tolerance we choose (e.g. 10^{-8}). The results of the measurements based on δv_z in all simulations are listed in Table 2.3. As shown in Figure 2.10, we plot the measured wavelengths (solid red lines) and the predicted constant phase plane orientations (dashed red lines) of the dominant mode at each selected height, which are quite consistent with

z	M_0	h	h_g	l_{vis}	LR (v0) $t/t_{\mathrm{sim}} = 300$		MR (v1) $t/t_{\mathrm{sim}} = 250$		HR (v2) $t/t_{\mathrm{sim}} = 150$		SHR (v3) $t/t_{\mathrm{sim}} = 100$		UHR (v4) $t/t_{\mathrm{sim}} = 100$	
					$\theta_{\max}$	λ	$\theta_{\max}$	λ	$\theta_{\max}$	λ	$\theta_{\max}$	λ	$\theta_{\max}$	λ
$(R_\star)$		(cm)	(cm)	(cm)	(deg)	(cm)	(deg)	(cm)	(deg)	(cm)	(deg)	(cm)	(deg)	(cm)
0.02	0.01	19760	148	433	87.36	7116	87.13	4277	86.44	1661	84.94	622	85.17	644
0.03	0.03	16438	123	506	85.98	8102	85.52	4202	84.13	1505	82.17	660	82.17	660
0.04	0.08	13133	98	568	82.86	6185	82.05	3804	80.31	1739	77.85	873	77.15	777
0.05	0.29	9887	73	843	76.32	6107	74.78	3636	71.90	1673	67.74	712	68.61	861

Table 2.3: Data measurements in linear phase of all simulations
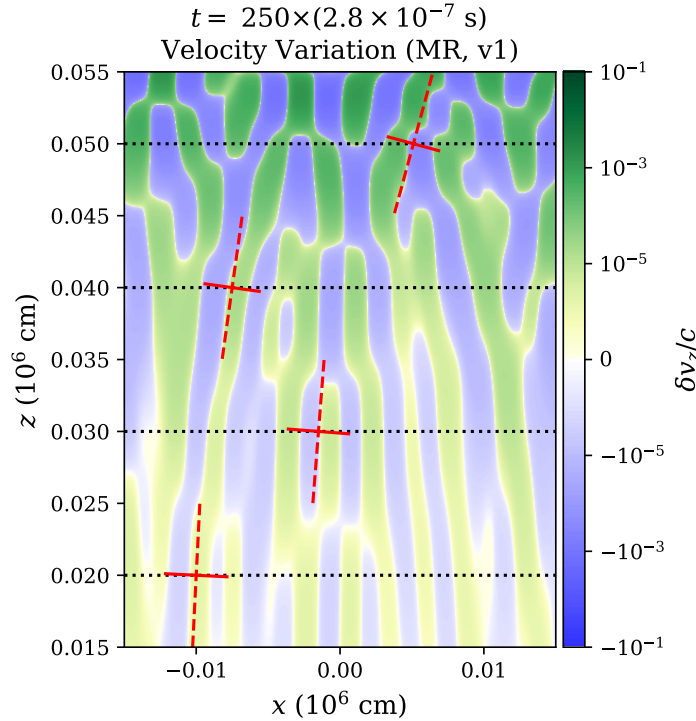
Figure 2.10:   Comparison of the tilt angles of the dominant modes at different heights in the MR simulation with that expected from linear theory. Dashed lines are oriented along constant phase surfaces, and solid lines indicate wavelength perpendicular to the constant phase surfaces.

the instability pattern observed in the simulation. However, we notice that the fastest growing wavelength at each height is not what we expected earlier as 2 grid zones in the MR simulation but it is ~ 50 grid zones instead. This is because of damping effects arising from numerical diffusion. In all versions of our photon bubble simulations, these numerical damping effects start to become important at wavelengths below ~ 50 grid

zones. This can be contrasted with the *ZEUS* simulations of Turner et al. (2005) of photon bubbles in the rapid diffusion regime, where numerical damping was significant at wavelengths below ~ 10 grid zones. Thus, the numerical damping at short length scales makes resolution a challenge.
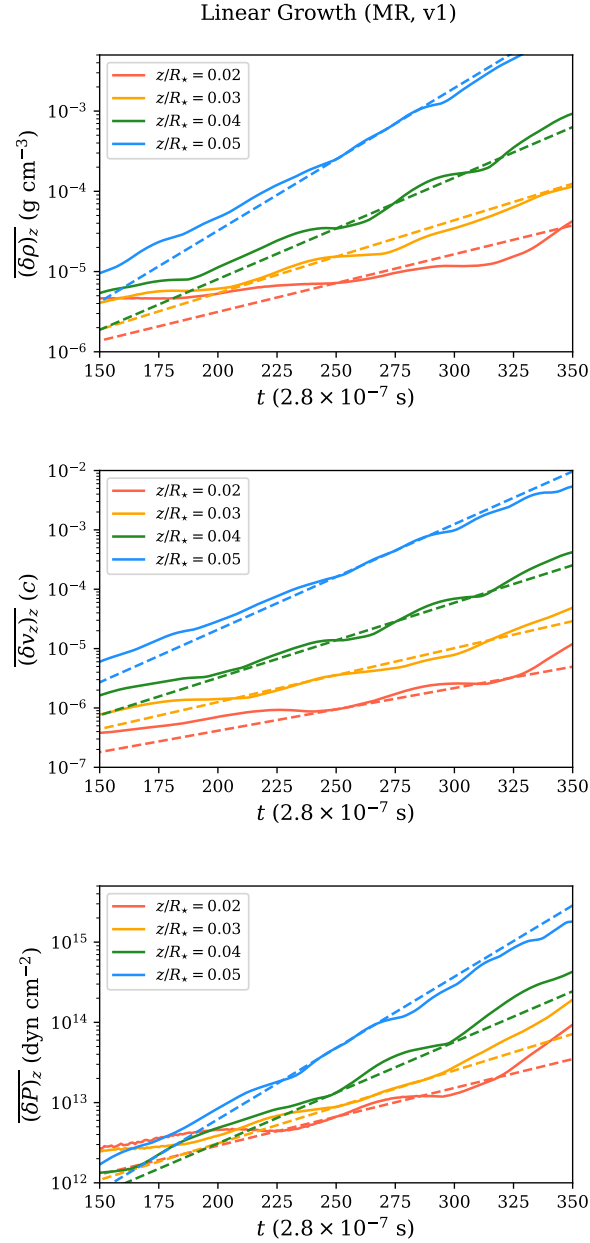
Figure 2.11:   Comparison of linear growth rates with behavior measured in the MR simulation.

With the measurements of the dominant wavelength at each height, we can compute the analytical growth rates and compare them with the simulation data as illustrated in Figure 2.11. In the MR simulation, the measured linear growth rates (solid lines) are fairly consistent with the analytical calculation (dashed lines), where the analytical calculation is based on the snapshot at $t/t_{\mathrm{sim}} = 250$. Similarly, we also compute the analytical growth rate in the MR and UHR simulations as a function of wavelength by selecting the angle θ_{max} corresponding to the maximum growth rate. As shown in Figure 2.12, each lines represent the analytical solutions at different heights. The solid
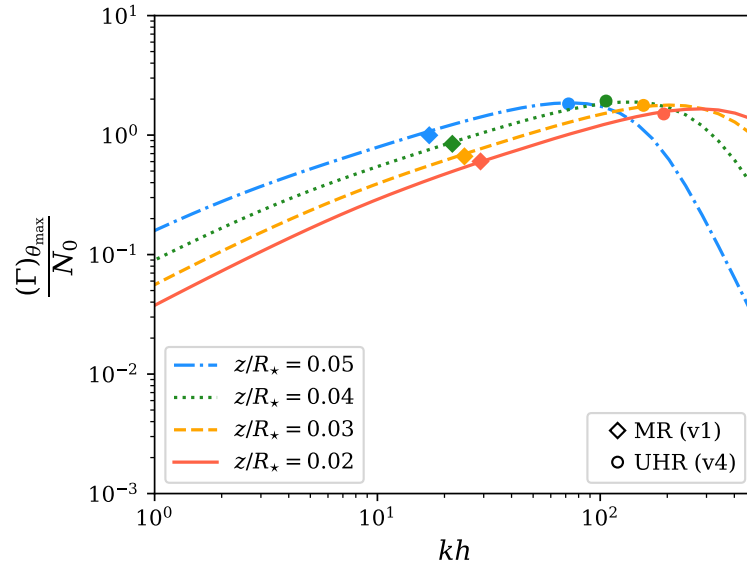
Figure 2.12: The analytical dependence of the growth rate, scaled with the sound crossing frequency over a scale height $N_0 = c_r/h$, at θ_{max} on wavenumber. The diamonds and dots represent the linear fits to the MR and UHR simulation data, respectively, given the measured wavelengths of the dominant modes.

diamonds and dots are the measurements of the dominant modes in the MR and UHR simulations respectively. The linear growth rates are generally larger in higher altitude regions simply because the radiation diffuses faster. The simulated growth rates of the dominant modes again are fairly consistent with the analytical solution. Note that the growth rate reaches a finite maximum and then declines toward shorter wavelengths

because of radiation viscosity.   The length scale of this peak growth rate is small and requires high resolution in the simulation.   Among the five simulations, only the SHR and UHR simulations roughly reach the analytical maximum growth rate of the photon bubble instability. Details will be discussed in the next section.

2.3.3   Resolution Dependence

According to the linear theory (see Appendix A for details), we expect that simulations of photon bubble instability will be resolution-dependent because the instability grows faster at shorter wavelengths until the wavelength reaches the maximum at radiation viscous length scale, which is small and thus requires high resolution. The shortest wavelength that can be resolved is at least two grid zones in order to resolve a crest and a trough, but numerical diffusion affects the results at much longer wavelengths than this. As we just discussed, we find that unstable modes roughly require at least 50 grid zones to avoid significant numerical damping in our MR resolution simulation. In the LR simulation, we perform similar measurements at $t/t_{\mathrm{sim}} = 300$ as shown in Table 2.3, where the fastest growing wavelengths are on average 47 grid zones, comparable to what we found in the MR simulation. Note that we select a later snapshot compared with the MR simulation because the dominant modes in the LR simulation have longer wavelength in general, and therefore grow more slowly. This trend continues as we keep increasing the resolution, until the simulation starts to resolve the radiation viscous length scale. The discrepancy of the growth rates at different heights increases when the dominant modes move toward longer wavelengths as shown in Figure 2.12, which indicates that the instability in the low altitude regions is suppressed and synchronized faster by the instability propagating downward from high altitudes. This complicates the mode analysis at the low altitudes. In short, simulations of photon bubbles need to have high enough

37

resolution that the more slowly growing modes at low altitude are at least able to start their linear growth phase before they are affected by downward propagation of the faster growing modes at high altitude. On the other hand, we find that the nonlinear outcome of both the LR and MR simulations are qualitatively similar, and they both collapse. However, the LR simulation takes longer to collapse, and the photon bubble channels that form have longer horizontal length scales.
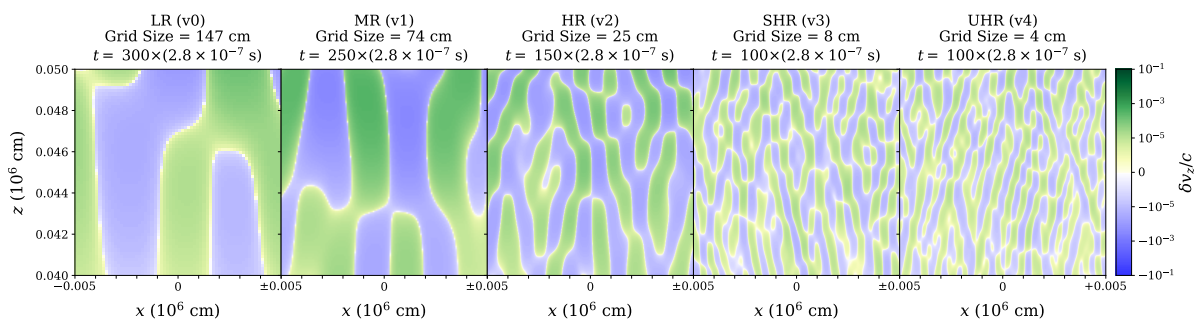
Figure 2.13:   Side-by-side comparison of linear-phase photon bubble instability at different resolutions, for the same portions of the simulation domains. The length scales of the dominant modes decrease with increasing resolution, until convergence is achieved at the viscous length scale for the two highest resolution simulations on the right.

In order to study the resolution dependence of photon bubble instability, we ran three extra simulations through the linear growth phase by increasing the grid cell size to 25 cm, 8 cm and 4 cm, respectively. Snapshots of the instability patterns of all five simulations are shown in Figure 2.13. The dominant wavelength keeps decreasing as the resolution increases until the SHR simulation at resolution ~ 8 cm. A further increase in resolution to ~ 4 cm in the UHR simulation produces hardly any change in the spatial scale of the photon bubble. As shown in Figure 2.14, we have roughly reached the convergence at grid cell size ~ 8 cm, where the dominant wavelength nearly reaches the radiation viscous length scale at each selected height.

The evolution in the nonlinear regime is also affected by resolution, as we show in Figure 2.15. The left panel shows that the mass-weighted height of the atmosphere
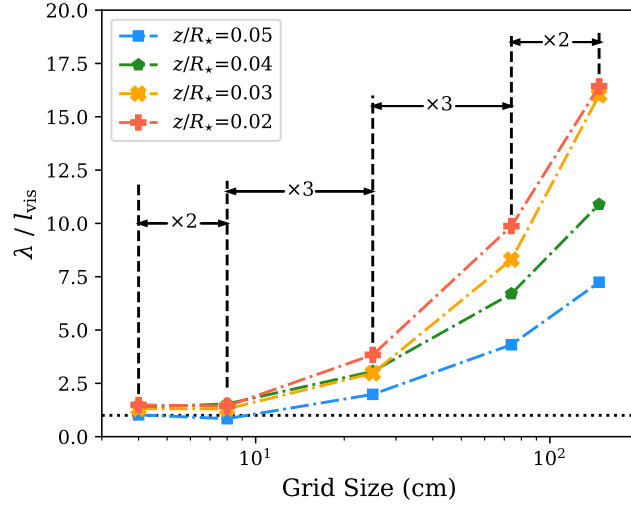
Figure 2.14:   Numerical convergence of the different resolution simulations, at different altitudes as indicated. The horizontal intervals $\times 2$ and $\times 3$ indicate the increased resolution factors between simulations. The horizontal dotted line indicates unity, and shows that the two highest resolution simulations have dominant wavelengths equal to the viscous length scale for maximum growth, in agreeement with linear theory.
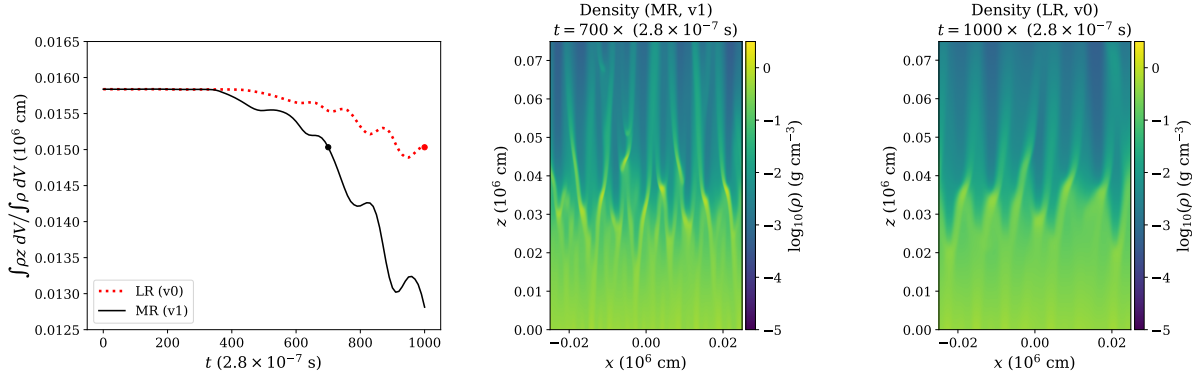
Figure 2.15:   Left: Evolution of mass-weighted height of the atmosphere in the high resolution (black) and low resolution (red dotted) simulations. Snapshots of the density distribution a times indicated by the points in the left panel (when both simulations have collapsed to the same height) are shown in the middle (high resolution) and right (low resolution) panels.

decreases as the system collapses. The MR simulation collapses more rapidly because it is able to resolve the faster growing shorter wavelength modes of the instability. These modes persist well into the nonlinear regime, as illustrated in the density snapshots shown in the middle and right hand panels of Figure 2.15. By simply counting the peaks in

the horizontal density variation at each height in the snapshot, we find that the average horizontal length scale in the snapshots are 3375 cm for the MR simulation and 6168 cm for the LR resolution simulation, which is consistent with the horizontal projection of the photon bubble wavelength in the high altitude regions. The ratio of 1.8 is close to the factor of two difference in grid resolution.

Figure 2.16 depicts the evolution of the vertical radiation flux in the two simulations. The left hand panel shows the vertical radiation flux averaged over the simulation domain,
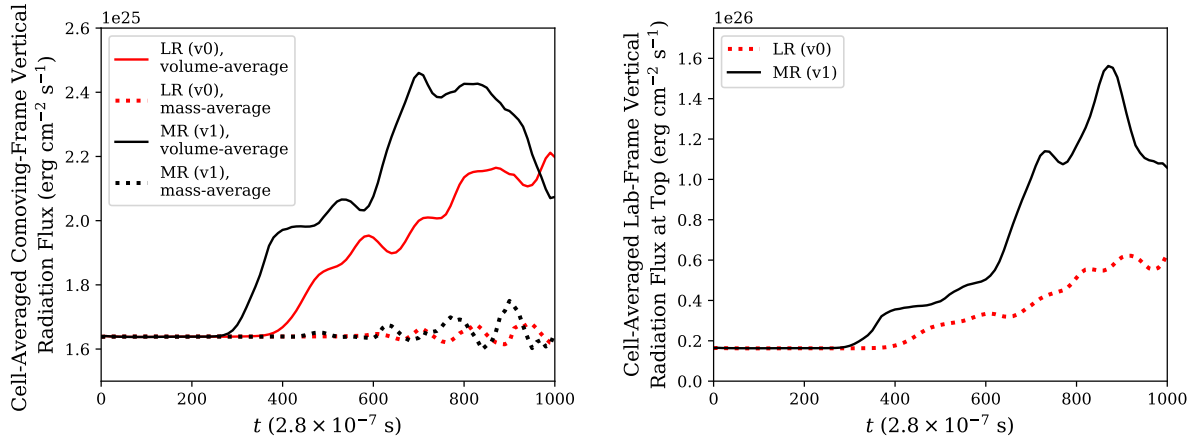
Figure 2.16:   Left: Evolution of volume-averaged (solid) and mass-averaged (dotted) comoving-frame vertical radiation fluxes in the high resolution (black) and low resolution (red) simulations. Right: Evolution of lab-frame vertical radiation flux leaving through the top of the simulation domain.

with solid curves showing a volume average and dotted curves showing a mass-weighted average. The latter is far below the former, illustrating the fact that photons are escaping preferentially through the low density channels formed by the photon bubble instability, and therefore the denser regions are no longer supported against gravity by radiation pressure, causing the collapse. The radiation escape rate is significantly higher for the MR simulation, which is why it collapses faster. The right panel shows the horizontally-averaged radiative flux that leaves through the top of the simulation domain. Again, the rate at which radiation leaves the simulation domain is significantly higher for the

MR simulation. Note that we did not evolve the HR, SHR and UHR simulations to the nonlinear regime because of limited computational resources.

The closest simulations to those we have presented here are those of Hsu et al. (1997), who also simulated the growth of photon bubbles in static atmospheres. Because of better computational resources available today, we have been able here to run simulations at much higher resolutions and use a more extended simulation domain. Even our lowest resolved simulation (LR) has grid cell sizes smaller by factor of ~ 2.4 than the finest grid used in Hsu et al. (1997). They also used grids that reduced resolution with altitude, which would cause slower growth of the photon bubble instability in these regions. Our simulations cover a broader parameter space of radiation diffusion, with M_0 ranging from ~ 0.005 to ~ 100. Our simulations also directly solve the full angle-dependent radiative transfer equation, whereas they used flux-limited diffusion. Therefore, we are able to reach length scales where photon viscosity is important, and even use grid cell sizes that are optically thin. The maximum growth rate of our photon bubbles is naturally limited by the radiation viscosity at high enough resolution. The magnetic field direction in our simulations is vertical (the same as the gravitational field) and thus our simulations have a left-right horizontal symmetry in the fastest growing photon bubble modes. Hsu et al. (1997) adopted a slightly tilted magnetic field instead, which breaks this symmetry of their photon bubbles, and the dominant modes only propagate in one direction. Finally, we solve the MHD equations so the gas motion is constrained by a dynamical magnetic field ($B = 10^{10}$ Gauss), while Hsu et al. (1997) impose 1D motion of the gas to mock up the effects of a strong magnetic field.

Despite these differences, the numerical outcomes in both sets of simulations are very similar. Both we and Hsu et al. (1997) find that photon bubbles align close to the equilibrium magnetic field in the lower altitudes where diffusion is slowest, and that in the nonlinear regime, the photon bubble instability drives the collapse of the atmosphere

starting from high altitudes. Hsu et al. (1997) also find that the density structures that form in the instability are smaller with higher numerical resolution, as we also find. However, they suggested that their photon bubbles tend to merge toward longer length scales in terms of their transport properties. In particular, although the density fluctuations are on smaller length scales with increasing resolution, they found that the radiation energy density is spatially smoother because of radiation diffusion. We find similar results but only at high altitude. As shown in Figure 2.5, the spatial structure of radiation energy density closely tracks that of density even well into the nonlinear regime at low altitudes. However, at high altitudes where the atmosphere is collapsing and radiation is able to diffuse much more quickly, we do see much broader structures in the radiation energy density, in agreement with Hsu et al. (1997).

2.4   Discussion and Conclusions

All of the numerical experiments we have done in this chapter are in preparation for a more global simulation of a neutron star accretion column. We have demonstrated here that we can successfully resolve photon bubbles and capture their nonlinear dynamics in a static medium. In the next chapter we will present our results on the impact of this instability on magnetically confined, accreting columns in Cartesian geometry. While the simulations here had horizontally periodic boundary conditions and therefore lacked a boundary confined against radiation pressure by magnetic tension, we nevertheless successfully managed to constrain the gas motion by the strong magnetic fields in radiative RMHD simulations. This is critical for a more global simulation in which the magnetic field will have to provide lateral confinement of the accretion column. There radiation will likely escape the column mostly from the sides (Basko & Sunyaev 1976), not the top as in the simulation here. Whether the spatial resolution of the grid is as much of an issue

in controlling the dynamics in that case, given the vertical shape of the photon bubble channels, remains to be seen. A global simulation will also require accretion of material from the top boundary, which we have not yet incorporated here. Such accretion is the only way that a steady-state column structure might develop against the photon bubble collapse that we found here.

We summarize our conclusions of this chapter as follows:

1. In the numerical simulation of the radiation-supported and magnetized atmosphere on neutron star, we resolve the characteristics of the photon bubble instability in the slow diffusion limit and explore the multi-mode behaviors depending on the radiative diffusion, propagation direction and wavelength. In particular, modes grow most quickly at altitude where radiative diffusion is faster, with wave fronts that are significantly inclined to the vertical. At depth where diffusion is more slow, the modes grow more slowly with wave fronts that are more aligned with the vertical magnetic field.

2. We confirm the consistency between the numerical simulation and the linear theory of photon bubble instability. The simulation results illustrate the robustness of the current code framework of ATHENA++ in the linear phase and provide more insights into the non-linear dynamics caused by the photon bubble instability. The faster growing, inclined modes at altitude spread downward. However, the slow diffusion modes at depth eventually grow and result in vertical concentrations of density on magnetic field lines, separated by more tenuous reasons which allow for more rapid diffusion of photons. This eventually always results in collapse of the atmosphere. How this gets modified in the presence of additional mass supply from the top is the subject of the next chapter.

3. We perform a resolution study and explore the resolution dependence of the photon

bubble instability in the simulation, which suggests that the dynamical system involved with the photon bubble instability requires high resolution to capture the correct dynamical effects. Low resolution simulations, while still collapsing, do so on longer time scales and with longer wavelengths because they are not able to resolve faster growing modes. This resolution dependence persists well into the nonlinear regime, with the size scale of the nonlinear density structures scaling approximately with the grid cell size. This contrasts with, other instabilities, e.g. Rayleigh-Taylor, whose linear growth rates increase toward shorter wavelength, but whose nonlinear structures have large length scale. Here the nonlinear outcome of the photon bubble instability is dominated by the shortest resolved wavelengths until the viscous length scale is reached. This represents a numerical challenge for simulating this instability.

The photon bubble instability causes all our simulations of static atmospheres to collapse, in agreement with the prediction of Begelman (2006). However, this still leaves open the question of what happens when fresh mass is supplied to an actual accreting column. Our work here lays the foundation for numerical simulations of magnetically confined, accreting columns on neutron stars, which enable us to resolve the photon bubble instability and study whether it affects existing models that assume a spatially smooth, stationary structure. The results of such simulations are in the following chapters.

Chapter 3

Simulations of Accretion Columns in Cartesian Geometry

This chapter is adapted from our research work published as Zhang, Blaes & Jiang (2022). In this chapter, we simulate the dynamics of vertically stratified neutron star accretion columns in Cartesian geometry. This chapter is organized as follows. In section 3.1, we review the equations of the conservation laws in gas and radiation, the numerical setup of the simulation domain, initial conditions, boundary conditions, numerical issues associated with variable inversion, and simulation parameters. In section 3.2, we discuss the simulation results for different accretion rates and column sizes, compute their time-averaged spatial structures and compare with the 1D standard model, discuss the physical origin of the vertical oscillations, and discuss a resolution study and the presence of photon bubbles in the simulations. In section 3.3, we discuss the validity of our simulations, compare with previous numerical works, and discuss the observational significance. We summarize our conclusions in section 3.4.

3.1 Numerical Method

3.1.1 Equations

Neutron star accretion columns are confined by strong magnetic fields (10^{9-12} G or even higher). These strong magnetic fields present challenges for numerical simulations, and all the early work on photon bubble instability adopted equations of motion in which the fluid was confined to move on infinitely rigid field lines, i.e. MHD was not explicitly included (Klein & Arons 1989; Klein et al. 1996; Kawashima & Ohsuga 2020). Here we include the full MHD dynamics. One resulting challenge is that the CFL condition on the time step in Newtonian MHD can greatly slow down the numerical simulation because the Newtonian Alfvén speed in low density regions (especially outside the column) can easily exceed the speed of light. We therefore employ relativistic MHD because the relativistic Alfvén speed is intrinsically limited by the speed of light.

We apply the numerical framework of radiative relativistic magnetohydrodynamics in ATHENA++ (Zhang et al. 2021) to simulate a magnetically confined, accreting column near the neutron star surface in Cartesian geometry. The governing equations are summarized below in the sequence of particle number conservation, momentum conservation, energy conservation and radiative transfer

$$\partial_0(\rho u^0) + \partial_j(\rho u^j) = S_{\mathrm{gr}1} \quad , \tag{3.1a}$$

$$\partial_0(w u^0 u^i - b^0 b^i) + \partial_j\left(w u^i u^j + \left(P_g + \frac{1}{2}b_\nu b^\nu\right)\delta^{ij} - b^i b^j\right) = S_{\mathrm{gr}2}^i - S_{r2}^i \quad , \tag{3.1b}$$

$$\partial_0\left[w u^0 u^0 - \left(P_g + \frac{1}{2}b_\nu b^\nu\right) - b^0 b^0\right] + \partial_j(w u^0 u^j - b^0 b^j) = S_{\mathrm{gr}3} - S_{r3} \quad , \tag{3.1c}$$

$$\partial_0 I + n^j \partial_j I = \mathcal{L}^{-1}(\bar{S}_r) \quad , \tag{3.1d}$$

where ρ is the fluid frame gas density and u^μ is the fluid four-velocity. Given the fluid

three-velocity v^i, we can calculate $(u^0, u^i) = \Gamma(1, v^i)$ in special relativity, where $\Gamma = (1 - v_j v^j)^{-1/2}$ is the Lorentz factor. The total fluid frame enthalpy w and the magnetic field four-vector b^μ are defined as follows

$$b^0 = u_j B^j, \quad b^i = \frac{1}{\Gamma}(B^i + b^0 u^i) \quad , \tag{3.2}$$

$$w = \rho + \frac{\gamma}{\gamma - 1} P_g + b_\nu b^\nu \quad , \tag{3.3}$$

where B^i is the magnetic field three-vector and P_g is the fluid frame gas pressure. We adopt an ideal gas with adiabatic index $\gamma = 5/3$. The quantities S_{gr1}, S^i_{gr2} and S_{gr3} are weak field gravitational source terms (see Appendix B for details).

In the radiative transfer equation (3.1d), I is the frequency-integrated, but angle-dependent intensity, and the unit vector n^i is the photon propagation direction. We adopt 40 radiation angles, which are in the plane of the 2D simulation. This is the same angular discretization that we used in chapter 2, and the details are described in Jiang (2021). Note that the radiative transport source term is initially computed in the fluid frame $(\bar{S}_r)$ and then Lorentz transformed back to the lab frame (S_r).[1] The operator $\mathcal{L}$ represents a Lorentz boost from the lab frame to the fluid frame and $\mathcal{L}^{-1}$ is its inverse. Therefore, $S_r = \mathcal{L}^{-1}(\bar{S}_r)$ and we have source terms in the lab frame exchanging momentum and energy between gas and radiation as follows

$$S^i_{r2} = \oint S_r n^i d\Omega \quad , \tag{3.4a}$$

$$S_{r3} = \oint S_r d\Omega \quad , \tag{3.4b}$$

where $d\Omega$ is the infinitesimal solid angle about the photon propagation direction n^i. The

---

[1]Throughout this chapter, radiation quantities in the fluid rest frame are indicated with a bar.

radiative transport source term in the fluid frame (Jiang 2021; Zhang et al. 2021) is

$$\bar{S}_r = \Gamma(1 - v_j n^j)\Bigg[\rho\kappa_s(\bar{J} - \bar{I})$$
$$+\rho\kappa_R\left(\frac{a_r T_g^4}{4\pi} - \bar{I}\right) + \rho(\kappa_P - \kappa_R)\left(\frac{a_r T_g^4}{4\pi} - \bar{J}\right) \qquad (3.4c)$$
$$+\rho\kappa_s\frac{4(T_g - \bar{T}_r)}{T_e}\bar{J}\Bigg] \quad ,$$

where $\bar{I} = \mathcal{L}(I)$ is the fluid-frame frequency-integrated intensity and $\bar{J} = (4\pi)^{-1}\oint \bar{I}d\bar{\Omega}$ is the fluid-frame zeroth angular moment of intensity. Other quantities are the electron scattering opacity κ_s, Rosseland mean absorption opacity κ_R, Planck mean absorption opacity κ_P, radiation density constant a_r, effective temperature of the radiation $\bar{T}_r = (4\pi\bar{J}/a_r)^{1/4}$, and electron rest mass energy expressed as a temperature $T_e \equiv m_e c^2/k_B$. The gas temperature is $T_g = P_g m/(\rho k_B)$, where m is the solar abundance mean molecular mass. In the source term (3.4c), the factor $\Gamma(1 - v_j n^j)$ outside the square brackets comes from the frame transformation, the first term in the square brackets refers to elastic scattering, the second and third terms represent absorption and emission processes, and the last term is an approximation for the gas-radiation heat exchange via Compton scattering (Blaes & Socrates 2003; Hirose et al. 2009).

Throughout this chapter we assume that the opacity is nonmagnetic isotropic Thomson scattering without polarization dependence. We also adopt a fully grey treatment of radiation transfer with an assumed blackbody spectrum, neglecting nonzero photon chemical potential effects. Magnetic scattering opacities in particular are likely to be important in the dynamics of actual accretion columns with stronger magnetic fields than we have employed here, and we intend to explore this in the next chapter. The simulations we present here will provide a physics baseline for these further investigations.

3.1.2   Simulation Domain

As we discovered earlier in chapter 2, the nonlinear behavior of the photon bubble instability is resolution-dependent and dominated by the shortest resolved wavelengths above the radiation viscous scale. Therefore, we prefer to adopt a Cartesian column initialized with a uniform vertical magnetic field so that the simulation can be configured on a uniform grid, which avoids the extra complexity introduced by the geometric dilution in any other kind of geometry. Such geometric dilution (e.g. in spherical or dipolar geometry) can naturally lead to non-uniform numerical behavior of the photon bubble instability, in particular by not resolving the short-wavelength faster growing modes at higher altitudes. However, this Cartesian geometry limits what parameter regimes we can simulate: the accretion rates in our simulations should be small enough that the height of the shock front is small compared to the stellar radius.

Our simulations are confined to the 2D x-z plane, and gas only moves in this plane. However, the radiation intensity propagation directions n^j are fully 3D. There are no spatial gradients in the y-direction perpendicular to the x-z plane, implying that there is also no y-component of radiation flux. Our 2D simulations can be interpreted as a vertical slice of a narrow wall-shaped column, e.g. as shown in the Fig.I of Basko & Sunyaev (1976).

The simulation domain is partitioned as illustrated in Figure 3.1. We define z_{top} as the height at the top of the simulation domain and d as the width at the bottom of the accretion column. (Again, d should be interpreted as the width of a narrow-walled column which is much shorter than the extent of the column in the y-direction perpendicular to the x-z plane. We are neglecting all spatial gradients in that y-direction in our 2D simulations.) Note that we add a gas-supported layer at the base and vacuum regions at the two sides as effective boundaries of the accreting column for numerical
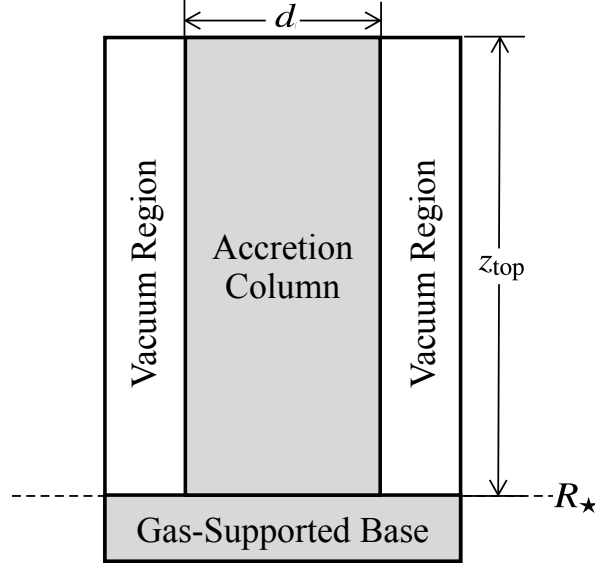
Figure 3.1: Partitioning of the simulation domain into different regions with distinct numerical treatments. The region labelled accretion column is the active, physical region where material accretes through the top boundary. On either side of this column is a vacuum region through which no material enters from the top, and in which an effective boundary condition is maintained by setting the density and gas pressure to their floor values. Underneath all these regions is a gas-pressure supported base with an artificially reduced gravitational acceleration in order to provide adequate spatial resolution, and which provides an effective base boundary condition. (See section 3.1.4 for details of all these effective boundary conditions.)

purposes, which will be discussed below in section 3.1.4.

We parameterize the accretion rate based on the effective luminosity L_{eff} and Eddington flux ratio ϵ respectively, where the effective luminosity is the area-weighted Eddington luminosity and the Eddington flux ratio is the ratio of the accretion luminosity L_{acc} to the effective Eddington luminosity. Given the Eddington luminosity $L_{\text{Edd}} = 4\pi GM_\star c/\kappa_s$ of a neutron star with mass $M_\star = 1.4 M_\odot$ and radius $R_\star = 10^6$ cm, we have

$$L_{\text{eff}} = \frac{A}{4\pi R_\star^2} L_{\text{Edd}} \quad , \tag{3.5}$$

$$L_{\text{acc}} = \frac{GM_\star \rho_{\text{acc}} A v_{\text{ff}}}{R_\star} = \epsilon L_{\text{eff}} \quad , \tag{3.6}$$

where A is the horizontal area of the accretion column on the neutron star surface and

ρ_{acc} is the accreting gas density at the free-fall speed $v_{\mathrm{ff}} = \sqrt{2GM_\star/(R_\star + z_{\mathrm{top}})}$ at the top of the simulation domain. Therefore, we can tune the accretion rate in terms of ρ_{acc} in the simulation by simply adjusting ϵ.

3.1.3   Initial Conditions

In standard models of neutron star accretion columns, which are based on the seminal work of Basko & Sunyaev (1976), the magnetic fields are strong enough to constrain the inflow to move along the field lines near the stellar surface. At high accretion rates, the incoming material free falls onto the neutron star and forms a shock above the stellar surface, where the region above the shock front is called the free-fall zone and the region below is called the sinking zone. At the bottom of the free-fall zone, the inflow is halted by the shock front which converts nearly all its kinetic energy into radiation energy. The sinking zone is radiation-dominated regardless of the magnetic pressure, where the gas is in approximate hydrostatic equilibrium between upward radiation force and downward gravity, with a slow subsonic sinking flow toward the neutron star surface. We follow this configuration to initialize our 2D numerical simulation.

In the beginning of the simulation, we assume that the vertical magnetic fields are strong and uniform across the whole domain, where $B_{x0} = 0$ and $B_{z0} = 8 \times 10^{10}$ G, where the subscript 0 refers to the initial condition. While this is somewhat below the 10^{12} G, or more, magnetic fields that are typical of high mass X-ray binary pulsars, it is large enough to rigorously confine the material in the accretion column. Higher fields will not affect the dynamics, and create numerical problems as they have energy densities which are too large compared to the gas pressure (see section 3.3.1 for details). It is true that higher fields can reduce the scattering opacity, but again, we are assuming constant Thomson opacity here (and the Planck and Rosseland mean absorption opacities have

51

negligible effects), and intend to explore the magnetic opacity effects in the next chapter.

Although we use radiative relativistic MHD in Athena++ (Beckwith & Stone 2011; Jiang 2021; Zhang et al. 2021) for the numerical simulation, only the free-fall region of the column is mildly relativistic ($\Gamma \simeq 1.31$) and the initial magnetic field is strong enough to enforce purely vertical motion of the gas. Therefore, we formulate the initial condition using Newtonian physics and assuming 1D gas motion along the magnetic fields for simplicity. The time-independent conservation laws for the initial condition can then be written as follows:

$$\frac{\partial}{\partial z}\left(\rho_0 v_{z0}\right) = 0 \quad , \tag{3.7a}$$

$$\rho_0 v_{z0}\frac{\partial v_{z0}}{\partial z} = -\frac{\partial P_{g0}}{\partial z} - \rho_0\left(g(z) - \frac{\kappa}{c}\bar{F}_{z0}\right) \quad , \tag{3.7b}$$

$$v_{z0}\frac{\partial}{\partial z}\left(\frac{1}{\gamma-1}P_{g0} + \bar{E}_{r0}\right) + \left(\frac{\gamma}{\gamma-1}P_{g0} + \bar{E}_{r0} + \bar{P}_{r0}\right)\frac{\partial v_{z0}}{\partial z} = -2\frac{\partial \bar{F}_{x0}}{\partial x} - \frac{\partial \bar{F}_{z0}}{\partial z} \quad , \tag{3.7c}$$

where the flux mean opacity $\kappa = \kappa_s + \kappa_R$ is the effective opacity for gas-radiation momentum coupling and $g(z) = GM_\star(R_\star + z)^{-2}$ is the gravitational acceleration. The factor of 2 before the $\partial \bar{F}_{x0}/\partial x$ term in (3.7c) comes from the radiative cooling on both sides of the column. We then follow the approximations in Basko & Sunyaev (1976) to simplify equations (3.7) and compute the 1D solution along the vertical direction ($\hat{z}$) to initialize the sinking zone. We apply the following approximations for the gas and radiation field:

1. Local thermal equilibrium (LTE) between the gas temperature and radiation effective temperature $T_{g0} = \bar{T}_{r0} \equiv T_0$.

2. Standard Eddington closure scheme between the zeroth and second angular moments of the radiation field

$$\bar{P}_{r0} = \frac{1}{3}\bar{E}_{r0} \quad . \tag{3.8}$$

52

3. Radiative transport in the diffusion approximation

$$\bar{F}_{x0} = -\frac{c}{\rho_0 \kappa} \frac{\partial \bar{P}_{r0}}{\partial x} \qquad . \tag{3.9}$$

4. We approximate horizontal gradients with a simple one zone finite difference between the center and each side of the column, assuming $\bar{F}_{x0} = 0$ at the center of the column and $\bar{P}_{r0} = 0$ at the sides. E.g. for the right half:

$$\frac{\partial \bar{F}_{x0}}{\partial x} \simeq \frac{2\bar{F}_{x0}}{d} \quad \text{and} \quad \frac{\partial \bar{P}_{r0}}{\partial x} \simeq -\frac{2\bar{P}_{r0}}{d} \qquad . \tag{3.10}$$

Recall that d is the column width. Therefore, the time-independent conservation laws (3.7) can be further reduced and rearranged for the convenience of numerical integration as follows

$$\frac{\partial T_0}{\partial z} = -\frac{3\rho_0 \kappa}{4a_r T_0^3} \frac{\bar{F}_{z0}}{c} \qquad , \tag{3.11a}$$

$$\frac{\partial \rho_0}{\partial z} = \frac{-\rho_0 \left(g(z) - \frac{\kappa}{c}\bar{F}_{z0} + \frac{k_{\mathrm{B}}}{m}\frac{\partial T_0}{\partial z} \right)}{(k_{\mathrm{B}} T_0/m) - v_{z0}^2} \qquad , \tag{3.11b}$$

$$\frac{\partial v_{z0}}{\partial z} = \frac{s_0}{\rho_0^2} \frac{\partial \rho_0}{\partial z} \qquad , \tag{3.11c}$$

$$\begin{aligned}
\frac{\partial \bar{F}_{z0}}{\partial z} = &-\frac{4ca_r T_0^4}{3\rho_0 \kappa d^2} - v_{z0}\left(\frac{3}{2}\frac{k_{\mathrm{B}}}{m}\rho_0 + 4a_r T_0^3 \right)\frac{\partial T_0}{\partial z} - \frac{3}{2}\frac{k_{\mathrm{B}}}{m}v_{z0}T_0\frac{\partial \rho_0}{\partial z} \\
&-\left(\frac{5}{2}\frac{k_{\mathrm{B}}}{m}\rho_0 T_0 + \frac{4}{3}a_r T_0^4 \right)\frac{\partial v_{z0}}{\partial z} \qquad ,
\end{aligned} \tag{3.11d}$$

where the mass accretion rate per unit area $s_0 = -\rho_0 v_{z0}$ is a constant. After the simulation domain and accretion parameters are determined, we can obtain the gas density in the free-fall region via (3.6) and then the free-fall speed v_{ff}. Given that the gas is cold (5×10^6 K, following Klein & Arons 1989) and the radiation flux is negligible at

the top, we can then continue the free-fall solution down to a specified height z_{int} which is high enough to be above the accretion shock and sinking region. We then integrate equations (3.11) downward until the vertical speed at the bottom decreases to a value $\sim 10^{-3}c$.

3.1.4   Boundary Conditions

As illustrated in Figure 3.1, besides the accretion column region, we also add a gas-supported layer at the base and two vacuum regions on both sides. These regions are artificial but necessary to serve as effective boundary conditions (hereafter soft boundaries) for better numerical performance compared with the direct implementation on the boundaries of the simulation domain (hereafter hard boundaries).

At the lower boundary of the simulation domain, we zero the horizontal components of the magnetic field while maintaining constant vertical component. We also apply reflective boundary conditions for both the gas and the radiation. Such a hard reflective boundary condition for the gas would inevitably lead to gas leakage out of the accreting column at an unphysically high rate since it simply copies the horizontal components of the velocity in the ghost zones, which lack magnetic confinement because we enforce purely vertical magnetic field there. To alleviate this problem, we introduce a thick gas-supported layer as an effective boundary for the sinking gas in the accretion column.

This gas-supported base mocks up the presence of the neutron star surface within the simulation domain. We initialize it to be cold ($T_{g0} = \bar{T}_{r0} = T_{\text{b}} = 5 \times 10^6$ K) and optically thick so that radiation pressure is negligible. It is fully supported against gravity by gas pressure but still constrained by the magnetic field. A realistic gas pressure scale height in the gravitational field of a neutron star is very small (~ 3.7 cm), and would require unnecessarily high resolution merely for an effective boundary. We therefore artificially

reduce the gravitational acceleration by a factor of 100 in the gas-supported layer to increase the scale height so that we do not waste too many grid zones. We initialize the gas-supported base in hydrostatic equilibrium and determine the gas density via $\rho_{\rm b} \propto \exp(-z/h_{\rm b})$, where $h_{\rm b} = RT_{\rm b}/g_{\rm b}(\sim 370~{\rm cm})$ is the scale height and $g_{\rm b} = GM_\star/(100R_\star^2)$ is the reduced gravitational acceleration at the neutron star surface.

The side boundary conditions also require careful treatment. In contrast to the static neutron star atmospheres that we simulated in chapter 2, where we used horizontally periodic boundary conditions, here we must use side boundary conditions that permit the formation of an accretion column that 1. allows for escape of photons from the side and 2. is horizontally confined by the magnetic field against the resulting sideways radiation pressure forces. We allow for the escape of photons by zeroing the intensity along all inward pointing propagation angles at the side boundaries. Barring any instabilities, the magnetic field we use is strong enough (with energy density at least 100 times larger than the total thermal pressure) that horizontal confinement is easily achieved. However, we have conducted numerical experiments with an outflow boundary condition for the gas on the side boundaries, and these always lead to escape of gas that drags the field along with it. This is simply because we did not impose an inward force at the boundary to compensate for the outward thermal pressure forces. Rather than do that, we instead impose a reflecting boundary condition at the side boundaries. As these boundaries are displaced from the actual accretion column, this still allows for dynamic confinement of the column by the magnetic field. In order to allow photons to horizontally escape from the actual accretion column, we also reset the density and gas temperature in the side regions to the floor values at each time step to mock up real vacuum conditions. These effective side boundary conditions have three major advantages:

1. We avoid the artificial accretion associated with an infalling density floor.

2. We guarantee that the vacuum regions are optically thin so that the radiation can freely leave the sides of the accretion column.

3. We prevent artificial gas ejection from the gas-supported base (where we have imposed artificial low gravity) in the side regions caused by irradiation heating from the accretion column.

In addition to our treatment in these effective side and bottom boundary regions, we still have to specify the boundary conditions at the actual edges of our simulation domain. We adopt an upper boundary condition for the magnetic field that zeroes out the horizontal component ($B_x = 0$) and maintains constant vertical magnitude ($B_z = 8 \times 10^{10}$ G) in the ghost zones. The simulations are fed with cold (5×10^6 K) and optically thick material with density ρ_{acc} that varies between simulations through the top boundary. This material free falls at speed v_{ff} into the simulation domain through the upper boundary of the free-fall zone. At both sides of the simulation domain, we adopt vacuum boundary conditions for the radiation (see section 2.2.2 for details) and reflective boundary conditions for both the gas and the magnetic field. At the very bottom, as noted previously, we use reflective boundary conditions for the radiation, where the intensity is specularly reflected from the boundary. The gas boundary condition is also reflective but the magnetic field is forced to be constant just like the upper boundary condition.

3.1.5   Issues with Variable Inversion

In addition, although we update the primitive variable inversion algorithm as described in chapter 2, it still fails in most low-density regions where the gas density is too low and the orders of magnitude difference between magnetic pressure and gas pressure causes difficulty in determining the gas pressure from the conservative total energy density. Because gas pressure is dynamically unimportant, this would not normally matter.

Version	Name	Mesh	d $(R_\star)$	z_{int} $(R_\star)$	z_{top} $(R_\star)$	Resolution (10^{-3}cells/cm)	ϵ	ρ_{acc} (10^{-4} g/cm^3)
0	HR-Narrow-100	192×1024	0.015	0.100	0.150	6.5	100	4.60
1	HR-Narrow-150	200×2400	0.015	0.125	0.350	6.8	150	6.90
2	HR-Wide-25	700×2048	0.060	0.340	0.350	5.8	25	1.15
3	MR-Wide-25	350×1024	0.060	0.340	0.350	2.9	25	1.15
4	LR-Wide-25	176×512	0.060	0.340	0.350	1.5	25	1.15

Table 3.1: Initialization parameters of our five accretion column simulations.

However, in low density regions, the noisily determined gas pressure leads to noise in the gas temperature and occasional unphysically high gas temperature regions. The radiation field would then be heated by this numerical noise because the gas temperature is used to compute the gas-radiation energy exchange source term (which is dominated by Compton scattering). In order to control such artificial heating of the radiation, we apply a density threshold ρ_{comp} which is selected to be the same as ρ_{acc} and only allow Compton scattering when the local density is greater than ρ_{comp}. However, this ad hoc fix works for the simulations presented here, but alternative approaches will need to be developed for strongly magnetized gas for simulations in more extreme regimes (e.g. global simulations where the accreting gas can be wind-captured, fed from a disk or the magnetar regime where the magnetic field strength can reach 10^{13-15} G).

3.1.6   Simulation Parameters

We have run five accretion column simulations with parameters listed in Table 3.1. We set up the first three versions (v0, v1, v2) by varying the column width and accretion rate to study how the column dynamics depends on these parameters. We take the first simulation (v0) as our fiducial simulation. We increase the accretion rate by a factor of 1.5 while maintaining the same column width in the second simulation (v1). The third simulation (v2) has the column 4 times wider while maintaining the same mass accretion rate and thus ϵ is 4 times smaller. These first three simulations all have

similar resolutions in both the horizontal and vertical directions. We set up the last two simulations (v3, v4) for a resolution study by decreasing the resolution by factors of 2 and 4, respectively, for the parameters of simulation v2, where the column exhibits a continually multi-peaked structure in the horizontal direction. Each simulation runs for $7100t_{\rm sim}$, where $t_{\rm sim} = 2.8 \times 10^{-7}$ s is the simulation time unit in this chapter.

The initial vertical profiles of various quantities in the accretion column are shown in Figure 3.2. The sharp changes in gas density and velocity clearly indicate the location of
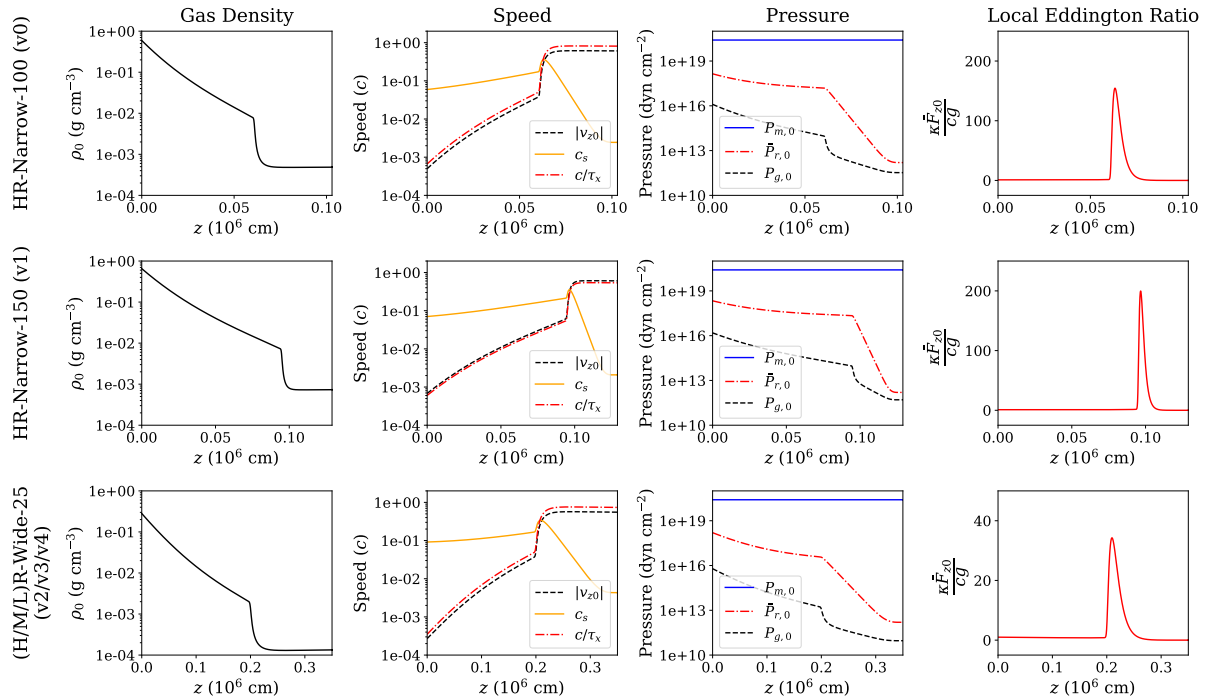
Figure 3.2: Initial condition in our simulations, computed using the 1D standard model. The top and middle row of panels correspond to simulations v0 and v1, while the bottom row corresponds to simulation v2 as well as simulations v3 and v4 used in our resolution study. From left to right, the panel columns show initial fluid frame density, various speeds (the vertical fluid speed, the sound speed, and the horizontal photon diffusion speed), various pressures (magnetic, radiation, and gas), and the vertical fluid-frame radiation flux (expressed as a local Eddington ratio).

the shock structure at the top of the sinking zone. As illustrated in the pressure plots, the column is radiation pressure dominated with strong magnetic confinement. Note that

P_m is the magnetic pressure and c_s is the adiabatic sound speed in the radiation and gas mixture, $\tau_x = \rho_0 \kappa d / 2$ is the horizontal optical depth of the column (from the center to the side) and thus c/τ_x represents the radiative diffusion speed inside the column in the horizontal direction.

3.2 Results

In the following subsections, we present and analyze the simulation results. In section 3.2.1, we summarize the dynamical behavior of the simulations. In section 3.2.2, we compare the time-averaged structures with the classical accretion column model. In section 3.2.3 we present a physical interpretation of the vertical oscillations. In section 3.2.4, we present evidence that photon bubbles are present in at least our highest resolution wide column simulation. Animations for all of the simulations are available online[2].

3.2.1 Dynamics in Column Accretion Simulations

In this section, we use three high-resolution simulations (v0, v1, v2) to illustrate three different dynamical behaviors of the accretion column. We first describe the fiducial simulation (v0) in detail and then discuss the changes that occur at higher accretion rate (v1) and wider size (v2).

As can be seen in the animations, each simulation first relaxes from the 1D initial condition which has no horizontal structure. Radiation quickly escapes from the sides due to the low horizontal optical depth in those regions. Hence the height of the shock front drops below the starting position along the sides due to less vertical radiation pressure support. This naturally leads to a curved, mound-shaped shock front enclosing the sinking region. This is illustrated in Figure 3.3, where we use the time-averaged

---

[2]`https://youtube.com/playlist?list=PLbQOoEYOCFpX935unYJWB3gfwhDwcKJ6c`

profiles of the fiducial simulation (v0) to compute the horizontal optical depth to the nearest side of the simulation domain at different altitudes.
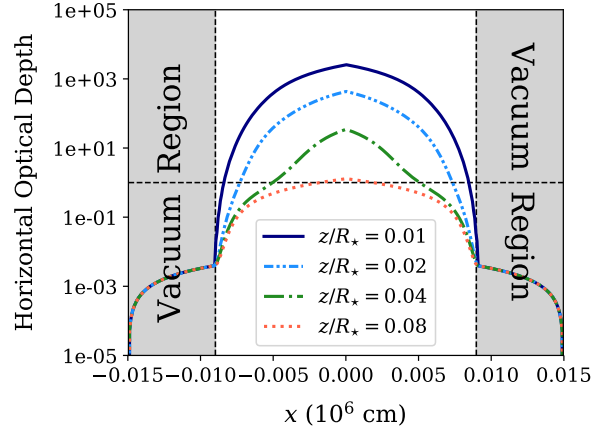
Figure 3.3: Horizontal optical depths at different altitudes based on the time-averaged profiles of the fiducial simulation v0. The optical depth is calculated from the nearest side of the simulation domain. The horizontal dashed line indicates optical depth unity, and demonstrates why the accretion column must adopt a round shape.

Once the relaxation of the initial condition finishes, the system gradually enters into a state of quasi-periodic vertical oscillation, which persists through the end of all five of our simulations. As illustrated in Figure 3.4 and in the online animations, these oscillations result in luminosity variations. Only the horizontal flux is depicted in this figure, as the flux escaping vertically is smaller by factors of at most 1.3×10^{-3}, and is therefore negligible. We explain the physical origin of these oscillations in section 3.2.3 below.

During these oscillatory epochs, the system continues to be heated by the dissipation of the kinetic energy of the incoming accretion flow at the shock front. That dissipated energy is rapidly transferred to the radiation field via the Compton process, which is then balanced by radiation diffusion, advection, and radiative cooling at the two sides of the column. The column below the shock is supported against gravity by the radiation pressure gradient, with the radiation diffusion time being much longer than the sound crossing time. With the exception of the existence of oscillations, all these properties are
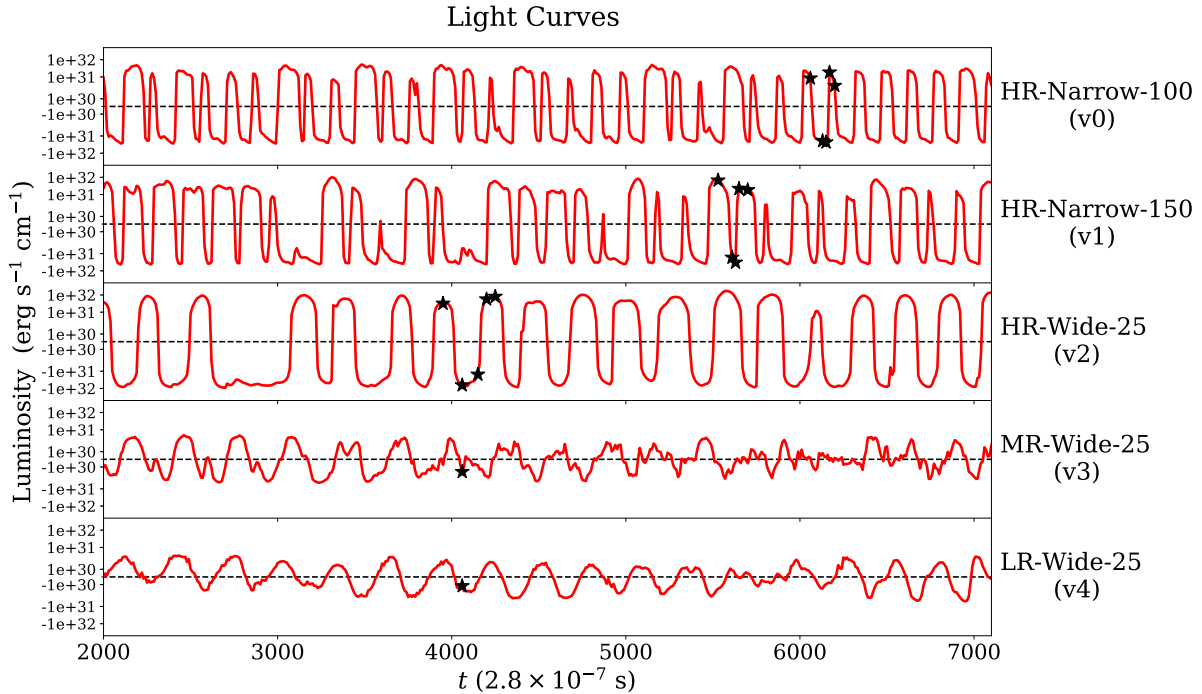
Figure 3.4: Variations in vertically integrated sideways luminosity about the time-average over the time interval depicted here (after relaxation from the initial condition) for our five simulations. The vertical flux leaving the domain is not included in this plot, but it is negligible. Black stars correspond to the snapshots shown in Figure 3.5, Figure 3.8, Figure 3.11, and Figure 3.18. Oscillations that have a flat-topped profile in the light curves of v0, v1, and v2, are associated with the formation of pre-shocks in the accretion flow. Such pre-shocks are absent during spike-shaped oscillations.

qualitatively consistent with the high-accretion rate static accretion column described by Basko & Sunyaev (1976). As we discuss in detail in section 3.2.3 below, however, such a static structure has a much longer vertical heat transport time compared to the sideways cooling time in the upper regions, and this must produce vertical oscillations in the column.

For each high-resolution simulation, we select 5 snapshots to illustrate the quasi-periodic behavior and examine their 2D profiles when the sinking region is most elongated or compressed to understand the column dynamics.

Oscillatory behavior in narrow accretion columns

The spatial distribution of fluid-frame density over one period of the quasi-periodic oscillation (indicated by black stars in Figure 3.4) in the fiducial simulation (v0) is shown in Figure 3.5.   The nonlinear oscillations of the center and two sides of the column are

Figure 3.5:   Selected 2D density snapshots over one full oscillation period $\simeq 140t_{\mathrm{sim}} = 3.9 \times 10^{-5}$ s in the fiducial simulation (v0). 2D profiles of other fluid quantities at the epochs of maximum ($6060t_{\mathrm{sim}}$) and minimum ($6150t_{\mathrm{sim}}$) vertical extent are shown in Figure 3.6 and Figure 3.7, respectively.

sometimes moving in opposite directions during the course of an oscillation period. This period ($\sim 5 \times 10^{-5}$ s) is extremely short and the oscillation amplitude decreases from the center towards the sides. During the oscillation, most of the gas is enclosed by the shock in the sinking region, which is optically thick and radiation dominated. Accretion power continues to heat the shock front. Bounded by the shock front, a portion of newly generated photons directly escapes out of the column into the vacuum regions and the rest are redistributed through the sinking region, largely through advection by the oscillating column structure. Because of the difference in vertical oscillation amplitude
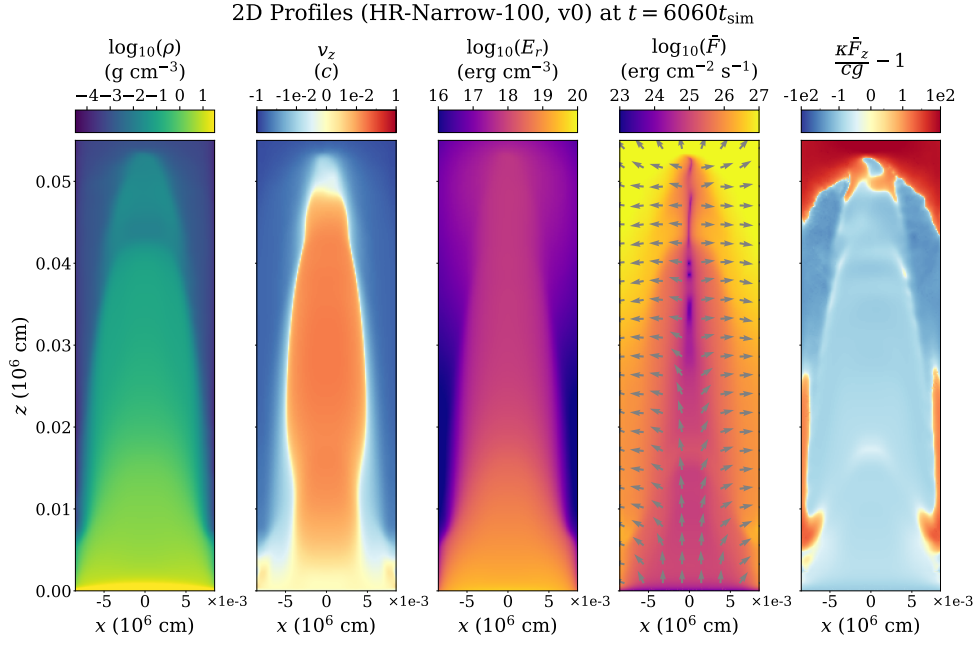
Figure 3.6: 2D profiles at $t = 6060 t_{\mathrm{sim}}$ in the fiducial simulation (v0). Note that for the vector variables, the arrows represent the direction and the color bar indicates the magnitude.

Figure 3.7: 2D profiles at $t = 6150 t_{\mathrm{sim}}$ in the fiducial simulation (v0). Note that for the vector variables, the arrows represent the direction and the color bar indicates the magnitude.

between the center and the sides, the column transitions between a symmetric single mound at maximum vertical extent to a triple-peaked structure at minimum vertical extent. We shall see that the high resolution wide column simulation v2 exhibits more complex behavior in its oscillations.

Figure 3.6 and Figure 3.7 show the interior structure of the column at the maximum and minimum heights of the oscillation, respectively. The fact that the sides and the center are not always moving in the same direction through the course of the oscillation is caused by the sides having greater cooling efficiency when the entire column is at its maximum height. They therefore lose vertical pressure support first and collapse faster, thereby exposing more central regions which can then cool more efficiently and collapse. The sides also rebound first after reaching minimum height, covering up the still collapsing center and irradiating it with more photons (second and fourth panels of Figure 3.7). This ultimately provides extra pressure support to the center causing it to expand vertically again so that the entire column reforms a single-peaked mound at maximum height.

When we increase the accretion rate (v1) in the narrow accretion column, the overall oscillation in the light curve remains very similar (second row of Figure 3.4). Figure 3.8 shows the density structure at different representative epochs during the oscillation.

Figure 3.9 and Figure 3.10 show various quantities at the epoch of maximum and minimum height, respectively. The vertical oscillation amplitude increases with the increased accretion rate, although the overall oscillatory structure remains roughly the same. Note that in the first and second panels of Figure 3.8, a pre-shock is quite prominent. This happens on occasions when there is enhanced vertical escape of radiation which can interact with the infalling material to form a shock above the main body of the sinking region. Indeed, we find that the radiation energy density and comoving frame radiation flux at altitude during these epochs are always larger than during epochs that lack a
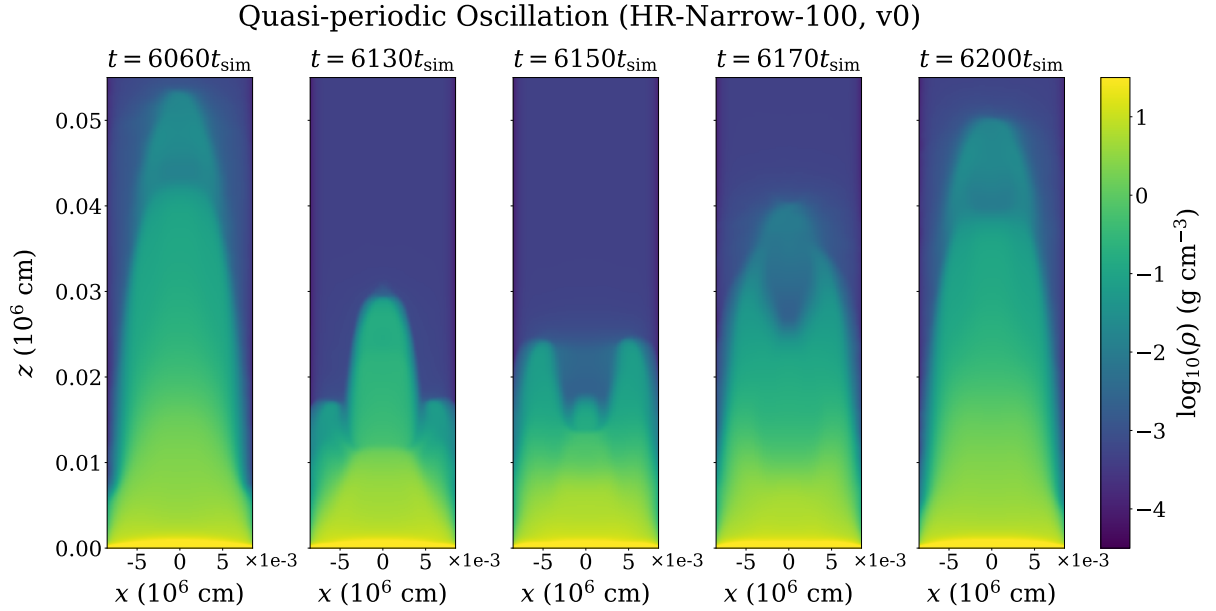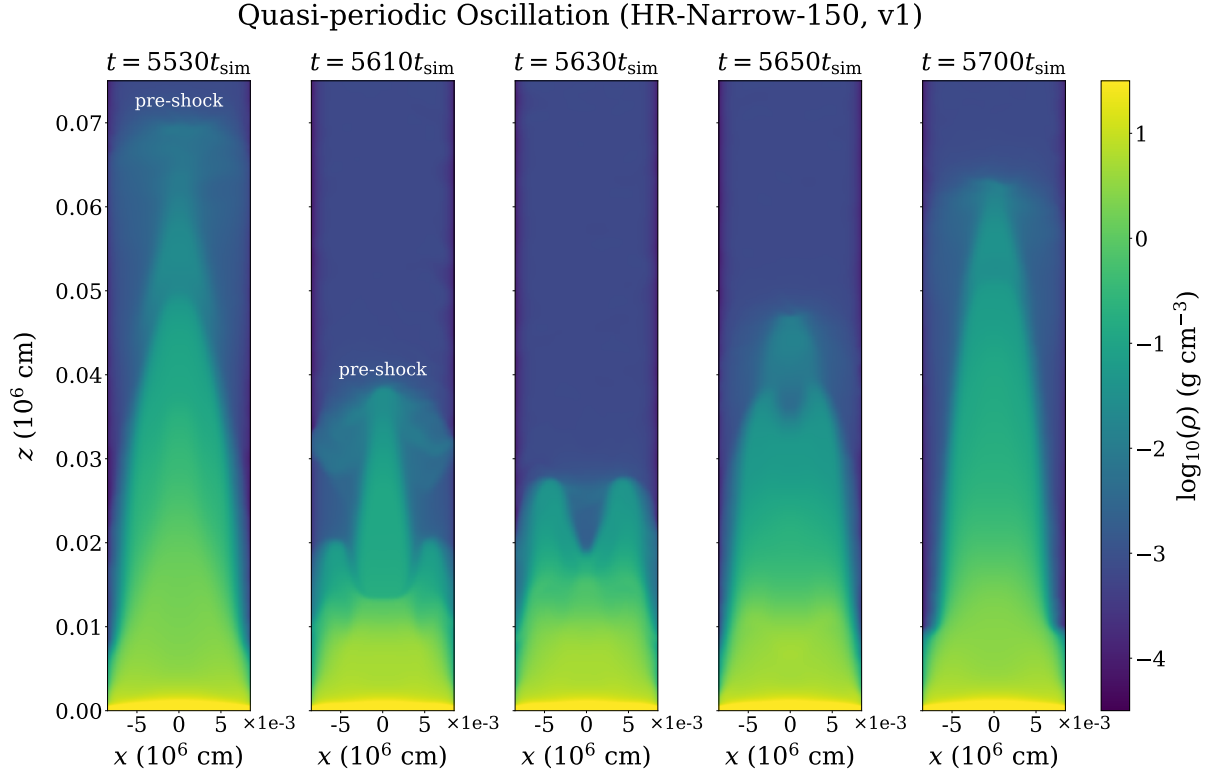
Figure 3.8:   Selected 2D density snapshots over one full oscillation period $\simeq 170t_{\rm sim} = 4.8 \times 10^{-5}$ s in the narrow column simulation at higher accretion rate (v1) that are associated with the pre-shock accreting pattern. 2D profiles of other fluid quantities at the epochs of maximum ($5530t_{\rm sim}$) and minimum ($5630t_{\rm sim}$) vertical extent are shown in Figure 3.9 and Figure 3.10, respectively.

pre-shock. The pre-shock formation often happens at the peak of the radiative emission and thus prevents the accretion flow from reaching low altitude. Since the new shock forms at high altitude, the incoming energy can be dissipated in advance, causing a delay of the energy supply to the low altitude region, which results in weaker oscillations in the next few periods that recharges the sinking region. This effect happens in both simulations v0 and v1, as shown in the top two panels of Figure 3.4, where the light curves exhibit a flat-topped shaped oscillation which are sometimes followed by several narrower peaks, or even quiescence. We have confirmed that all flat-topped oscillations in both simulations are associated with a pre-shock accreting pattern (as in the first and second
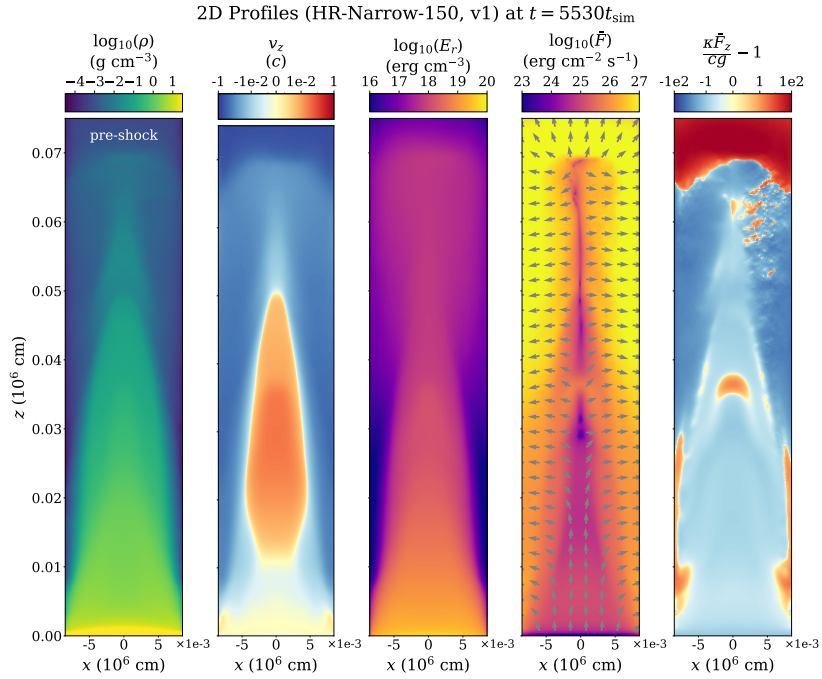
Figure 3.9: 2D profiles at $t = 5530t_{\mathrm{sim}}$ in the narrow column simulation at higher accretion rate (v1). Note that for the vector variables, the arrows represent the direction and the color bar indicates the magnitude.
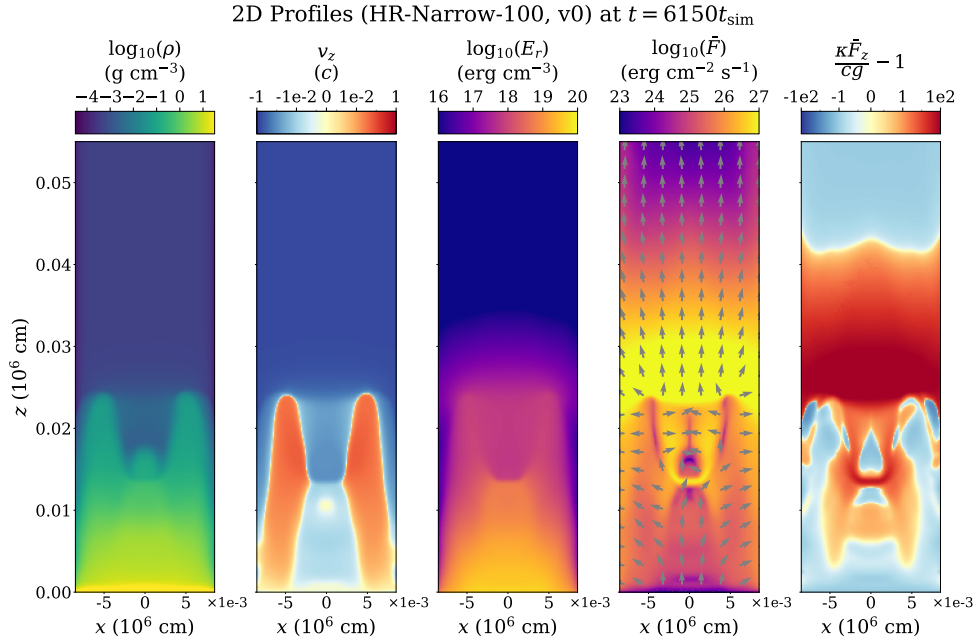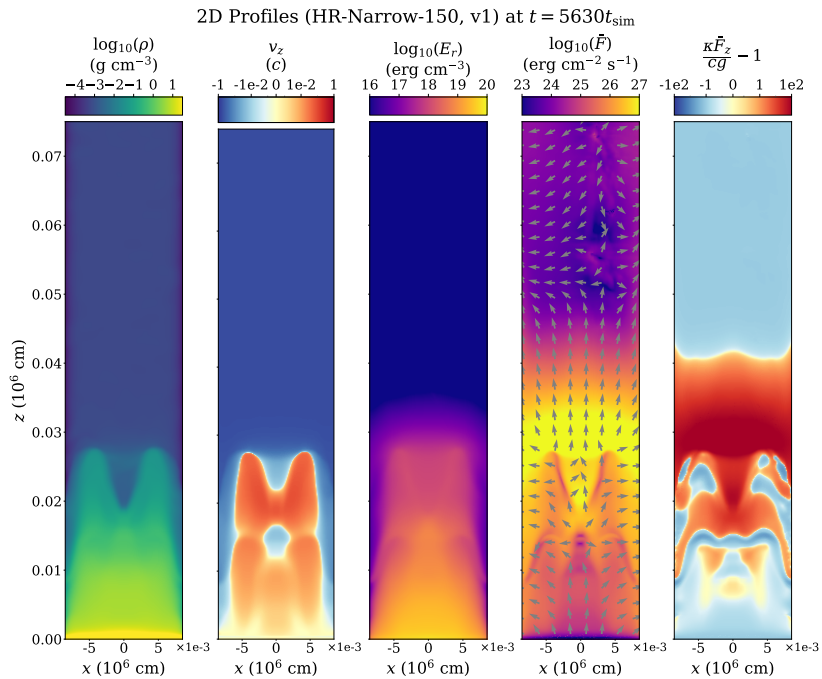

Figure 3.10: 2D profiles at $t = 5630t_{\mathrm{sim}}$ in the narrow column simulation at higher accretion rate (v1). Note that for the vector variables, the arrows represent the direction and the color bar indicates the magnitude.

panels of Figure 3.8), and peak-shaped oscillations which lack this pre-shock structure (as in the first panel of Figure 3.5). Flat-topped oscillation epochs with pre-shocks are more common in the higher accretion rate simulation v1.

Oscillatory behavior in wide accretion column

In simulation v2, we increase the column width with respect to the fiducial simulation v0, maintaining the same total accretion rate and therefore reducing the local Eddington ratio. Figure 3.11 shows the density structure at representative epochs during the oscillation. Figure 3.12 and Figure 3.13 show quantities at the epochs of maximum and
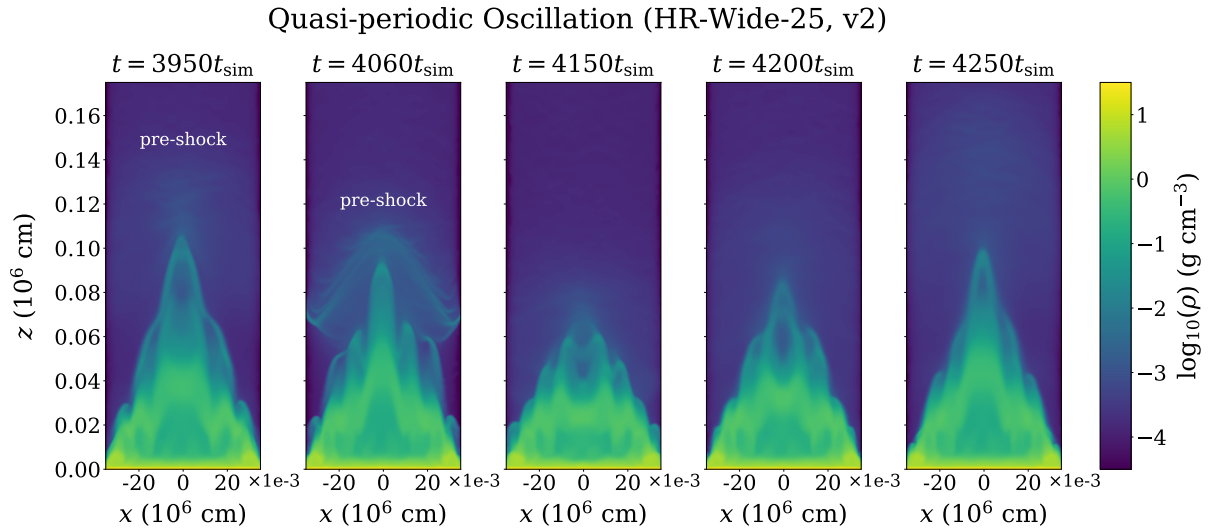
Figure 3.11: Selected 2D density snapshots over one full oscillation period $\simeq 300t_{\mathrm{sim}} = 8.4 \times 10^{-5}$ s in the high-resolution wide column simulation (v2). In contrast to the narrow column simulations v0 (Figure 3.5) and v1 (Figure 3.8), this simulation shows complex multiple peaks at all phases of the oscillation. 2D profiles of other fluid quantities at the epochs of maximum ($3950t_{\mathrm{sim}}$) and minimum ($4150t_{\mathrm{sim}}$) vertical extent are shown in Figure 3.12 and Figure 3.13, respectively.

minimum height, respectively. In contrast to the transition between a single-peaked maximum vertical extent and a triple-peaked minimum vertical extent exhibited in the narrow column simulations v0 and v1, Figure 3.11 shows that the wide column simulation v2 exhibits a more complex multi-peaked horizontal structure throughout the oscillation.

2D Profiles (HR-Wide-25, v2) at $t = 3950 t_{\mathrm{sim}}$
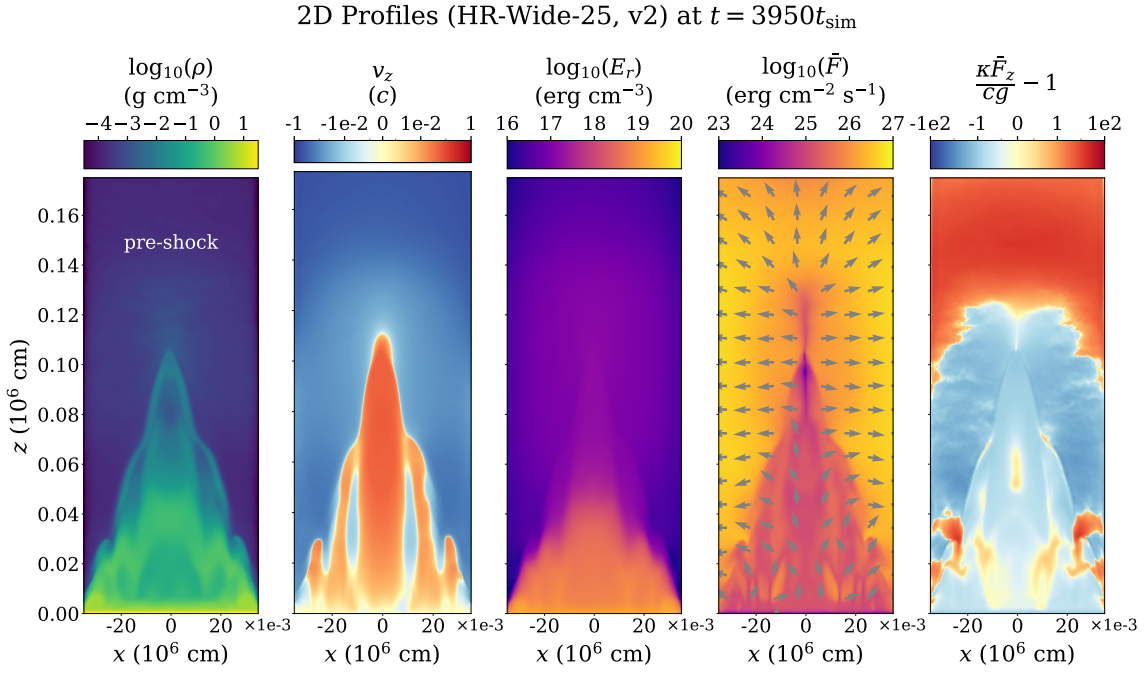
Figure 3.12: 2D profiles at $t = 3950 t_{\mathrm{sim}}$ in the high-resolution wide column simulation (v2). Note that for the vector variables, the arrows represent the direction and the color bar indicates the magnitude.

2D Profiles (HR-Wide-25, v2) at $t = 4150 t_{\mathrm{sim}}$
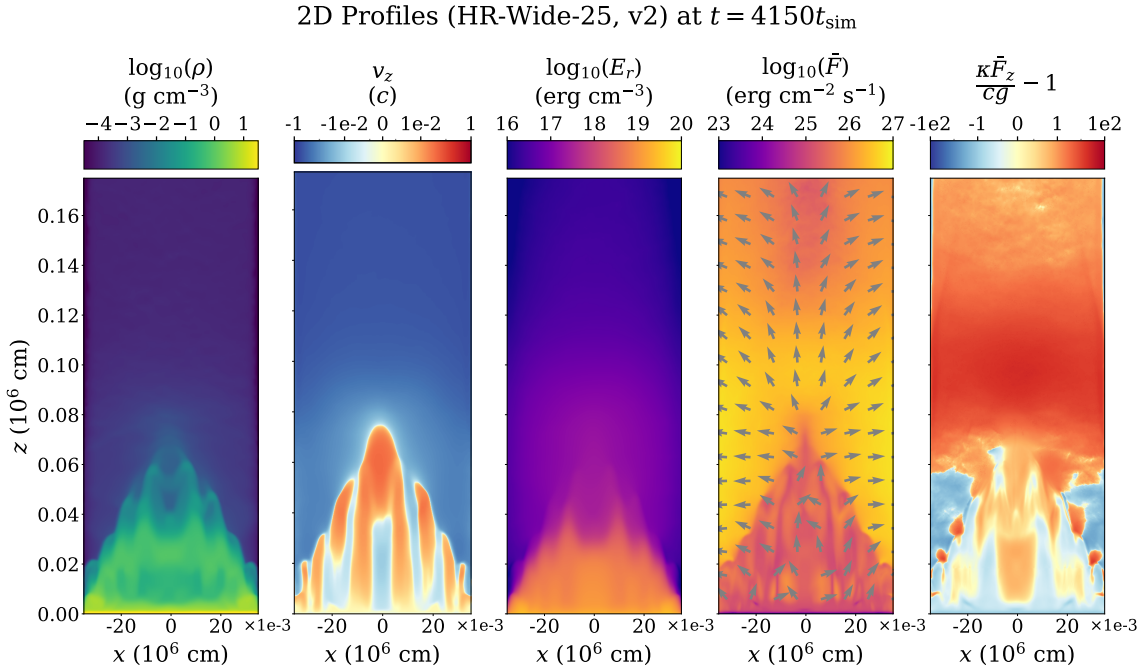
Figure 3.13: 2D profiles at $t = 4150 t_{\mathrm{sim}}$ in the high-resolution wide column simulation (v2). Note that for the vector variables, the arrows represent the direction and the color bar indicates the magnitude.

The vertical channels in this multi-peaked structure allow more radiation to propagate upward and interact with the incoming accretion flow. (The vast majority of the radiation still leaves from the sides of the domain, in agreement with the 1D standard model.) This again causes the formation of a pre-shock near the maximum vertical extent of the oscillation (first and second panels of Figure 3.11). As in the narrow column simulations, this results in flat-topped shaped oscillations in the light curve which, however, are more prominent in v2 because the horizontal structure maintains the pre-shock over much of the oscillation time interval. There are intervals in v1 where the light curve stays close to its quiescent value (~ 3100 and $4100 \times 2.8 \times 10^{-7}$ s), and this also happens in v2 at $\sim 2900 \times 2.8 \times 10^{-7}$ s. This appears to be happening because the pre-shock dissipates and radiates much of the accretion power, which then is not stored in the column structure itself. The amplitude of the oscillation in the wide column simulation v2 is larger than in the narrow column simulation, substantially in height and slightly in the luminosity variation. Recall that simulations v0 and v2 have the same total accretion rate, but the wider column in v2 has a longer horizontal radiation diffusion time. This ultimately results in a taller, more massive column that accumulates a greater total radiation energy, and this in turn increases the oscillation time scale and the oscillation amplitude.

Inside the sinking region in v2, there is a curved density inversion at lower altitudes ($z \sim 0.04 \times 10^6$ cm at the column center), which oscillates at much smaller amplitude compared to the shock front itself. This nearly stationary structure differs from that usually assumed in 1D standard models of neutron star accretion columns in being a vertical density inversion within the sinking zone. Such density inversions can exist in the radiation dominant magnetized medium as long as the vertical radiation flux can fully provide the support by adjusting the radiation energy density gradient to scale proportionately to the gas density (see section A.3 for details). These density inversion structures are (nearly) hydrostatic entropy modes.

Porosity

Neutron star accretion columns can in principle emit super-Eddington fluxes through their sides because of the confinement by strong magnetic fields, and this is also happening here in our simulations. In addition to this, density inhomogeneities can create an effectively porous medium that permits an overall vertical super-Eddington flux without creating an overall radiation pressure force that exceeds gravity, simply because the flux will tend to be larger in the lower density regions (e.g. Shaviv 1998; Begelman 2001). Our accretion column simulations clearly exhibit substantial density inhomogeneities, and we have attempted to quantify this by defining

$$\mathcal{P}(z,t) \equiv \frac{\langle \rho \kappa \rangle \left\langle |\bar{F}_z| \right\rangle}{\left\langle \rho \kappa |\bar{F}_z| \right\rangle} \quad , \tag{3.12}$$

as a height and time-dependent porosity factor with respect to vertical radiation transport, where the angle brackets refer to a horizontal average. Porosity factors greater than unity indicate that the average fluid-frame vertical flux $\bar{F}_z$ is producing less horizontally-averaged vertical radiation pressure than would be the case for a horizontally homogeneous medium. Depending on the epoch, we sometimes measure porosity factors as high as ten at certain heights, but this is generally due to the shape of the surface of the accretion column, e.g. significant vertical flux exists in the low density side regions of the mound-shaped column, or we get a notch of low density at the top of the center of the column as in the middle panels of Figure 3.5 and Figure 3.8. More relevant to the support of the column itself is that we find that the somewhat static low density region below $z \sim 0.025 \times 10^6$ cm in the wide column simulation v2 (see Figure 3.11) has a porosity of $\simeq 3$ at all epochs.
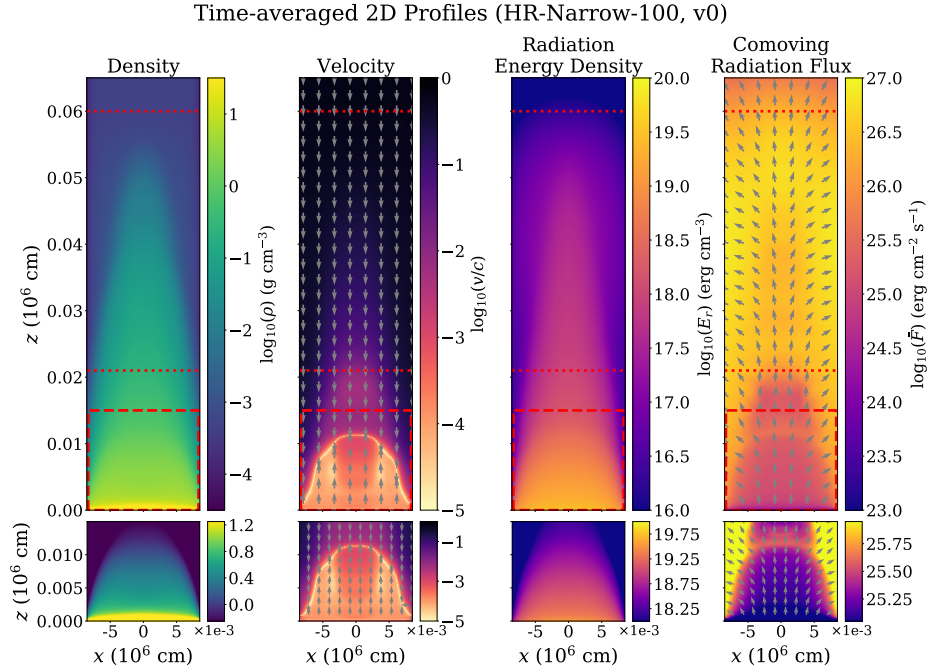
Figure 3.14: 2D time-averaged profiles of the fiducial simulation (v0) after the simulation finishes its relaxation roughly at $t = 2000t_{\mathrm{sim}}$. Note that for the vector variables, the arrows just represent the direction. The horizontal red dotted lines delineate the region affected by the vertically oscillating accretion shock, and are also shown in the 1D profiles in Figure 3.16. The lower panels show the regions indicated by the red dashed boxes in the upper panels, but with different color bar scales to show more detail.

3.2.2   Time-averaged profiles

The high-frequency oscillation is challenging to observe with existing X-ray facilities because it requires the instrument to have enough signal to noise over these short time scales $\sim 10~\mu$s of oscillations that are not perfectly coherent. Partly for this reason, and partly to compare with the 1D standard model, we now discuss the time-averaged structure of our simulated accretion columns. This is shown in Figure 3.14 for the narrow column simulation v0 and in Figure 3.15 for the wide column simulation v2.

More detail of the time-averaged structure of all three of our high resolution simulations is shown in Figure 3.16. This depicts the vertical profiles of various quantities all measured at the $x = 0$ center of the column, as well as the horizontal radiation flux
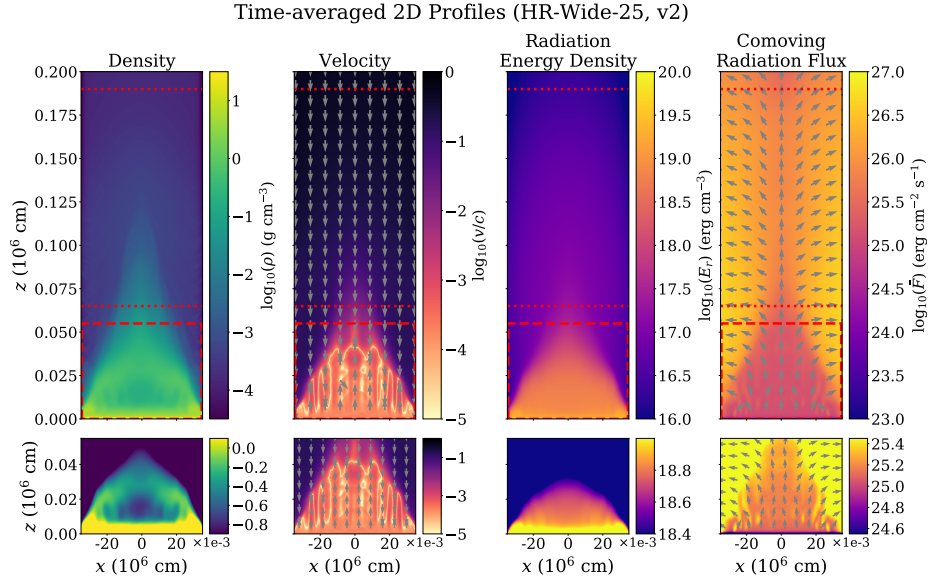
Figure 3.15: Same as Figure 3.14, but for the high-resolution wide column simulation (v2).

averaged over the two sides of the column and the horizontally averaged vertical radiation flux. Also plotted in this figure are the initial conditions (dashed lines) for each of the three simulations, which represent the structure predicted by the 1D standard model. The major differences between this model and the time-averaged profiles of the simulations come from the nonlinear oscillatory behaviors in the accretion column. The discontinuity of the 1D profile calculated from the 1D standard model is the location of the static accretion shock front. These discontinuities are smoothed out in the time-averaged profiles of our simulations because of the time-averaging over the oscillations. The vertical extent of the region affected by the oscillating shock in the time-averaged profile is indicated by vertical dotted lines in Figure 3.16. The top and bottom of this region roughly correspond to the following locations in the time-averaged vertical velocity profile:

1. The base of the shock oscillation region roughly corresponds to where the vertical flow velocity transitions from being dynamical in magnitude to the much smaller

settling speeds within the low altitude regions of the column. Below this height, the vertical velocity is always the small settling speed, but above this height, the time-averaged velocity is much larger because it averages the free-fall speed of material above the shock when it is low to the settling speed below the shock when it is high.

2. The top of the shock oscillation region corresponds to the point where the velocity of vertical flow first deviates from (the radiatively decelerated) free-fall speed. It also corresponds to where the time-averaged density first starts to rise inward, although there is no sharp density discontinuity as it has been smeared out in the time-average.

Most of the radiation escapes from the sides of our oscillating columns, and this of course remains true in the time-average. The second to last row of Figure 3.16 shows the vertical profile of this sideways emission in each of our three high resolution simulations, and it is apparent that the sideways emission is dominated by the regions below the maximum height of the shock. All of this is consistent with the 1D standard model. However, the time-averaged vertical radiation fluxes in the lab frame are mostly negative as shown in the bottom row of Figure 3.16. Note that the vertical radiation flux in the fluid frame must remain positive to support the column structure so the accretion power must be injected into the sinking region via advection associated with the oscillatory motion.

As highlighted by the red dashed box in the first column of Figure 3.15, the 2D time-averaged density profile of the wide column simulation still exhibits a density inversion below the shock oscillation region. (This is also evident in the upper right panel of Figure 3.16.) In other words, the smaller amplitude oscillating density inversion below the instantaneous shock location in version 2 (discussed in the last paragraph of sub-

Time-averaged 1D Profiles
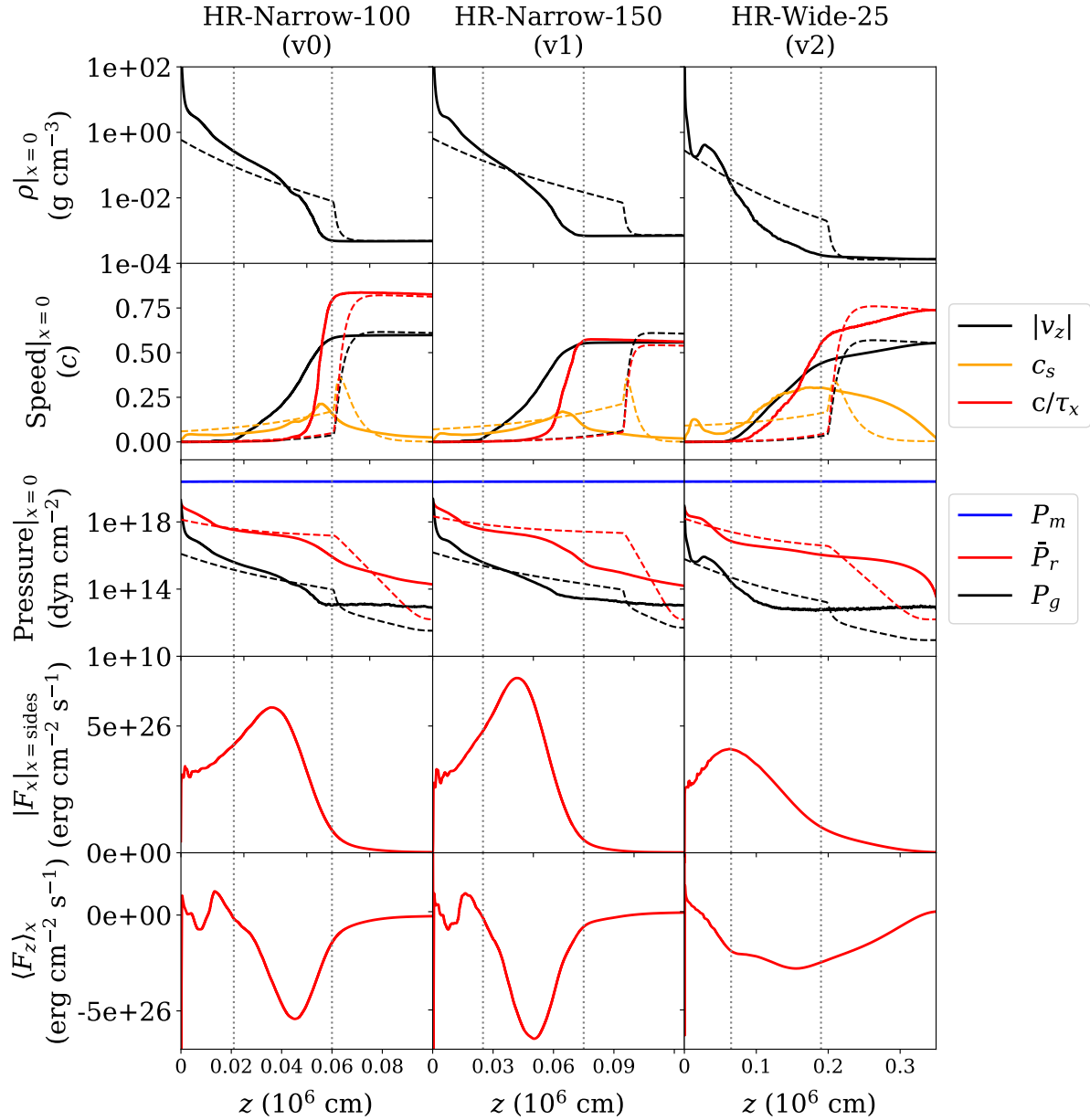
Figure 3.16: Time-averaged vertical profiles of density (top row), various speeds (second row), pressures (third row) at the $x = 0$ center of the column from our three high resolution simulations as labelled in the column titles. Also shown are the horizontal radiation flux averaged over both sides (fourth row) and the vertical radiation flux horizontally averaged over the column (last row). Dashed curves in these figures show the initial condition, which also represents the expectations from the 1D standard model. Vertical dotted lines indicate the vertical spatial extent of the center of the column ($x = 0$) over which the oscillating shock moves.

section 'Oscillatory behavior in wide accretion column' in section 3.2.1) has not been time-averaged out. This confirms that it is relatively steady even in the oscillatory column. In the 2D time-averaged velocity profiles (second columns of both Figure 3.14 and Figure 3.15), significant small-scale horizontal structure only exists in the wide column simulation, and this structure is also visible in all the other profiles (density, radiation energy density, and co-moving radiation flux). These structures all have a characteristic horizontal length scale, and this is the same scale that is apparent in the instantaneous oscillatory behavior. The fact that this has not been smoothed out in the time average suggests that this is a robust scale due to some underlying physics. In section 3.2.4, we suggest that this is due to photon bubble instability.

3.2.3   Physical Origin of Accretion Column Oscillations

The oscillation periods in the light curves shown in Figure 3.4 are ($\simeq 4 - 8 \times 10^{-5}$ s), which is comparable but longer than the free-fall timescale ($\sim 10^{-5}$ s). We contend that the physical origin of these oscillations is not dynamical, but thermal. It is fundamentally due to the inability of vertical advection in the settling flow and radiative diffusion to spread the accretion power liberated mostly below the accretion shock to the base of the column on a time scale short enough to balance the radiative cooling from the sides of the column. We demonstrate this quantitatively here with an approximate analysis of the heat transport and cooling time scales. Along the way, we find that we can also perform a good quantitative estimate of the oscillation period.

We begin by considering epochs in the oscillations when the columns have reached their maximum vertical extent: $t = 6060 t_{\mathrm{sim}}$ for v0, $t = 5530 t_{\mathrm{sim}}$ for v1, and $t = 3950 t_{\mathrm{sim}}$ for v2. Because the oscillation period is longer than the free fall time, the column at these epochs is still in approximate vertical hydrostatic equilibrium. We can then estimate how

long it takes heat to be transported from the accretion shock at height z_sh in the middle $(x = 0)$ of the column down to a given height z:

$$t_\mathrm{heat}(z) = \frac{z_\mathrm{sh} - z}{v_\mathrm{heat}} \quad . \tag{3.13}$$

Here $v_{\mathrm{heat},z}$ is the heat transport speed at height z, given by

$$v_\mathrm{heat} = \left. \frac{-F_z}{\bar{E}_r} \right|_{x=0} \quad , \tag{3.14}$$

where F_z is the lab frame radiative flux and $\bar{E}_r$ is the fluid frame radiation energy density.

To estimate the cooling time, it is important to account for the mound shape of the accretion shock which bounds the mound. We use the shock front gas density at $x = 0$ to roughly contour the mound shape, as shown by the red dashed contours in the 2D density profiles of Figure 3.17. We can then compute the timescale of horizontal radiation diffusion (t_cool) as

$$t_\mathrm{cool}(z) = \frac{(x_r - x_l)/2}{c/\tau_x} \quad , \tag{3.15}$$

where x_l and x_r refer to the left and right boundary of the contoured sinking region, respectively. The horizontal optical depth within the sinking region is defined by

$$\tau_x = \frac{1}{2} \int_{x_l}^{x_r} \rho \kappa dx \quad . \tag{3.16}$$

As shown in Figure 3.17, $t_\mathrm{cool} < t_\mathrm{heat}$ in the upper regions, indicating that heat transport from the accretion shock cannot balance the cooling from the sides. The accretion shock must therefore collapse, quasi-hydrostatically, down to the depth where $t_\mathrm{cool} \simeq t_\mathrm{heat}$. The vertical dotted line shows the location where the two time scales are equal, and below this line $t_\mathrm{cool} > t_\mathrm{heat}$ so that heat from the shock will exceed cooling.
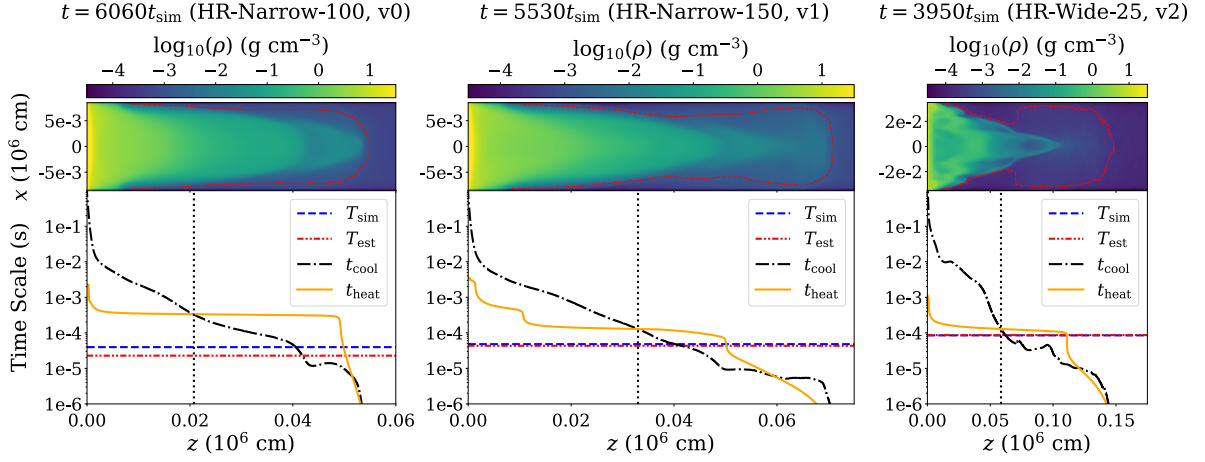
Figure 3.17: Comparison of different time scales at particular epochs corresponding to the maximum vertical extent of the column oscillation in simulations v0, v1, and v2 from left to right as indicated. The 2D colour plots show the instantaneous density distribution at these epochs, with the red dashed contour indicating a density corresponding to the post-accretion shock density in the middle of the column ($x = 0$). The black dot-dashed curve in each plot indicates the horizontal cooling time through radiative diffusion at each height. The orange solid curve is the time it takes heat to diffuse or advect vertically from the top of the column down to the height indicated. The vertical dotted lines indicate the location where these two time scales are equal, and are consistent with the location of the accretion shock at epochs of minimum vertical extent in the oscillation in the simulations. The red dot-dot-dashed lines show our estimate of the oscillation period from equation (3.17e), which agrees well with the measured oscillation periods in the simulations (blue dashed lines).

The column will therefore become over-pressured, and drive the shock back upward. We therefore expect the shock to oscillate up and down, with its lowest height being approximately the location of the vertical dotted line in Figure 3.17 where these two time scales are in balance (hereafter z_{bot}): $0.021R_\star$ for v0, $0.033R_\star$ for v1, and $0.059R_\star$ for v2. In fact, these heights are in excellent agreement with the lowest shock heights that we measure from the simulations (see $t = 6150t_{sim}$ for v0 in Figure 3.5, $t = 5630t_{sim}$ for v1 in Figure 3.8, and $t = 4150t_{sim}$ for v2 in Figure 3.11).

The physics of this quasi-hydrostatic oscillation is therefore fundamentally related to heat transport and cooling, and we can further demonstrate this by estimating its period from a measure of the global cooling time of the upper portion of the column

that is participating in the oscillation. We do this by computing the enclosed radiation energy (ΔE_r) and comparing it to the radiative heating (F_{heat}) from the top (z_{sh}) and the bottom (z_{bot}). (The bottom heating amounts to at most 28% of the total.) Since the radiative cooling mainly depends on the side area, which varies considerably during the course of the oscillation, we adopt the sideways time-averaged radiation flux to compute the radiative cooling (F_{cool}). Our estimate of the oscillation period (T_{est}) then proceeds as

$$\Delta E_r = \int_{z_{\text{bot}}}^{z_{\text{sh}}} \int_{x_l}^{x_r} E_r(t_{\text{peak}}, x, z) dx dz \quad , \tag{3.17a}$$

$$W = \int_{z_{\text{bot}}}^{z_{\text{sh}}} \int_{x_l}^{x_r} \bar{P}_r(t_{\text{peak}}, x, z) \frac{\partial v_z(t_{\text{peak}}, x, z)}{\partial z} dx dz \quad , \tag{3.17b}$$

$$F_{\text{heat}} = \int_{x_l}^{x_r} \left[F_z(t_{\text{peak}}, x, z_{\text{bot}}) + F_z(t_{\text{peak}}, x, z_{\text{sh}}) \right] dx \quad , \tag{3.17c}$$

$$F_{\text{cool}} = \int_{z_{\text{bot}}}^{z_{\text{sh}}} \left[\langle F_x(t, x_l, z) \rangle_t + \langle F_x(t, x_r, z) \rangle_t \right] dz \quad , \tag{3.17d}$$

$$T_{\text{est}} = \frac{2 \Delta E_r}{F_{\text{cool}} - (F_{\text{heat}} + W)} \quad , \tag{3.17e}$$

where $\bar{P}_r$ is the fluid-frame radiation pressure and v_z is the gas vertical velocity, and t_{peak} refers to when the oscillating column is at its maximum extent. The *pdV* work W is volume-integrated within the contoured sinking region. The factor of 2 in (3.17e) is based on the approximation that the same amount of time is spent in the collapse and expansion phases, which is definitely not true due to the nonlinear nature of this oscillation. Nevertheless, as shown in Figure 3.17, T_{est} is in excellent agreement with the direct measurements (T_{sim}) of the oscillation period from the simulations, particularly in v1 and v2. Note that among v0, v1, and v2, the *pdV* work W is only $\sim 1\%$ of F_{heat}. The distributed adiabatic compression is therefore negligible and cannot support the column.

3.2.4   Photon Bubbles and Resolution Dependence

Brief Review of Photon Bubble Instability

Ever since the pioneering linear instability analysis by Arons (1992), it has been expected that "photon bubbles" would be present in neutron star accretion columns. The term "photon bubbles" suggests buoyant, bubble-like structures, but in fact this is not what this phenomenon represents, and the term is therefore highly misleading. On length scales where photons diffuse rapidly, the "photon bubble" really amounts to a radiatively amplified acoustic wave that evolves to form a train of shocks (Begelman 2001; Turner et al. 2005). This rapid diffusion regime might manifest in the outer, low optical depth regions of neutron star accretion columns, but the cores of these columns are in the slow-diffusion regime. There the instability is due to radiative amplification of entropy fluctuations, which is best understood in terms of phase lags between pressure and density perturbations caused by finite gas inertia, in response to radiative forcing. We refer the reader to section 2.1 and Appendix A for a full description. For a vertical magnetic field, the nonlinear outcome of the instability in this regime consists of nearly vertical wavefronts of density, with photons diffusing vertically more rapidly in the low density regions. In a static atmosphere with no resupply of fresh material through accretion, this instability causes the atmosphere to collapse (see chapter 2 for details). The instability always grows fastest at shorter wavelengths, until either the radiation viscous length scale is reached (see section A.2), or the scale height associated with gas pressure (Blaes & Socrates 2003), whichever is larger.

If the slow-diffusion version of this instability manifests itself in our simulations, we would expect nearly vertical wave fronts of density, i.e. vertical columnar patterns that move horizontally. All three of our high resolution simulations v0, v1, and v2 manifest such structure, and the photon bubble instability is a likely candidate. Unfortunately,

demonstrating this in the narrow column simulations is difficult because the distinct columns only manifest during certain phases of the overall vertical oscillation, and moreover occur across a length scale that spans both the rapid and slow-diffusion regimes. On the other hand, the wide column simulation has many high and low columnar structures in density, that are present at all times through the oscillation. They also exhibit a distinct inward horizontal pattern speed that is evident in the animations. We provide further evidence here that these structures are indeed an outcome of the photon bubble instability.

Resolution Dependence

In section 2.3.3, we performed a resolution study on photon bubbles in static atmospheres that confirmed the behavior of increasing growth rate toward shorter wavelengths. Here we conduct a similar resolution study of the wide column accretion simulation: if the multi-peaked structure is due to photon bubble instability, the number of peaks should scale with spatial resolution.

We ran an additional two simulations v3 and v4 with factors of 2 and 4 lower resolution, respectively, compared to the high-resolution wide column simulation (v2). In Figure 3.18 we show snapshots of the density profile of these three wide column simulations at $t = 4060 t_{\mathrm{sim}}$. The dependence of horizontal structure with resolution is clear. In the high-resolution simulation (v2), there are seven peaks in the shock fronts. In the medium-resolution simulation (v3) where the resolution is decreased by a factor of 2, there are only three shock front peaks. In the low-resolution simulation (v4) where the resolution is decreased by another factor of 2, the shock structure is single-peaked. The decreasing number of shock front peaks therefore tracks the decreasing factor of resolution. This resolution dependence is indicative of modes that grow fastest at the smallest resolvable length scales. This resolution dependence is consistent with unstable
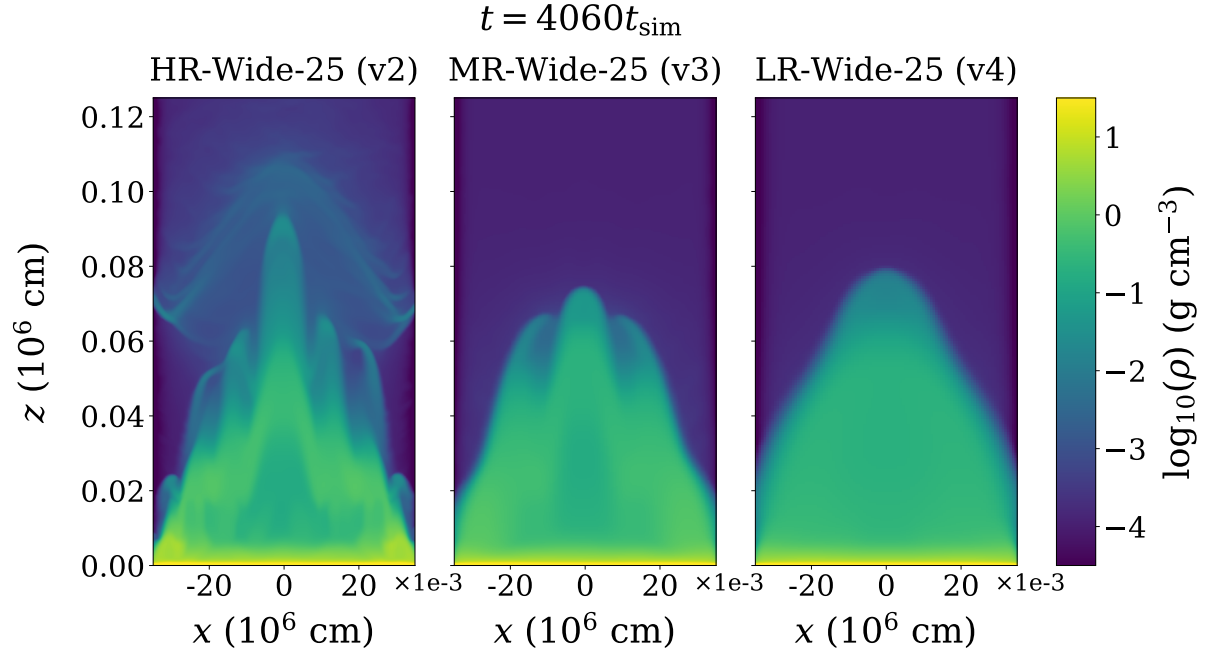
Figure 3.18: Snapshots of the density structure at $t = 4060t_{\mathrm{sim}}$ in our wide column simulations at different resolutions: high (left), medium (middle), and low (right).

modes that grow faster at shorter length scales, and is precisely the behavior of the linear photon bubble instability and its nonlinear outcome (see chapter 2).

None of the high resolution simulations here, including the wide column simulation v2, resolve the viscous length scale, which is approximately 10 cm, about a factor of 15 smaller than the grid scale in each simulation. Resolving such small scales is very expensive and may not even be possible for more global simulations of neutron star accretion columns with existing computational resources. However, at least for the simulations here, these horizontal structures only modify the column dynamics by increasing the oscillation amplitude without changing its period (see Figure 3.4 which shows light curves for all our simulations). Hence we have reached convergence in terms of characteristic time scales present in the light curves and the nonlinear dynamics.

Note that the light curve of the medium resolution simulation (v3) exhibits more noisy behavior than either the low resolution (v4) or high resolution (v2) simulations.

This is because v3 is at just high enough resolution to start exhibiting multi-peaked horizontal structure. The light curve becomes better behaved with the addition of more multiple peaks at higher resolution. That the multi-peaked structure in v2 produces enhanced vertical radiation transport can be seen by comparing this simulation to the lower resolution simulations v3 and v4. Note that these latter simulations do not form a pre-shock (cf. Figure 3.18). As can be seen in the animations of v2, v3, and v4, both the radiation energy density and the flux at altitude are much higher in v2 compared to v3 and v4. In fact, the vertical flux above $z = 0.15 \times 10^6$ cm is at least ten times higher in v2 at all epochs.

Although we believe that we have reached numerical convergence in terms of the light curve behavior, the presence of increasing horizontal structure with increased resolution implies that the time-averaged structures are not converged. This may be an issue when comparing predictions of spectra and polarization from these time-averaged profiles with observations integrated over time scales longer than the very short oscillation period. On the other hand, the additional density inversion that forms below the accretion shock oscillating region appears to be robust, and is therefore likely to be independent of further increase in resolution. Unfortunately, increasing resolution appears to exacerbate the variable inversion problem in our numerical algorithm and results in more noise in the gas temperature. Clearly more work is needed to address this numerical problem.

Linear Phase of Photon Bubbles

To further demonstrate that these horizontal structures are in fact related to photon bubbles, we searched for the linear phase of photon bubble growth and compared that behavior to the analytic linear theory (see Appendix A). Although the linear theory applies to static atmospheres with infinite horizontal extent, not oscillating accretion columns, the radiation sound speed is still much greater than both the fluid velocity and

radiation diffusion speed in the sinking region, so we are in the slow-diffusion regime with instantaneous near-hydrostatic equilibrium. The photon bubble instability mechanism should therefore still operate, and because the photon bubble growth times are fast ($\sim 10~\mu$s), we should be able to observe their linear growth phase.
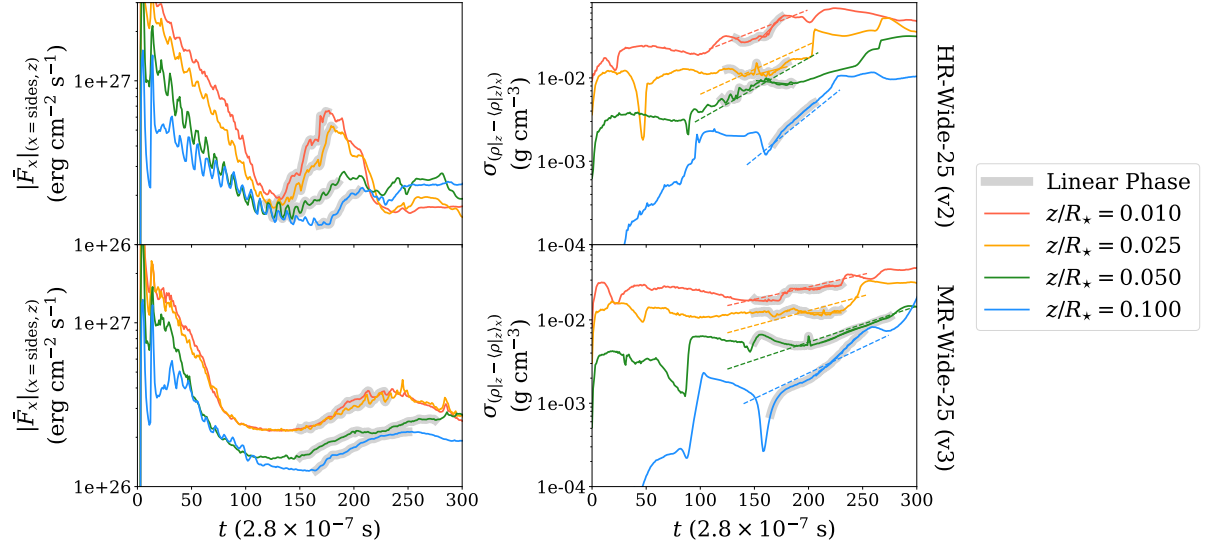
Figure 3.19: Linear growth of photon bubble instability in the relaxation epoch in the high-resolution and medium-resolution wide column simulations (v2 and v3). The left column shows the evolution of the fluid-frame radiation flux averaged over the two sides and the right column refers to the evolution of the density variation, where the linear growth phase is indicated by the grey shaded area.

Since the horizontal multi-peak structure only appears in the high-resolution (v2) and medium-resolution (v3) simulations, and not in the low resolution simulation (v4), we analyze just the first two. As shown in the left column of Figure 3.19, immediately after launching the simulation, radiation leaves the column through the sides. This flux declines until photon bubbles start to grow. The linear phase is indicated by the grey shading and indicates approximately exponential growth, except perhaps at $z/R_\star = 0.025$ (the orange curve) in density. The dashed lines indicate the predicted local WKB maximum growth rates from the linear dispersion relation for photon bubbles in a *static, non-accreting* atmosphere (for details see section A.2), which are in rough agreement

with what we observe in the simulations. In particular, two facts are worth noting that are consistent with identification with photon bubbles: the growth rates increase with height, and they increase with numerical resolution (v2 grows faster than v3).

3.3 Discussion

3.3.1 Validity of the Parameter Regime in Simulations

The typical magnetic fields inferred for accretion columns are $\gtrsim 10^{12}$ G. However, in our simulations, we cannot adopt such high field strengths because they exceed the tolerance of the variable inversion algorithm for resolving the gas pressure, which is crucial at the step of computing the radiative transport source term (3.4c). Therefore we have to maintain the ratio of gas pressure to magnetic pressure as large as possible in order to obtain sufficient precision in the numerical value of gas pressure. Fortunately, the main effect of the strong magnetic fields is to horizontally confine the gas, and there is very little effect on the vertical dynamics. This allows us to adopt a magnetic field that is strong enough for gas confinement (8×10^{10} G in our case) and keep the correct dynamics of the accretion column.

One way in which the choice of magnetic field could be more significant is its effect on the electron scattering opacity. We assume isotropic Thomson scattering, which is valid for the low field strength and high temperatures in our simulations here, and would continue to be valid up to field strengths approaching $\sim 10^{12}$ G. Magnetic scattering opacities are likely to affect the nonlinear dynamics above these field strengths.

3.3.2   Comparison with Previous Works

The 1D models of accretion columns at high accretion rate by Basko & Sunyaev (1976) and, more recently, West et al. (2017a) neglect horizontal gradients in the column structure. As such, these columns have a top-hat shape, i.e. they neglect the actual two-dimensional mound shape that must exist in reality. Because of this assumed geometry, they necessarily under-estimate the horizontal radiation diffusion speed, and therefore over-estimate the column height. This explains in part why the time-averaged shock height from our simulations, is lower than the 1D model prediction of Basko & Sunyaev (1976), as shown in Figure 3.16. The other important difference between these 1D models and our simulations is that the simulations have dynamical, nonlinear oscillations. In the stationary 1D standard model, accretion power can only be released in the region below the shock by the loss of gravitational potential energy by the slowly sinking material. This suggests two problems: 1. when the sinking region has a small height, the gravitational energy liberated by the sinking gas is insufficient to support the column structure. 2. when the sinking region is high, the hydrostatic equilibrium can be hardly maintained by a process (vertical advection) that is necessarily much longer than the dynamical time. In fact, these columns are not stationary, but undergo considerable dynamical motion up and down. It is this dynamical motion that then redistributes accretion power vertically as the material radiates. This dynamical mechanism of redistributing the accretion power liberated at the shock front is fundamentally why the oscillations exist and, indeed, persist. The photon bubble instability itself is not the cause of the oscillations. However, photon bubbles enhance vertical diffusive transport and appear to enhance the coherence of the light curve oscillation by aiding in the formation of pre-shocks that result in flat-topped luminosity variations in the light curve.

The pioneering numerical simulations of accretion columns by Klein & Arons (1989)

and Klein et al. (1996) also exhibited oscillatory behavior with time scales between 0.1 and 1 ms. This is qualitatively consistent with our simulations, although their oscillation period is slightly longer than ours (~ 0.05 ms), likely due to the fact that our columns simulated here are smaller in height. The most recent numerical work on accretion columns prior to our work was done by Kawashima & Ohsuga (2020), who also discovered the development of similar finger-shaped density structures.

Note that the simulations of Klein & Arons (1989) and Kawashima & Ohsuga (2020) found that the multiple-bubble structure disappeared for lower accretion rates. However, this may have been a resolution effect. As the accretion rate decreases, the local Eddington ratio in the sinking zone also decreases, which leads to larger gas density because more gas pressure gradient is required to support the column. Therefore, the radiation diffuses more slowly in the low luminosity case. This directly shifts the peak of the photon bubble growth rate to shorter wavelengths (see section A.2 for details) making it harder to resolve the instability. Moreover, the geometric dilution introduced by any non-Cartesian geometry, e.g. spherical (Kawashima & Ohsuga 2020) and dipolar (Klein & Arons 1989) coordinate systems, naturally decreases the resolution at higher altitude. This loss of resolution will prevent the development of photon bubble behavior at short wavelengths.

3.3.3   Observational Significance

Our long-term plan is to quantify the dynamics and observables of neutron star accretion columns for X-ray pulsars above the critical luminosity (Basko & Sunyaev 1976; Becker et al. 2012) through the use of numerical simulations. Because of our use of Cartesian geometry in this chapter, we are forced to restrict consideration to modest accretion rates and X-ray luminosities so that the column height is much less than the

radius of the star. We intend to pursue more global simulations of higher accretion rate, larger columns in future.

There are in fact some X-ray sources that pass through the accretion rate regime of our Cartesian simulations: high enough that the sinking zone is developed but also low enough that the height of the accretion shock front does not exceed $\sim R_\star$, in particular transient X-ray pulsars such as EXO2030+375, 4U0015+63, KS1947+300, and V0332+53 (Terrell & Priedhorsky 1984; Parmar et al. 1989; Whitlock et al. 1989; Borozdin et al. 1990; Reig & Nespoli 2013). It is noteworthy that the emission patterns of these sources transition between pencil beam and fan beam, and this is usually interpreted in terms of the critical luminosity when an optically thick accretion column is thought to form, according to the Basko & Sunyaev (1976) theory. The existence of nonlinear oscillations and photon bubble dynamics, which we have shown here to result in a lower time-averaged height of the accretion column compared to 1D models, probably does not affect this conclusion as an optically thick column is still required to host this dynamics. Moreover, we have found here that photon bubble dynamics does not alter the overall fact that an accretion column tends to produce fan beam emission: both the instantaneous and time-averaged cooling of the column is dominated by sideways emission from the column.

The main observable difference is the presence of high frequency variability ($\sim 20\,\mathrm{kHz}$), as also pointed out in the pioneering work of Klein et al. (1996) who predicted significant variability power at frequencies $\sim$1-10 kHz. Indeed, this has been invoked to explain putative high frequency variability in the X-ray pulsar Cen X-3 (e.g. Jernigan et al. 2000). However this observed noise component may actually have been an artifact of the splitting up of photon counts in RXTE/PCA sub-bands (Revnivtsev et al. 2015). An attempt to analyze lightcurve data of the bright X-ray pulsar V0332+53 that avoided this problem was attempted by Revnivtsev et al. (2015), who found no extra high frequency noise component to the level of 0.5 percent. It would be worthwhile searching for

high frequency features in the light curves of other X-ray pulsars given how robust are the oscillations that we have found here. It is likely that the oscillation frequencies will depend on the column height and accretion geometry, and more global simulations that take into account the diverging magnetic field geometry will be necessary to quantify this.

3.4   Conclusions

We summarize our conclusions of this chapter as follows:

1. Our simulations more or less agree with standard 1D models of supercritical accretion, in that an optically thick accretion column forms with an accretion shock at the top of the column. The column is supported against gravity by radiation pressure gradients, and most of the cooling takes place through the sides of the column (fan-beam radiation), as in the original models of Inoue (1975) and Basko & Sunyaev (1976). However, in order to establish thermal equilibrium, the sinking material must be supplied with heat at all altitudes to balance the local sideways cooling. Because the PdV work on the sinking material is small, and the time scale of vertical heat transport from the accretion shock is very much longer than the local cooling in the upper regions of the mound-shaped column, the column must cool and collapse. This then produces a shorter, denser column with a longer sideways cooling time, which then overheats and re-expands. This is the origin of the oscillations that we observe. Oscillations were also reported by Klein et al. (1996) and attributed to photon bubbles, but we suspect that they may have been due to the same mechanism that we have found here.

2. The shock fronts in our simulations in general have lower altitudes, both instanta-

neously and in the time-average, than those in the standard 1D model. The basic reason for this is that the finite horizontal one-zone approximation of the 1D models under-estimates the efficiency of cooling from the sides due to the fact that the accretion column actually has more of a 2D mound shape.

3. Photon bubbles do not appear to be directly responsible for either the vertical oscillations or the enhanced cooling compared to 1D models. Instead, they are a further complication that produces a complex multi-peaked horizontal structure when the instability is spatially well-resolved. We have demonstrated that this is so by showing that these structures have similar linear growth rates and resolution dependencies to the linear photon bubble instability. While we have not achieved numerical convergence on the photon bubble structures, the overall oscillation period of the column is not affected by spatial resolution, though the light curve has a smoother oscillatory shape at high spatial resolution.

4. Both the high-frequency oscillation and photon bubble dynamics facilitate the vertical redistribution of energy dissipated at the shock front to various altitudes so that the column structure can be maintained. Whether this continues to be the case for more global accretion columns in spherical/dipolar geometry is the subject of our work in chapter 5.

Chapter 4

Simulations of Cartesian Accretion Columns with Magnetic Opacity

This chapter is adapted from our research work published as Sheng, Zhang, Blaes & Jiang (2023). In this chapter, we explore the dynamical effects of magnetic opacity in Cartesian accretion columns. This chapter is organized as follows. In section 4.1, we describe the numerical methods that we employ in the simulations. In section 4.2, we present our simulation results, discuss the physics that drives their behavior, and discuss the properties of the emergent radiation. In section 4.3, we discuss some of the numerical caveats and also mention some observationally testable predictions. We then summarize our results in section 4.4.

4.1 Numerical Method

4.1.1 Equations

We follow the numerical treatments in chapter 3 to solve the fluid conservation laws together with radiative transfer incorporating magnetic opacity. The governing equations

are summarized as follows:

$$\partial_0(\rho u^0) + \partial_j(\rho u^j) = S_{\mathrm{gr1}} \quad , \tag{4.1a}$$

$$\partial_0(wu^0 u^i - b^0 b^i) + \partial_j \left(wu^i u^j + \left(P_{\mathrm{g}} + \frac{1}{2} b_\nu b^\nu \right) \delta^{ij} - b^i b^j \right) = S^i_{\mathrm{gr2}} - S^i_{r2} \quad , \tag{4.1b}$$

$$\partial_0 \left[wu^0 u^0 - \left(P_g + \frac{1}{2} b_\nu b^\nu \right) - b^0 b^0 \right] + \partial_j(wu^0 u^j - b^0 b^j) = S_{\mathrm{gr3}} - S_{r3} \quad , \tag{4.1c}$$

$$\partial_0 I + n^j \partial_j I = \mathcal{L}^{-1}(\bar{S}_r) \quad , \tag{4.1d}$$

where the gas density ρ and gas pressure P_{g} are defined in the fluid rest frame. The four-velocity is defined as $(u^0, u^i) = \Gamma(1, v^i)$, where $\Gamma = (1 - v_j v^j)^{-1/2}$ is the Lorentz factor and the three-velocity v^i is in units of the speed of light. The quantity I is the frequency-integrated radiation intensity and is a function of position and photon propagation direction n^i. Note that Latin indices indicate the spatial components of a three-vector (i.e. here $i = 1, 2, 3$ refer to x, y, z, respectively), and Greek indices refer to the time-spatial components of a four-vector. Given the three-vector magnetic field B^i, its four-vector form $b^\mu = (b^0, b^i)$ and total enthalpy w are given by:

$$b^0 = u_j B^j, \quad b^i = \frac{1}{u^0}(B^i + b^0 u^i) \quad , \tag{4.2a}$$

$$w = \rho + \frac{\gamma}{\gamma - 1} P_g + b_\nu b^\nu \quad . \tag{4.2b}$$

Here the adiabatic index $\gamma = 5/3$ is assumed for the ideal gas. The gravitational source terms S_{gr1}, S^i_{gr2}, and S_{gr3} are derived from general relativity in the weak field limit, and can be found in section B.2. In equation (4.1d), $\mathcal{L}^{-1}$ is the Lorentz boost operator from the comoving frame to the lab frame. The source term of the radiative transport $\bar{S}_r$ is intrinsically defined in the comoving frame, while the radiation source terms S^i_{r2} and S_{r3} that exchange momentum and energy between gas and radiation are defined in

the lab frame. Both of their formulations can be found in (3.4), except here we adopt the magnetic opacity κ_m for photon-electron scattering. The details of the magnetic opacity we use in our simulations can be found in section E.3. In the previous chapter, we assumed for simplicity that the scattering opacity was isotropic and constant and given by the Thomson value κ_T. However, this can significantly overestimate the photon-electron interaction when the magnetic field is strong at low gas temperatures. Moreover, magnetic electron scattering is anisotropic and polarization dependent. Nevertheless, a Rosseland and polarization-averaged opacity can be derived which is approximately isotropic (Arons et al. 1987; section E.3). It is this magnetic opacity κ_m that we use to replace the Thomson opacity that we adopted in our previous simulations. Figure 4.1 shows the temperature dependence of this magnetic opacity for different magnetic field strengths. The magnetic opacity significantly increases with gas temperature T until it reaches a peak value of $1.95\kappa_T$ at $kT = 0.385$ times the electron cyclotron energy $\hbar\omega_{ce}$. It then returns to Thomson at higher temperatures.
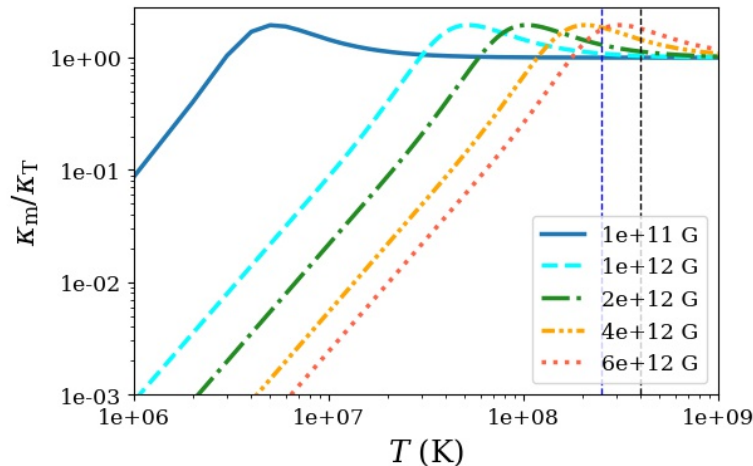
Figure 4.1: Temperature-dependence of the magnetic opacities that we use in our simulations, in units of the Thomson opacity. Each curve represents the different magnetic fields that we adopt for our simulations. The vertical dashed lines indicate the approximate maximum temperatures achieved at the base of the column in our simulations: $\sim 2.5 \times 10^8$ K for the low accretion rate (Lowacc) simulations, and $\sim 4 \times 10^8$ K in the high accretion rate (Highacc) simulations.

4.1.2   Simulation Setup

Simulation Parameters

For our simulations, we select version 2 (HR-Wide-25) in chapter 3 as the prototype, and vary its magnetic field strength and accretion rate to explore the dynamical changes of the accretion column with magnetic opacity. For all of our simulations, the mesh grids are set to be 700×2048 in the horizontal and vertical directions, respectively. The domain height is $0.35R_\star$, and the width of the accretion column region is $0.06R_\star$, where we adopt a neutron star radius $R_\star = 10^6$ cm.

Version	Name	Magnetic field $(10^{12}$ G$)$	ϵ	ρ_{acc} $(10^{-4}$ g/cm$^3)$
1	Lowacc01	0.1	25	1.15
2	Lowacc1	1	25	1.15
3	Lowacc2	2	25	1.15
4	Lowacc4	4	25	1.15
5	Lowacc6	6	25	1.15
6	Highacc4	4	375	17.25
7	Highacc6	6	500	23.00

Table 4.1: Names and global parameters of all the simulations. The magnetic fields listed are only used for the computation of the magnetic opacity. The actual magnetic field used in the MHD was initialized to be 8×10^{10} G for all the simulations.

The global parameters that we vary in our seven simulations are listed in Table 4.1. For the first five simulations, we vary the magnetic fields that we use to compute the magnetic opacities, from 10^{11} G (Lowacc01) to 6×10^{12} G (Lowacc6). Simulations Lowacc1 $(10^{12}$ G$)$ to Lowacc6 span the range of magnetic fields inferred from electron cyclotron line observations in X-ray pulsars (Staubert et al. 2019), but we include Lowacc01 to compare with our previous Thomson scattering simulations. For simulations Highacc4 and Highacc6, we increase the accretion rates for the simulations with the two strongest magnetic fields, in order to build up higher accretion columns. The parameter ϵ is the accretion rate expressed as a local Eddington ratio and ρ_{acc} is the density of the

incoming accretion flow at the top boundary. Both of their definitions can be found in equation (3.6) in chapter 3.

Boundary and Initial Conditions

The numerical setup of the simulation domain is identical to that of chapter 3, where the actual accretion column region is at the center with two vacuum regions on both sides and a gas-supported base at the bottom as effective boundaries. The boundary conditions of the simulation domain are also the same as what we used in chapter 3, and we summarize them as follows. The bottom boundary is reflective for both gas and radiation, and the magnetic fields are set to be constant and vertical. The side boundaries are reflective for both gas and magnetic fields, but allow the radiation to escape freely (i.e. a radiation vacuum boundary condition, see section 2.2.2). Although the boundary conditions at the sides of the simulation domain are reflective for the magnetic field, the field at the edge of the actual accretion column inside the two vacuum regions is not so constrained. The magnetic fields at the top boundary are set to be constant and vertical. A cold accretion flow is injected from the top boundary within the accretion column region, where the comoving radiation fields are set to be isotropic and in local thermal equilibrium. Outside the accretion column region, the top boundary is outflow for the gas and vacuum for the radiation so they are free to escape.

For the five simulated accretion columns at the low accretion rate ($\epsilon = 25$), we adopt as initial condition the 1D solution of the one-zone stationary model with Thomson opacity (for details, see section 3.1.3). For the high accretion rate simulations, we start from the the corresponding low accretion rate simulation that uses the same magnetic field, select a snapshot when the accretion column is in the quasi-steady state, and restart it using the higher accretion rate. To prevent numerical failures associated with a sudden accretion rate change, we slowly and linearly increase the accretion rate from $t = 3000t_{\mathrm{sim}}$

to $t = 4000 t_{\mathrm{sim}}$, where the selected simulation time unit is $t_{\mathrm{sim}} = 2.8 \times 10^{-7}$ s in this chapter.

4.1.3   Additional Numerical Treatments

The magnetic pressure in neutron star accretion columns is larger than the thermal pressure by orders of magnitude. As a result, the variable inversion algorithm in ATHENA++ in going from conservative to primitive variables (including gas pressure) can fail to numerically resolve the small gas pressure. This introduces numerical noise in determining the gas temperature which is used to define opacities and emissivities. We therefore adopt an initial vertical magnetic field of 8×10^{10} G for the actual magnetohydrodynamics (MHD) in all of the simulations presented in this chapter. This is sufficiently strong to confine the column against horizontal radiation pressure forces, and to constrain the matter to move vertically. It is also low enough to avoid excessive numerical noise from the variable inversion in the sinking zone of the accretion column. Hence, the magnetic fields listed in Table 4.1 are purely used for the computation of the magnetic opacity, and not in the MHD itself.

However, the variable inversion algorithm can still fail in the low-density, free-fall region, which introduces substantial numerical noise into the gas temperature there. Because the magnetic opacity depends on temperature, the opacity can also be noisy, and in fact sometimes achieves artificially high values when the temperature noise is substantial. This can result in a strong interaction between the gas and radiation above the shock front. In some of our early numerical experiments, this effect gradually destabilized the accretion column and eventually led to ejection of the incoming accretion flow above the shock front. In reality, the matter in the free-fall zone has low temperature and so low magnetic opacity. Therefore, in our simulations, we adopt a small, but nonzero, fixed

value of the magnetic opacity ($\kappa_{\mathrm{m}} = 0.06\kappa_{\mathrm{T}}$) in the free-fall zone in order to eliminate this artificial noise and smoothly handle the transition between the free-fall zone and sinking zone.

4.2   Results

As noted above, our simulations with low accretion rates started from a 1D, Thomson scattering initial condition. This always overestimates the column height because of (1) the underestimated cooling efficiency from the oversimplified top-hat column shape and (2) the altered radiation-gas interaction from magnetic opacity. (We discuss the effects of this in detail in section 4.2.2.) Therefore, the sinking zone quickly collapses and reaches a new equilibrium state where gravity is roughly balanced by the adjusted radiation pressure support. After the accretion column has relaxed from the initial condition, the system gradually enters into a quasi-steady state with high-frequency oscillations that persist to the end of the simulation, similar to what we found in chapter 3. For the simulations with high accretion rates, the column also reaches a quasi-steady state with oscillations. However, at late times both the column height and the oscillation amplitude dramatically increase due to an instability associated with the fact that the opacity increases with temperature at these high magnetic fields (see section 4.2.6).

4.2.1   Behavior at Weak Magnetic Fields and Low Accretion Rate

In Figure 4.2, we present the density distribution over one full oscillation period of Lowacc01 as an illustration of the oscillatory behavior. As discussed in chapter 3, the oscillation originates from the instantaneous mismatch between replenishment of internal

energy and sideways radiative cooling. When the accretion column is most vertically extended, the sideways radiative cooling is maximized, while the heat that is mostly generated at the shock front cannot be transported to the bottom fast enough to balance this cooling. Hence, the column structure begins to collapse due to insufficient radiation pressure support. When the accretion column is compressed to its lowest height, the sideways cooling is minimized and the low altitude shock front over-heats the column, resulting in vertical expansion.
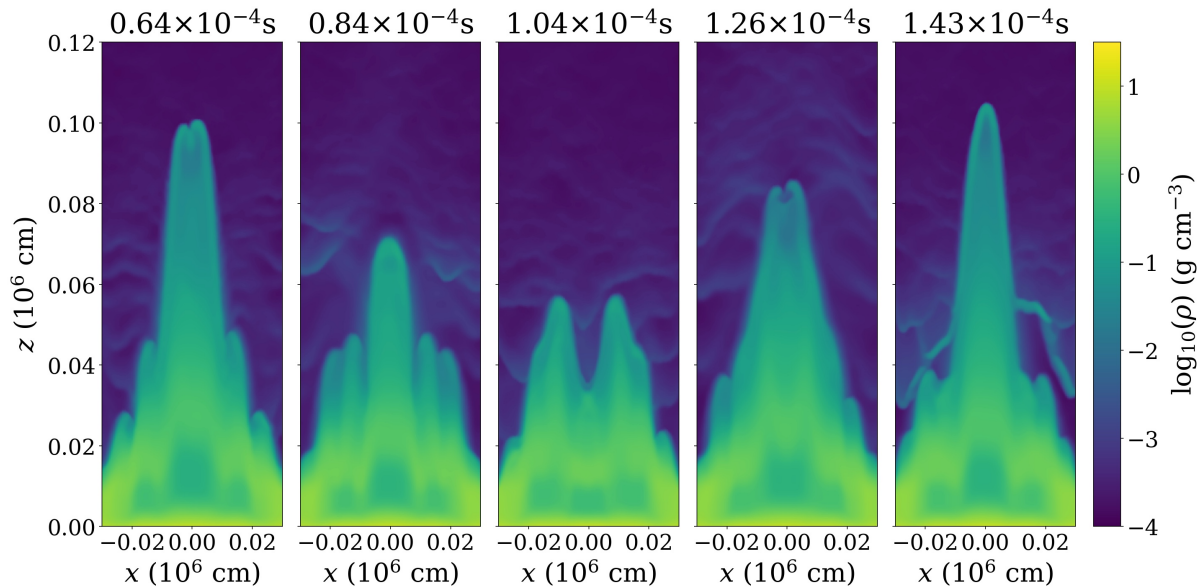
Figure 4.2: Snapshots of the density distribution in simulation Lowacc01, covering approximately one oscillation period of the shock at the center of the column. (The times indicated in the panels correspond to the same origin as the time axis used to plot light curves in Figure 4.9.)

Figure 4.3 also shows the presence of vertical finger-like structures that propagate horizontally inward toward the center of the column. These are a manifestation of the entropy waves that are associated with the photon bubble instability in the slow radiation diffusion regime (see chapter 3 and chapter 5). These entropy waves are present in all of our simulations, but have little effect on the fundamental oscillatory dynamics, nor do they alter the oscillation frequency.

97
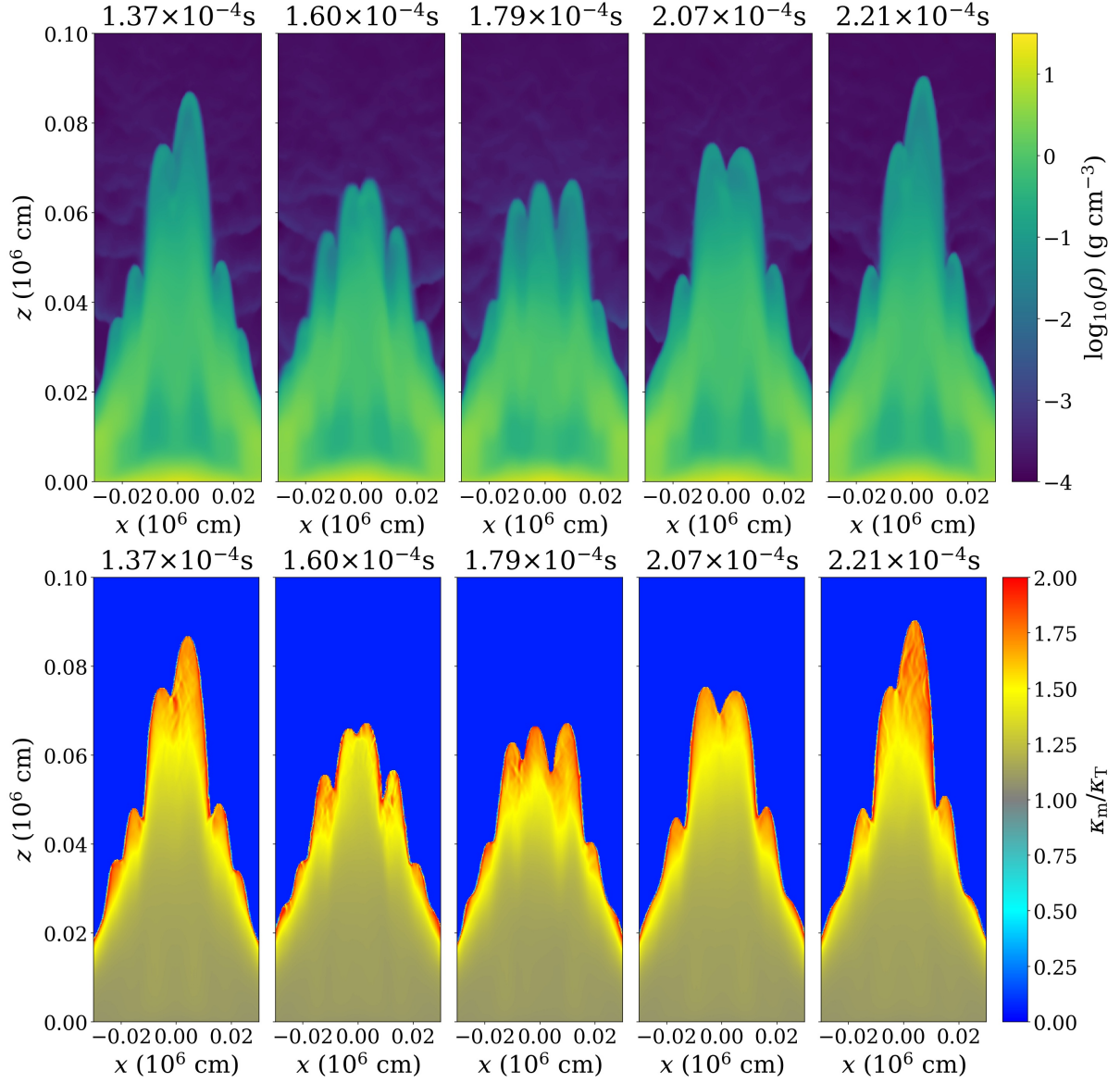
Figure 4.3: Snapshots of the density distribution in simulation Lowacc1, covering approximately one oscillation period.

Compared with the analogous simulation using Thomson opacity (see HR-Wide-25 in chapter 3), all the simulations using magnetic opacity lack the long-lived, coherent pre-shock structures because of the weak gas-radiation interaction when the gas temperature is far below the cyclotron energy in the free-fall zone. Nevertheless, as is evident from Figure 4.2, density fluctuations do occur in the free-fall zone, particularly in the weaker

magnetic field low accretion rate simulations. As we discuss more extensively below in section 4.2.4, these simulations exhibit the strongest variability, and that variability is responsible for these fluctuations due to the interaction of the upward radiation field from the column. The less variable simulations show significantly reduced fluctuations in the free-fall zone. We also found that the pre-shock structure disappeared when the magnetic field decreased with height in the split monopole geometry of chapter 5, simply because of the reduced ram pressure at higher altitudes.

Lowacc01 has such a weak magnetic field that the temperature width of the opacity peak is easily surmounted in the shock and much of the sinking zone is supported by Thomson opacity. (See the 10^{11} G curve in Figure 4.1: almost all of the temperature range toward the base of the column is in the Thomson regime). It is therefore closest in its behavior to the simulations in chapter 3 and chapter 5 that assumed pure Thomson opacity. Figure 4.3 depicts both the density and opacity in the stronger magnetic field simulation Lowacc1. As illustrated by the 10^{12} G magnetic field curve in Figure 4.1, the stronger magnetic field produces a wider opacity peak in temperature space. This is evident in the lower panel of Figure 4.3. As material crosses the shock, the temperature climbs over the opacity peak and results in a high opacity in the post-shock plasma. Going downward into the sinking zone, the opacity declines as we are past the opacity peak, eventually approaching the Thomson opacity in the deep interior. Lowacc1 still shows substantial vertical shock oscillations and inward propagating entropy waves that were evident in Lowacc01. As we will see in the next section, the effects of the opacity on the dynamics and structure of the column become much more important as we increase the magnetic field still further.

4.2.2   Effects Arising from Changing Magnetic Field

In this section, we use the five low accretion rate simulations (Versions 1 to 5, Lowacc01 - Lowacc6) to study how the dynamical behavior of the accretion column varies with changes in opacity caused by changes in magnetic field strength, at fixed accretion rate. Naively, one might expect that increasing the magnetic field would tend to decrease the overall opacity, so the radiation pressure force on the plasma would decrease, and the time-averaged height of the accretion column would therefore decrease. The time-averaged density profiles for the low accretion rate simulations are shown in Figure 4.4, and do in fact show a decrease in column height with increasing field strength. However, for this accretion rate, Figure 4.5 shows that the opacity actually generally increases, not decreases, in the time-averaged column structure as the magnetic field increases from Lowacc01 to Lowacc4. Only in going from Lowacc4 to Lowacc6 does the opacity decrease, and the column then almost becomes a surface hot spot.

Once again, Figure 4.1 provides the explanation for this behavior. Although the shapes of the opacity curves are all very similar in this logarithmic plot, the actual linear temperature width is very small at low magnetic field strengths and increases toward higher field. For the lowest magnetic field (Lowacc01 in the left-most panel of Figure 4.5), the opacity across the shock jumps right through the peak into the Thomson regime. The low values of the opacity at the surface, indicated by the cyan color in Figure 4.5, are simply due to the time-averaging over the vertical oscillation of the shock, so that at those locations one is averaging over the near-zero opacity in the free-fall zone and the Thomson opacity in the sinking zone. As we discussed in the previous section, Lowacc1 transitions through the opacity peak to almost reach Thomson in the interior, but the time-averaged opacity structure (second panel from the left in Figure 4.5) does not exhibit the actual peak opacity because of the averaging over lower opacities in the
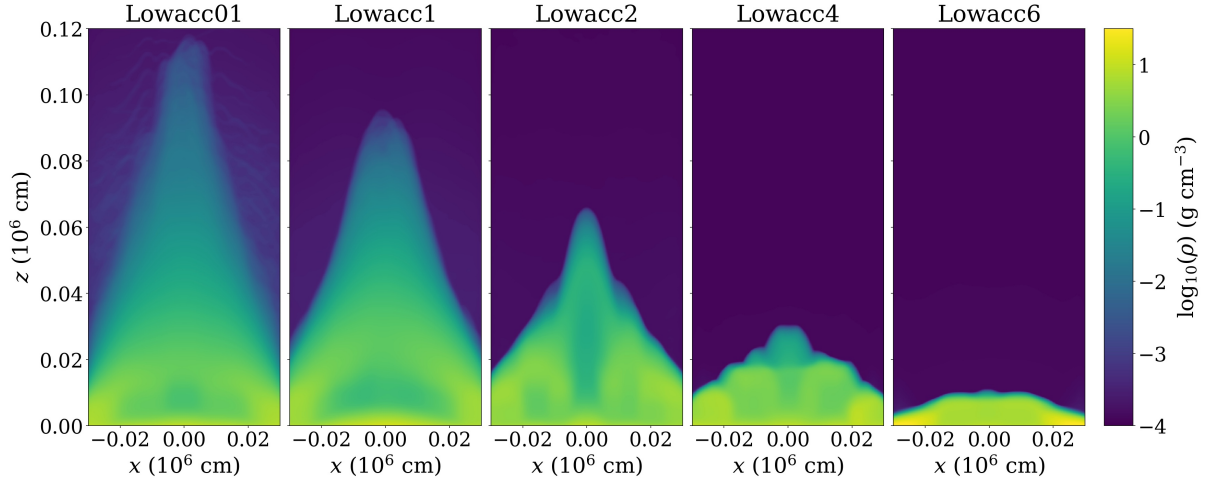
Figure 4.4: Time-averaged density profiles of simulations Lowacc01 to Lowacc6 from $t = 6000t_{\mathrm{sim}}$ to $t = 13000t_{\mathrm{sim}}$. The accretion rate is the same in all these simulations, and the only thing that changes is the magnetic field used to determine the opacity, increasing from 10^{11} G on the left to 6×10^{12} G on the right.
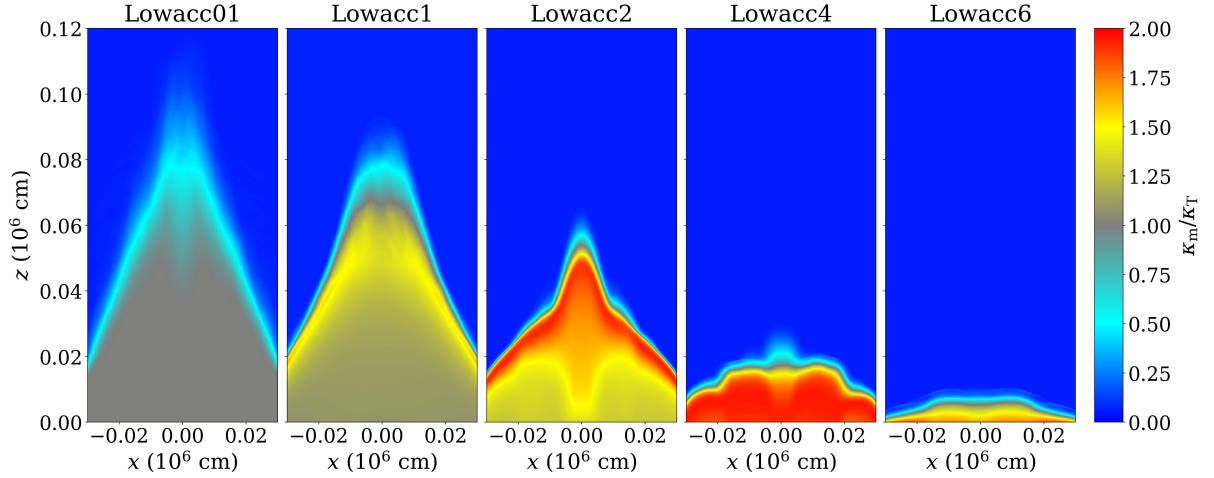
Figure 4.5: Time-averaged opacity profiles of simulations Lowacc01 to Lowacc6 from $t = 6000t_{\mathrm{sim}}$ to $t = 13000t_{\mathrm{sim}}$.

vertically oscillating shock. As one moves to the simulations with still higher magnetic field, the wider and wider opacity peak becomes better and better resolved in the time-average, and the opacity in the deep interior never declines back down to Thomson. In Lowacc4, the opacity is close to the peak value everywhere in the sinking zone, and finally in Lowacc6 the temperature jump across the shock and down to the base of the column is

too small for the opacity to quite reach the peak. (Note the location of the intersection of the base temperature indicated by the left vertical line in Figure 4.1 with the 6×10^{12} G magnetic opacity curve.) The opacity therefore increases as one moves downward toward higher temperatures in what is left of the sinking zone. Further increase of the magnetic field would evidently result in too little post-shock opacity to support a column, and we would be left with a hot spot.

We are still left with the question as to why the column height decreases with increasing magnetic field in going from Lowacc1 to Lowacc4, even while the opacity is increasing inside the column. Let us begin by comparing Lowacc1 and Lowacc2. Lowacc2 has significantly increased opacity just below the shock compared to Lowacc1, simply because it has a wider opacity peak. This appears to provide a further barrier to vertically distributing the accretion power liberated in the shock to the rest of the column. Instead, more of the accretion power is radiated outward from the shock. This results in a shorter column, and a column that does not oscillate vertically as much as in the weaker magnetic field case. As we discussed above, these vertical oscillations are also a direct way of redistributing the accretion power vertically, but this also is now failing in the shorter column. As we continue to increase the magnetic field from Lowacc2 to Lowacc4 the post-shock opacity is even larger, and the column height again decreases, becoming almost a hot spot configuration. A concomitant feature of our simulations is that the vertical displacement amplitude of the oscillation declines with increasing magnetic field strength at fixed accretion rate. As we discuss in more detail in section 4.2.4 below, this, in turn, results in a smaller luminosity variability amplitude.

The postshock opacity declines in moving from Lowacc4 to Lowacc6, because the opacity peak is now so wide that the peak is not reached in Lowacc6. And yet the column height still decreases. This is due to a second important contribution to the decrease in column height which is evident from Table 4.2. Despite the fact that simulations

Lowacc01-Lowacc6 have the same accretion rate, they do not have the same emitted luminosity. In fact, the luminosities of the simulated columns show a decreasing trend with stronger magnetic field, except in going from Lowacc1 to Lowacc2, where the luminosity slightly increases. The reason for this is that as the column height declines (driven by the postshock opacity variation), the sideways emitting area declines and, at the same time, the shock-liberated accretion power is brought closer to the stellar surface. This means that more of the accretion power is able to advect through the sinking zone and into the relatively cold neutron star base layer, and this is also a contributing factor to the decrease of the column height. It is this effect that dominates the decrease in going from Lowacc4 to Lowacc6. In going from Lowacc1 to Lowacc2, the post-shock opacity reaches its maximum possible value, and this is what causes Lowacc2 to have a slightly higher fraction of radiated accretion power.

4.2.3   Effects Arising from Changing Accretion Rate

Our highest field strength simulations at low accretion rate (Lowacc4 and Lowacc6) resulted in very short accretion columns. One would expect that increasing the accretion rate in these two magnetic field regimes would produce more luminosity and radiation pressure support, resulting in taller columns. We did this in simulations Highacc4 and Highacc6, and we present the resulting time-averaged density and opacity in Figure 4.6 and Figure 4.7, respectively. Highacc4 has the same magnetic field (4×10^{12} G) as Lowacc4, but an accretion rate that is 15 times larger. Highacc6 has the same magnetic field (6×10^{12} G) as Lowacc6, but an accretion rate that is 20 times larger. As expected, the increased accretion rates in these two simulations result in taller structures, and in fact taller than the weak magnetic field, low accretion rate simulation Lowacc01. As indicated in Table 4.2, no more than ten percent of the accretion power is transferred to

103

the neutron star base, compared to $\simeq 40$ percent in the low accretion rate simulations Lowacc4 and Lowacc6. A taller column with its much larger surface area (and higher postshock opacity in these two cases) is better able to release the accretion power in emergent radiation.
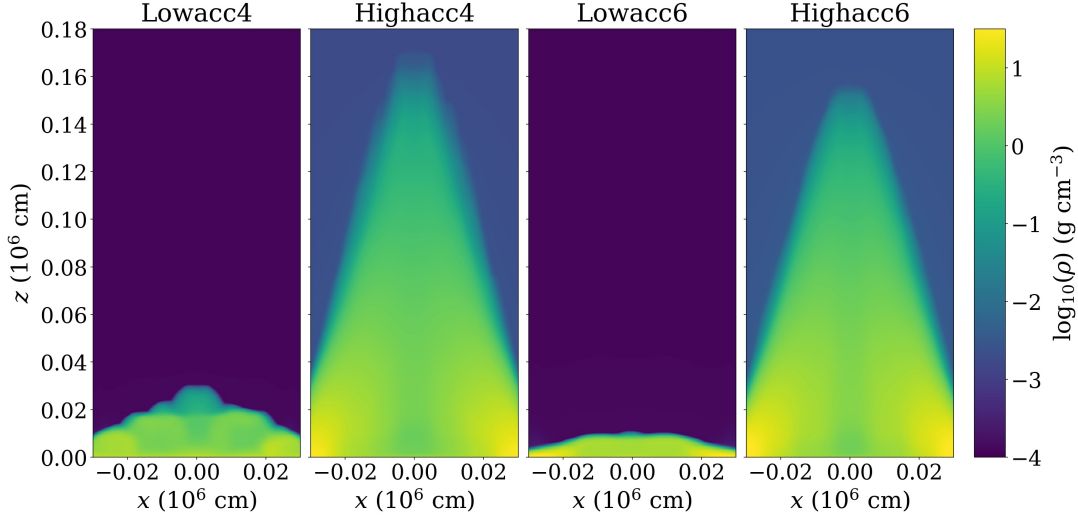
Figure 4.6: Comparison of the time-averaged density profiles of simulations with the same magnetic field strength but different accretion rates, from $t = 6000t_{\text{sim}}$ to $t = 13000t_{\text{sim}}$. The two panels at the left are for 4×10^{12} G magnetic fields, and the two on the right are for 6×10^{12} G.
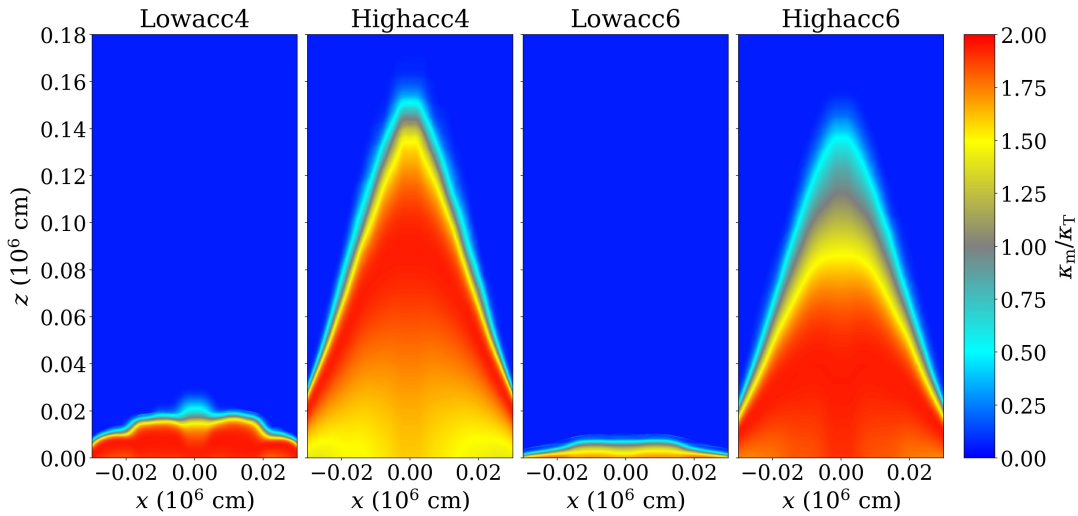
Figure 4.7: Time-averaged magnetic opacity profiles of simulations with the same magnetic field strength but different accretion rates, from $t = 6000t_{\text{sim}}$ to $t = 13000t_{\text{sim}}$

Figure 4.8 shows the time-dependent behavior of both the density and the opacity over a time interval of 1.4×10^{-4} s in simulation Highacc6. As we discuss in more detail in the next subsection, this corresponds to one oscillation period in the peak frequency of the power spectrum of the light curve of this simulation. Comparing Figure 4.8 to Figure 4.2 and Figure 4.3, it is apparent that the structure of the column is varying much more dramatically in the latter, weaker magnetic field simulation. This is true even though these simulations produce columns with comparable time-averaged heights. We discuss why this is in the next subsection.
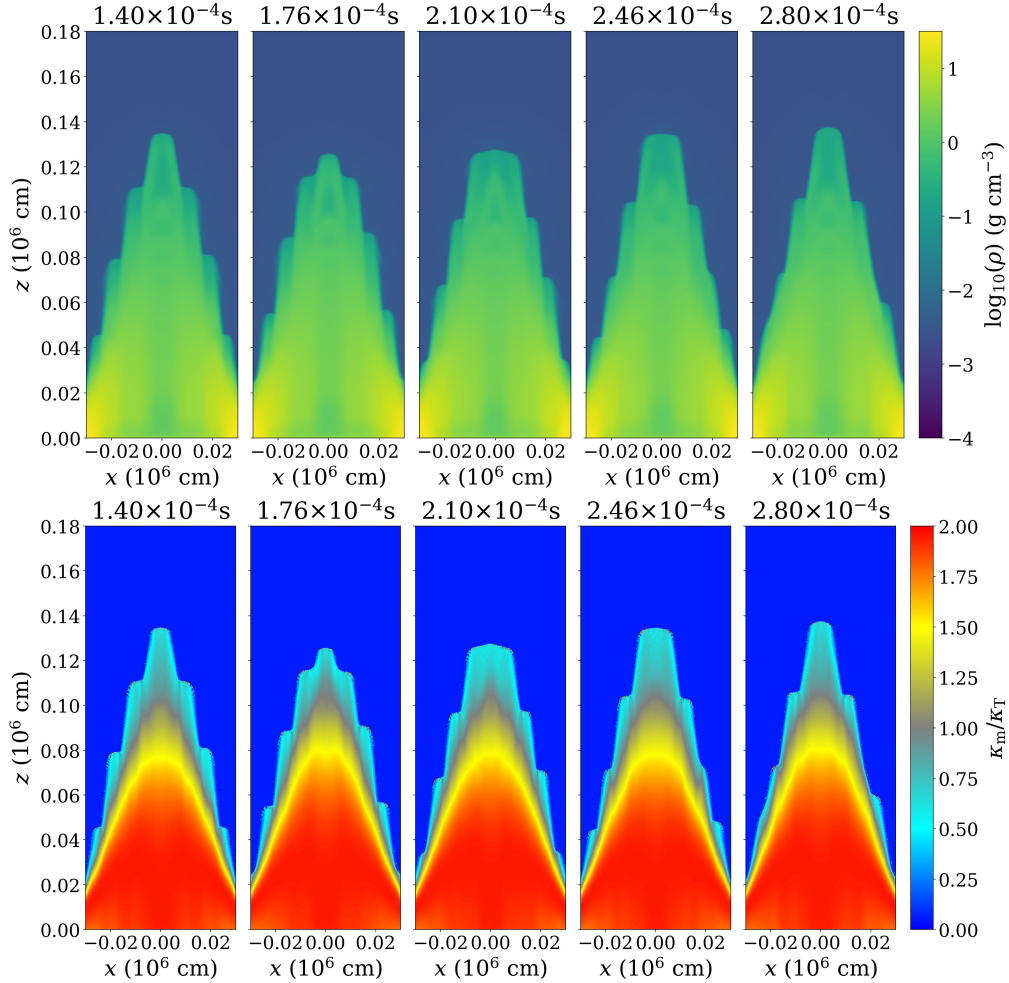
Figure 4.8: Snapshots of the density distribution and opacity distribution in simulation Highacc6 over an interval of 1.4×10^{-4} s. This corresponds to approximately one oscillation period in the light curve for this simulation.

4.2.4   Variability

Figure 4.9 depicts the luminosity light curves of all the simulations. We compute these light curves by simply summing the horizontal and vertical lab-frame fluxes times cell face areas for cells near the photosphere. Because the velocity of the flow is restricted by the magnetic field to be almost exactly vertical, there is almost no difference between the lab frame and fluid frame horizontal radiation fluxes. However, for simulations Highacc4 and Highacc6, which ran for a much longer time than the Lowacc simulations, some horizontal motion began to occur as the effective boundary at the base overheats and we start to lose magnetic confinement. This produces artificial high frequency, Alfvénic oscillations in the lab frame flux and we have removed these from the light curves in Figure 4.9 by using the fluid frame horizontal flux.

Name	$\langle L \rangle / L\text{acc}$	$\sigma(L)/\langle L \rangle$	$\langle L_x \rangle / \langle L \rangle$	$\langle L_x/L \rangle$
Lowacc01	0.875	0.271	0.843	0.858
Lowacc1	0.659	0.139	0.890	0.892
Lowacc2	0.666	0.056	0.966	0.965
Lowacc4	0.577	0.054	0.375	0.373
Lowacc6	0.548	0.036	0.138	0.137
Highacc4	0.909	0.044	0.956	0.956
Highacc6	0.961	0.042	0.986	0.987

Table 4.2: Time-averaged radiated luminosity as fraction of accretion power, standard deviation of light curve variability, and two methods of to determine the fan beam fraction: the ratio of mean horizontal luminosity to mean luminosity, and mean of the horizontal luminosity fraction.

All the light curves in Figure 4.9 show significant high frequency variability, including quasi-periodic oscillations (QPOs) with varying degrees of coherence. Power spectra of these light curves are shown in Figure 4.10, and the relative amplitude of the most significant QPOs are listed in Table 4.2. In our Thomson scattering simulations in chapter 3 and chapter 5, we showed that the origin of these oscillations is due to a breakdown in thermal equilibrium caused by the fact that advection of heat in the settling
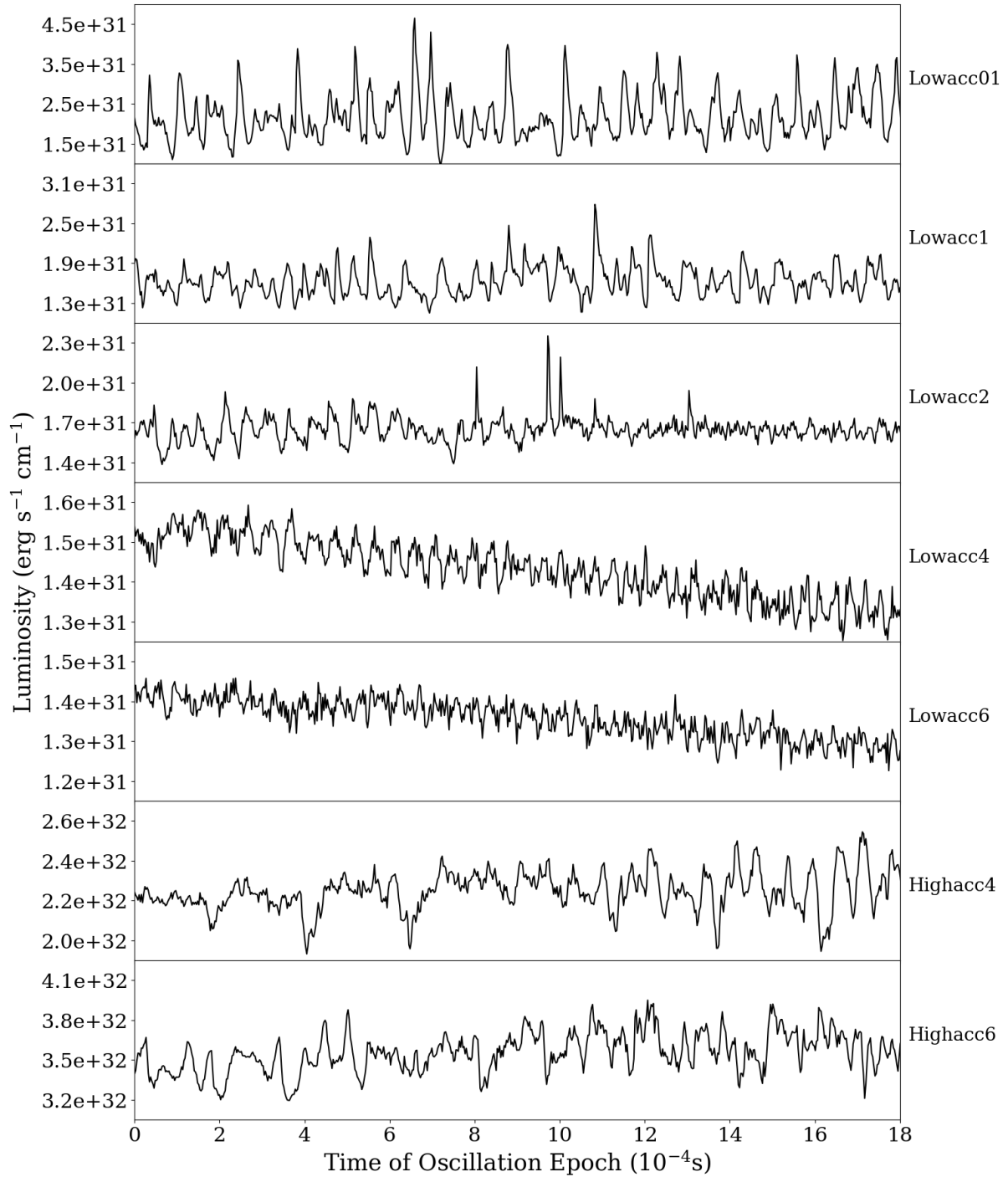
Figure 4.9: Light curve variation of all simulations, starting from times when the simulations achieved an approximate steady state with persistent oscillations (6000 t_{sim} for the low accretion rate simulations Lowacc01-Lowacc6, 11000 t_{sim} for the Highacc4 and Highacc6 simulations.
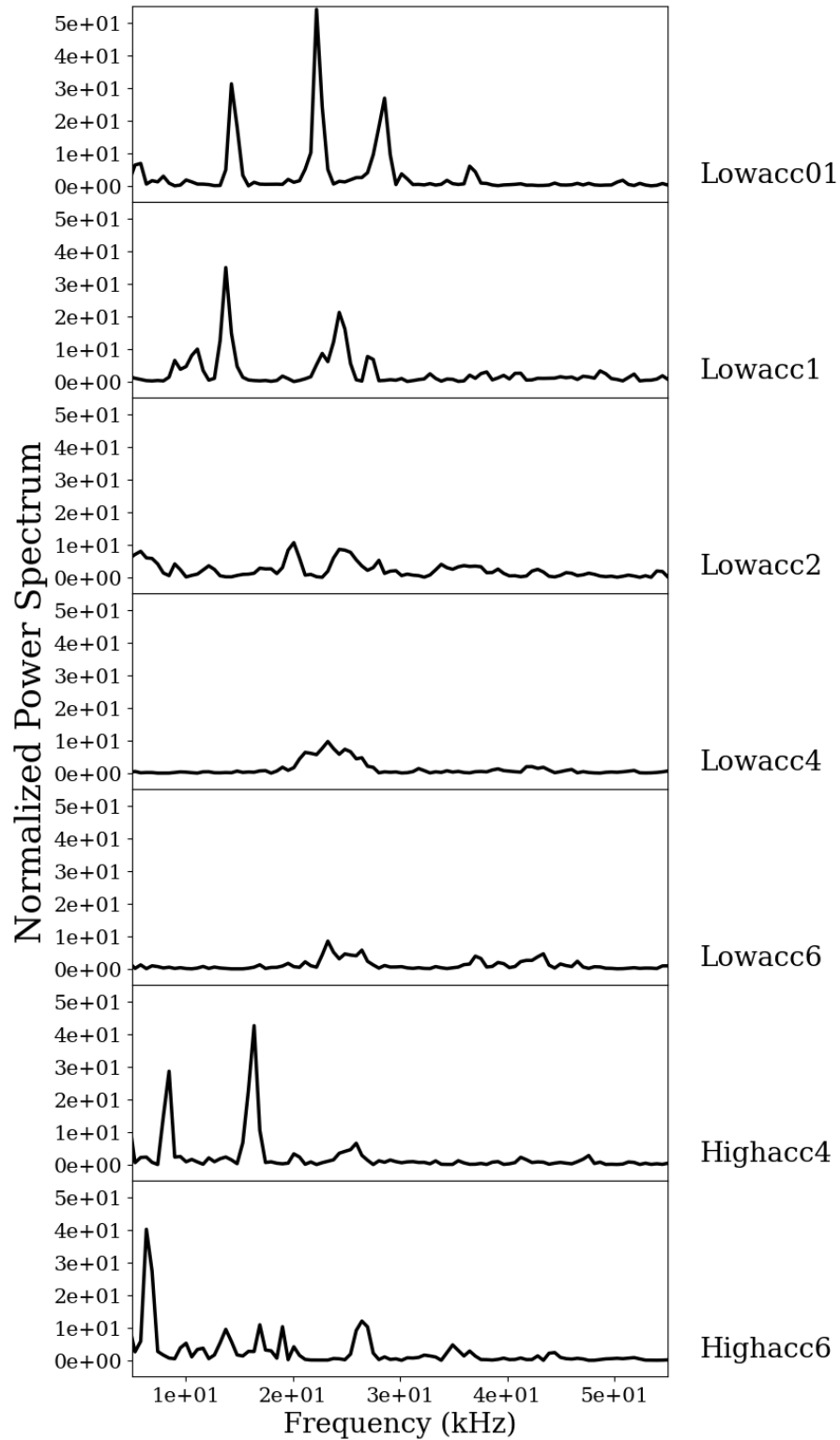
Figure 4.10: Power spectrum of each simulation computed using Welch's method.

flow and PdV work are generally unable to balance the sideways radiative cooling when the column is at maximal vertical extent. The column therefore overcools and the shock height falls, resulting then in overheating which causes the shock to rise again. This can vary with horizontal position within the column as separate vertical fingers oscillate up and down. That this is happening here in these magnetic opacity simulations is shown in Figure 4.11, which compares the power spectrum of shock height variations at different horizontal locations in Highacc4 with the luminosity power spectrum. Clearly the three most significant QPOs in the latter match the shock height oscillations at different horizontal locations. Note that more light curve power is in the middle frequency QPO, while the most shock height power is in the lowest frequency QPO. These two QPOs are in a $2 : 1$ frequency ratio, and the relationship between shock height and emitted light is not likely to have the same proportionality at different harmonics in these non-sinusoidal oscillations.

Consistent with their physical origin, the frequencies of these oscillations are related (inversely) with the local cooling time at that horizontal section of the column. For example, for taller accretion columns, the shock front generally needs to oscillate with a sufficiently large vertical amplitude to replenish the heat to support the bottom region, and this also leads to a longer oscillation time and lower oscillation frequency. This is exactly what we see in Table 4.2 and Figure 4.10 as the stronger magnetic field in simulations Lowacc01 to Lowacc6 results in shorter accretion columns. In particular, when the magnetic field is sufficiently strong (e.g. Lowacc4 and Lowacc6), the accretion column almost collapses into a hot spot and then oscillates fast with a small amplitude. Since the sideways cooling area is small, the variations in the light curve are very small. However, when we restore taller column heights by increasing the accretion rates in these high magnetic field cases (Highacc4 and Highacc6), oscillations with lower frequencies occur.
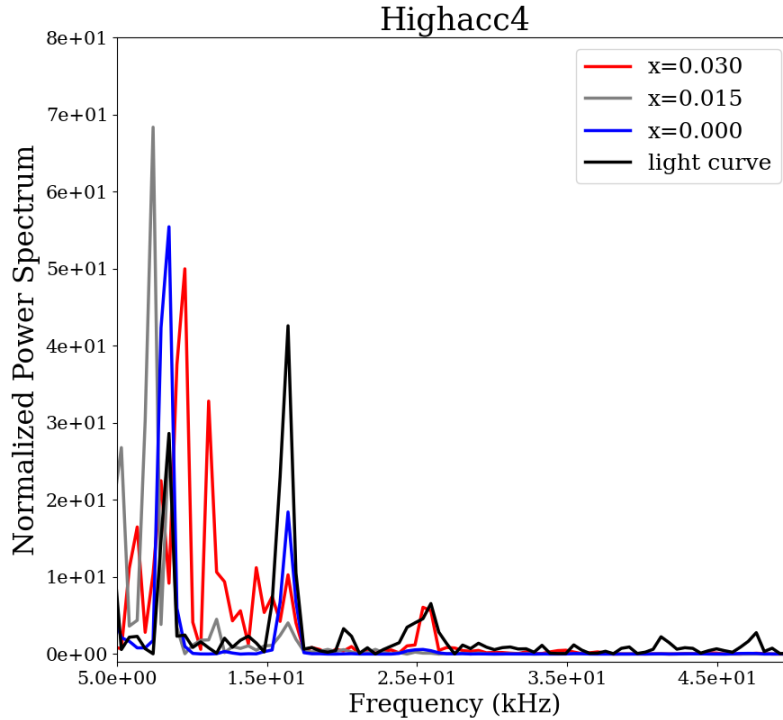
Figure 4.11: Power spectrum of shock height as a function of horizontal position for simulation Highacc4.

However, the oscillation amplitude in the high accretion rate simulations is substantially less than that in the low accretion rate simulations of comparable height, particularly Lowacc01. This is true both in luminosity, and in the overall shock height variation. In fact, the main body of the sinking zone away from the oscillating shock has an almost static structure apart from the presence of horizontally-propagating entropy waves. The high accretion rate simulations have higher horizontal optical depth (by one to two orders of magnitude throughout most of the column in the case of Highacc6) than in Lowacc01, both because the density is higher and because the opacity is larger. Hence the cooling time is longer and the column is better able to establish a balance between heating from accretion power and radiative cooling. It is only in the upper part of the column where thermal equilibrium is unable to be established because of the more rapid

diffusive cooling, and this is the region that oscillates. While the increased opacity in the lower, high temperature regions enables these regions to achieve thermal balance, but it turns out that this temperature dependence also leads to a new unstable behavior at late times, and we discuss this further below in section 4.2.6.

4.2.5   Angular Distribution of Emergent Radiation

When the neutron star accretion forms a hot spot at a relatively low accretion rate or in a strong surface magnetic field, the accreting material is halted at the stellar surface and releases mechanical energy into radiation. Since the incoming flow is cold and has low opacity, it is transparent and radiation can directly leave the system upwards (i.e. pencil beam). However, when the accretion rate is sufficiently high, the accretion flow is shocked above the stellar surface and forms a radiation pressure supported, optically thick region below which radiation emerges from the sides (i.e. fan beam).

The fact that classical models of accretion columns produce fan beam radiation patterns is simply due to the fact that most of the emission area is on the sides, even though the accretion shock itself is at the top of the column. In our 2D, more mound-shaped columns, the sides still have more emitting area, and the shock itself covers this mound-shape, so that significant direct dissipation of the accretion power is also happening along the sides of the column.

The angular distribution of the emitted radiation is therefore of course determined by both the geometry and surface brightness distribution of the photosphere of the column. In Figure 4.12, we compare the instananeous fraction of emergent radiation that is in a fan-beam across all the simulations, computed from the integral of horizontal flux leaving the photosphere divided by total luminosity. We also list the time-averaged fan beam ratio in Table 4.2, computed in two different ways: the ratio of time-averaged horizontal

luminosity to time-averaged total luminosity, and the time-average of the ratio. Despite the strong variability exhibited in Figure 4.12, particularly in Lowacc01 and Lowacc1, these two methods of averaging produce very consistent results.
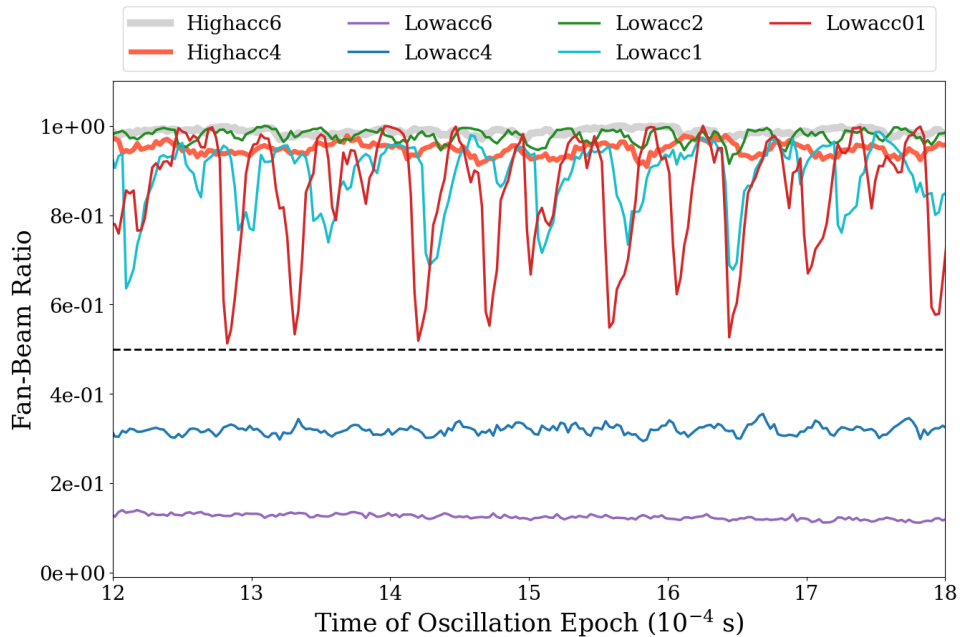
Figure 4.12: Ratio of the side luminosity to the total luminosity as a function of time in all seven simulations. The time here corresponds to epochs 12-18$\times 10^{-4}$ s in Figure 4.9.

For simulations Lowacc4 and Lowacc6 with short, flat columns (almost hot-spots), the fan-beam fraction is significantly below 0.5 (e.g. Lowacc4 and Lowacc6) and the emergent radiation is therefore more like the classical pencil-beam of 1D models. In all the other simulations, the system develops a columnar structure, where most radiation escapes sideways in a fan-beam pattern (i.e. fan-beam fraction above 0.5). However, the low-accretion columns in relatively low magnetic fields (Lowacc01 and Lowacc1) exhibit large variations of radiation beaming patterns, which result from the large shock oscillation amplitude. In particular, when the accretion column is mostly compressed (e.g. middle panel in Figure 4.2), the sideways cooling is minimized and the system is over-heated with quite a large fraction of radiation leaving from the top. For similar heights of columnar

structure, the variation of the fan-beam fraction in the case of high accretion rates and strong magnetic fields (Highacc4 and Highacc6) is in general smaller because the shock front oscillates with much smaller amplitude.

4.2.6   Opacity-Driven Instability in the High Accretion Rate Simulations

Figure 4.13 shows the temporal behavior of the shock height at the middle of the column for simulation Highacc4, extending well beyond the time range shown in Figure 4.9. Both the shock oscillation amplitude and the average height of the shock increase dramatically beyond $t = 40 \times 10^{-4}$ s. Simulation Highacc6 also shows evidence of this behavior, though we were unable to track it for as long as Highacc4. We never observed such behavior in any of our pure Thomson scattering simulations in chapter 3 and chapter 5. This suggests the presence of an additional unstable mechanism in the column dynamics that is directly related to the temperature-dependence of the magnetic scattering opacity.
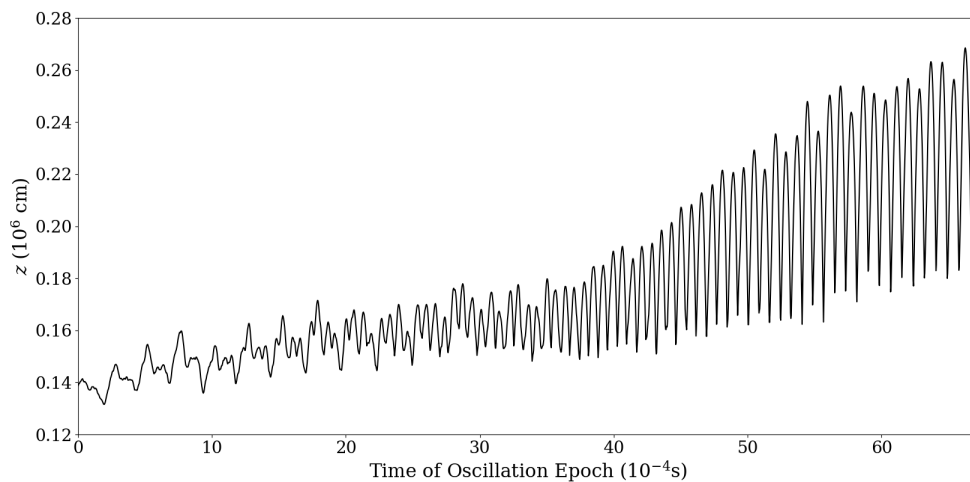
Figure 4.13: Height of the accretion shock at the $x = 0$ middle of the column as a function of time for simulation Highacc4. The time axis is the same as in Figure 3.4, but extended for much longer.

Under conditions of pure Thomson scattering and a vertical magnetic field, the maximum growth rate of the photon bubble instability occurs for near horizontal propagation directions in the slow diffusion regime (for details see Appendix A) and propagation directions at 45 degrees in the rapid diffusion regime (Gammie 1998). As we show in section A.4, a magnetic opacity that increases with temperature modifies the photon bubble dispersion relation such that unstable growth can occur for vertical propagation in the slow diffusion regime. The physics of this unstable growth differs from the pure photon bubble instability, and while it is slower than the photon bubble instability, we suggest that it is the cause of the growth that takes place at late times in Figure 4.13.

Because of the broad temperature width of the magnetic opacity peak in both High-acc4 and Highacc6, the postshock material does not reach the opacity peak and the opacity therefore increases further with temperature and depth in the column (see Figure 4.7 and Figure 4.8). The time-averaged opacity structure in simulation Lowacc1 shown in Figure 4.5 also appears to show a region of opacity increasing with temperature, but this is an artifact of the time-averaging. The instantaneous opacity structure shown in Figure 4.3 shows no such behavior. Hence only Highacc4 and Highacc6 have extended regions in which the opacity is below the peak and therefore increases with temperature, and it is only these simulations that exhibit this unstable behavior.

We have solved the full dispersion relation (A.7) for conditions along the $x = 0$ midline for a snapshot of Highacc4 at $t = 25.46 \times 10^{-4}$ s, shortly before the unstable behavior in Figure 4.13 becomes evident. The results are shown in Figure 4.14 as a function of height in the column, for two different wavelengths and for vertical wave vectors (angle between wave vector and magnetic field $\theta = 0$). We also solved the approximate dispersion relation (A.24) for this instability, which is wavelength-independent, and the result is very similar. The unstable region in the center of the column covers exactly the range of heights where the opacity increases with depth and temperature. Growth rates near
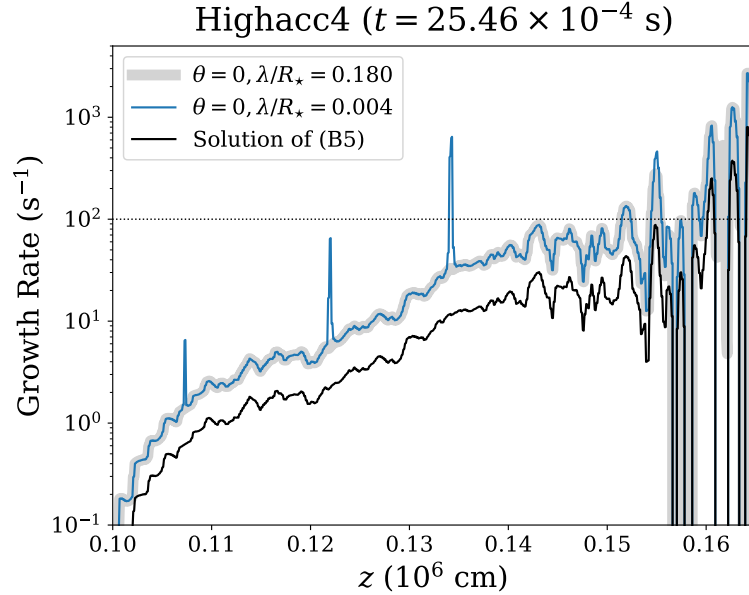
Figure 4.14: Predicted growth rate of the instability driven by the temperature-dependent magnetic opacity from linear instability theory in a static medium (section A.4). The solution is consistent with the rough growth time scale of the oscillation amplitude that is evident in Figure 4.13, indicated by the horizontal dotted line.

the top of the column are ~ 100 s^{-1}, and this is consistent with the growth time scale $\sim 10^{-2}$ s in Figure 4.13.

All of this is based on short wavelength WKB theory and so is difficult to apply to our actual column structure. Moreover, the central shock of the accretion column is already highly dynamic due to the basic thermal oscillation driven by the mismatch between heating and cooling, so linear perturbation theory on a static structure cannot be applied. Nevertheless, the predicted growth rates are comparable to what we see in these simulations, and it is suggestive that only Highacc4 and Highacc6 exhibit this behavior, and only Highacc4 and Highacc6 have vertically extended regions at lower temperatures than where the peak opacity occurs. It is important to note that our opacities depend only on temperature, and not density. More accurate opacities (Suleimanov et al. 2022) will have some density dependence, and these can also excite instability, even in the rapid diffusion regime (section A.4).

4.3   Discussion

4.3.1   Numerical Caveats

We remind the reader that we treat the neutron star as a classical gas pressure dominated region and only allow heat transport by advection and radiation transport (for details see chapter 3). This effective boundary condition is designed to minimize the boundary effects on the overall column dynamics. However, the fact that advection of heat into the neutron star is a contributing factor to the overall height of the shorter column simulations Lowacc4 and Lowacc6 suggests that this boundary condition might affect the overall scaling between accretion rate and column height. Our treatment of the neutron star surface neglects degeneracy pressure, which affects the heat capacity, and also neglects thermal conduction by electrons. It would be worthwhile in future to incorporate a more accurate treatment of the interface between the accretion column and the neutron star when the columns are approaching the hot spot regime, in order to more accurately determine how the column height varies with accretion rate. However, we suspect that the overall dynamics of the column will not be affected significantly.

At very late times, both Highacc4 and Highacc6 exhibit sudden flares of radiation from one side of the base of the column, and this rapidly causes the simulation to crash. This is an unphysical behavior that arises from the effective lower boundary condition, where the neutron star surface has heated sufficiently that radiation pressure starts to bend the magnetic field. As we mentioned in section 4.1.3, the field we use in the MHD is lower than the field used to determine the opacities in order to avoid errors in the conservative to primitive variable inversion. Further work is needed to implement a variable inversion that would allow us to run at higher magnetic fields, in addition to improving the physics of the bottom boundary condition. This would better enable us to determine the long-term outcome of the opacity driven instability that manifested in

these simulations at late times.

4.3.2   Opacity Due to Pair Production

We have shown in section 4.2.6 that instabilities can be present in accretion columns where the magnetic opacity is below the peak and therefore increases with temperature. After we completed our simulations, new opacity calculations by Suleimanov et al. (2022) were published. These demonstrate that there is an even sharper increase of opacity with temperature when the medium is hot enough that pair production becomes significant (Figure 4.15). If this regime can exist within the column, we suspect that it will be a
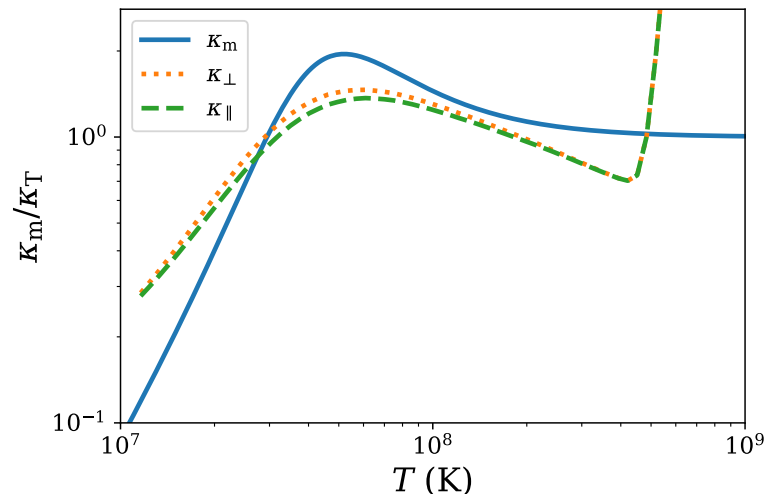
Figure 4.15: Comparison between our magnetic opacity (solid line) and the perpendicular (dotted line) and parallel (dashed line) opacities of Suleimanov et al. (2022), assuming $B = 1 \times 10^{12}$ G and $\rho = 1$ g cm^{-3}. The very sharp increase in opacity at temperatures above 4×10^8 K is due to the onset of electron-positron pair production.

site of strong instability. However, it may be that this opacity feature acts as a wall that cannot be reached in a real accretion column, because it may limit the temperature at the base of the column. Once the accretion rate becomes high enough and the bottom of the accretion column starts to enter into the pair production regime, the strong opacity boost may provide additional radiation support and cause the column to expand. This

expansion can then cool the accretion column and bring the base temperature below the pair production value via the extra sideways emission. However, similar to what we have found in the column oscillation, this expansion might then overcool the bottom of the column, contracting the column structure and heating the base back towards pair production. This again suggests a strong destabilizing mechanism at high accretion rates and strong magnetic fields, in which a steady-state column simply cannot exist. It would be interesting to simulate this in future, and we are currently working on an algorithm for angle and polarization-dependent opacities for use in ATHENA++. It would also be worthwhile to search for observational evidence of enhanced variability in this regime.

4.3.3   Observational Significance

One dimensional model fits to the observed pulse profiles of X-ray pulsars often require a mixture of fan and pencil-beam emission geometries, particularly at intermediate luminosities (e.g. Klochkov et al. 2008; Becker et al. 2012). As shown in Figure 4.12, our high accretion rate simulations Highacc4 and Highacc6 both show almost pure (> 90 percent) fan-beam emission. However, in our lower accretion rate simulations, only Lowacc2 exhibits an almost pure fan beam emission pattern. Lower magnetic field strengths instead produce a strongly oscillating column with an emission pattern that can vary between approximately half fan and pencil-beam and full fan-beam. The time-average of these oscillations still result in > 80 percent fan-beam, but this may be a contributing factor to the need for some pencil-beam emission for intermediate luminosities. At the highest magnetic field strengths (Lowacc4 and Lowacc6), the beam patterns are fairly steady in time, with roughly 40 percent fan-beam in the case of Lowacc4, due largely to the fact that the vertical and horizontal projections of the photosphere are comparable in size. Lowacc6 is almost a hot spot, and emits only only 14 percent of its luminosity in a

fan-beam. It would therefore be interesting to explore observationally how the emission geometry depends not only on luminosity but also on magnetic field strength inferred from cyclotron lines. That geometry can be strongly dependent on observed photon energy (Iwakiri et al. 2019), so post-processing of simulations such as ours would also be a useful way of confronting the observational constraints.

Accretion columns are observed to exhibit an inverse correlation between the luminosity and the magnetic field strength as measured by the energy of cyclotron lines (Tsygankov et al. 2010; Doroshenko et al. 2017; Staubert et al. 2019; Mushtukov & Tsygankov 2022). One possible explanation for this is that higher luminosities correspond to taller columns which then sample weaker magnetic fields in a diverging field geometry (but see Poutanen et al. 2013 for an alternative explanation). In simulations Lowacc4 and Highacc4, we increase the accretion rate of the column in the same magnetic field, and the column is taller. Although we use a uniform, vertical magnetic field in the simulations, we can crudely estimate the corresponding decrease in field strength in a more realistic dipole geometry. The luminosity increases by a factor of ~ 23.59, while the magnetic field strength at half the height of the column would decrease by a factor of ~ 0.82. Similarly, when comparing simulations Lowacc6 and Highacc6, the luminosity increases by a factor of ~ 35.07 and the magnetic field would decrease by a factor of ~ 0.81. These numbers are actually very close to the observed behavior of V 0332+53 (Tsygankov et al. 2010; Doroshenko et al. 2017), where the luminosity increases by a factor of ~ 20 and the observed magnetic field strength decreases by a factor of ~ 0.8. However, this source is inferred to have a surface field strength that is slightly weaker (2.6×10^{12} G) than these two pairs of simulations. Moreover, as we have a uniform magnetic field in our simulations, the magnetic opacities may differ at higher altitudes. However, this difference is unlikely to significantly impact our results since the post-shock gas temperature should be sufficiently high so that the opacity is near the Thomson regime. In addition, as our

accretion columns are relatively short (~ 0.1 neutron star radius), this crude estimation might still be reasonable. Nevertheless, future simulations must incorporate the variation of magnetic field with height for a more accurate evaluation of this inverse correlation.

The QPOs that arise from the vertically shock oscillations are at frequencies in excess of $\simeq 5$ kHz for the simulations we have presented in this chapter, and this may prove challenging to observe directly with existing X-ray facilities. However, the opacity-driven instability at high magnetic field strengths grows on much longer time scales $\simeq 0.01$ s. It is unclear how this will saturate and manifest in the lightcurve, as we were unable to run our simulations for long enough before the effective bottom boundary condition failed. Even so, it suggests the possibility of longer time-scale variability that may be more easily observable for high magnetic field X-ray pulsars, whose fields are observed to extend up to as high as 6.6×10^{12} G (Yamamoto et al. 2014; Staubert et al. 2019). Further investigation of this instability with future simulations is therefore warranted.

4.4 Conclusions

1. We have extended our Cartesian simulations in chapter 3 to incorporate polarization-averaged, temperature-dependent magnetic scattering opacities. These can dramatically affect both the dynamics and the time-averaged structure of the accretion column. For weak magnetic fields ($\simeq 10^{11}$ G, simulation Lowacc01), the opacities inside the sinking zone are close to Thomson, and the column dynamics is very similar to what we found in chapter 3, the main difference being that coherent pre-shocks in the free-fall zone are largely absent because the opacity in that cold infalling material is much less than Thomson. For higher magnetic field strengths, magnetic opacities produce much more significant differences, a result that is perhaps not surprising given that neutron star columns are supported against gravity

by radiation pressure.

2. Increasing the magnetic field strength increases the temperature at which the opacity peaks, and also increases the width of that peak in temperature space, both effects scaling directly with the magnetic field strength. At fixed accretion rate, increasing the magnetic field strength generally increases the post-shock opacity as an approximately fixed temperature jump across the shock is less and less able to climb over the opacity peak. Despite the fact that the opacity in the interior of the column is on average larger, the time-averaged column height is reduced. This is partly because a larger fraction of the immediate post-shock accretion power is radiated away rather than advecting into the higher opacity post-shock regions, and partly because more accretion power flows into the neutron star at the base of the column.

3. Again at fixed accretion rate, the taller columns at weaker magnetic field strengths $10^{11}-10^{12}$ G exhibit strong vertical oscillations. While entropy waves (slow diffusion photon bubbles) are clearly present as horizontally-inward propagating waves, these oscillations are actually a result of global thermal imbalance, with over-cooling at maximum vertical extension and over-heating at minimum vertical extension. This is the same mechanism that produced oscillations in our previous Thomson scattering simulations, both in Cartesian geometry (see chapter 3) and split monopole geometry (see chapter 5). The amplitude of these oscillations is large enough to cause the angular distribution of emitted radiation to oscillate from $50-80$ percent fan beam at minimum vertical extent to 100 percent fan beam. This might be a contributing factor to the need for 1D models to sometimes require a mixture of pencil beam and fan beam to explain observed light curves (e.g. Klochkov et al. 2008; Becker et al. 2012; Iwakiri et al. 2019). The amplitude of these oscillations is

reduced and the frequency is increased as the field strength increases at fixed accretion rate. The angular distribution of emitted radiation is almost entirely fan beam until the field strength gets high enough that the column height is short enough to transition into almost a pure (~ 85 percent) pencil beam emitting hot spot (this happens at 6×10^{12} G at the low accretion rates considered here). Increasing the accretion rate at these higher magnetic field strengths restores the height of the column and the nearly 100 percent fan beam emission, but the oscillation amplitude remains quite low. The mere fact that higher accretion rate results in taller columns may contribute to explaining the observed inverse correlation of cyclotron line energy with accretion rate during supercritical phases of accretion (Tsygankov et al. 2006; Jaisawal & Naik 2016; Staubert et al. 2019). But our simulations would also predict that the critical accretion rate separating hot spots (pencil beam emission, positive correlation between cyclotron energy and accretion rate) and columns (fan beam emission, negative correlation between cyclotron energy and accretion rate) should itself be a function of magnetic field strength across difference sources.

4. We have identified a new instability in the column that exists when the field strength is high enough that the opacity within the column increases inward with increasing temperature. In the two high accretion rate simulations here, this instability grows on a time scale of ~ 0.01 s. While we were not able to fully investigate the nonlinear outcome of this instability due to numerical issues, it may contribute to enhanced variability on this time scale for high magnetic field neutron stars.

Chapter 5

Simulations of Accretion Columns in Split-Monopole Magnetic Fields

This chapter is adapted from our research work published as Zhang, Blaes & Jiang (2023). In this chapter, we conduct more global simulations of accretion columns in split-monopole fields at higher accretion rates.[1] The chapter is organized as follows. In section 5.1, we summarize the numerical technique and simulation setup. In section 5.2, we describe our simulation results, including the build-up of the column, its oscillatory behavior, the emergent light curves, comparison with the 1D stationary model, the energetics of the column, and the characterization and behavior of entropy waves. In section 5.3, we discuss several numerical caveats that might influence the simulation outcomes, how entropy waves affect the dynamics, compare our work to previous work in the literature, and discuss the observational significance of our simulations. In section 5.4, we summarize our conclusions.

---

[1]We choose a split-monopole field rather than a more strongly converging dipole or quadrupole field because it enables us to adopt field lines that are nearly along the spherical polar grid. This helps avoid numerical issues associated with inversion of conservative to primitive variables in strong magnetic fields. A split-monopole field still captures the essential geometric effect of an inward converging field, more and more strongly confining the accretion flow in the lateral direction.

5.1 Numerical Method

5.1.1 Equations

Neutron star accretion columns are transversally confined against radiation pressure forces by strong magnetic fields. These fields lead to Newtonian Alfvén speeds that exceed the speed of light in the low density, free-fall region. A Newtonian MHD simulation would therefore be forced to use very small time steps to achieve numerical accuracy and stability. We avoid this problem by using the radiative relativistic MHD techniques that we developed in our previous work (Zhang et al. 2021), but now adapted to spherical polar coordinates (Stone et al. 2020; Jiang 2021). The conservation laws are summarized below in the sequence of mass, momentum, and energy conservation in the gas, and radiative transfer:

$$\partial_0(\rho u^0) + \nabla_j(\rho u^j) = S_{\text{gr1}} \quad , \tag{5.1a}$$

$$\partial_0(wu^0u^i - b^0b^i) + \nabla_j\left(wu^iu^j + (P_g + P_m)\,\delta^{ij} - b^ib^j\right) = S^i_{\text{gr2}} - S^i_{r2} \quad , \tag{5.1b}$$

$$\partial_0\left[wu^0u^0 - (P_g + P_m) - b^0b^0\right] + \nabla_j(wu^0u^j - b^0b^j) = S_{\text{gr3}} - S_{r3} \quad , \tag{5.1c}$$

$$\partial_0 I + n^j\nabla_j I = \mathcal{L}^{-1}(\bar{S}_r) \quad . \tag{5.1d}$$

Here ρ is the gas density in the fluid rest frame and δ^{ij} is the Kronecker delta. Using velocity in units of the speed of light ($c = 1$), the gas four-velocity is defined as $(u^0, u^i) = \Gamma(1, v^i)$, where v^i is the gas three-velocity and $\Gamma = (1 - v_jv^j)^{-1/2}$ is the Lorentz factor. Given the three-vector of magnetic field B^i and fluid-frame gas pressure P_g, we can then define the four-vector of magnetic field b^μ, magnetic pressure P_m, gas enthalpy w_g, and

the total enthalpy w as follows:

$$b^0 = u_j B^j, \quad b^i = \frac{1}{\Gamma}(B^i + b^0 u^i) \quad , \tag{5.2a}$$

$$P_m = \frac{1}{2} b_\nu b^\nu \quad , \tag{5.2b}$$

$$w_g = \rho + \frac{\gamma}{\gamma - 1} P_g \quad , \tag{5.2c}$$

$$w = w_g + b_\nu b^\nu \quad , \tag{5.2d}$$

where the adiabatic index of idea gas $\gamma = 5/3$ is adopted in our computation. Note that we use Latin and Greek indices to denote the three-vector (e.g. $i = 1, 2, 3$) and the four-vector (e.g. $\mu = 0, 1, 2, 3$) components, respectively. The radiation intensity field I is defined in the lab frame, as well as the unit vector of the photon propagation direction n^i. Since ∇_i is expressed in spherical polar coordinates (r, θ, ϕ), extra geometric terms are introduced by the advection terms in both the relativistic MHD equations and radiative transfer equations, which can be found in Stone et al. (2020) and Davis & Gammie (2020), respectively. The quantities S_{gr1}, S^i_{gr2}, S_{gr3} are gravitational source terms derived by reducing the full general relativistic conservation laws to the weak field limit (for details see Appendix B). Similarly, S^i_{r2} and S_{r3} are radiation source terms for momentum and energy, respectively, computed from the lab-frame moments of the radiation intensity (Jiang 2021). Finally, $\bar{S}_r$ consists of the fluid-frame emissivity, absorption and scattering source terms (3.4c), with $\mathcal{L}^{-1}$ being the Lorentz boost operator from the comoving to lab frame. Here, we denote the radiation quantities in the comoving frame with overbars.

For simplicity, our study of the column dynamics in the split-monopole field configuration assumes that electron scattering is Thomson, i.e. isotropic with no dependence on magnetic field and polarization. Our computation of radiative transfer is frequency-integrated, assuming a blackbody spectrum and neglecting non-zero photon chemical

125

potential effects. In our future work, we will further investigate the dynamical effects caused by magnetic opacity in more global column structure. This chapter aims instead to obtain insight on the dynamical effects introduced by geometric dilution (e.g. r^2 for the spherical polar geometry used here) and high accretion rates.

5.1.2   Simulation Setup

As shown in chapter 2, the slow-diffusion photon bubble instability is highly resolution-dependent. We therefore first studied accretion column dynamics using a Cartesian grid where numerical resolution was spatially constant (see chapter 3). However, we found there that the global characteristics of the accretion column (e.g. shock height and oscillation frequency) are almost independent of resolution and therefore photon bubbles do not alter the more global dynamics of the column. This at least partially alleviates any concern related to numerical convergence of the column dynamics introduced by changes in spatial resolution in curvilinear coordinate grids. For this reason, we adopt an axisymmetric, 2D spherical polar geometry in this chapter, with a radial (split-monopole) magnetic field in the initial condition. This enables us to explore accretion column dynamics at higher accretion rates, but we still limit the column height to be comparable to or less than the stellar radius in order to be qualitatively valid compared with a more realistic dipolar geometry. The accretion column in the simulations in this chapter are axisymmetric mounds at the magnetic pole. Unlike the 2D Cartesian column simulations in chapter 3, where the simulated column was a slice through a long, thin wall of accreting material, here with this axisymmetric 2D structure of the accretion column we compute the entire escaping radiation field.

Global Parameters and Simulation Domain

The grid cells are uniformly sampled in the $\hat{\theta}$-direction with a constant polar angle interval $\Delta\theta$. We maintain the same aspect ratio for all cells, so the radial width Δr increases by a fixed factor $(1 + \Delta\theta)$ between radially adjacent cells. Although the gas properties are defined in the 2D r-θ plane in axisymmetry, the radiation intensity field is configured in 3D angular grids with 64 angle directions.

We adopt a neutron star mass $M_\star = 1.4 M_\odot$ and radius $R_\star = 10^6$ cm for our calculations. The global geometry of the column is specified by the polar angle column width θ_c and maximum radius r_c, which needs to be set sufficiently large to cover both the free-fall and sinking zones. The accretion rate of the column can be parameterized by the local Eddington ratio ϵ, which is the ratio of area-weighted effective Eddington luminosity (L_{eff}) and accretion luminosity on the surface of neutron star (L_{acc}):

$$L_{\text{eff}} = \frac{A}{4\pi R_\star^2} L_{\text{Edd}} \quad , \tag{5.3a}$$

$$L_{\text{acc}} = \frac{G M_\star \rho_{\text{acc}} A v_{\text{ff}}}{R_\star} \quad , \tag{5.3b}$$

$$\epsilon = L_{\text{acc}} / L_{\text{eff}} \quad . \tag{5.3c}$$

Here $A = 4\pi R_\star^2 \sin^2(\theta_c/2)$ is the transverse area of the column on the neutron star surface and $L_{\text{Edd}} = 4\pi G M_\star c/\kappa_s$ refers to the Eddington luminosity of the entire neutron star, where we adopt $\kappa_s = 0.34$ g cm^{-2} as the electron scattering opacity. Both the free-fall speed $v_{\text{ff}} = \sqrt{2 G M_\star / R_\star}$ and accreting inflow density ρ_{acc} are defined on the neutron star surface for convenience and they can be further re-scaled to set up the top boundary condition given different column heights by multiplying by factors of $(R_\star/r_c)^{1/2}$ and $(R_\star/r_c)^{3/2}$, respectively. Therefore, the value of ϵ determines the local accretion rate and density at the top of the column.
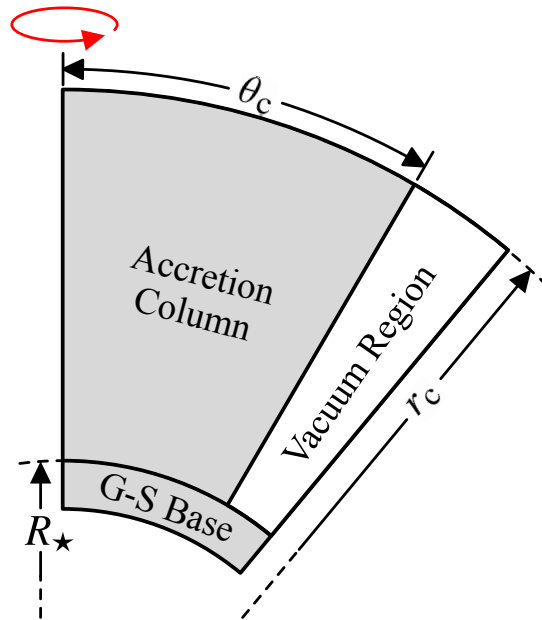
Figure 5.1: Geometry of the simulation domain, together with the effective boundary condition regions: the vacuum region on the outside of the column and the gas-pressure supported surface of the neutron star. The red loop is a reminder that the 2D simulation is axisymmetric.

Similar to our previous study of columns in Cartesian geometry (see chapter 3), the simulation domain is partitioned into 3 different regions for distinct numerical treatments. As illustrated in Figure 5.1, the central region (denoted by 'Accretion Column') is the main simulation region on which we focus our analyses in this chapter. The lower region (denoted by 'G-S Base') and side region (denoted by 'Vacuum Region') are the effective boundaries that mock up the gas pressure-supported base and vacuum region, respectively. Our treatment of these regions will be described in detail in next section.

Initial and Boundary Conditions

Our previous work in chapter 3 used an initial condition of a stationary accretion column in thermal and hydrostatic equilibrium with only vertical gradients. Here we instead build up the accretion column using an initial condition of pure cold free-fall inflow. The gas in the actively simulated region ('Accretion Column' in Figure 5.1)

is initialized using the free-fall gas profile assigned with gas density $(R_\star/r)^{3/2}\rho_{\text{acc}}$ and downward radial velocity $-(R_\star/r)^{1/2}v_{\text{ff}}$ given a fixed accretion rate. The gas is assumed to be cold ($T_{\text{floor}} = 5 \times 10^6$ K, following Klein & Arons 1989) in the beginning, so the initial gas pressure is $(R_\star/r)^{3/2}\rho_{\text{acc}}k_{\text{B}}T_{\text{floor}}/m$. The initial magnetic field is entirely radial (split-monopole) and therefore decreases with radius as r^{-2}. We adopt a surface magnetic field $B_\star = 10^{11}$ G, adequate to laterally confine the resulting column against radiation pressure. This is below the typical field strength of high-mass X-ray binary pulsars ($\gtrsim 10^{12}$ G). However, such strong magnetic fields will not affect the column dynamics, and they exacerbate the problem of variable inversion from conservative variables to primitive variables, in particular in resolving the small gas internal energy (see detailed discussion in section 3.3.1). The radiation field of the initial inflow is assumed to be isotropic and in local thermal equilibrium (LTE) with the cold gas in the fluid rest frame.

We adopt a similar strategy of setting boundary conditions as in section 3.1.4: effective boundaries (hereafter, soft boundaries) are designed to mock up the neutron star surface ('G-S Base' in Figure 5.1) at the bottom and the side vacuum region outside the accretion column ('Vacuum Region' in Figure 5.1). The actual boundaries of the simulation domain (hereafter, hard boundaries) are applied directly at the top and polar axis boundaries of the active accretion column ('Accretion Column' in Figure 5.1) and at the exterior edges of the soft boundary regions. Detailed justification for the soft boundary arrangements can be found in section 3.1.4, but we briefly review them here.

The gas-supported base is the layer below the active region of the accretion column and is initialized in hydrostatic equilibrium with an isothermal non-degenerate cold gas ($T_{\text{b}} = 5 \times 10^6$ K). We adopt a neutron star surface density $\rho_\star = 10^6$ g cm^{-3} to calculate the gas density profile at the base $\rho_{\text{b}} = \rho_\star \exp\left(-r/h_{\text{b}}\right)$, where $h_{\text{b}} = R_\star T_{\text{b}}/g_{\text{b}}$ is the scale height. We set the effective gravitational acceleration g_{b} to be smaller than the surface

gravitational acceleration $g_\star = GM_\star/R_\star^2$ by at least a factor of 500 in our simulations so that a scale height can be resolved by at least 5 grid cells to numerically maintain the hydrostatic equilibrium. The initial magnetic and radiation intensity fields are set to be the same as the active accretion column region. The height of the gas-supported base is set to 6 scale heights for each simulation.

The advantage of using this effective boundary is that the magnetic confinement at the bottom of the accretion column can be automatically achieved without directly implementing any cumbersome boundary condition that invokes artificial magnetic tension and pressure forces. However, as the accretion column evolves, the gas-supported base will be continuously heated, causing radiation diffusion, and radiation pressure forces, towards the side. Although the tendency to laterally bend magnetic field is small because of the huge gas inertia, this tendency is finite and can keep accumulating. As long as the simulation runs sufficiently long, this will eventually tilt the magnetic field away from the radial direction which will then fail to confine the accretion column above. To alleviate this numerical issue, we adopt an exponential damping of the lateral velocity in the base on a sound crossing time across a grid cell (t_s) using $d \ln v_\theta = -dt/t_s$, where v_θ refers to the instantaneous lateral speed.

The vacuum effective boundary at the side is an optically thin region where the density and gas pressure are both set to the floor values at all times but the velocity and magnetic fields are allowed to evolve. This soft side boundary is necessary to simultaneously achieve both the transverse magnetic confinement and the free escape of photons at the side. The width of the vacuum region is set to be 10% of the domain size. The initial velocity in this region is set to be 0. The magnetic and radiation intensity fields are initially set the same as in the active accretion column region. More details about this effective boundary condition can be found in section 3.1.4.

The hard boundary conditions of the simulation domain are similar to the Cartesian

columns (see chapter 3) except the central boundary, where the polar wedge boundary condition (Stone et al. 2020) is adopted for both gas and radiation. This enforces the axisymmetric constraint of no velocity, magnetic field, or radiation flow through the pole. Note that the computation in spherical polar coordinates can have numerical problems from the geometric terms when the polar region is highly resolved. For example, the problem can arise from the subtraction of similar numbers in the geometric terms if the interval between adjacent polar angles is too small. This can lead to inaccurate outcomes when computing the surface flux from the variable reconstruction at the cell face near the polar region. Therefore, we lower the order of the reconstruction near the polar region to avoid this numerical effect.

The bottom hard boundary condition of the simulation domain is reflective for both gas and radiation, and enforces the same magnetic field as the initial condition. The outer side boundary conditions of the gas and magnetic field are set to be reflective as well but the radiation uses a vacuum boundary condition so that it can escape (see section 2.2.2). At the top, the cold gas (5×10^6 K) is set to free fall from the boundary within the active accretion column region with its density $(R_\star/r_c)^{3/2}\rho_{acc}$ at downward radial velocity $-(R_\star/r_c)^{1/2}v_{ff}$, while the radiation intensity field is set to be isotropic and in LTE with the gas in the comoving frame. Outside the accretion column region, the top boundary condition above the vacuum region is simply set to be outflow for the gas (see section 2.2.2) and vacuum for the radiation. The magnetic field at the top of the domain is fixed as in the initial condition.

Simulation Parameters

We simulated four accretion columns in a split-monopole magnetic field with various widths and accretion rates, plus an extra two for a resolution study. Parameters for these simulations are listed in Table 5.1. We take Version 0 as our fiducial simulation

Version	Name	Mesh	r_c ($R_\star$)	θ_c	$R_\star \Delta\theta$ (cm)	ϵ	ρ_{acc} (10^{-4} g cm^{-3})	Accretion Rate (10^{16} g s^{-1})	Total Time (t_{sim})
0 (Fiducial)	Narrow-500	7040×256	2.5	0.03	130	500	23.00	12.54	2651
1	Narrow-50	4544×256	1.8	0.03	130	50	2.30	1.25	2651
2	Wide-50	5504×512	6.0	0.15	326	50	2.30	31.28	3535
3	Wide-20	4224×512	4.0	0.15	326	20	0.92	12.51	1768
4	Narrow-500-MR	3520×128	2.5	0.03	260	500	23.00	12.54	884
5	Narrow-500-LR	1728×64	2.5	0.03	521	500	23.00	12.54	884

Table 5.1: Global parameters used to set up our six accretion column simulations. The first four simulations aim to explore the dynamical dependence on the global parameters (i.e. accretion rates and column widths), and the last two simulations are a resolution study of the fiducial simulation. Note that what we are calling wide column simulations still have a small opening angle (0.15 radians, much less than unity).

and set up Version 1 by decreasing the accretion rate by a factor of 10. We also set up two accretion column simulations $3\times$ wider than the fiducial column, where the first one (Version 2) has the same ϵ and the second one (Version 3) decreases the accretion rate by a factor of 2.5. We lower the resolution by a factor of 2.5 for the two wide column simulations due to the high computational cost. Besides these four simulations exploring the parameter space of column width and accretion rate, we also conduct a resolution study by decreasing the resolution by factor of 2 and 4 with respect to the fiducial version. In this chapter, we perform our analysis of the simulation output data dumps with the time resolution $t_{sim} = 2.8 \times 10^{-6}$ s.

5.2   Results

We focus our discussion here on the results of our fiducial simulation, which shares many properties with the other simulations. We comment where necessary how the global parameters of column width and accretion rate affect the results of our other simulations. In section 5.2.1, we describe how the accretion column is built up by forming a sinking zone under the accretion shock. In section 5.2.2, we discuss the oscillatory behavior of the accretion column in detail. In section 5.2.3, we present the light curves of all

the simulations and discuss how the shock oscillation affects the emergent radiation by showing their variability power spectra. In section 5.2.4, we compare the time-averaged profiles with the 1D stationary model incorporating different shapes of the sinking zone. In section 5.2.5, we examine the energetics of the accretion column, and show how radial advection competes with pdV work in providing thermal pressure support of the accretion column. In section 5.2.6, we identify the entropy wave existing in the sinking zone and conduct a resolution study of the fiducial simulation. A set of movies of various quantities in our four high-resolution simulations is available online at this YouTube link[2].

5.2.1   Build-up of Column

All the simulations are initialized with only the cold gas free-falling onto the neutron star, where the gas can reach speeds at the stellar surface of up to $\sim 0.64c$ ($\Gamma = 1.31$). This gas is immediately halted by the rigid neutron star surface and forms a shock that releases much of its kinetic energy into radiation. A portion of the radiation directly escapes sideways, and the rest propagates upward and interacts with the incoming accretion flow. Note that radiation diffusion into the neutron star is negligible because the diffusion time scale below the stellar surface is much longer than the cooling time scale of the column itself. At the high accretion rates we adopt here, the radiation pressure support exceeds the ram pressure and the gravity of the downward gas flow and therefore pushes the shock away from the stellar surface as shown in the left four panels of Figure 5.2. The shock front keeps rising until an equilibrium is roughly achieved among radiation pressure support, ram pressure, and gravity. Hence, a radiation pressure dominated region below the shock front is naturally formed as Basko & Sunyaev (1976) predicted, which we call the 'sinking zone'. This region is thoroughly confined by the magnetic field, with the highest plasma beta (thermal pressure/magnetic pressure)

---

[2]`https://youtube.com/playlist?list=PLbQOoEYOCFpWubAItXtHIIRdGhlBuftch`

Build-up of Accretion Column in Fiducial Simulation
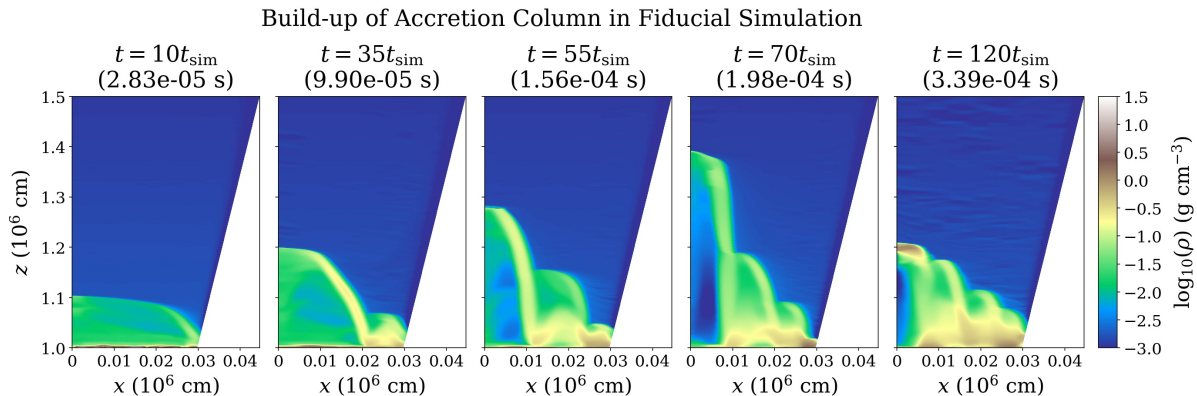
Figure 5.2: 2D density profiles during the column build-up epoch of the fiducial simulation. These five snapshots illustrate how the column is built up from the cold accretion flow. After the column structure is established at $\simeq 70t_{\mathrm{sim}}$, the accretion column soon enters into a long-lived, oscillatory phase.

occurring at the base of the sinking zone, and ranging from 0.03 to 0.08 for the different simulations.

While the shock is elevating and the sinking zone is being established, a wave is generated at the outer part of the column and then propagates towards the center as shown beginning at $t = 35t_{\mathrm{sim}}$ (the second panel in Figure 5.2). As we discuss below in section 5.2.6, this is the entropy wave associated with the slow-diffusion photon bubble instability (Arons 1992; Appendix A). This entropy wave is periodically excited as shown in the snapshot at $t = 55t_{\mathrm{sim}}$ (the third panel in Figure 5.2), and a lateral structure consisting of radial fingers forms that resembles what we observed in the Cartesian column simulations (see version 2 in section 3.2.1). The height of each 'finger' increases towards the center of the column and these 'fingers' build up a mound-shaped column structure. The generation of these entropy waves persists through all our simulations, propagating from the outermost parts of the column inward to the polar axis. Recall that the gas is magnetically constrained to move only radially along the field lines as the finger-shaped structures oscillate up and down. Therefore, the wave pattern that propagates inwards is entirely driven by the phase differences of the oscillations at different transverse locations.

As the waves reach the polar axis, they merge with the finger-shaped structure there that oscillates up and down (see $t = 70t_{\mathrm{sim}}$ and $t = 120t_{\mathrm{sim}}$ in Figure 5.2).

5.2.2   High-Frequency Oscillatory Behavior

After the accretion column finishes the build-up of the sinking zone, it starts to oscillate at high frequency ($\gtrsim$kHz) and this oscillation persists through the end of the simulation. The physical origin of this oscillation is similar to what we found in our previous Cartesian simulations: it is caused by the instantaneous imbalance between global heating and cooling due to inefficient radial energy transport. Indeed, if we estimate twice the cooling time using the same method as in section 3.2.3 (i.e. assuming that the contraction and expansion of the accretion column take approximately the same amount of time), we find a value of $\sim 0.5\ \mu$s, comparable to the period measured from the simulation ($\sim 0.2\ \mu$s). Note that we do not see any evidence of the formation of pre-shocks in our split monopole simulations, in contrast to the Cartesian simulations of chapter 3 where pre-shocks formed in the free-fall region and then fell onto the sinking zone.

Both the oscillation amplitude and frequency show considerable variation with transverse location in the column. This is evident from Figure 5.3, which shows the shock height (r_{sh}) at different transverse positions as a function of time. Note that the shock oscillations are quite coherent at any particular transverse location. The oscillation amplitude is highest, and the frequency is lowest, at the center (polar axis) of the column. In Figure 5.4, we present 2D density profiles over a time span equal to the oscillation period at the center of the column in the fiducial simulation. The physical reason for the transverse variation in oscillation frequency is that the closer one is to the polar axis, the longer it takes for radiation to diffuse outward in the transverse direction. This implies a longer time scale for the system to respond to heating or cooling closer to the polar axis.

Radial Oscillation of Shock Front
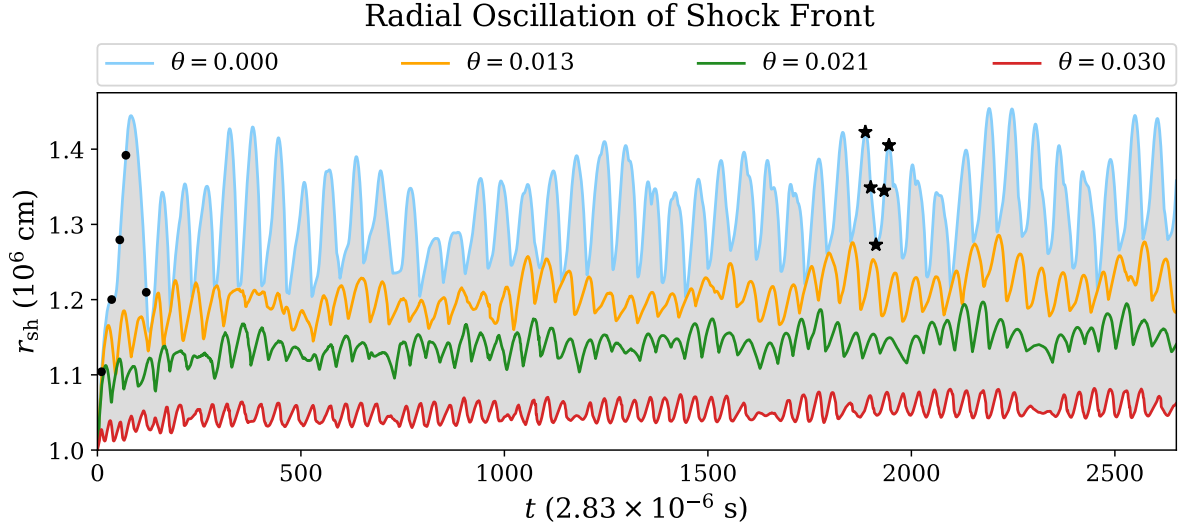
Figure 5.3: Oscillation of the shock fronts at different transverse positions in the fiducial simulation. The shock oscillation amplitude increases, and the frequency decreases, towards the polar axis of the column. The shaded region indicates the range of the shock oscillation amplitude from the polar axis to the outer edge of the accretion column. The five black dots refer to the snapshots in Figure 5.2 and the five black stars represent the snapshots in Figure 5.4.
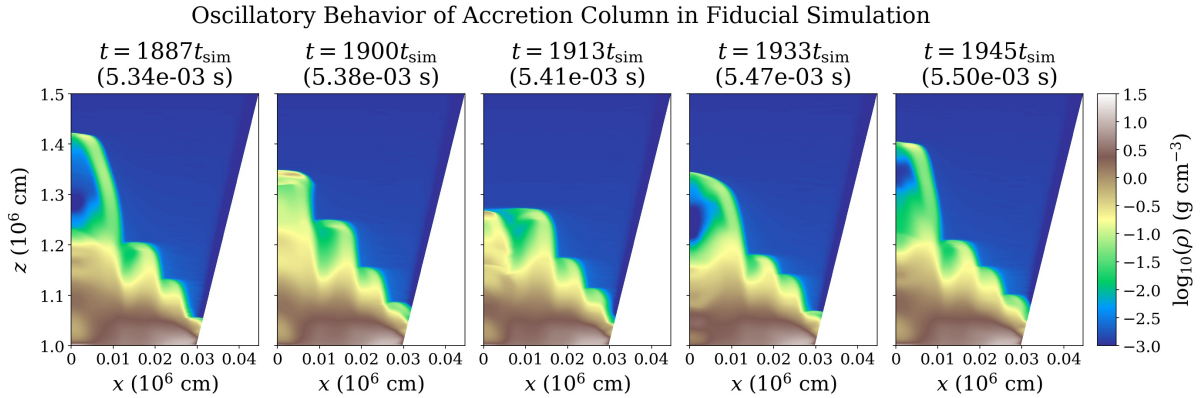
Figure 5.4: 2D density profiles over one polar axis oscillation period of the accretion column for the fiducial simulation.

In Figure 5.5 and Figure 5.6, we present 2D profiles of other quantities at the maximum ($t = 1887t_{\mathrm{sim}}$) and minimum ($t = 1913t_{\mathrm{sim}}$) heights of the oscillation at the polar axis. The finger-shaped pattern is prominent in the radial velocity (v_r, see the upper left panels in Figure 5.5 and Figure 5.6), with the gas in adjacent finger-shaped regions
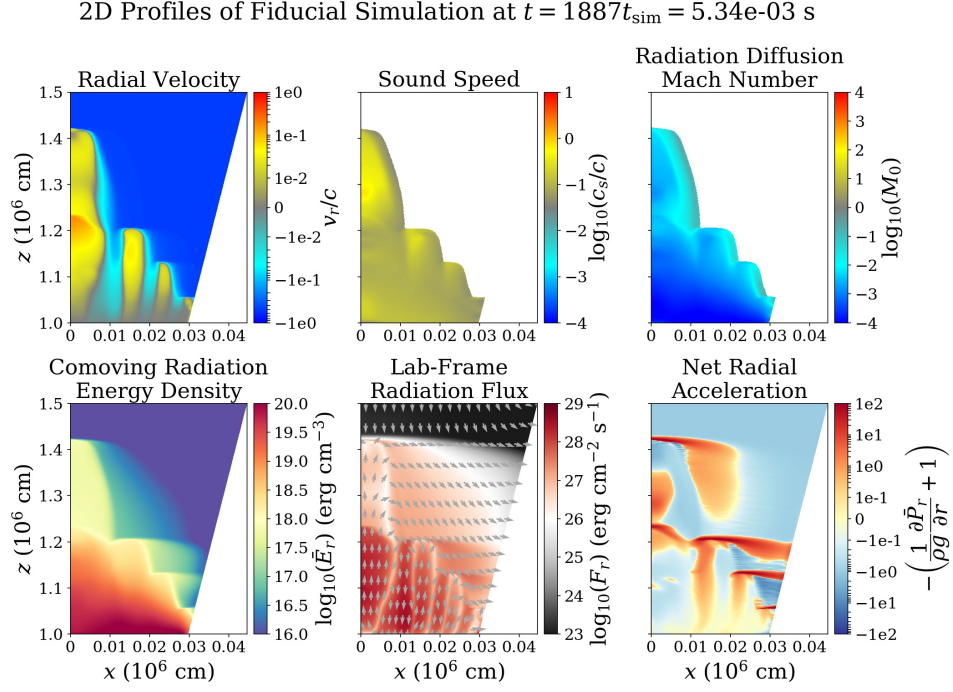
Figure 5.5: 2D profiles of six quantities in the fiducial simulation when the accretion column is mostly extended at $t = 1887t_\mathrm{sim}$ (see the first panel of Figure 5.4).
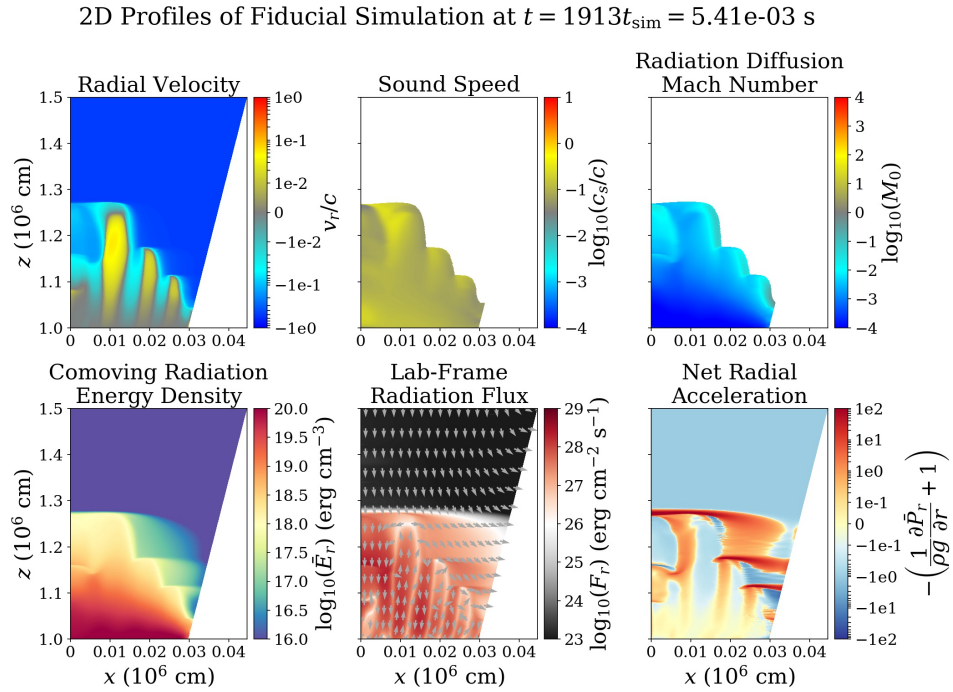
Figure 5.6: 2D profiles of six quantities in the fiducial simulation when the accretion column is mostly compressed at $t = 1913t_\mathrm{sim}$ (see the middle panel of Figure 5.4).

137

moving in opposite directions. As we discuss in detail in section 5.2.6, this propagating wave pattern toward the polar axis is a manifestation of the entropy modes that are associated with the slow-diffusion photon bubble instability.

The sound speed (c_s) is dominated by radiation pressure and is mildly relativistic ($\sim 0.1c$, see upper second panels in Figure 5.5 and Figure 5.6) in the sinking zone during the oscillation. This is in general faster than the magnitude of the gas velocity ($\sim 0.01c$), so that the oscillations are nearly hydrostatic, except during outward moving phases along the polar axis where the radial speed can slightly exceed the sound speed. This agrees with the fact that the net radial acceleration is only tens of percents of the local gravitational acceleration throughout most of the sinking zone (see the lower right panels in Figure 5.5 and Figure 5.6). The radiation diffusion Mach number (M_0) refers to the ratio of the radiation diffusion speed c/τ (where τ is the optical depth over a pressure scale height) to the sound speed (A.4). As shown in the upper third panels in Figure 5.5 and Figure 5.6, M_0 is small everywhere in the sinking zone, indicating that the radiation diffuses much more slowly ($\sim 10^{-4}c$) compared with the sound speed (as well as the gas velocity). Hence, the sinking zone is always in the slow-diffusion regime during the oscillation.

During the oscillation, the radial component of lab-frame radiation flux (F_r) is dominated by the advection and therefore its direction is the same as the gas radial velocity, while the transverse component indicates the sideways cooling process (see the lower middle panels in Figure 5.5 and Figure 5.6). When the finger-shaped structure is most elongated, cooling of the accretion column becomes most efficient due to the maximum sideways cooling area. Global cooling exceeds heating at this time, and the column therefore loses radiation pressure support against gravity and thus collapses. When the column is at its minimum height, the sideways cooling area of the sinking zone is the smallest, and heating then exceeds the sideways cooling, leading to the column structure

expanding radially outward again. Because the over-cooling of the innermost region is usually stronger at maximum radial extent than the over-heating at minimum radial extent, the innermost finger structure of the accretion column always collapses faster than its expansion.

5.2.3   Luminosity Variation

The oscillatory behavior of the accretion column produces variability in the emergent radiation in all our simulations, as illustrated in Figure 5.7. Various parameters measured
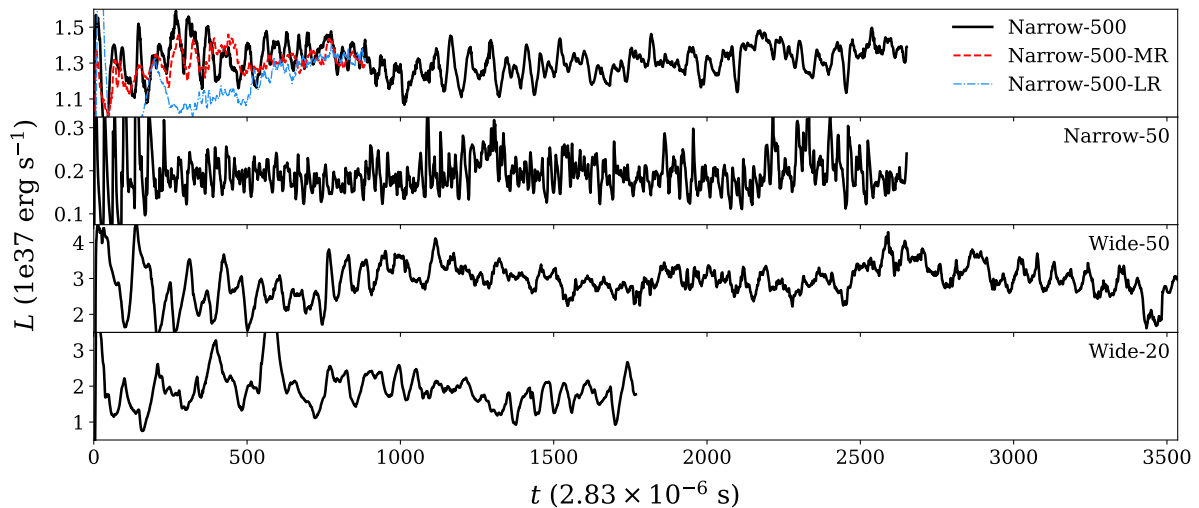
Figure 5.7: Light curves of all six accretion column simulations which have different accretion rates, different column widths, and/or different resolution.

from these light curves are listed in Table 5.2. These include the time-averaged luminosity $\langle L \rangle$ as well as the time-averaged apparent luminosity $\langle L_{\mathrm{iso}} \rangle$ that an observer might infer from seeing only one accretion column at one magnetic pole. For the latter we measured the side area of the cone enclosing the edge of the accretion column, up to a height that captures 99 percent of the emitted luminosity in the time-average. We then enhanced $\langle L \rangle$ by the ratio of the surface area of the neutron star to this area. Table 5.2 also lists the standard deviation of the luminosity $\sigma(L)$ scaled with that mean, which is positively

Version	Name	$\langle L \rangle$ $(10^{37}$ erg s$^{-1})$	$\langle L_{\text{iso}} \rangle$ $(10^{39}$ erg s$^{-1})$	$\sigma(L)/\langle L \rangle$ (%)	f_{peak} (kHz)	f_{break} (kHz)
0 (Fiducial)	Narrow-500	1.31	3.27	6.28	5.86	9.66
1	Narrow-50	0.19	0.57	19.28	10.35	15.87
2	Wide-50	3.02	0.30	12.67	2.00	6.19
3	Wide-20	1.85	0.11	19.74	3.45	6.55
4	Narrow-500-MR	1.32	4.09	3.90	6.08	11.05
5	Narrow-500-LR	1.31	4.41	2.92	6.89	22.06

Table 5.2: Parameters of the light curves for all six simulations.

correlated across our simulations with the oscillation amplitude of the accretion shock on the polar axis.

All of our light curves exhibit quasi-periodic oscillations (QPOs), and we include their frequencies f_{peak} in Table 5.2. These frequencies range from ∼2 to 10 kHz, depending on the simulation parameters. Increasing the accretion rate at fixed column width generally results in smaller fractional variability and lower QPO frequencies (compare versions 0 to 1, and versions 2 to 3). As we discussed in section 3.2.3, the oscillations are driven by a mismatch between the ability to distribute accretion energy radially in the column and the cooling at each height. Higher accretion rate generally results in a taller column so that it takes longer for radial advection in the sinking flow to distribute energy from the shock downward, resulting in lower frequencies in the oscillation. As we discuss in more detail below in section 5.2.5, pdV work by the sinking flow also becomes more important and provides a local source of energy to balance the cooling, so that the oscillation amplitude is reduced. Increasing the column width at fixed effective Eddington ratio reduces the fractional variability and decreases the QPO frequency (compare versions 1 and 2). Because the transverse diffusion time is longer in a wider column, cooling is less efficient, partially alleviating the mismatch and reducing the amplitude of the oscillation. The longer cooling time also results in a longer oscillation period.

Figure 5.8 shows a power spectrum of the light curve of the fiducial simulation, as
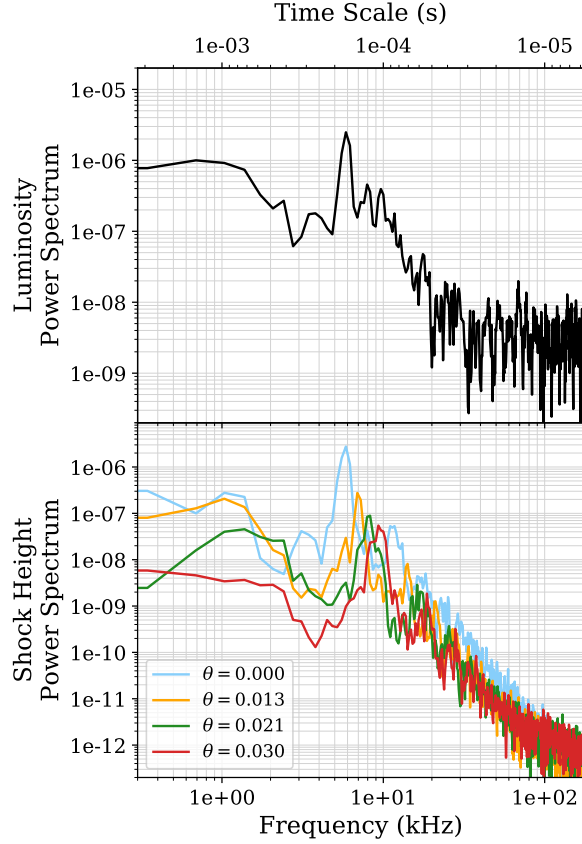
Figure 5.8: Power spectra of the light curve and shock oscillation height at various transverse locations in the fiducial simulation. The power spectra are calculated using Welch's method with a Hann window function, a segment length of 2.9 ms, and a sampling interval of t_{sim}. These two plots suggest that the light variation arises from the shock oscillations, where the light curve is dominated by the shock oscillation in the innermost region.

well as a power spectrum of the shock height at various transverse locations. The QPO in the luminosity power spectrum consists of a peak together with an asymmetric shoulder extending to a higher frequency f_{break}. All our simulations exhibit this characteristic QPO shape, and we also list the values of f_{break} in Table 5.2. The reason for this breadth in frequency space is that the shock height oscillates with different amplitudes and frequencies depending on the transverse location within the accretion column (recall Figure 5.3). The shock height at the polar axis center of the column oscillates with the highest amplitude and lowest frequency, and this produces the main peak f_{peak} in the light

curve power spectrum, particularly as the high amplitude results in a large oscillating sideways emitting area. The higher frequency, smaller amplitude shock oscillations away from the polar axis contribute to the high frequency shoulder in the light curve power spectrum, with f_{break} corresponding to the shock oscillation frequency at the outer edge of the column. As is evident from Table 5.2, wider columns show larger values of $f_{\text{break}}/f_{\text{peak}}$, and therefore broader high frequency shoulders in log frequency space.

5.2.4   Time-averaged Profiles

The accretion column is highly dynamical, but its short oscillation time scale ($\lesssim 1$ ms) may make it challenging to detect with existing observational facilities. Virtually all observational studies of accreting neutron stars average over longer time scales. Here we therefore time-average our simulations in order to make contact with such observations. Figure 5.9 shows 2D time-averaged profiles of various quantities in the fiducial simulation.
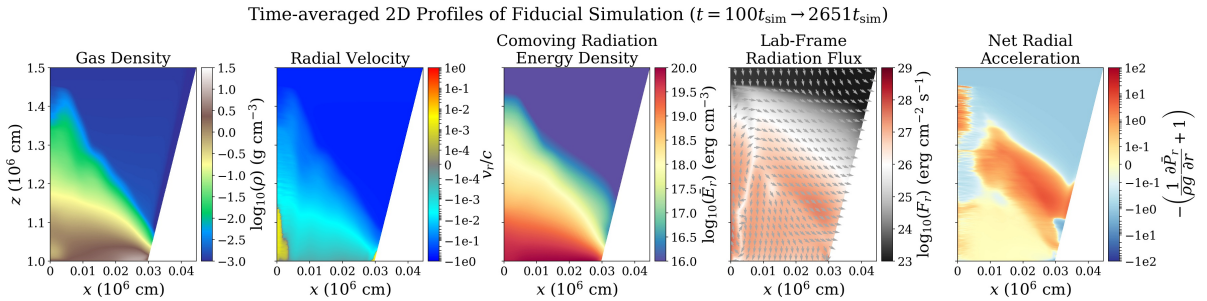
Figure 5.9: Time-averaged 2D profiles of density, mass-weighted radial velocity, co-moving energy density, lab frame radiation flux, and mass-weighted radial acceleration in the fiducial simulation. The shock structure and entropy wave are smeared out by the time average.

The jump in density and other quantities associated with the oscillating shock front has been smoothed out, as has radial finger structures associated with the propagating entropy waves. The latter is in contrast to what we found in the time-averaged profiles of the Cartesian simulations (see Figure 3.15, where the pre-shock disturbed the entropy

wave in the sinking zone, causing it to leave residual vertical striations in the time average.

As shown in the first and third panels of Figure 5.9, the gas density and the radiation internal energy in the sinking zone increase exponentially inward towards the stellar surface. Despite the fact that the gas below the shock front oscillates along the magnetic field lines, the second panel of Figure 5.9 shows that the time-averaged, mass-weighted velocity away from the polar axis is small and downward, consistent with the physical picture of Basko & Sunyaev (1976) and with the overall sinking flow of accreting matter. Note, however, that gas in the lower part of the central polar axis region is moving outward in the time average, because the collapse is faster than the expansion of the innermost finger structure. The sinking zone achieves approximate hydrostatic equilibrium in its time average, as indicated by the nearly zero mass-weighted radial acceleration in the last panel of Figure 5.9. Even though the comoving radiation flux must be upward in the sinking zone to provide support against gravity, the lab-frame radiation flux away from the polar axis is still downward, as shown in the second to last panel of Figure 5.9. Hence, the downward advection must be dominant over the upward radial diffusion and this transports the heat from the shock front to the bottom of the column.

In chapter 3, we found that the time-averaged mound shape of the shock front has a higher cooling efficiency compared to the assumed top-hat geometry in the one-zone model of Basko & Sunyaev (1976). Here, we attempt a comparison of our 2D simulation results with the approximate 1D stationary solution. We do this by numerically integrating the column profiles at the polar axis $\theta = 0$ starting above the shock and going inward to the stellar surface by using the 1D stationary model equations. We adopt the time-averaged radial profile from the simulation in the free-fall zone, and then integrate the 1D equations inward starting from $r = 1.5R_\star$ (the point at which the density starts to increase because of the smoothed-out, oscillating shock). In order to explore how the mound shape geometry influences the trend of the profiles, we also introduce

a shape function that approximately accounts for the mound shape of the shock front. The details of the formulation can be found in appendix A of Zhang et al. (2023).

We adopt four different shape functions, which are shown on top of the time-averaged density in the fiducial simulation in Figure 5.10. The cyan dot-dot-dashed line refers to
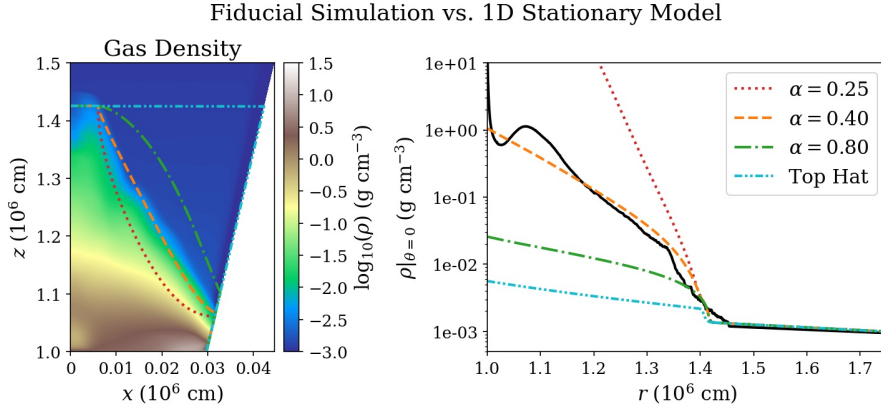
Figure 5.10: Comparison between the time-averaged density profile and the 1D stationary model using different shapes of the sinking zone. In the left panel, the curves in various line styles and colors represent different assumed shapes for the sinking–zone integration. In the right panel, the black solid curve is the simulation data, while other curves represent the integrated results from the 1D stationary model using the corresponding shape functions as shown in the left panel. The $\alpha = 0.40$ shape function is closest to the simulated 2D shape in the left panel, consistent with the fact that the corresponding 1D stationary solution is closest to the radial profile of the simulation data along the polar axis in the right panel.

the top-hat shape. Green dot-dashed, orange dashed, and red dotted lines corresponds to different values of the geometric index parameter α in equation A2 of Zhang et al. (2023): $\alpha = 0.8, 0.4, 0.25$, respectively, where larger α values approach the top-hat shape. In the right panel of Figure 5.10, we present the integrated results using these different shape functions, and compare them to the time-averaged simulated radial density profile at $\theta = 0$ (black solid line). The more top-hat shapes at high values of α have more laterally distributed density, which tends to result in slower transverse radiative diffusion. Thermal equilibrium therefore forces them to have lower densities in the column compared to the shapes with small values of α. A value of $\alpha = 0.40$ (orange dashed line) produces a mound

shape that closely resembles that of the time-averaged simulated density profile, and the 1D radial profile is reasonably consistent with that of the simulation along the polar axis. A top-hat geometry always overestimates the shock height because it underestimates the cooling efficiency.

Note that the net radial acceleration in the sinking zone is nearly zero in the time average (see the last panel of Figure 5.9), while the instantaneous radiation pressure support can exceed the local Eddington limit in certain locations (see e.g. the last panels of Figure 5.5 or Figure 5.6). This super-Eddington comoving radial flux is enabled by the density inhomogeneities within the accretion column, where the flux is larger in the lower density finger-shaped channels (Begelman 2001; Shaviv 1998). To properly measure this effect, we define the porosity as:

$$\mathcal{P}(r,t) \equiv \frac{\langle\rho\kappa\rangle\,\langle|\bar{F}_{r,r}|\rangle}{\langle\rho\kappa|\bar{F}_{r,r}|\rangle} \quad , \tag{5.4}$$

where $\bar{F}_{r,r}$ is the radial comoving radiation flux, and κ is the flux mean opacity, which in our simulations is dominated by Thomson opacity. The angle bracket represents a spatial average in the polar direction, which we do in two ways: from the polar axis to the accretion shock or last confining field line, whichever comes first (i.e. just from the actual sinking zone), or from the polar axis to the last confining field line, even if this includes the free-fall region. The latter would be appropriate for 1D models that assume a top hat geometry rather than the actual mound shape of the time-averaged column structure. In Figure 5.11, we display the time-averaged porosities computed in both ways as a function of radial position, for all four of our high-resolution simulations. We generally find the porosity to be greater than unity in the sinking zone, consistent with super-Eddington radial fluxes. Note, however, for the fiducial simulation, the porosity as computed just from the sinking zone is near unity at almost all radii, which explains why
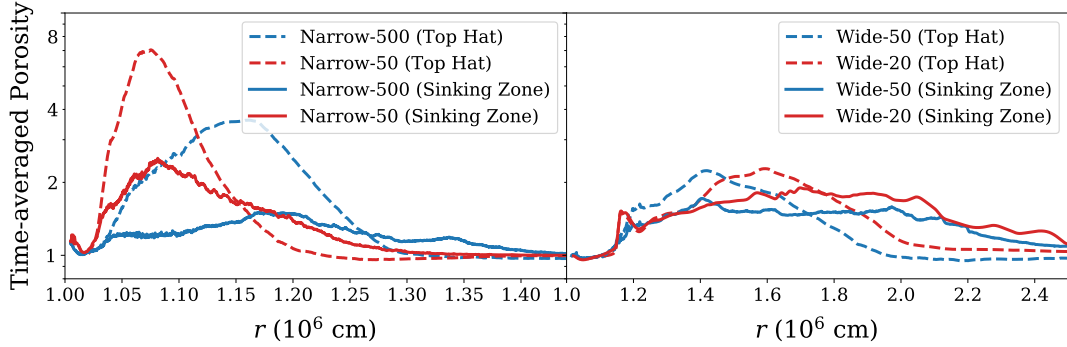
Figure 5.11: Time-averaged porosity as a function of radial position measured in our two narrow column simulations (left) and our two wide column simulations (right). Solid curves show averages of the porosity below the instantaneous position of the shock, i.e. the transverse average at a particular radius and time extends from the polar axis to the portion of the shock which has that radius, or to the edge of the column. Dashed curves show the porosity calculated from transverse averages from the polar axis to the edge of the outermost confining field line. This can include portions of the free-fall region, but is the appropriate measure to use for 1D models with top hat column shapes. The porosity is greater than unity throughout the sinking zone in all cases, indicating super-Eddington radial fluxes. Note that for Wide-20, we smooth the curve to remove the artificial discontinuities arising from finite time sampling over a relatively large amplitude oscillation.

a simple hydrostatic model with the correct time-averaged mound shape produces a radial density profile that agrees with the simulation data (the $\alpha = 0.4$ case in Figure 5.10). These porosity profiles could in principle be used to improve 1D models of accretion columns.

5.2.5   Energetics of Accretion Columns

The structure of the accretion column is very sensitive to the balance between its heating and cooling processes, and we analyze these in detail here, focusing on the sinking zone. Recall that the gas in the sinking zone moves much more slowly than the speed of light, so we can examine the rate of change of energy terms in the Newtonian regime. These are, respectively, advection, pdV work, transverse radiation diffusion, and radial

radiation diffusion, and are defined as follows:

$$\dot{E}_{\text{advc}} = - \oint \left(\frac{P_g}{\gamma - 1} + \bar{E}_r \right) v_r dA_r \quad , \tag{5.5a}$$

$$\dot{E}_{pdV} = - \int \left(P_g + \bar{P}_r \right) \frac{\partial}{\partial r} \left(r^2 v_r \right) dV \quad , \tag{5.5b}$$

$$\dot{E}_{\text{diff},\theta} = - \oint \bar{F}_{r,\theta} dA_\theta \quad , \tag{5.5c}$$

$$\dot{E}_{\text{diff},r} = - \oint \bar{F}_{r,r} dA_r \quad . \tag{5.5d}$$

Here $\bar{P}_r$ is the comoving radiation pressure and $\bar{F}_{r,\theta}$ refers to the transverse comoving radiation flux. dA_r and dA_θ refer to the differential area elements in the radial and polar directions, respectively. The quantity dV is the volume element in spherical polar coordinates. More detail on how we compute these quantities can be found in appendix B of Zhang et al. (2023).

In Figure 5.12, we analyze the energetics inside the sinking zone of the fiducial simulation as a function of time. As shown in the upper panel of Figure 5.12, both the advection process and the pdV work contribute to increasing the internal energy of the system. Sideways diffusion of radiation is the dominant cooling process, and the emergent radiation is therefore in the fan-beam pattern. As shown in the lower panel of Figure 5.12, the overall heating and cooling roughly reaches thermal equilibrium.

In our Cartesian simulations in chapter 3, the accretion rates were moderate and the shock heights were much lower than here. We found in those cases that the advection process always dominated over the pdV work in increasing the internal energy. Our simulations in this chapter develop taller column structures in spherical polar geometry at higher accretion rates. The convergence of the magnetic confinement over a larger radial range results in a pdV work that is now comparable and sometimes larger than the advection, which is more consistent with the physical picture described in the 1D

Energetics of Fiducial Simulation
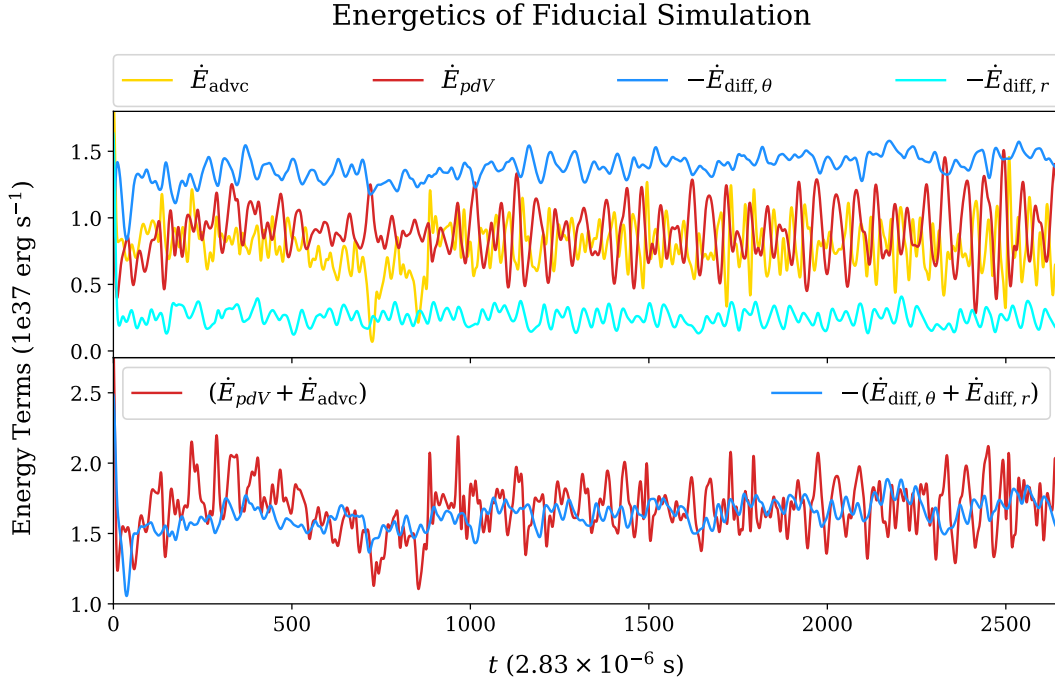
Figure 5.12: Energetics of the sinking zone in the fiducial simulation. In the upper panel, the major cooling mechanism of the accretion column is the sideways radiation emission (blue curve), which completely dominates the emission in the radial direction (cyan curve). Internal energy input comes from both advection (gold curve) and pdV work (red curve). The lower panel shows that all the heating and cooling terms achieve an approximate thermal equilibrium. Note that we have smoothed the curves by box car time-averaging the data over $4t_{\rm sim}$ ($\sim 10^{-5}$ s) in order to remove variability on time scales much shorter than the oscillation time scale of the column.

stationary model by Basko & Sunyaev (1976). The ratio of time-averaged pdV work to advection $\left\langle \dot{E}_{pdV} \right\rangle_t / \left\langle \dot{E}_{\rm advc} \right\rangle_t$ is 1.17 in the fiducial simulation. Version 1 has the same column width, but ten times less accretion rate and therefore a shorter column, so this ratio is reduced to 0.64. For the wider column simulation Version 2, which has the same area-weighted accretion rate, this ratio increases to 3.84. Reduction of the accretion rate of this wide column (Version 3) again decreases the ratio, in this case to 1.66.

The competition between radiative advection and pdV work in supplying internal energy to balance cooling is important because it relates to the mechanism that drives the overall radial oscillations of the column structure. In the short column, Cartesian

simulations we presented in chapter 3, pdV work was negligible and radiation advection brought energy inward from the shock front to balance cooling. However, this balance was not achievable in a time-steady configuration, resulting in oscillations between phases where the column was tall and cooling exceeded heating, to phases where the column was short and heating exceeded cooling. The presence of significant pdV work in the simulations of this chapter can provide a more local mechanism to balance cooling, just as in the original 1D stationary model of Basko & Sunyaev (1976). Figure 5.13 shows
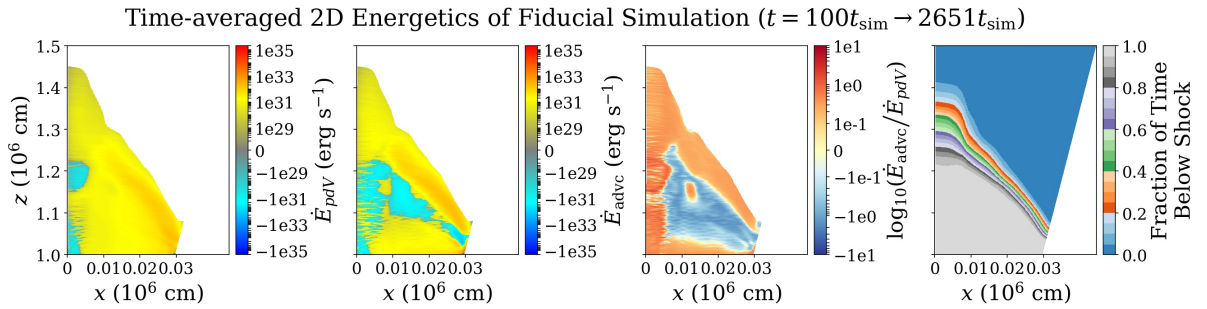
Figure 5.13: 2D distribution of the rate of change of internal energy due to radial advection (left) and pdV work (middle left), and their ratio (middle right). The right-most panel shows the fraction of time a given point likes below the radially oscillating shock front.

the time-averaged 2D structure of advection and pdV work, as well as their ratio. In the time average, the pdV work dominates the radiation advection except at the top, on the polar axis, and near the neutron star surface.

The advection dominated region near the shock originates from the shock oscillation, which is proved generating most of the light variation in section 5.2.3. The right-most panel of Figure 5.13 shows the fraction of time during the shock oscillation that a particular point in space is below the accretion shock (i.e. 1 implies that the point is always below the shock front and 0 implies that the region is always radially outside the shock front). It is particularly noteworthy that radiation advection dominates the rate of increase of internal energy precisely in the region where the shock is oscillating. This

strongly suggests that the oscillation that is responsible for the variations in the light curve in section 5.2.3 originates from exactly the same mechanism that we identified in section 3.2.3.

In the bottom region, the pdV work does not produce sufficient heat to support the base of the column and the advection must then be driven to transport the extra heat to the bottom, which is also indicated by the downward time-averaged lab-frame radiation flux (see the fourth panel of Figure 5.9).

Note from the first and second panels of Figure 5.13 that both the pdV work and the radiation advection along the polar axis below the shock oscillation region are cooling, not heating, in the time-average. This is again related to the fact that the time-averaged, mass-weighted velocity near the lower polar region is outward, not inward (see second panel of Figure 5.9). This also exacerbates the inability of the column to achieve a balance between heating and cooling, and may be a contributing factor to why the central finger structure along the polar axis has the largest oscillation amplitude.

5.2.6   Entropy Wave and Resolution Study

As we noted above in section 5.2.1, the wave pattern that propagates inward toward the polar axis strongly resembles a similar wave pattern that developed in our Cartesian simulations in chapter 3. Because those simulations started with an initial condition consisting of an accretion column, we were able to show that the wave pattern resulted from the growth of the slow diffusion photon bubble instability (an unstable entropy mode). Here, since the accretion column is built up dynamically from a free-fall flow in our new simulations, there is no steady background state in which to identify the growth of the unstable entropy mode.

However, deep in the column, the wave amplitude is relatively small and arguably

t/t_{sim}	400	890	1500	2160	2510
	$\rightarrow$520	$\rightarrow$1010	$\rightarrow$1620	$\rightarrow$2270	$\rightarrow$2630
$v_{\mathrm{p,sim}}/c$	1.88e-3	2.14e-3	2.21e-3	2.30e-3	2.22e-3
$v_{\mathrm{p,exp}}/c$	1.91e-3	1.98e-3	2.07e-3	2.03e-3	2.14e-3

Table 5.3: Comparison between the measured phase velocity and the theoretically expected phase velocity of the entropy wave in five different epochs of the fiducial simulation. The simulation measurements are highly consistent with the expectation from the linear theory.

in the linear regime, and in the fiducial simulation it has short enough wavelengths to be in the WKB regime. We can therefore measure its phase velocity in the simulation $v_{\mathrm{p,sim}}$, and compare it to the expected value $v_{\mathrm{p,exp}}$ from the linear dispersion relation for the slow diffusion photon bubble instability (Arons 1992; A.11). We measure the phase velocity in multiple epochs of the fiducial simulation by tracking a selected wave front propagating inward from the side toward the polar axis. For the expected phase velocity, we solve the dispersion relation by first adopting a background state corresponding to the time average of the epochs over which we measure the simulated phase velocity. We did this by selecting the mode that had the maximum linear growth rate at the measured wavelength. More detail about the measurement and calculation can be found in appendix C of Zhang et al. (2023). The results are summarized in the Table 5.3, where the simulation measurements and the theoretical expectations are very consistent. This result is robust because there is no other characteristic speed near this regime. The sound speed is $\sim 0.1c$ and the radiation diffusion speed is $\sim 10^{-4}c$. Therefore, the wave patterns that we observe in the simulation are indeed the entropy mode.

Note that the local entropy wave dispersion relation that we use to calculate the phase velocity assumes a background with no transverse spatial variation, and therefore does not distinguish inward from outward transverse propagation. We only observe inward transverse propagation from the sides to the center, and this is due to the fact that the sinking zone is mound-shaped, i.e. it is shorter on the sides than at the center. Consider

an outward radial motion of the side of the column. This provides more shielding of the material immediately on the inside, reducing its sideways cooling, and causing it to expand radially in response as it overheats. This in turn shields material further inward, causing it to expand radially. Similarly, an inward radial oscillation at the sides provides less shielding of material on the inside, enhancing the sideways cooling and causing that material to contract radially. All of this leads to inward propagation of the entropy wave. Outward propagation does not occur because a radial expansion or contraction of the taller inner material has negligible effect on the shielding of the shorter material further out.

Another characteristic of the entropy wave is its resolution dependence, as a higher resolution can result in a faster growing mode at the shorter resolved wavelength until the radiation viscous length scale is reached (see section 2.3.3 and section A.2). We have performed a resolution study on the fiducial simulation by running two additional simulations with decreased resolution by factors of 2 (Version 4) and 4 (Version 5). The results resemble what we found in a similar resolution study in chapter 3 (see section 3.2.4). As shown in Figure 5.14, the number of fingers decreases by the same factor as the decrease in resolution, and the shape of the column becomes less peaked toward the polar axis. Despite these changes with resolution, the global oscillation frequency remains roughly the same, only slightly increasing with decreasing resolution (Table 5.2). This robustness of the frequency with resolution is similar to what we found in the Cartesian simulations in chapter 3. What increase in frequency is present appears to be due to a smaller oscillating region after losing the finger-shaped structure, and the fact that the presence of fingers decreases the overall cooling efficiency of the column. In chapter 3, the dependence of the cooling on the horizontal shape of the Cartesian column is less sensitive than in an axisymmetric column. Having more resolved fingers in the Cartesian geometry therefore does not affect the cooling as much as it does here in the axisymmetric
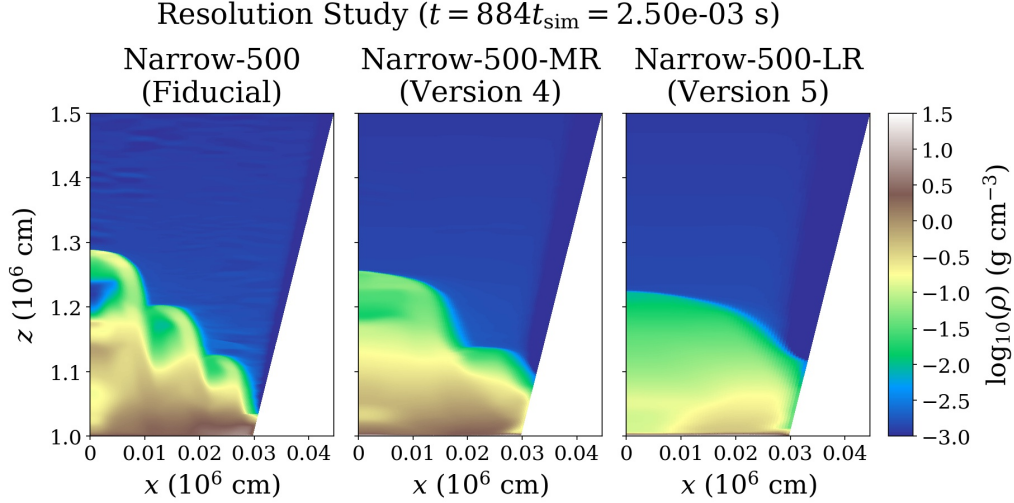
Figure 5.14: Snapshots of the density structure at $t = 884t_{\rm sim}$ in our narrow column simulations at different resolutions from high (left) to low (right).

geometry. Even with this increased sensitivity, the oscillation frequency depends only weakly on resolution.

5.3 Discussion

5.3.1 Numerical Caveats

There exist some numerical caveats in our simulations. We discuss them in detail here.

Geometric Dilution and Resolution

The spherical polar coordinate grid that we use here has decreasing resolution with radius, and this might affect the growth and propagation of the entropy waves at different altitudes. As shown in chapter 2, the slow-diffusion photon bubble instability that arises from the entropy wave grows faster at shorter wavelengths, until the radiation viscous length scale is resolved. The viscous length scale in the sinking zone of the fiducial

simulation ranges from ~ 400 cm at the stellar surface to ~ 2000 cm at $r = 1.2R_{\star}$, and requires at least ~ 50 grid cells to resolve. So in fact our grid is closest to the viscous length scale at larger radii.

Bottom Boundary Condition

Recall that we adopt an effective bottom boundary that mocks up the neutron star surface layer. In our simulations, the neutron star surface is heated via Compton scattering by energetic photons generated inside the sinking zone. In reality, such heat should flow into the neutron star and establish a thermal equilibrium with the accretion column. However, since we adopt a reflective boundary condition below the neutron star surface layer, the heat accumulates and can eventually lead to an increased temperature of the bottom layer, which might overheat the simulated accretion column. Thus, we set up a very thick effective bottom boundary in our simulations so that the heat capacity is large enough that the temperature increases only very slowly after the sinking zone is built up. Note that we assume a nondegenerate ideal gas equation of state (EOS) for the effective bottom boundary, which overestimates the heat capacity and, as we already stated, underestimates the heat conduction into the neutron star. This can obviously be further improved by properly treating the thermal properties of the neutron star surface with the correct EOS (e.g. Negele & Vautherin 1973).

Dependence on the Magnetic Field

As in chapter 3, we adopt a surface magnetic field strength of 10^{11} G in our simulations, which is lower than the typical high-mass X-ray binary pulsars ($\gtrsim 10^{12}$ G). However, as long as the magnetic field is strong enough to confine the transverse motion of the gas, it does not alter the dynamics of the accretion column. However, this would not be true if we accounted for the dependence of opacity on magnetic field strength,

rather than the simple Thomson opacity that we have assumed here. The photon energy and polarization-averaged flux-mean opacity can be significantly reduced below Thomson for temperatures below the cyclotron energy (e.g. Arons 1992). Incorporation of magnetic opacity effects can therefore reduce the height of the column, and may significantly effect its dynamics. These effects will be explored in our future work.

5.3.2 Relationship of Oscillations to the Entropy Waves

In section 5.2.6 we demonstrated that the entropy waves that are present in the fiducial simulation have phase speeds that are consistent with the linear, slow diffusion photon bubble instability dispersion relation. However, this does not explain the frequencies of the entropy waves that are actually present. In particular, the frequency of arrival of successive wave fronts of the entropy wave can at times be remarkably close to the oscillation frequency of the central finger-shaped structure along the polar axis. Nevertheless, as we showed in our Cartesian simulations in chapter 3, that oscillation frequency is determined simply by the overall net cooling time of the column.

In fact, recall from our resolution study in section 5.2.6 that the dominant frequency of the light curve is only weakly affected by the entropy waves, the small dependence being due to the effect of these waves on the overall shape of the column, which slightly alters its cooling rate. At the same time, the different oscillating fingers themselves have higher frequencies as one moves outward from the center, because they have individual cooling times that are shorter. A close examination of the arrival frequencies of successive entropy wave fronts toward the center in the fiducial simulation show that they arrive with frequencies ranging from 5.76 to 8.46 kHz, close to the QPO frequency: the peak at $f_{\mathrm{peak}} = 5.86$ kHz and the edge of the extended plateau $f_{\mathrm{break}} = 9.66$ kHz. We therefore suggest that the entropy waves that are present in the saturated state are in frequency

155

resonance with the radial oscillation frequencies of the individual fingers. This is also consistent with the behavior of the wider column simulations, which have broader QPO plateaus, and appear to have multiple entropy wave modes that are excited.

5.3.3   Comparison with Previous Works

Our accretion column simulations develop finger-shaped structures (which might be called 'photon bubbles') introduced by the unstable entropy waves, which appear to resemble what Klein & Arons (1989) and Klein et al. (1996), found in their 2D simulations. In particular, they share similar high-frequency oscillatory behavior. Klein & Arons (1989) and Klein et al. (1996) attributed these oscillations to photon bubbles, but our resolution studies (section 3.2.4 and section 5.2.6) suggest that the oscillatory behaviors arise instead from the inability of the column to maintain a stationary balance between accretion power heating and radiative cooling (see section 3.2.3 in chapter 3 and section 5.2.5). Note that Klein & Arons (1989) observed mergers of their photon bubbles toward larger spatial structures. We see similar behavior in our wide column simulations, in that the accretion shock forms wide localized mound shapes, inside of which the shorter wavelength entropy waves still propagate. We remind the reader that the spatial scales of the entropy wave are in fact resolution-dependent. However, this has only a small effect on the QPO frequency.

Kawashima & Ohsuga (2020) have also done simulations of neutron star accretion columns in monopole geometry. Their initial and boundary conditions differ from ours, as they start with an extended, uniform mass distribution out of hydrostatic equilibrium that then free-falls onto the neutron star surface. In their simulations, the flow breaks up into narrow, dense channels that accrete and surround broad, underdense regions that undergo radiation pressure-driven outflow. They do not find evidence of a quasi-

stationary, oscillating structure such as we find. This could be due to the fact that their accretion luminosity exceeds the global Eddington luminosity of the entire neutron star by large factors, much larger than the sub-Eddington luminosities of our simulations here.

Abolmasov & Lipunova (2022) recently reported time-dependent, one-dimensional simulations of accretion columns in a dipolar magnetic geometry. Intriguingly, they found that their accretion shocks at the top of the optically thick columns exhibited radial high frequency oscillations, though in contrast to what we find here, their shock oscillations were damped with time. Their oscillation period is close to the radial sound propagation time through the column, whereas our oscillations are nearly hydrostatic. Hence it appears that they have found a damped acoustic oscillation. The reason why they did not find the longer time scale thermal oscillation that we have found here may be due to their 1D approximation. Our column has a changing shape which is overheated at its most compressed state, then overcooled at its most expanded state because it has a larger sideways cooling area. This effect of changing shape would not be accounted for in their 1D model.

In our previous Cartesian simulations (see chapter 3), we purposely limited the accretion rate so that the column height never became a significant fraction of the neutron star radius. Here the split monopole magnetic geometry has allowed us to break this constraint and move to higher luminosities with some realism, although the field does not diverge as quickly as, say, a more realistic dipole or higher order multipole field. There are two main physical differences between our previous short-column, Cartesian simulations and the current, taller and geometrically diluted simulations. First, we find no prominent pre-shock behavior in the fiducial simulation here, even though pre-shocks were prominent in the Cartesian simulations. This may be because the density in the free-fall region decreases more rapidly with radius in the diverging magnetic field, so that

there is less ram pressure in the free-fall region. On the other hand, simulation Wide-20 (Version 3) does show occasional shock structures near the polar axis in the free-fall region.

Second, pdV work was a negligible contribution to increasing internal energy in the sinking zone of the short Cartesian simulations. Instead, radiation advection was the dominant source of increasing internal energy, but this transport mechanism downward from the accretion shock was unable to balance radiative cooling in a stationary fashion, and this is what drove the oscillations. In the taller simulations here, pdV work plays an increasingly important role, both with increasing accretion rate and column height. This is because of the sideways compression that is present in the split monopole geometry, compared to Cartesian simulations at comparable local Eddington ratios. The latter fact suggests that it would be even more important in dipole and quadrupole magnetic field geometries. It is possible that tall accretion columns in more diverging magnetic field geometries might achieve an equilibrium between pdV work and radiative cooling, akin to the physical picture in the 1D model of Basko & Sunyaev (1976). However, that column would still be unstable to the slow-diffusion photon bubble instability. Moreover, accounting for magnetic opacities will result in shorter columns, and we will explore this effect in our future work.

Finally, we emphasize again that that the 2D shape of the column determines the cooling efficiency, and radial profiles of various quantities within the sinking zone depend sensitively on this. The column also has significant porosity. We have demonstrated in section 5.2.4 how these effects can in principle be accounted for in 1D models.

5.3.4   Observational Significance and Future Work

Compared to the Cartesian simulations in chapter 3, we are now in the accretion regime of many X-ray pulsars and even the low luminosity end of ULXs. These new simulations are therefore more useful for comparing with observations. In agreement with the pioneering work of Klein et al. (1996), our new simulations strongly suggest that high luminosity X-ray pulsars should exhibit high frequency oscillations (2-10 kHz, depending on parameters). Detection of such high frequencies will likely be challenging with existing X-ray timing facilities, and indeed has a somewhat checkered history (Jernigan et al. 2000; Revnivtsev et al. 2015), but we still feel that attempts are worthwhile given how robust is this physics.

An additional observable effect might be the effects of the changed time-averaged structure of the column, compared to 1D models, on predicted spectra and polarization. Our simulations can be post-processed to make such predictions. Note that the bulk velocities in the column are less than the electron thermal speed by factors of two to one hundred, with a median value of around ten. We therefore expect thermal Comptonization to dominate over bulk Comptonization, and this will enhance the thermalization of the emergent radiation with the gas temperature.

Finally, there is currently a debate in the ULX community concerning how their apparent super-Eddington luminosities can be achieved. One way is to have a strong magnetic field in the neutron star leading to a significant magnetic reduction of opacity. Such low magnetic opacity can largely reduce the gas-radiation interaction and permit a much higher accretion rate within the accretion column (Mushtukov et al. 2015). Another way is to have strong geometric beaming from the surrounding optically thick accretion flow (Abarca et al. 2021), though this might result in the smearing out of the observed neutron star spin pulsations (Mushtukov et al. 2021). It will be important to test this

claim with future numerical simulations that include the more global structure of the accretion flow.

5.4   Conclusions

We summarize our conclusions as follows:

1. The light curves in all of our simulations display high-frequency $(2-10\,\mathrm{kHz})$ QPOs. These QPOs are dominated in the power spectrum by a peak frequency originating from the oscillating polar axis region of the accretion column, but include an extended plateau toward higher frequencies due to the higher frequency shock oscillations further out from the polar axis. The peak frequency and fractional amplitude depend on the global parameters of the accretion column, being lower for higher accretion rates or wider columns.

2. We have confirmed that when the accretion rate is supercritical, a radiation-pressure dominated sinking zone is formed as predicted by Basko & Sunyaev (1976). In our simulations, the sinking zone appears to be mound-shaped, which can significantly affect the cooling efficiency and thus modify the radial structure of the accretion column. We demonstrate the consistency between the time-averaged profile of the fiducial simulation and the 1D stationary model provided it accounts for the correct shape function. Accounting for porosity (which is not that different from unity in the fiducial simulation) should also improve 1D models. One final effect is that the oscillations smooth out the shock structure in the time-average, an effect which cannot be accounted for in 1D models that assume shock jump conditions.

3. In our simulations, the accretion column is mainly cooled by sideways emission of radiation. This cooling is balanced by increases of internal energy due to pdV work

and radial radiation advection. The pdV work arises in part from the sideways compression of the converging magnetic field toward the neutron star surface. Radiation advection originates mostly from the radial oscillations within the column. When the accretion column is wider or has higher accretion rate, pdV work becomes more important compared to advection. We expect that pdV work will be even more important for dipolar or quadrupolar field geometries.

4. We observe the entropy wave that is associated with the slow-diffusion photon bubble instability in our simulations. While the properties of this wave depends on numerical resolution, we confirm that the dominant oscillation frequency depends only weakly on these properties. This is consistent with what we found in chapter 3. What effects the entropy wave has on the oscillation are due to the altered mound shape of the column and resulting change in cooling efficiency.

Chapter 6

Future Plan

Unveiling the nature of radiation pressure dominated accretion is a problem of wide interest in the physics of luminous accretion-powered sources, such as quasars. The most extreme examples are ULXs, which are the most super-Eddington of accretion-powered X-ray sources ($> 10^{39}$ erg/s). ULXs were generally thought to be powered by accretion onto an intermediate-mass black hole or a stellar-mass black hole with strongly beamed radiation. However, the recent discovery of pulsating ULXs (e.g. Bachetti et al. 2014) has shown that some of ULXs are actually accreting neutron stars. Other sources powered by accreting neutron stars are X-ray pulsars, which typically accrete at sub-Eddington rates.

In neutron star accretion, a strong magnetic field anchored in the neutron star truncates the inner accretion disk near the Alfvèn radius (i.e. Region 3 in Figure 6.1). Within this truncation region, the accreting matter is magnetically constrained and then forms a curtain-shaped structure on the magnetosphere (i.e. Region 2 in Figure 6.1). Near the stellar surface, the accretion flow is shocked and radiates the accretion power in the form of either a hotspot or an accretion column (i.e. Region 1 in Figure 6.1). However, how a neutron star can accrete in the super-Eddington regime is still not well understood.

There is a debate about this. One hypothesis is to permit a very high accretion rate by significantly reducing the opacity in a strong magnetic field up to the magnetar regime (Mushtukov et al. 2015). An alternative is to produce a strong beaming effect from the funnel-like accretion flow (Abarca et al. 2021).

Near the neutron star surface, the interaction between the radiation and strongly magnetized plasma is anisotropic and polarization-dependent. This has been explored in many 1D stationary models of accretion columns. But our simulation results discussed above demonstrate that the accretion column is not stationary but oscillates quasi-periodically. Hence, the 1D stationary models cannot correctly resolve the dynamics or even the time-averaged structure. All of this will affect theoretical expectations of the variability, spectrum, and polarization that are measured with current or upcoming X-ray space missions. In fact, IXPE have found that the observed polarizations of two strongly magnetized X-ray pulsars, Her X-1 and Cen X-3 (Doroshenko et al. 2022; Tsygankov et al. 2022), are far below the predictions of the classical theoretical model.

In order to disclose the underlying physics of the existing observations and further explore the dynamics of a super-Eddington accretion onto a neutron star, our long-term plan is to extend our simulations of neutron star accretion to a more global regime. We plan to conduct a series of simulations for each labeled region in Figure 6.1 to explore whether or how steady accretion can be achieved. Using one global simulation is nearly impossible because the dynamics in each region requires different time and length scales to be resolved. These regions are causally connected inwards by the mass accretion and the magnetic field, but outwards by radiation feedback. It is therefore preferable to simulate from inside to outside so that the inner boundary condition can be correctly and accurately specified from one region to another. We have successfully simulated the most inner region (i.e. Region 1; see previous chapters for details), but resolving and updating some technical issues are necessary to begin the simulations of more outwards regions. In

the following sections, we provide our proposed solutions in detail to the following issues: 1. resolving the gas temperature with the variable inversion scheme using entropy in the strong magnetic field regime. 2. numerically implementing the dipole coordinates system for global neutron star accretion. 3. employing a novel numerical approach to solve the polarized radiative transfer and predict related observables.
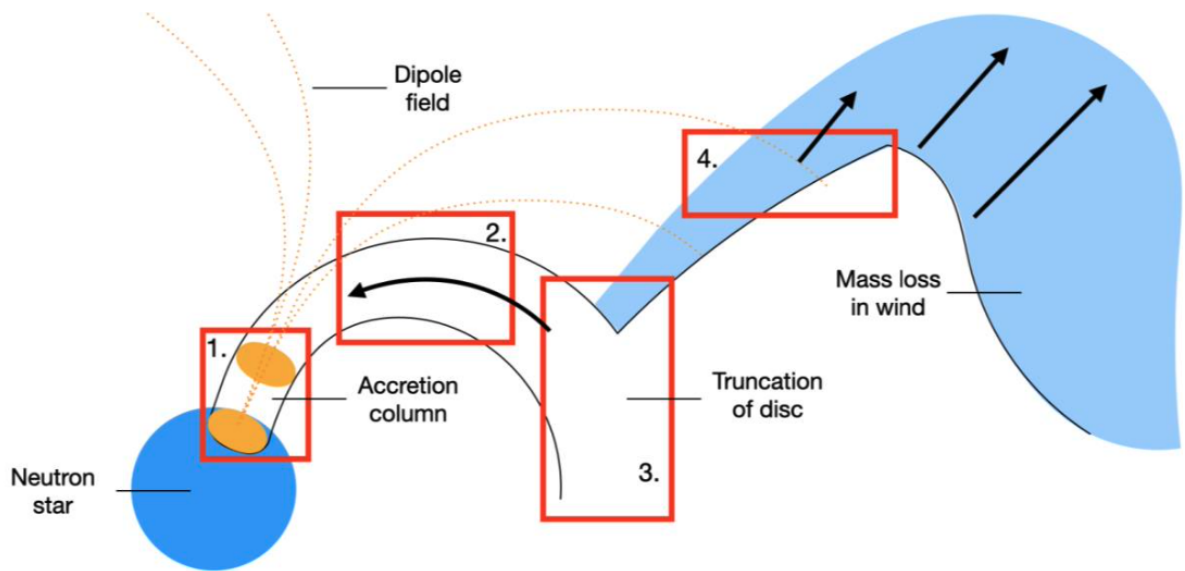
Figure 6.1: Schematic diagram that suggests a series of simulations to study super-Eddington accretion onto a neutron star (figure credit: Matthew Middleton). All four regions with labeled numbers are causally related at different time/length scales. Region 1 represents the strongly magnetized, radiation pressure dominated column of plasma, which has already been simulated in pervious chapters. Region 2 refers to the magnetically confined accretion flow that forms in a curtain-shaped structure along the magnetosphere. Region 3 is near the Alfvén radius, where the magnetic pressure is comparable to the ram pressure. Region 4 can be either the wind from the supercritical disk or the geometrically thin disk further out.

6.1   Variable Inversion with Entropy

The inability to accurately resolve the gas temperature is a common issue in regions with low density and strong magnetic fields across all of our accretion column simulations. In particular, the unresolved gas temperature can be unphysically high and enter

into the radiation source term, leading to spurious emission of radiation. In our previous simulations, we employed multiple ad hoc fixes to ensure the numerical stability. For example, we applied a density cut to limit the Compton scattering process, which alleviates the noise introduced by artificially high temperature of the gas. However, none of those temporary remedies can robustly and fundamentally solve the problem.

In Appendix C, we demonstrate that the selection of the conservative variables can significantly alter the performance of the variable inversion in the regime of neutron star column accretion. The failure of resolving the gas temperature is essentially caused by the inaccurate conservative variables. In our numerical tests (for details see section C.3), the variable inversion algorithm in most unphysical regions are actually numerically converged. It turns out that in strong magnetic field regime, any numerical noise in conservative density, energy, and magnetic fields can be amplified in the gas pressure by a large factor (approximately from 10^6 to 10^8 in the numerical tests in section C.3). Such numerical noise can be easily produced by e.g. the truncation errors of the cell-centered magnetic field, the discretization of the radiation angles, etc.

To address this issue, we propose a direct evaluation of the gas temperature from the first law of thermodynamics, which naturally avoid the coupling of the gas thermal energy and the magnetic energy. Therefore, we need to update the total entropy separately using the entropy equation in addition to the original conservative laws. The detail reasoning can be found in section C.1. The variable inversion algorithm with the total entropy is summarized in section C.2, which corrects some typos in Beckwith & Stone (2011). Note that our approach is not to replace the total energy equation with the entropy equation. This is because the numerical performance of the total energy equation near the shock is expected to be inherently better than using the total entropy equation, mainly due to the jump condition. Instead, we only use the total entropy to fix the unphysical gas temperature at each time step.

165

6.2   Dipole Coordinate System

The gas near a strongly magnetized neutron star is confined to only move along the field lines. Hence, a dipole coordinate system is more intrinsic in terms of simulating the gas motion in a strong dipole magnetic field. In dipolar grids, we can guarantee the high accuracy of the variable inversion to resolve the gas temperature, which is essential in the neutron star column accretion that is radiation pressure dominated and has strong magnetic field. Another advantage of the dipole coordinates is to avoid the numerical truncation errors from the reconstruction of the magnetic field at the cell center. When the magnetic field lines are not aligned with the grids, such truncation errors can be significant in the strong magnetic field regime, which can artificially heat the gas. Therefore, we plan to adopt the dipole coordinate system in the future for more global simulations. A typical dipole coordinate system (p, q, ϕ) can be summarized in the spherical coordinates (r, θ, ϕ) as follows

$$p = -r^{-2n} \cos^n \theta \quad , \tag{6.1a}$$

$$q = r^{-\frac{m}{2}} \sin^m \theta \quad , \tag{6.1b}$$

$$\phi = \phi \quad , \tag{6.1c}$$

where the indices n and m are free parameters to choose. A more general dipole coordinate system can be expressed as

$$\tilde{p} = O_p(p) \quad , \tag{6.2a}$$

$$\tilde{q} = O_q(q) \quad , \tag{6.2b}$$

$$\phi = \phi \quad , \tag{6.2c}$$

where the operators $O_p(p)$ and $O_q(q)$ require to be invertible and differentiable. The detail derivation of above dipole coordinate systems (6.1) and (6.2) can be found in Appendix D. In section 6.2.1, we summarize the operations in dipolar geometry for the numerical implementation. In section 6.2.2, we briefly discuss how to select a proper dipole coordinate system for different objectives.

6.2.1   Numerical Implementation of Dipole Coordinate System

In this section, we present a summary of the necessary definitions and operations in the dipole coordinate system for the numerical implementation. The detail derivations can be found in section D.3. Since the inverse of dipolar coordinates to spherical coordinates is non-trivial, it is more convenient to express the dipolar operations in spherical coordinates. However, it is important to note that the actual numerical computation still updates the conservative quantities in the dipolar basis.

We start with the scale factors of the given dipolar coordinate system (6.1).

$$h_p = \frac{1}{|n|\sqrt{1+3\cos^2\theta}} \frac{r^{2n+1}}{|\cos\theta|^{n-1}} \quad , \tag{6.3a}$$

$$h_q = \frac{2}{|m|\sqrt{1+3\cos^2\theta}} \frac{r^{\frac{m+2}{2}}}{(\sin\theta)^{m-1}} \quad , \tag{6.3b}$$

$$h_\phi = r\sin\theta \quad . \tag{6.3c}$$

where $r(p,q)$ and $\theta(p,q)$ can be solved via a quartic equation (D.15). The analytical expression for its root that is required for the coordinate transformation is given by Swisdak (2006), which has been numerically tested to be stable and accurate in section D.2.

Here, we summarize the dipole coordinates as a function of spherical coordinates below:

$$
\text{if } q \neq 0 \qquad\qquad\qquad\qquad \text{if } q = 0
$$

$$
\begin{cases}
r = uq^{-\frac{2}{m}} \\[2mm]
\theta = \begin{cases} \arcsin u^{\frac{1}{2}} & , \text{if } p < 0 \\[2mm] \pi - \arcsin u^{\frac{1}{2}} & , \text{if } p > 0 \end{cases} \\[4mm]
\phi = \phi
\end{cases}
\qquad
\begin{cases}
r = |p|^{-\frac{1}{2n}} \\[2mm]
\theta = \begin{cases} 0 & , \text{if } p < 0 \\[2mm] \pi & , \text{if } p > 0 \end{cases} \\[4mm]
\phi = \phi
\end{cases}
\tag{6.4}
$$

where

$$
u(p,q) = \frac{4\mathbb{U}}{(1+\mathbb{U})(1+\sqrt{2\mathbb{U}-1})} \quad , \qquad
\mathbb{U} = \frac{1}{2}\left(\frac{\mathbb{A}^2 + \mathbb{A}\mathbb{B} + \mathbb{B}^2}{\mathbb{B}}\right)^{\frac{3}{2}} \quad ,
$$

$$
\mathbb{A} = \left(\frac{256}{27}\mathbb{C}\right)^{\frac{1}{3}} \quad , \qquad
\mathbb{B} = \left(1 + \sqrt{1 + \frac{256}{27}\mathbb{C}}\right)^{\frac{2}{3}} \quad ,
\tag{6.5}
$$

$$
\mathbb{C} = p^{\frac{2}{n}} q^{-\frac{8}{m}} \quad .
$$

The differential area and volume in dipole geometry are

$$
d\sigma_{pq} = h_p h_q \, dpdq \quad ,
\tag{6.6a}
$$

$$
d\sigma_{p\phi} = h_p h_\phi \, dpd\phi \quad ,
\tag{6.6b}
$$

$$
d\sigma_{q\phi} = h_q h_\phi \, dqd\phi \quad ,
\tag{6.6c}
$$

$$
d\tau = h_p h_q h_\phi \, dpdqd\phi \quad .
\tag{6.6d}
$$

The area and volume of dipolar grids can then be numerically integrated to specify area-weighted and volume-weighted variables. To solve the conservation laws, we also need to specify the geometric source terms, which can be obtained from the explicit form of the

tensor divergence in the dipole coordinates.

$$(\boldsymbol{\nabla} \cdot \mathbf{T})_p = \boldsymbol{\nabla} \cdot (\mathrm{T}_{pp}\hat{\boldsymbol{p}} + \mathrm{T}_{qp}\hat{\boldsymbol{q}} + \mathrm{T}_{\phi p}\hat{\boldsymbol{\phi}}) + \mathbb{C}_{\mathrm{T}1}\mathrm{T}_{pq} - \mathbb{C}_{\mathrm{T}2}\mathrm{T}_{qq} - \mathbb{C}_{\mathrm{T}3}\mathrm{T}_{\phi\phi} \quad , \tag{6.7a}$$

$$(\boldsymbol{\nabla} \cdot \mathbf{T})_q = \boldsymbol{\nabla} \cdot (\mathrm{T}_{pq}\hat{\boldsymbol{p}} + \mathrm{T}_{qq}\hat{\boldsymbol{q}} + \mathrm{T}_{\phi q}\hat{\boldsymbol{\phi}}) + \mathbb{C}_{\mathrm{T}2}\mathrm{T}_{qp} - \mathbb{C}_{\mathrm{T}1}\mathrm{T}_{pp} - \mathbb{C}_{\mathrm{T}4}\mathrm{T}_{\phi\phi} \quad , \tag{6.7b}$$

$$(\boldsymbol{\nabla} \cdot \mathbf{T})_\phi = \boldsymbol{\nabla} \cdot (\mathrm{T}_{p\phi}\hat{\boldsymbol{p}} + \mathrm{T}_{q\phi}\hat{\boldsymbol{q}} + \mathrm{T}_{\phi\phi}\hat{\boldsymbol{\phi}}) + \mathbb{C}_{\mathrm{T}3}\mathrm{T}_{\phi p} + \mathbb{C}_{\mathrm{T}4}\mathrm{T}_{\phi q} \quad , \tag{6.7c}$$

$$\text{where} \quad \begin{cases} \mathbb{C}_{\mathrm{T}1} = \left[2n\left(\dfrac{\cos\theta}{|\cos\theta|} - 1\right) - \left(2\dfrac{\cos\theta}{|\cos\theta|} + 1\right) + \dfrac{6\cos^2\theta}{1 + 3\cos^2\theta} \right] \dfrac{|m|}{m} \dfrac{\sin\theta}{(1 + 3\cos^2\theta)^{\frac{1}{2}}} \dfrac{1}{r} \\[3mm] \mathbb{C}_{\mathrm{T}2} = 6\dfrac{|n|}{n} \dfrac{\cos\theta(1 + \cos^2\theta)}{(1 + 3\cos^2\theta)^{\frac{3}{2}}} \left(\dfrac{|\cos\theta|}{\cos\theta}\right)^{n-1} \dfrac{1}{r} \\[3mm] \mathbb{C}_{\mathrm{T}3} = 3\dfrac{|n|}{n} \left(\dfrac{|\cos\theta|}{\cos\theta}\right)^{n-1} \dfrac{\cos\theta}{(1 + 3\cos^2\theta)^{\frac{1}{2}}} \dfrac{1}{r} \\[3mm] \mathbb{C}_{\mathrm{T}4} = \dfrac{|m|}{m} \dfrac{3\cos^2\theta - 1}{\sin\theta(1 + 3\cos^2\theta)^{\frac{1}{2}}} \dfrac{1}{r} \end{cases} . \tag{6.7d}$$

For the generalized dipolar coordinates (6.2), we just need to replace the scale factors with

$$h_{\tilde{p}} = h_p/|O'_p| \quad , \tag{6.8a}$$

$$h_{\tilde{q}} = h_q/|O'_q| \quad . \tag{6.8b}$$

The divergence of the tensor can be then adjusted as

$$(\boldsymbol{\nabla} \cdot \mathbf{T})_{\tilde{p}} = \boldsymbol{\nabla} \cdot (\mathrm{T}_{\tilde{p}\tilde{p}}\hat{\boldsymbol{p}} + \mathrm{T}_{\tilde{q}\tilde{p}}\hat{\boldsymbol{q}} + \mathrm{T}_{\phi\tilde{p}}\hat{\boldsymbol{\phi}}) + \mathbb{C}_q\mathbb{C}_{\mathrm{T}1}\mathrm{T}_{\tilde{p}\tilde{q}} - \mathbb{C}_p\mathbb{C}_{\mathrm{T}2}\mathrm{T}_{\tilde{q}\tilde{q}} - \mathbb{C}_p\mathbb{C}_{\mathrm{T}3}\mathrm{T}_{\phi\phi} \tag{6.9a}$$

$$(\boldsymbol{\nabla} \cdot \mathbf{T})_{\tilde{q}} = \boldsymbol{\nabla} \cdot (\mathrm{T}_{\tilde{p}\tilde{q}}\hat{\boldsymbol{p}} + \mathrm{T}_{\tilde{q}\tilde{q}}\hat{\boldsymbol{q}} + \mathrm{T}_{\phi\tilde{q}}\hat{\boldsymbol{\phi}}) + \mathbb{C}_p\mathbb{C}_{\mathrm{T}2}\mathrm{T}_{\tilde{q}\tilde{p}} - \mathbb{C}_q\mathbb{C}_{\mathrm{T}1}\mathrm{T}_{\tilde{p}\tilde{p}} - \mathbb{C}_q\mathbb{C}_{\mathrm{T}4}\mathrm{T}_{\phi\phi} \tag{6.9b}$$

$$(\boldsymbol{\nabla} \cdot \mathbf{T})_\phi = \boldsymbol{\nabla} \cdot (\mathrm{T}_{\tilde{p}\phi}\hat{\boldsymbol{p}} + \mathrm{T}_{\tilde{q}\phi}\hat{\boldsymbol{q}} + \mathrm{T}_{\phi\phi}\hat{\boldsymbol{\phi}}) + \mathbb{C}_{\mathrm{T}3}\mathrm{T}_{\phi\tilde{p}} + \mathbb{C}_{\mathrm{T}4}\mathrm{T}_{\phi\tilde{q}} \tag{6.9c}$$

where $\mathbb{C}_p = |O'_p|/O'_p$ and $\mathbb{C}_q = |O'_q|/O'_q$.

6.2.2   How to Select an Appropriate Dipole Coordinate System

There are many choices of orthogonal dipolar basis (e.g. Kageyama et al. 2006; Swisdak 2006). All of them can be recovered by our generalized dipolar coordinates (6.2) given the specific selections of n, m, O_p and O_q. In Kageyama et al. (2006), their three dipole coordinate systems can be recovered by taking

$$
\begin{aligned}
(n, m, O_p, O_q) &= (1, 2, p, q) & &\implies (\mu, \chi, \phi) \\
(n, m, O_p, O_q) &= \left(\frac{1}{2}, 2, p, q\right) & &\implies (\mu', \chi, \phi) \\
(n, m, O_p, O_q) &= \left(1, 2, \frac{\operatorname{arcsinh}(a_p p)}{\operatorname{arcsinh}(a_p)}, q\right) & &\implies (\psi, \chi, \phi)
\end{aligned}
\tag{6.10}
$$

,

where a_p is a tuning parameter to redistribute the grid spacing of p. The coordinate systems (μ, χ, ϕ), (μ', χ, ϕ) and (ψ, χ, ϕ) here are consistent with the definitions used in Kageyama et al. (2006). The coordinate system used in Swisdak (2006) can be recovered by taking $n = 1$, $m = -2$, $O_p = -p$ and $O_q = q$ in our generalized coordinates.

There are many ways to construct orthogonal dipolar basis for different purpose by selecting suitable n, m, O_p and O_q. The principle of tuning these free parameters is to find a proper grid distribution for the simulation domain. Therefore, we first need to understand how these parameters and operators change the grid spacing. Given (6.1) and (6.3), we know where is the singularity and how the grid scale changes as functions of r and θ, which can be summarized as below:

1. To have a complete domain of $0 < \theta < \pi$, (6.1) and (6.3) requires an odd positive integer $n \leq 1$, which forces $n = 1$. However, there is no such restriction for a hemisphere, e.g. $\theta \in (0, \pi/2)$ or $(\pi/2, \pi)$.

2. If $\theta \in \{0, \pi\}$ is included, (6.1) and (6.3) would require $0 < m \leq 1$ and problem has to be 2D without ϕ because the geometric source terms associated with $\mathrm{T}_{\phi\phi}$ would

blow up according to (6.7).

3. The grid spacing is more concentrated near the pole given larger n and smaller m, and vice versa.

4. According to (6.2) and (6.8), operators O_p and O_q need to be bijective (invertible) and differentiable. Note that O_p and O_q do not need to be smooth everywhere since they are only required to be differentiable at cell center and faces.

5. Operators O_p and O_q serve as the redistribution functions of p and q, respectively. Since the dipolar grids in general are diluted far from the poles, we usually want O_p and O_q to be steeper near 0 and flatter towards $\pm\infty$, such as the ArcSinh function used in Kageyama et al. (2006).

Here, we provide two examples to illustrate how to select appropriate dipole coordinate systems. Note that we uniformly sample the value of $\tilde{p}$ and $\tilde{q}$ in all the examples. The first example is a typical accretion column on the northern hemisphere of a neutron star, where the length unit is in neutron star radius $R_\star$. The domain of the column is set via $z|_{\theta=0} \in [R_\star, 2.5R_\star]$ and $\theta|_{z=R_\star} \in [0, 0.25]$. We adopt $(n, m, O_p, O_q) = (1, 2, p, q)$ as our fiducial version. We first keep the same n and m and use

$$O_p = \frac{\text{arcsinh}(a_p p)}{\text{arcsinh}(a_p)} \quad \text{and} \quad O_q = \frac{\text{arcsinh}(a_q q)}{\text{arcsinh}(a_q)}$$

in sequence, where the tuning parameters are selected as $a_p = 5 \times 10^4$ and $a_q = 5 \times 10^2$. As shown in the first row of Figure 6.2, p is redistributed away from the pole by O_p and q is redistributed towards the pole by O_q. Similar grid redistribution can be achieved by decreasing n and m as illustrated in the second row of Figure 6.2. To understand the grid distribution, we can check the corresponding scale factors as functions of $z|_{\theta=0}$ and $\theta|_{z=R_\star}$ as shown in Figure 6.3. To construct more uniform distributed grids, we prefer to
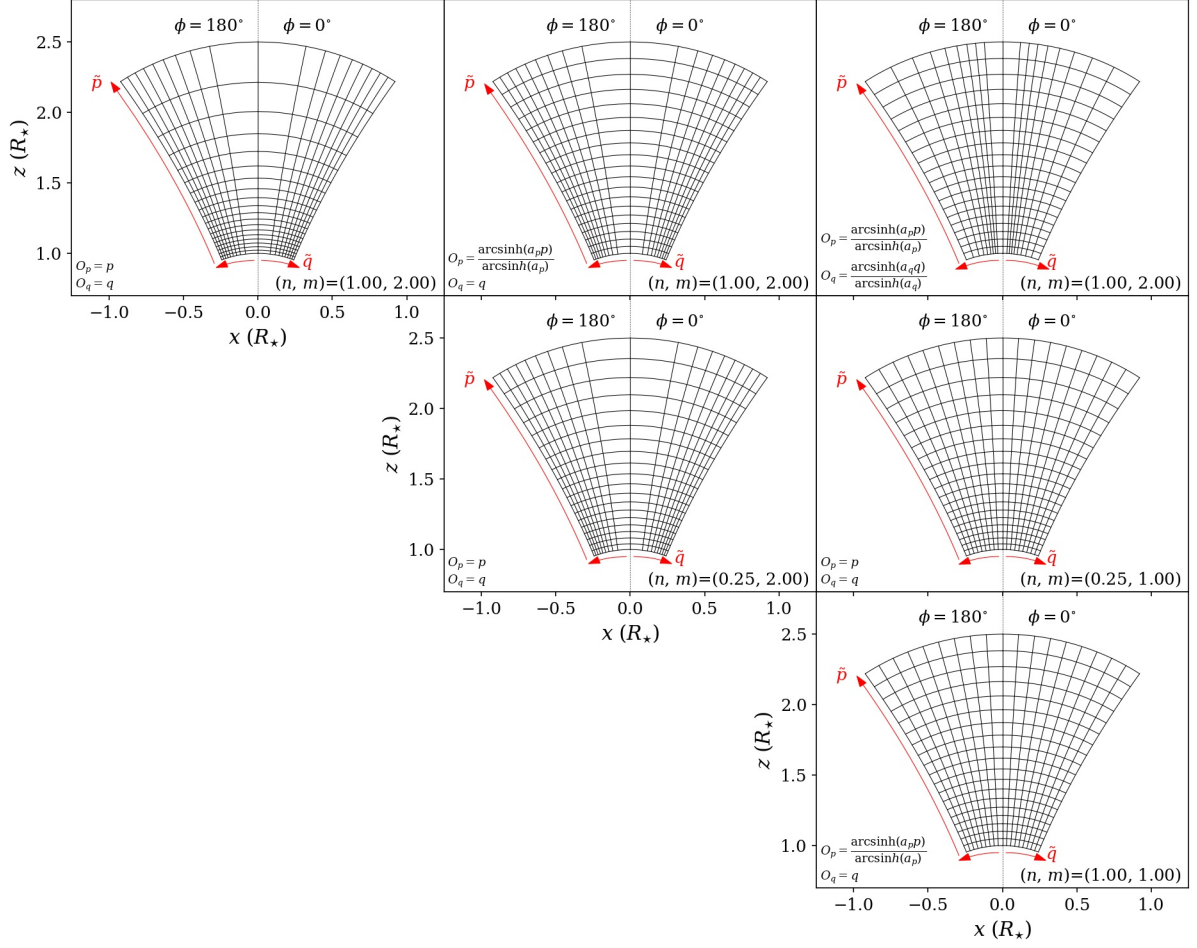
Figure 6.2: The dipolar grid configurations of the neutron star accretion column using different selections of (n, m, O_p, O_q).

have the curve of the scale factor as flat as possible, which explain why the selections of

$$(n, m, O_p, O_q) = \left(1, 1, \frac{\text{arcsinh}(a_p p)}{\text{arcsinh}(a_p)}, q\right) \text{ and } (n, m, O_p, O_q) = (0.25, 1, p, q)$$

as shown in the last two panels in the third column of Figure 6.2 have more uniform grid spacing.

The second example is for more global problems, such as a neutron star accretion curtain. Similar example are also illustrated in Kageyama et al. (2006). The grids are set by $\theta \in [20°, 40°]$ on the surface of northern hemisphere, follow the dipolar field lines
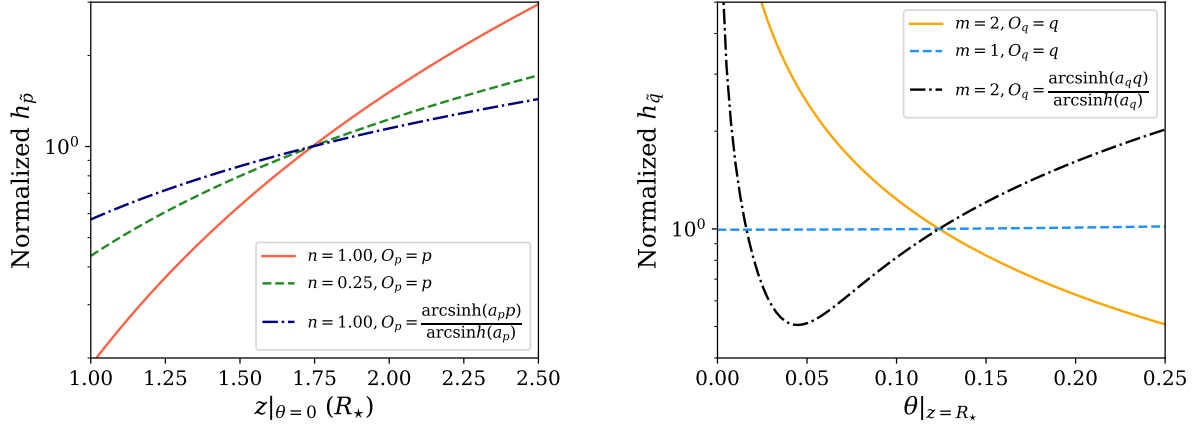
Figure 6.3: The grid scale distribution of the neutron star accretion column. More flat curve corresponds to more uniform grid distribution along the direction of the corresponding coordinate.

and end up on the surface of southern hemisphere. Recall that the domain can only be extended to $\theta \in (0, \pi/2)$ when $n < 1$. If $n < 0$, p diverges to the negative infinity and thus we only expand the domain to $p = -50$ in such case. Similar as the first example, we adopt $(n, m, O_p, O_q) = (1, 2, p, q)$ as our fiducial version. As shown in the first row of Figure 6.4, when we decrease n to 0.5 while keep others the same, p becomes less concentrated near the pole. When n is decreased to -0.5, p becomes more concentrated near the equator (i.e. $\theta = \pi/2$). In the second row of Figure 6.4, the grid spacing of q becomes more uniform when we decrease m as expected. However, in this setup, the main issue of the grid distribution is not in q but p. In the last row of Figure 6.4, we apply the ArcSinh operators to dilute the grids near the pole as in the first example but with the tuning parameters $a_p = a_q = 100$. Although the redistribution of ArcSinh in q resembles directly decreasing m, the redistribution of ArcSinh in p behaves much better than directly decreasing n. Therefore, the selection of

$$(n, m, O_p, O_q) = \left(1, -2, \frac{\mathrm{arcsinh}(a_p p)}{\mathrm{arcsinh}(a_p)}, q\right)$$
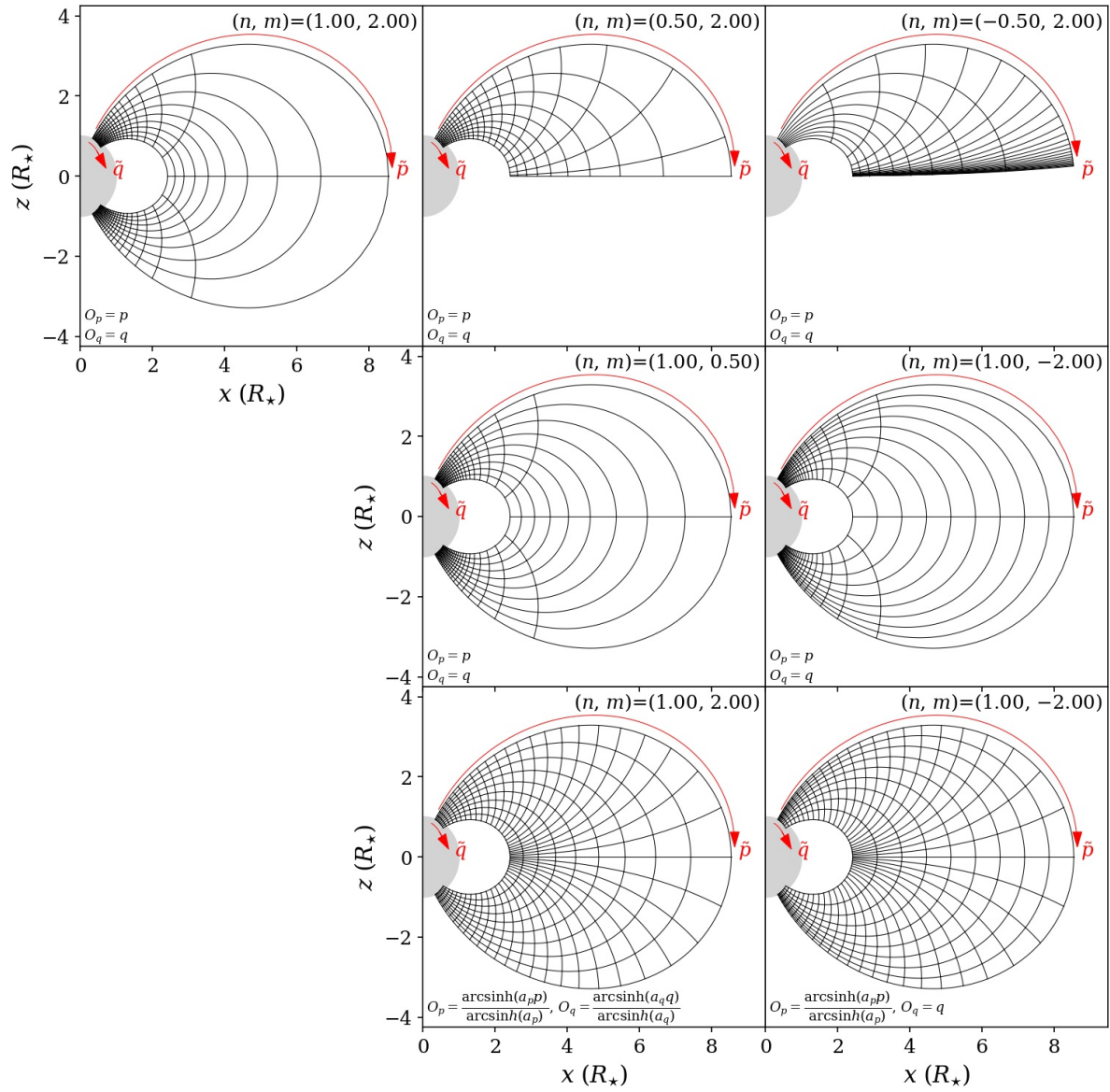
Figure 6.4: The dipolar grid configurations of a more global structure with different selections of (n, m, O_p, O_q).

for our second example is the best pick.

6.3   Solving the Polarized Radiation Transfer

In this section, we describe how the polarized radiation transfer can be solved numerically, which will be implemented as an extension of the current ATHENA++ radiation module in our future plan. The detail derivation of the polarized radiative transfer equation is in Appendix E. Here, we briefly summarize the polarized radiative transfer equation (also see E.32) and how we plan to adopt the operator splitting approach to solve it. Given the Stokes parameter vector $\boldsymbol{S}_\nu = (I_\nu, Q_\nu, U_\nu, V_\nu)^T$ as the basis of the radiation field, the polarized radiative transfer equation can be expressed in form of

$$\frac{1}{c}\frac{\partial \boldsymbol{S}_\nu}{\partial t} + \hat{\boldsymbol{n}} \cdot \nabla \boldsymbol{S}_\nu = \boldsymbol{j}_\nu - \chi_{\nu,\mathrm{a}} \boldsymbol{S}_\nu + \boldsymbol{\Lambda}_{\mathrm{scat,em}} + \boldsymbol{\Lambda}_{\mathrm{scat,ab}} \quad , \tag{6.11}$$

where $\hat{\boldsymbol{n}}$ is the unit vector of the radiation propagation direction and $\boldsymbol{j}_\nu = (j_\nu, 0, 0, 0)^T$ represents the unpolarized thermal emission. With gas density ρ and thermal absorption opacity $\kappa_{\nu,\mathrm{a}}$, the thermal absorption coefficient is defined as $\chi_{\nu,\mathrm{a}} = \rho \kappa_{\nu,\mathrm{a}}$. The emission and absorption terms due to the magnetic Thomson scattering are

$$\boldsymbol{\Lambda}_{\mathrm{scat,em}} = \frac{3}{4} n_e \sigma_T \begin{Bmatrix} \oint \frac{d\Omega'}{4\pi} \left[M_{11} I_\nu(\hat{\boldsymbol{n}}') + M_{12} Q_\nu(\hat{\boldsymbol{n}}') + M_{13} U_\nu(\hat{\boldsymbol{n}}') + M_{14} V_\nu(\hat{\boldsymbol{n}}') \right] \\ \oint \frac{d\Omega'}{4\pi} \left[M_{21} I_\nu(\hat{\boldsymbol{n}}') + M_{22} Q_\nu(\hat{\boldsymbol{n}}') + M_{23} U_\nu(\hat{\boldsymbol{n}}') + M_{24} V_\nu(\hat{\boldsymbol{n}}') \right] \\ \oint \frac{d\Omega'}{4\pi} \left[M_{31} I_\nu(\hat{\boldsymbol{n}}') + M_{32} Q_\nu(\hat{\boldsymbol{n}}') + M_{33} U_\nu(\hat{\boldsymbol{n}}') + M_{34} V_\nu(\hat{\boldsymbol{n}}') \right] \\ \oint \frac{d\Omega'}{4\pi} \left[M_{41} I_\nu(\hat{\boldsymbol{n}}') + M_{42} Q_\nu(\hat{\boldsymbol{n}}') + M_{43} U_\nu(\hat{\boldsymbol{n}}') + M_{44} V_\nu(\hat{\boldsymbol{n}}') \right] \end{Bmatrix} \quad , \tag{6.12a}$$

$$\boldsymbol{\Lambda}_{\mathrm{scat,ab}} = -n_e \begin{pmatrix} \sigma_{11} & \sigma_{12} & 0 & \sigma_{14} \\ \sigma_{12} & \sigma_{11} & 0 & 0 \\ 0 & 0 & \sigma_{11} & 0 \\ \sigma_{14} & 0 & 0 & \sigma_{11} \end{pmatrix} \begin{pmatrix} I_\nu \\ Q_\nu \\ U_\nu \\ V_\nu \end{pmatrix} \quad , \tag{6.12b}$$

where n_e is the electron number density and σ_T is the Thomson scattering cross section. The primed quantities Ω' and $\hat{\boldsymbol{n}}'$ refer to the solid angle and propagation direction of the incident

radiation, respectively. The Muller matrix element M_{ij} can be found in either (E.24) or (E.35), where indices $i, j \in \{1, 2, 3, 4\}$. The cross section σ_{ij} is angle integrated from the Mueller matrix element (see E.27 for explicit expressions).

We adopt the operator splitting approach to solve above polarized radiative transfer equation, following the numerical framework of ATHENA++ radiation module (Jiang et al. 2014; Jiang 2021). In this framework, the advection and source term are solved separately, which allows us to construct an implicit method to update the Stokes parameters. In order to solve the source term, it is necessary to further divide the emission and absorption processes of magnetic Thomson scattering. This is because the angle dependency in the scattering attenuation can cause a large matrix to be inverted. Therefore, the operator splitting can be summarized into three steps. Here, we construct these three parts for our future numerical implementation. For the advection step, we simply follow the original design in ATHENA++ and solve

$$\frac{1}{c}\frac{\partial \boldsymbol{S}_\nu}{\partial t} + \hat{\boldsymbol{n}} \cdot \nabla \boldsymbol{S}_\nu = 0 \quad . \tag{6.13a}$$

For the operator splitting of the source terms, we intentionally construct the following equations

$$\frac{1}{c}\frac{\partial \boldsymbol{S}_\nu}{\partial t} = -\chi_{\nu,\mathrm{a}}(\boldsymbol{S}_\nu - \boldsymbol{J}_\nu) + \boldsymbol{\Lambda}_{\mathrm{scat,ab}} + \boldsymbol{\mathcal{F}}(J, H, K) \quad , \tag{6.13b}$$

$$\frac{1}{c}\frac{\partial \boldsymbol{S}_\nu}{\partial t} = \boldsymbol{j_\nu} - \chi_{\nu,a}\boldsymbol{J}_\nu + \boldsymbol{\Lambda}_{\mathrm{scat,em}} - \boldsymbol{\mathcal{F}}(J, H, K) \quad , \tag{6.13c}$$

where $\boldsymbol{\mathcal{F}} = (\mathcal{F}_I, \mathcal{F}_Q, \mathcal{F}_U, \mathcal{F}_V)^T$ is the complementary term that only depends on the angular moments of Stokes parameters. This is artificially designed to enforce satisfying the first moment equation (i.e. momentum conservation) when solving equation (6.13b) and the zeroth moment equation (i.e. energy conservation) when solving equation (6.13c). Both source terms are designed to be solved implicitly and the detail numerical treatments are discussed in the following sections.

6.3.1 Solving Attenuation Part

The source term equation that includes the attenuation part is

$$
\frac{1}{c}\frac{\partial}{\partial t}
\begin{pmatrix} I_\nu \\ Q_\nu \\ U_\nu \\ V_\nu \end{pmatrix}
= -\chi_{\nu,\mathrm{a}}
\begin{pmatrix} I_\nu - J_{I,\nu} \\ Q_\nu - J_{Q,\nu} \\ U_\nu - J_{U,\nu} \\ V_\nu - J_{V,\nu} \end{pmatrix}
- n_e
\begin{pmatrix}
\sigma_{11} & \sigma_{12} & 0 & \sigma_{14} \\
\sigma_{12} & \sigma_{11} & 0 & 0 \\
0 & 0 & \sigma_{11} & 0 \\
\sigma_{14} & 0 & 0 & \sigma_{11}
\end{pmatrix}
\begin{pmatrix} I_\nu \\ Q_\nu \\ U_\nu \\ V_\nu \end{pmatrix}
+
\begin{pmatrix} \mathcal{F}_I \\ \mathcal{F}_Q \\ \mathcal{F}_U \\ \mathcal{F}_V \end{pmatrix}
, \quad (6.14\mathrm{a})
$$

where

$$
\begin{pmatrix} \mathcal{F}_I \\ \mathcal{F}_Q \\ \mathcal{F}_U \\ \mathcal{F}_V \end{pmatrix}
= \frac{n_e}{4\pi}\int d\Omega
\begin{pmatrix}
\sigma_{11} & \sigma_{12} & 0 & \sigma_{14} \\
\sigma_{12} & \sigma_{11} & 0 & 0 \\
0 & 0 & \sigma_{11} & 0 \\
\sigma_{14} & 0 & 0 & \sigma_{11}
\end{pmatrix}
\begin{pmatrix} I_\nu \\ Q_\nu \\ U_\nu \\ V_\nu \end{pmatrix}
. \quad (6.14\mathrm{b})
$$

The complementary term $\mathcal{F}$ can be explicitly expressed in terms of the zeroth (J), first (H), and second (K) angular moments of Stokes parameters $I_\nu, Q_\nu, U_\nu,$ and V_ν.

$$
\begin{aligned}
\mathcal{F}_I =\, & n_e\sigma_T\left\{ \left[\frac{1}{2}\frac{1+\eta^2}{(1-\eta^2)^2}+\frac{1}{2}\right]J_{I,\nu} + \left[\frac{1}{2}\frac{1+\eta^2}{(1-\eta^2)^2}-\frac{1}{2}\right]K_{I,\nu}^{zz} \right. \\
& \left. + \left[-\frac{1}{2}\frac{1+\eta^2}{(1-\eta^2)^2}+\frac{1}{2}\right]J_{Q,\nu} + \left[\frac{1}{2}\frac{1+\eta^2}{(1-\eta^2)^2}-\frac{1}{2}\right]K_{Q,\nu}^{zz} + \left[\frac{2\eta}{(1-\eta^2)^2}\right]H_{V,\nu}^z \right\},
\end{aligned} \quad (6.15\mathrm{a})
$$

$$
\begin{aligned}
\mathcal{F}_Q =\, & n_e\sigma_T\left\{ \left[-\frac{1}{2}\frac{1+\eta^2}{(1-\eta^2)^2}+\frac{1}{2}\right]J_{I,\nu} + \left[\frac{1}{2}\frac{1+\eta^2}{(1-\eta^2)^2}-\frac{1}{2}\right]K_{I,\nu}^{zz} \right. \\
& \left. + \left[\frac{1}{2}\frac{1+\eta^2}{(1-\eta^2)^2}+\frac{1}{2}\right]J_{Q,\nu} + \left[\frac{1}{2}\frac{1+\eta^2}{(1-\eta^2)^2}-\frac{1}{2}\right]K_{Q,\nu}^{zz} \right\},
\end{aligned} \quad (6.15\mathrm{b})
$$

$$
\mathcal{F}_U = n_e\sigma_T\left\{ \left[\frac{1}{2}\frac{1+\eta^2}{(1-\eta^2)^2}+\frac{1}{2}\right]J_{U,\nu} + \left[\frac{1}{2}\frac{1+\eta^2}{(1-\eta^2)^2}-\frac{1}{2}\right]K_{U,\nu}^{zz} \right\}, \quad (6.15\mathrm{c})
$$

$$
\mathcal{F}_V = n_e\sigma_T\left\{ \left[\frac{2\eta}{(1-\eta^2)^2}\right]H_{I,\nu}^z + \left[\frac{1}{2}\frac{1+\eta^2}{(1-\eta^2)^2}+\frac{1}{2}\right]J_{V,\nu} + \left[\frac{1}{2}\frac{1+\eta^2}{(1-\eta^2)^2}-\frac{1}{2}\right]K_{V,\nu}^{zz} \right\},
$$

$$(6.15\mathrm{d})$$

where $\eta \equiv \omega_{ce}/\omega$ is the ratio between the electron cyclotron frequency $\omega_{ce} = eB_0/(m_e c)$ and radiation angular frequency ω. Here, B_0 is the magnitude of the strong external

radiation field.

Note that U_ν can be directly updated implicitly because it has no off-diagonal component and therefore is intrinsically decoupled from other Stokes parameters. For I_ν, Q_ν, and V_ν, we need to construct a matrix to implicitly update them together. The equation (6.13b) can then be discretized in the following manner:

$$\left(\mathbf{I}(N) + c\Delta t \mathbf{A}_1\right) \boldsymbol{U}_\nu^{n+1} = \boldsymbol{U}_\nu^n \quad , \tag{6.16a}$$

$$\left[\mathbf{I}(3N) + c\Delta t \begin{pmatrix} \mathbf{A}_1 & \mathbf{A}_2 & \mathbf{A}_3 \\ \mathbf{A}_2 & \mathbf{A}_1 & \mathbf{O} \\ \mathbf{A}_3 & \mathbf{O} & \mathbf{A}_1 \end{pmatrix}\right] \begin{pmatrix} \boldsymbol{I}_\nu^{n+1} \\ \boldsymbol{Q}_\nu^{n+1} \\ \boldsymbol{V}_\nu^{n+1} \end{pmatrix} = \begin{pmatrix} \boldsymbol{I}_\nu^n \\ \boldsymbol{Q}_\nu^n \\ \boldsymbol{V}_\nu^n \end{pmatrix} \quad , \tag{6.16b}$$

where $\mathbf{I}$ refers to the identity matrix and N is the total number of the discrete solid angles of radiation. The superscripts n and $n+1$ refer to the current and future time step, respectively. The matrices in above equation are defined as

$$\mathbf{A}_1 = \begin{pmatrix} (1-w_1)\chi_{I,1} & -w_2\chi_{I,2} & \cdots & -w_N\chi_{I,N} \\ -w_1\chi_{I,1} & (1-w_2)\chi_{I,2} & \cdots & -w_N\chi_{I,N} \\ \vdots & \vdots & \ddots & \vdots \\ -w_1\chi_{I,1} & -w_2\chi_{I,2} & \cdots & (1-w_N)\chi_{I,N} \end{pmatrix} \quad , \tag{6.17a}$$

$$\mathbf{A}_2 = \begin{pmatrix} (1-w_1)\chi_{Q,1} & -w_2\chi_{Q,2} & \cdots & -w_N\chi_{Q,N} \\ -w_1\chi_{Q,1} & (1-w_2)\chi_{Q,2} & \cdots & -w_N\chi_{Q,N} \\ \vdots & \vdots & \ddots & \vdots \\ -w_1\chi_{Q,1} & -w_2\chi_{Q,2} & \cdots & (1-w_N)\chi_{Q,N} \end{pmatrix} \quad , \tag{6.17b}$$

$$\mathbf{A}_3 = \begin{pmatrix} (1-w_1)\chi_{V,1} & -w_2\chi_{V,2} & \cdots & -w_N\chi_{V,N} \\ -w_1\chi_{V,1} & (1-w_2)\chi_{V,2} & \cdots & -w_N\chi_{V,N} \\ \vdots & \vdots & \ddots & \vdots \\ -w_1\chi_{V,1} & -w_2\chi_{V,2} & \cdots & (1-w_N)\chi_{V,N} \end{pmatrix} \, , \qquad (6.17c)$$

where

$$\chi_{I,i} = n_e\sigma_{11,i} + \chi_{\nu,a} = n_e\sigma_T \left[\frac{1}{2}(f+1) + \frac{1}{2}(f-1)\hat{n}_{z,i}^2 \right] + \chi_{\nu,a} \quad , \qquad (6.18a)$$

$$\chi_{Q,i} = n_e\sigma_{12,i} = n_e\sigma_T \left[\frac{1}{2}(1-f) + \frac{1}{2}(f-1)\hat{n}_{z,i}^2 \right] \quad , \qquad (6.18b)$$

$$\chi_{V,i} = n_e\sigma_{14,i} = 2n_e\sigma_T g\hat{n}_{z,i} \quad . \qquad (6.18c)$$

Here we define the following auxiliary quantities for convenience:

$$f \equiv \frac{1+\eta^2}{(1-\eta^2)^2} \qquad\qquad g \equiv \frac{\eta}{(1-\eta^2)^2} \quad . \qquad (6.19)$$

Since the determinant of $\mathbf{A}_1$, $\mathbf{A}_2$, and $\mathbf{A}_3$ are all zero, these block matrices are not invertible. However, $\mathbf{I} + c\Delta t\mathbf{A}_1$ is guaranteed to be invertible because it has full rank, where the analytical form can be expressed as

$$\left[(\mathbf{I} + c\Delta t\mathbf{A}_1)^{-1} \right]^{ij} = \frac{\mathcal{C}_\Pi}{|\mathbf{I} + c\Delta t\mathbf{A}_1|(1 + c\Delta t\chi_{I,i})} \left[(1 - \mathcal{C}_\Sigma)\delta_{ij} + \frac{w_j c\Delta t\chi_{I,j}}{1 + c\Delta t\chi_{I,j}} \right] \quad , \qquad (6.20)$$

where $|\mathbf{I} + c\Delta t\mathbf{A}_1|$ is the determinant and the two auxiliary coefficients are defined as

$$\mathcal{C}_\Pi = \prod_{k=1}^{N} (1 + c\Delta t\chi_{I,k}) \, , \qquad\qquad \mathcal{C}_\Sigma = \sum_{k=1}^{N} \frac{w_k c\Delta t\chi_{I,k}}{1 + c\Delta t\chi_{I,k}} \quad . \qquad (6.21)$$

179

The full matrix can be inverted iteratively as follows

$$
\begin{pmatrix}
\mathbf{I} + c\Delta t \mathbf{A}_1 & \mathbf{O} & \mathbf{O} \\
\mathbf{O} & \mathbf{I} + c\Delta t \mathbf{A}_1 & \mathbf{O} \\
\mathbf{O} & \mathbf{O} & \mathbf{I} + c\Delta t \mathbf{A}_1
\end{pmatrix}
\mathbf{V}^n = \mathbf{I} -
\begin{pmatrix}
\mathbf{O} & \mathbf{A}_2 & \mathbf{A}_3 \\
\mathbf{A}_2 & \mathbf{O} & \mathbf{O} \\
\mathbf{A}_3 & \mathbf{O} & \mathbf{O}
\end{pmatrix}
\mathbf{V}^{n-1} \quad , \qquad (6.22)
$$

where the initial guess of $\mathbf{V}$ can simply be

$$
\mathbf{V}^0 =
\begin{pmatrix}
(\mathbf{I} + c\Delta t \mathbf{A}_1)^{-1} & \mathbf{O} & \mathbf{O} \\
\mathbf{O} & (\mathbf{I} + c\Delta t \mathbf{A}_1)^{-1} & \mathbf{O} \\
\mathbf{O} & \mathbf{O} & (\mathbf{I} + c\Delta t \mathbf{A}_1)^{-1}
\end{pmatrix} \quad . \qquad (6.23)
$$

This iterating method can converge quickly when the diagonal components are much larger than the off-diagonal components, which are mostly the cases for the actual simulation where most of the sampled radiation frequency is away from the cyclotron peak.

6.3.2   Solving Emission Part

The source term equation that includes the emission part (see 6.13c) does not contain any Stokes parameters explicitly. Hence, we can integrate it for each angular moment to close the system. Recall the equation (6.13c)) in explicit form

$$
\frac{1}{c}\frac{\partial}{\partial t}
\begin{pmatrix}
I_\nu \\
Q_\nu \\
U_\nu \\
V_\nu
\end{pmatrix}
= j_\nu
\begin{pmatrix}
1 \\
0 \\
0 \\
0
\end{pmatrix}
- \chi_{\nu,a}
\begin{pmatrix}
J_{I,\nu} \\
J_{Q,\nu} \\
J_{U,\nu} \\
J_{V,\nu}
\end{pmatrix}
-
\begin{pmatrix}
\mathcal{F}_I \\
\mathcal{F}_Q \\
\mathcal{F}_U \\
\mathcal{F}_V
\end{pmatrix}
$$

$$+\frac{3}{4}n_e\sigma_T \begin{cases} \oint \frac{d\Omega'}{4\pi}\left[M_{11}I_\nu(\hat{\boldsymbol{n}}') + M_{12}Q_\nu(\hat{\boldsymbol{n}}') + M_{13}U_\nu(\hat{\boldsymbol{n}}') + M_{14}V_\nu(\hat{\boldsymbol{n}}')\right] \\ \oint \frac{d\Omega'}{4\pi}\left[M_{21}I_\nu(\hat{\boldsymbol{n}}') + M_{22}Q_\nu(\hat{\boldsymbol{n}}') + M_{23}U_\nu(\hat{\boldsymbol{n}}') + M_{24}V_\nu(\hat{\boldsymbol{n}}')\right] \\ \oint \frac{d\Omega'}{4\pi}\left[M_{31}I_\nu(\hat{\boldsymbol{n}}') + M_{32}Q_\nu(\hat{\boldsymbol{n}}') + M_{33}U_\nu(\hat{\boldsymbol{n}}') + M_{34}V_\nu(\hat{\boldsymbol{n}}')\right] \\ \oint \frac{d\Omega'}{4\pi}\left[M_{41}I_\nu(\hat{\boldsymbol{n}}') + M_{42}Q_\nu(\hat{\boldsymbol{n}}') + M_{43}U_\nu(\hat{\boldsymbol{n}}') + M_{44}V_\nu(\hat{\boldsymbol{n}}')\right] \end{cases}. \tag{6.24}$$

We can further express each equation in a more specific form:

$$
\begin{aligned}
\frac{1}{c}\frac{\partial I_\nu}{\partial t} = {} & j_\nu - \chi_{\nu,a}J_{I,\nu} + n_e\sigma_T\left\{ \left[-\frac{1}{4}(2f-1) + \frac{3}{4}(f-1)\hat{n}_z^2\right]J_{I,\nu} + \left[-\frac{1}{4}(f-1) - \frac{3}{4}\hat{n}_z^2\right]J_{Q,\nu} \right. \\
& + \left[\frac{1}{4}(f-1) + \frac{3}{4}\hat{n}_z^2\right]\left(K_{I,\nu}^{zz} + K_{Q,\nu}^{zz}\right) + \left[\frac{3}{4}\frac{\hat{n}_x^2 + \hat{n}_y^2\eta^2}{(1-\eta^2)^2}\right]\left(K_{I,\nu}^{xx} + K_{Q,\nu}^{xx}\right) \\
& + \left[\frac{3}{4}\frac{\hat{n}_y^2 + \hat{n}_x^2\eta^2}{(1-\eta^2)^2}\right]\left(K_{I,\nu}^{yy} + K_{Q,\nu}^{yy}\right) + \left[\frac{1}{2}g\left(3\hat{n}_z^2 - 1\right)\right]H_{V,\nu}^z \\
& + \left[\frac{3}{4(1-\eta^2)}\right]\left[2\hat{n}_x\hat{n}_y\left(K_{I,\nu}^{xy} + K_{Q,\nu}^{xy} - P_{Q,\nu}^s - P_{U,\nu}^{zc}\right)\right. \\
& \qquad\qquad + 2\hat{n}_x\hat{n}_z\left(K_{I,\nu}^{xz} + K_{Q,\nu}^{xz} - H_{U,\nu}^y + \eta H_{V,\nu}^x\right) \\
& \qquad\qquad \left.\left. + 2\hat{n}_y\hat{n}_z\left(K_{I,\nu}^{yz} + K_{Q,\nu}^{yz} + H_{U,\nu}^x + \eta H_{V,\nu}^y\right) + \left(\hat{n}_x^2 - \hat{n}_y^2\right)\left(-P_{Q,\nu}^c + P_{U,\nu}^{zs}\right)\right]\right\},
\end{aligned} \tag{6.25a}
$$

$$
\begin{aligned}
\frac{1}{c}\frac{\partial Q_\nu}{\partial t} = {} & -\chi_{\nu,a}J_{Q,\nu} + n_e\sigma_T\left\{ \left[\frac{1}{4}\left(3\hat{n}_z^2 - 1\right)(f-1)\right]J_{I,\nu} + \left[-\frac{1}{2}(f+1) + \frac{3}{4}\left(1-\hat{n}_z^2\right)\right]J_{Q,\nu} \right. \\
& + \left[-\frac{1}{2}(f-1) - \frac{3}{4}\left(1-\hat{n}_z^2\right)\right]\left(K_{I,\nu}^{zz} + K_{Q,\nu}^{zz}\right) + \left[\frac{3}{4}\frac{\hat{n}_x^2 + \hat{n}_y^2\eta^2}{(1-\eta^2)^2}\right]\left(K_{I,\nu}^{xx} + K_{Q,\nu}^{xx}\right) \\
& + \left[\frac{3}{4}\frac{\hat{n}_y^2 + \hat{n}_x^2\eta^2}{(1-\eta^2)^2}\right]\left(K_{I,\nu}^{yy} + K_{Q,\nu}^{yy}\right) + \left[-\frac{3}{2}g\left(1-\hat{n}_z^2\right)\right]H_{V,\nu}^z \\
& + \left[\frac{3}{4(1-\eta^2)}\right]\left[2\hat{n}_x\hat{n}_y\left(K_{I,\nu}^{xy} + K_{Q,\nu}^{xy} - P_{Q,\nu}^s - P_{U,\nu}^{zc}\right)\right. \\
& \qquad\qquad + 2\hat{n}_x\hat{n}_z\left(K_{I,\nu}^{xz} + K_{Q,\nu}^{xz} - H_{U,\nu}^y + \eta H_{V,\nu}^x\right) \\
& \qquad\qquad + 2\hat{n}_y\hat{n}_z\left(K_{I,\nu}^{yz} + K_{Q,\nu}^{yz} + H_{U,\nu}^x + \eta H_{V,\nu}^y\right) + \left(\hat{n}_x^2 - \hat{n}_y^2\right)\left(-P_{Q,\nu}^c + P_{U,\nu}^{zs}\right) \\
& \qquad\qquad + \cos 2\phi\left(-K_{I,\nu}^{xx} + K_{I,\nu}^{yy} - K_{Q,\nu}^{xx} + K_{Q,\nu}^{yy} + 2P_{Q,\nu}^c - 2P_{U,\nu}^{zs}\right) \\
& \qquad\qquad \left.\left. + \sin 2\phi\left(-2K_{I,\nu}^{xy} - 2K_{Q,\nu}^{xy} + 2P_{Q,\nu}^s + 2P_{U,\nu}^{zc}\right)\right]\right\},
\end{aligned} \tag{6.25b}
$$

181

$$\frac{1}{c}\frac{\partial U_\nu}{\partial t} = -\chi_{\nu,a}J_{U,\nu} + n_e\sigma_T\left\{\left[-\frac{1}{2}(f+1)\right]J_{U,\nu} + \left[-\frac{1}{2}(f-1)\right]K_{U,\nu}^{zz}\right.$$

$$+ \left[\frac{3}{4(1-\eta^2)}\right]\left[2\hat{n}_x\left(K_{I,\nu}^{yz} + K_{Q,\nu}^{yz} + H_{U,\nu}^x + \eta H_{V,\nu}^y\right)\right.$$

$$+ 2\hat{n}_y\left(-K_{I,\nu}^{xz} - K_{Q,\nu}^{xz} + H_{U,\nu}^y - \eta H_{V,\nu}^x\right) \tag{6.25c}$$

$$+ \hat{n}_z\sin 2\phi\left(K_{I,\nu}^{xx} - K_{I,\nu}^{yy} + K_{Q,\nu}^{xx} - K_{Q,\nu}^{yy} - 2P_{Q,\nu}^c + 2P_{U,\nu}^{zs}\right)$$

$$\left.\left.+ \hat{n}_z\cos 2\phi\left(-2K_{I,\nu}^{xy} - 2K_{Q,\nu}^{xy} + 2P_{Q,\nu}^s + 2P_{U,\nu}^{zc}\right)\right]\right\},$$

$$\frac{1}{c}\frac{\partial V_\nu}{\partial t} = -\chi_{\nu,a}J_{V,\nu} + n_e\sigma_T\left\{\left[\frac{3}{2}g\right]\hat{n}_z\left(J_{I,\nu} + K_{I,\nu}^{zz} - J_{Q,\nu} + K_{Q,\nu}^{zz}\right)\right.$$

$$+ [-2g]H_{I,\nu}^z + \left[-\frac{1}{2}(f+1)\right]J_{V,\nu} + \left[\frac{3}{2}f\right]\hat{n}_zH_{V,\nu}^z + \left[-\frac{1}{2}(f-1)\right]K_{V,\nu}^{zz}$$

$$+ \left[\frac{3}{4(1-\eta^2)}\right]\left[2\hat{n}_x\left(\eta K_{I,\nu}^{xz} + \eta K_{Q,\nu}^{xz} - \eta H_{U,\nu}^y + H_{V,\nu}^x\right)\right. \tag{6.25d}$$

$$\left.\left.+ 2\hat{n}_y\left(\eta K_{I,\nu}^{yz} + \eta K_{Q,\nu}^{yz} + \eta H_{U,\nu}^x + H_{V,\nu}^y\right)\right]\right\}.$$

Since there are 28 moments to be solved, we have 29 equations in total to complete the closure, where 28 are the moment equations and one is the energy equation that exchange the heat between gas radiation. Here, we list all the moments that needs to be solved, which contain 8 for I_ν:

$$J_{I,\nu}, H_{I,\nu}^z, K_{I,\nu}^{zz}, K_{I,\nu}^{yy}, K_{I,\nu}^{xx}, K_{I,\nu}^{xy}, K_{I,\nu}^{xz}, K_{I,\nu}^{yz} \quad, \tag{6.26a}$$

9 for Q_ν:

$$J_{Q,\nu}, K_{Q,\nu}^{zz}, K_{Q,\nu}^{yy}, K_{Q,\nu}^{xx}, K_{Q,\nu}^{xy}, K_{Q,\nu}^{xz}, K_{Q,\nu}^{yz}, P_{Q,\nu}^c, P_{Q,\nu}^s \quad, \tag{6.26b}$$

6 for U_ν:

$$J_{U,\nu}, K_{U,\nu}^{zz}, H_{U,\nu}^x, H_{U,\nu}^y, P_{U,\nu}^{zc}, P_{U,\nu}^{zs} \quad, \tag{6.26c}$$

and 5 for V_ν:

$$J_{V,\nu}, K_{V,\nu}^{zz}, H_{V,\nu}^z, H_{V,\nu}^y, H_{V,\nu}^x \quad, \tag{6.26d}$$

where the angular moments of I_ν are defined as

$$
J_{I,\nu} = \frac{1}{4\pi} \oint I_\nu d\Omega \qquad H^i_{I,\nu} = \frac{1}{4\pi} \oint \hat{n}^i I_\nu d\Omega \qquad\qquad K^{ij}_{I,\nu} = \frac{1}{4\pi} \oint \hat{n}^i \hat{n}^j I_\nu d\Omega \quad , \quad (6.27a)
$$

$$
P^c_{I,\nu} = \frac{1}{4\pi} \oint \cos 2\phi I_\nu d\Omega \quad P^{zc}_{I,\nu} = \frac{1}{4\pi} \oint \hat{n}_z \cos 2\phi I_\nu d\Omega \quad , \qquad\qquad\qquad (6.27b)
$$

$$
P^s_{I,\nu} = \frac{1}{4\pi} \oint \sin 2\phi I_\nu d\Omega \quad P^{zs}_{I,\nu} = \frac{1}{4\pi} \oint \hat{n}_z \sin 2\phi I_\nu d\Omega \quad . \qquad\qquad\qquad (6.27c)
$$

The angular moments for Q_ν, U_ν, and V_ν are defined similarly, where we simply replace the subscript 'I' with 'Q', 'U', and 'V', respectively, to annotate their corresponding moments. Note that we can use $J = K^{xx} + K^{yy} + K^{zz}$ to eliminate two moment equations. Therefore, we only need to integrate 26 moment equations at each frequency at most to update the emission source terms. After these moments are implicitly updated, we can then use them to update the Stokes parameters. The 7 moment equations for I_ν are

$$
\frac{1}{c}\frac{\partial J_{I,\nu}}{\partial t} = j_\nu - \chi_{\nu,a} J_{I,\nu} \ , \tag{6.28}
$$

$$
\frac{1}{c}\frac{\partial H^z_{I,\nu}}{\partial t} = 0 \ , \tag{6.29}
$$

$$
\begin{aligned}
\frac{1}{c}\frac{\partial K^{zz}_{I,\nu}}{\partial t} =& \frac{1}{3} j_\nu - \left[\frac{1}{3}\chi_{\nu,a} - \frac{1}{30}(f-2)n_e\sigma_T\right] J_{I,\nu} \\
&- \left[\frac{1}{30}(f+2)n_e\sigma_T\right]\left(J_{Q,\nu} - K^{zz}_{I,\nu} - K^{zz}_{Q,\nu}\right) - \left[-\frac{2g}{15}n_e\sigma_T\right] H^z_{V,\nu} \ ,
\end{aligned} \tag{6.30}
$$

$$
\begin{aligned}
\frac{1}{c}\frac{\partial K^{xx}_{I,\nu}}{\partial t} =& \frac{1}{3} j_\nu - \left[\frac{1}{3}\chi_{\nu,a} + \frac{1}{30}(2f - 3\eta g - 1)n_e\sigma_T\right] J_{I,\nu} \\
&- \left[\frac{1}{30}(f - 3\eta g - 1)n_e\sigma_T\right]\left(J_{Q,\nu} - K^{zz}_{I,\nu} - K^{zz}_{Q,\nu}\right) \\
&- \left[\frac{1}{10(1-\eta^2)}n_e\sigma_T\right]\left(-K^{xx}_{I,\nu} - K^{xx}_{Q,\nu} + P^c_{Q,\nu} - P^{zs}_{U,\nu}\right) - \left[\frac{g}{15}n_e\sigma_T\right] H^z_{V,\nu} \ ,
\end{aligned} \tag{6.31}
$$

$$
\frac{1}{c}\frac{\partial K^{xy}_{I,\nu}}{\partial t} = -\frac{n_e\sigma_T}{10(1-\eta^2)}\left(-K^{xy}_{I,\nu} - K^{xy}_{Q,\nu} + P^s_{Q,\nu} + P^{zc}_{U,\nu}\right) \ , \tag{6.32}
$$

$$
\frac{1}{c}\frac{\partial K^{xz}_{I,\nu}}{\partial t} = -\frac{n_e\sigma_T}{10(1-\eta^2)}\left(-K^{xz}_{I,\nu} - K^{xz}_{Q,\nu} + H^y_{U,\nu} - \eta H^x_{V,\nu}\right) \ , \tag{6.33}
$$

$$
\frac{1}{c}\frac{\partial K^{yz}_{I,\nu}}{\partial t} = -\frac{n_e\sigma_T}{10(1-\eta^2)}\left(-K^{yz}_{I,\nu} - K^{yz}_{Q,\nu} - H^x_{U,\nu} - \eta H^y_{V,\nu}\right) \ . \tag{6.34}
$$

The 8 moment equations for Q_ν are

$$\frac{1}{c}\frac{\partial J_{Q,\nu}}{\partial t} = -\left[\chi_{\nu,a} + \frac{f}{4}n_e\sigma_T\right]J_{Q,\nu} - \left[\frac{f}{4}n_e\sigma_T\right]\left(-J_{I,\nu} + 3K_{I,\nu}^{zz} + 3K_{Q,\nu}^{zz}\right)$$
$$- \left[gn_e\sigma_T\right]H_{V,\nu}^z \ , \tag{6.35}$$

$$\frac{1}{c}\frac{\partial K_{Q,\nu}^{zz}}{\partial t} = -\left[\frac{1}{60}(-7f+4)n_e\sigma_T\right]J_{I,\nu} - \left[\frac{1}{3}\chi_{\nu,a} + \frac{1}{60}(7f+4)n_e\sigma_T\right]J_{Q,\nu}$$
$$- \left[\frac{1}{60}(13f-4)n_e\sigma_T\right]\left(K_{I,\nu}^{zz} + K_{Q,\nu}^{zz}\right) - \left[\frac{g}{5}n_e\sigma_T\right]H_{V,\nu}^z \ , \tag{6.36}$$

$$\frac{1}{c}\frac{\partial K_{Q,\nu}^{xx}}{\partial t} = -\left[\frac{1}{60}(-f-6\eta g-2)n_e\sigma_T\right]J_{I,\nu} - \left[\frac{1}{3}\chi_{\nu,a} + \frac{1}{60}(7f-6\eta g-2)n_e\sigma_T\right]J_{Q,\nu}$$
$$- \left[\frac{1}{60}(13f+6\eta g+2)n_e\sigma_T\right]\left(K_{I,\nu}^{zz} + K_{Q,\nu}^{zz}\right) - \left[\frac{2g}{5}n_e\sigma_T\right]H_{V,\nu}^z$$
$$- \left[\frac{n_e\sigma_T}{10(1-\eta^2)}\right]\left(-K_{I,\nu}^{xx} - K_{Q,\nu}^{xx} + P_{Q,\nu}^c - P_{U,\nu}^{zs}\right) \ , \tag{6.37}$$

$$\frac{1}{c}\frac{\partial K_{Q,\nu}^{xy}}{\partial t} = -\frac{3n_e\sigma_T}{20(1-\eta^2)}\left(K_{I,\nu}^{xy} + K_{Q,\nu}^{xy} - P_{Q,\nu}^s - P_{U,\nu}^{zc}\right) \ , \tag{6.38}$$

$$\frac{1}{c}\frac{\partial K_{Q,\nu}^{xz}}{\partial t} = -\frac{n_e\sigma_T}{10(1-\eta^2)}\left(-K_{I,\nu}^{xz} - K_{Q,\nu}^{xz} + H_{U,\nu}^y - \eta H_{V,\nu}^x\right) \ , \tag{6.39}$$

$$\frac{1}{c}\frac{\partial K_{Q,\nu}^{yz}}{\partial t} = -\frac{n_e\sigma_T}{10(1-\eta^2)}\left(-K_{I,\nu}^{yz} - K_{Q,\nu}^{yz} - H_{U,\nu}^x - \eta H_{V,\nu}^y\right) \ , \tag{6.40}$$

$$\frac{1}{c}\frac{\partial P_{Q,\nu}^c}{\partial t} = -\frac{n_e\sigma_T}{4(1-\eta^2)}\left(-J_{I,\nu} + 2K_{I,\nu}^{xx} + K_{I,\nu}^{zz} - J_{Q,\nu} + 2K_{Q,\nu}^{xx} + K_{Q,\nu}^{zz} - 2P_{Q,\nu}^c\right.$$
$$\left. + 2P_{U,\nu}^{zs}\right) \ , \tag{6.41}$$

$$\frac{1}{c}\frac{\partial P_{Q,\nu}^s}{\partial t} = -\frac{n_e\sigma_T}{2(1-\eta^2)}\left(K_{I,\nu}^{xy} + K_{Q,\nu}^{xy} - P_{Q,\nu}^s - P_{U,\nu}^{zc}\right) \ . \tag{6.42}$$

The 6 moment equations for U_ν are

$$\frac{1}{c}\frac{\partial J_{U,\nu}}{\partial t} = -\left[\chi_{\nu,a} + \frac{1}{2}(f+1)n_e\sigma_T\right]J_{U,\nu} - \left[\frac{1}{2}(f-1)n_e\sigma_T\right]K_{U,\nu}^{zz} \ , \tag{6.43}$$

$$\frac{1}{c}\frac{\partial H_{U,\nu}^x}{\partial t} = -\frac{n_e\sigma_T}{2(1-\eta^2)}\left(-K_{I,\nu}^{yz} - K_{Q,\nu}^{yz} - H_{U,\nu}^x - \eta H_{V,\nu}^y\right) \ , \tag{6.44}$$

$$\frac{1}{c}\frac{\partial H_{U,\nu}^y}{\partial t} = -\frac{n_e\sigma_T}{2(1-\eta^2)}\left(K_{I,\nu}^{xz} + K_{Q,\nu}^{xz} - H_{U,\nu}^y + \eta H_{V,\nu}^x\right) \ , \tag{6.45}$$

$$\frac{1}{c}\frac{\partial K_{U,\nu}^{zz}}{\partial t} = -\left[\frac{1}{3}\chi_{\nu,a} + \frac{1}{6}(f+1)n_e\sigma_T\right]J_{U,\nu} - \left[\frac{1}{6}(f-1)n_e\sigma_T\right]K_{U,\nu}^{zz} \ , \tag{6.46}$$

184

$$\frac{1}{c}\frac{\partial P_{U,\nu}^{zc}}{\partial t} = -\frac{n_e\sigma_T}{4(1-\eta^2)}\left(K_{I,\nu}^{xy} + K_{Q,\nu}^{xy} - P_{Q,\nu}^{s} - P_{U,\nu}^{zc}\right) \ , \tag{6.47}$$

$$\frac{1}{c}\frac{\partial P_{U,\nu}^{zs}}{\partial t} = -\frac{n_e\sigma_T}{8(1-\eta^2)}\big(J_{I,\nu} - 2K_{I,\nu}^{xx} - K_{I,\nu}^{zz} + J_{Q,\nu} - 2K_{Q,\nu}^{xx} - K_{Q,\nu}^{zz} + 2P_{Q,\nu}^{c}$$
$$\tag{6.48}$$
$$- 2P_{U,\nu}^{zs}\big) \ ,$$

The 5 moment equations for V_ν are

$$\frac{1}{c}\frac{\partial J_{V,\nu}}{\partial t} = -\left[\chi_{\nu,a} + \frac{1}{2}(f+1)n_e\sigma_T\right]J_{V,\nu} - [2gn_e\sigma_T]\,H_{I,\nu}^{z} - \left[\frac{1}{2}(f-1)n_e\sigma_T\right]K_{V,\nu}^{zz} \ , \tag{6.49}$$

$$\frac{1}{c}\frac{\partial H_{V,\nu}^{z}}{\partial t} = -\left[\frac{g}{2}n_e\sigma_T\right]\left(-J_{I,\nu} - K_{I,\nu}^{zz} + J_{Q,\nu} - K_{Q,\nu}^{zz}\right) - \left[\frac{f}{2}n_e\sigma_T\right]\left(-H_{V,\nu}^{z}\right) \ , \tag{6.50}$$

$$\frac{1}{c}\frac{\partial H_{V,\nu}^{y}}{\partial t} = -\frac{n_e\sigma_T}{2(1-\eta^2)}\left(-\eta K_{I,\nu}^{yz} - \eta K_{Q,\nu}^{yz} - \eta H_{U,\nu}^{x} - H_{V,\nu}^{y}\right) \ , \tag{6.51}$$

$$\frac{1}{c}\frac{\partial H_{V,\nu}^{x}}{\partial t} = -\frac{n_e\sigma_T}{2(1-\eta^2)}\left(-\eta K_{I,\nu}^{xz} - \eta K_{Q,\nu}^{xz} + \eta H_{U,\nu}^{y} - H_{V,\nu}^{x}\right) \ , \tag{6.52}$$

$$\frac{1}{c}\frac{\partial K_{V,\nu}^{zz}}{\partial t} = -\left[\frac{1}{3}\chi_{\nu,a} + \frac{1}{6}(f+1)n_e\sigma_T\right]J_{V,\nu} - \left[\frac{2g}{3}n_e\sigma_T\right]H_{I,\nu}^{z} - \left[\frac{1}{6}(f-1)n_e\sigma_T\right]K_{V,\nu}^{zz} \ . \tag{6.53}$$

The last energy equation is

$$\frac{\rho k_B}{(\gamma-1)\mu m_p}\frac{dT_g}{dt} = -\int\left(j_\nu - \chi_{\nu,a}J_{I,\nu}\right)d\nu d\Omega \ , \tag{6.54}$$

where ρ is gas density and T_g is gas temperature. Constants k_B and m_p refer to Boltzmann constant and proton mass, respectively. The parameter μ is mean molecular weight and γ is the adiabatic index of the gas. Note that for frequency-integrated or single-frequency intensity, we can simply solve a 27×27 matrix for the scattering emission source term to update the radiation intensity. However, for a multi-frequency group, we need to construct a matrix that includes all the moments in the whole frequency range. For example, if we sample N frequencies, we need to solve a $(26N + 1) \times (26N + 1)$ matrix. In a practical manner, we can solve each block matrix in the following sequence: $(j_\nu, J_{I,\nu})$, $(K_{I,\nu}^{zz}, J_{Q,\nu}, K_{Q,\nu}^{zz}, H_{V,\nu}^{z})$, $(K_{I,\nu}^{xx}, K_{Q,\nu}^{xx}, P_{Q,\nu}^{c}, P_{U,\nu}^{zs})$, $(K_{I,\nu}^{xy}, K_{Q,\nu}^{xy}, P_{Q,\nu}^{s}, P_{U,\nu}^{zc})$,

$(K_{I,\nu}^{xz}, K_{Q,\nu}^{xz}, H_{U,\nu}^{y}, H_{V,\nu}^{x})$, $(K_{I,\nu}^{yz}, K_{Q,\nu}^{yz}, H_{U,\nu}^{x}, H_{V,\nu}^{y})$, $(J_{U,\nu}, K_{U,\nu}^{zz})$, $(J_{V,\nu}, H_{I,\nu}^{z}, K_{V,\nu}^{zz})$, where the largest matrix we need to invert is merely 4×4.

Appendix A

Derivation of Photon Bubble Instability

A.1 Conservation Laws in the Newtonian Limit

A radiation-supported and magnetized plasma is unstable in a gravitational field (Arons 1992; Gammie 1998). Here we rederive the dispersion relation for the linear instability, incorporating the effects of radiation viscosity. The numerical simulations presented in this thesis use special relativistic magnetohydrodynamics and a kinetic treatment of the radiation transfer. However, for the linear instability analysis here, it is sufficient to use Newtonian equations with fluid restricted to move along the vertical $(\hat{z})$ magnetic field direction, and to treat the radiation transport within the diffusion approximation. The system is then governed by the following equations:

$$\frac{\partial \rho}{\partial t} + \frac{\partial}{\partial z}(\rho v) = 0 \quad , \tag{A.1a}$$

$$\rho \frac{\partial v}{\partial t} + \rho v \frac{\partial v}{\partial z} = -\frac{\partial P}{\partial z} - \rho g + \frac{\partial}{\partial x}\left(\eta \frac{\partial v}{\partial x}\right) + \frac{\partial}{\partial z}\left[\left(\frac{4\eta}{3} + \zeta\right)\frac{\partial v}{\partial z}\right] \quad , \tag{A.1b}$$

187

$$\frac{\partial P}{\partial t} + v\frac{\partial P}{\partial z} + \frac{4}{3}P\frac{\partial v}{\partial z} = -\frac{1}{3}\frac{\partial F_{r,x}}{\partial x} - \frac{1}{3}\frac{\partial F_{r,z}}{\partial z} \quad , \tag{A.1c}$$

$$F_{r,x} = -\frac{c}{\rho\kappa}\frac{\partial P}{\partial x} \quad , \tag{A.1d}$$

$$F_{r,z} = -\frac{c}{\rho\kappa}\frac{\partial P}{\partial z} \quad . \tag{A.1e}$$

We approximate the total thermal pressure $P \simeq P_r$ as being entirely due to radiation. The horizontal radiation flux $F_{r,x}$ is perpendicular to the magnetic field and the vertical radiation flux $F_{r,z}$ is along the magnetic field. We also assume a constant vertical gravitational acceleration g, and assume an isotropic opacity κ that only depends on density and gas pressure. We have included shear (η) and bulk (ζ) viscosity effects in the momentum equation (A.1b), but have neglected viscous dissipation terms in the energy equation (A.1c) as these would be nonlinear (second order) in the velocity. Arons (1992) also considered viscosity in their original analysis of the photon bubble instability, but only included the $4\eta/3$ term (cf. equation (4) from that paper). They neglected the shear term arising from horizontal ($\hat{\boldsymbol{x}}$) gradients in the vertical velocity v. We find that these prove to be very important in the slow diffusion regime, where the most unstable modes have much larger horizontal gradients than vertical gradients.

In the static, plane-parallel equilibrium, mass conservation (A.1a) and energy conservation (A.1c) become trivial, leaving us with

$$\frac{\partial P_0}{\partial z} = -\rho_0 g \quad , \tag{A.2a}$$

$$F_{r,x0} = 0 \quad , \tag{A.2b}$$

$$F_{r,z0} = \frac{cg}{\kappa_0} \quad , \tag{A.2c}$$

where the subscript '0' refers to the equilibrium state. Linear perturbations about this

equilibrium then evolve according to

$$\frac{\partial \delta \rho}{\partial t} + \frac{\partial \rho_0}{\partial z} \delta v + \rho_0 \frac{\partial \delta v}{\partial z} = 0 \quad , \tag{A.3a}$$

$$\rho_0 \frac{\partial \delta v}{\partial t} = -\frac{\partial \delta P}{\partial z} - \delta \rho g + \frac{\partial}{\partial x}\left(\eta_0 \frac{\partial \delta v}{\partial x} \right) + \frac{\partial}{\partial z}\left[\left(\frac{4\eta_0}{3} + \zeta_0 \right) \frac{\partial \delta v}{\partial z} \right] \quad , \tag{A.3b}$$

$$\frac{\partial \delta P}{\partial t} + \delta v \frac{\partial P_0}{\partial z} + \frac{4}{3} P_0 \frac{\partial \delta v}{\partial z} = -\frac{1}{3}\frac{\partial \delta F_{r,x}}{\partial x} - \frac{1}{3}\frac{\partial \delta F_{r,z}}{\partial z} \quad , \tag{A.3c}$$

$$\delta F_{r,x} = -\frac{c}{\rho_0 \kappa_0} \frac{\partial \delta P}{\partial x} \quad , \tag{A.3d}$$

$$\delta F_{r,z} = -\frac{c}{\rho_0 \kappa_0} \frac{\partial \delta P}{\partial z} - \frac{cg}{\kappa_0}\left[(1 + \Theta_\rho)\frac{\delta \rho}{\rho_0} + \frac{1}{4}\Theta_T \frac{\delta P}{P_0} \right] \quad , \tag{A.3e}$$

where 'δ' in front of the variables refers to an Eulerian perturbation, and we define the two logarithmic derivatives of opacity as

$$\Theta_\rho = \frac{\partial \ln \kappa_0}{\partial \ln \rho_0} \quad \text{and} \quad \Theta_T = \frac{\partial \ln \kappa_0}{\partial \ln T_0} \quad . \tag{A.3f}$$

In what follows, we define some auxiliary parameters, most of which are consistent with the definitions used in Arons (1992) and Gammie (1998).

$$
\begin{aligned}
c_r^2 &= \frac{4P_0}{3\rho_0} \quad , & h &= \frac{c_r^2}{g} \quad , \\
N_0 &= \frac{c_r}{h} \quad , & M_0 &= \frac{c}{\rho_0 \kappa_0 h c_r} \quad , \\
k^2 &= k_x^2 + k_z^2 \quad , & \mu &= \frac{k_z}{k} \quad ,
\end{aligned}
\tag{A.4}
$$

where c_r is the radiation sound speed and h is the corresponding scale height. N_0 is the radiation sound crossing frequency, where N_0^{-1} represents the time it takes to cross the scale height h with the radiation sound speed c_r. M_0 is the Mach number of radiation diffusion, where $c/(\rho_0 \kappa_0 h)$ is the radiation diffusion speed. We are in the slow diffusion regime if $M_0 \ll 1$. After the system is perturbed, we have the total wavenumber k, the

horizontal wavenumber k_x and the vertical wavenumber k_z, where μ is the cosine of the angle θ between the directions of wave propagation ($\hat{\boldsymbol{k}}$) and magnetic field ($\hat{\boldsymbol{z}}$).

A.2 Dispersion Relation

Because the equilibrium is static and homogeneous in the horizontal direction, we can, without loss of generality, assume that all perturbations depend on x and time t according to $\propto \exp[i(k_x x - \omega t)]$. Equations (A.3a)-(A.3e) can then be combined to form two coupled ordinary differential equations in z:

$$-\omega^2 \delta v = \frac{i\omega}{\rho_0} \frac{d\delta P}{dz} + \frac{g}{\rho_0} \frac{d}{dz}(\rho_0 \delta v) - \frac{i\omega}{\rho_0} \frac{d}{dz}\left[\left(\frac{4\eta_0}{3} + \zeta_0\right)\frac{d\delta v}{dz}\right] + \frac{i\omega\eta_0}{\rho_0}k_x^2 \delta v \quad , \tag{A.5a}$$

$$\begin{aligned}
-i\omega\delta P = \rho_0 g \delta v - \rho_0 c_r^2 \frac{d\delta v}{dz} - \frac{k_x^2 c}{3\rho_0 \kappa_0}\delta P \\
- i\frac{c}{3\omega}\frac{d}{dz}\left[\frac{i\omega}{\rho_0 \kappa_0}\frac{d\delta P}{dz} + \frac{g}{\rho_0 \kappa_0}(1 + \Theta_\rho)\frac{d}{dz}(\rho_0 \delta v) + \frac{i\omega g}{4\kappa_0}\Theta_T \frac{\delta P}{P_0}\right] \quad .
\end{aligned} \tag{A.5b}$$

Apart from the neglect of nonlinearities, these equations are exact. In the limit of infinite opacity, where radiative diffusion is negligible, they can be further combined to give an equation for vertical adiabatic sound waves in a viscous, strongly magnetized inhomogeneous medium:

$$\frac{d}{dz}\left(\rho_0 c_r^2 \frac{d\delta v}{dz}\right) + \rho_0 \omega^2 \delta v = i\omega\frac{d}{dz}\left[\left(\frac{4\eta_0}{3} + \zeta_0\right)\frac{d\delta v}{dz}\right] - i\omega\eta_0 k_x^2 \delta v \quad . \tag{A.6}$$

Note that the $(g/\rho_0)d(\rho_0\delta v)/dz$ term on the right hand side of (A.5a) completely cancels when this is done.

For finite opacity, equations (A.5a)-(A.5b) cannot be combined directly, and we are forced to employ a short-wavelength vertical WKB approximation with perturbations having a z-dependence of the form $\exp\left(i\int^z k_z(z')dz'\right)$. We then directly replace all z-

derivatives in equations (A.5a)-(A.5b) with ik_z. In so doing, we continue to maintain the cancellation of the $(g/\rho_0)d(\rho_0\delta v)/dz$ terms that led to (A.6). This treatment of the WKB approximation results in the following cubic dispersion relation

$$
\omega^3 + \left[ik^2\left(\frac{c}{3\rho_0\kappa_0} + V\right) + \frac{\mu kcg\Theta_T}{9\rho_0\kappa_0 c_r^2}\right]\omega^2 - \left[\mu^2 k^2 c_r^2 + \frac{k^3 cV}{3\rho_0\kappa_0}\left(k - \frac{i\mu g\Theta_T}{3c_r^2}\right)\right]\omega
$$
$$
- \frac{cg}{3\rho_0\kappa_0}\left[\mu(1-\mu^2)k^3 - \frac{i}{3}\mu^2 k^2 \frac{g}{c_r^2}\Theta_T - \mu^3 k^3\Theta_\rho\right] = 0 \quad , \tag{A.7}
$$

where the viscous effects are in the quantity V defined as

$$
V \equiv \frac{1}{\rho_0}\left[\mu^2\left(\frac{4\eta_0}{3} + \zeta_0\right) + (1-\mu^2)\eta_0\right]. \tag{A.8}
$$

If we assume a constant opacity (i.e. $\Theta_\rho = \Theta_T = 0$) and neglect viscosity, this is almost the same as the cubic dispersion relation found by Arons (1992), the small differences arising from the difference in our WKB treatment. It also recovers the slow diffusion dispersion relation (36) of Gammie (1998) if we neglect the ω^3 term. In the rapid diffusion regime as $M_0 \to \infty$ (small κ_0), (A.7) also recovers equation (34) of Gammie (1998).

As noted above, Arons (1992) did actually consider radiation viscosity effects on vertical gradients in vertical velocity, and concluded that they would be unimportant for optically thick wavelengths. For isotropic Thomson scattering, the radiation shear viscosity is

$$
\eta_0 = \frac{8P_0}{9\kappa_0\rho_0 c} \tag{A.9}
$$

(Masaki 1971). If we assume comparable bulk viscosity, then $V \sim c_r^2/(\kappa_0\rho_0 c)$, in which case the viscous terms in the dispersion relation (A.7) are all negligible for optically thick wavelengths, in agreement with the assertion of Arons (1992). However, this ignores the angle factor μ. In particular, the horizontal velocity gradients that were neglected in the viscous treatment of Arons (1992) are important in the slow diffusion limit. If we neglect

the ω^3 term and solve the resulting quadratic equation in the slow diffusion limit, we find that the instability growth rate peaks at wavenumber $k = 2\pi/l_{\mathrm{vis}}$, where

$$l_{\mathrm{vis}} = \frac{4\pi}{3\kappa_0\rho_0}\frac{k_x}{k_z} = \frac{4\pi}{3\kappa_0\rho_0}\frac{\sqrt{1-\mu^2}}{\mu}. \tag{A.10}$$

This can be much larger than the wavelength of unit optical depth $(\kappa_0\rho_0)^{-1}$ if $k_x \gg k_z$, i.e. μ is small, and this is precisely the orientation of fastest growing slow diffusion modes.

For the convenience of numerical calculation, we can normalize (A.7) by the radiation sound crossing frequency N_0 as

$$\begin{aligned}
\left(\frac{\omega}{N_0}\right)^3 &+ \left[i(kh)^2\left(\frac{1}{3}M_0 + \frac{V}{hc_r}\right) + \frac{1}{9}\mu(kh)M_0\Theta_T\right]\left(\frac{\omega}{N_0}\right)^2 \\
&- \left[\mu^2(kh)^2 + \frac{1}{3}(kh)^3M_0\left(\frac{V}{hc_r}\right)\left(kh - \frac{i}{3}\mu\Theta_T\right)\right]\left(\frac{\omega}{N_0}\right) \\
&- \frac{1}{3}M_0\left[\mu(1-\mu^2)(kh)^3 - \frac{i}{3}\mu^2(kh)^2\Theta_T - \mu^3(kh)^3\Theta_\rho\right] = 0 \quad .
\end{aligned} \tag{A.11}$$

The dispersion relation (A.11) can be numerically solved in different diffusion regimes as a function of wavenumber and angle. To demonstrate its numerical solution, we adopt a constant opacity for the sake of simplicity. The resulting instability growth rate $\Gamma = \mathrm{Im}\{\omega\}$ is depicted in Figure A.1 for various values of the diffusion parameter M_0. The peak of the instability growth rate shifts towards $90°$ as radiation diffusion becomes slower (smaller M_0) and the instability grows faster as the wavelength becomes shorter, until the viscous scale l_{vis} is reached. All of these characteristics can be found in our numerical simulations of slow-diffusion photon bubble instability (see chapter 2 in detail), which shows the consistency between the linear theory and the simulation. We stress that our simulation algorithm has no explicit radiation viscosity at all. Instead, this comes for free because we are solving the angle-dependent radiative transfer equation. Hence the agreement between the simulations and the analytic theory we have presented
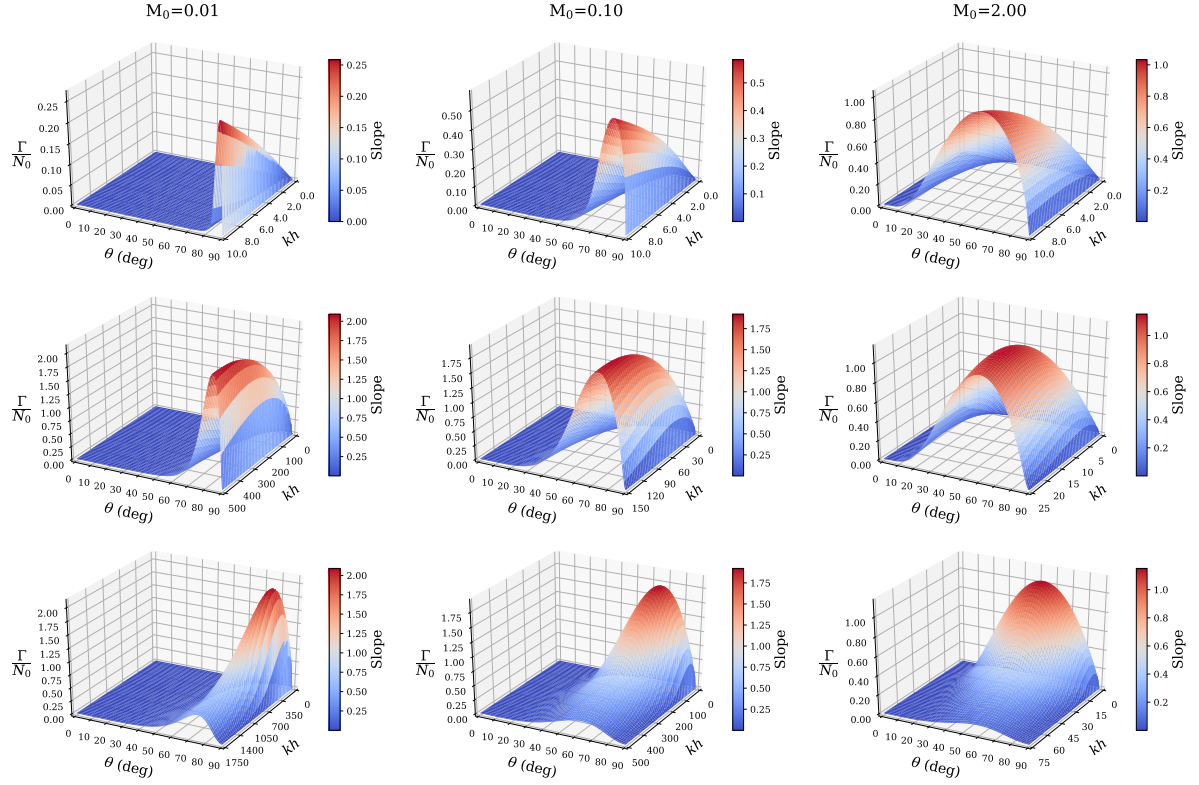
Figure A.1:   Analytical solution of the instability growth rate based on the dispersion relation (A.11), for $c_r/c = 0.05$.

is a nontrivial success.

A.3   Origin of Photon Bubble Instability

We briefly discuss here the physical origin of the photon bubble instability in the slow-diffusion regime, assuming a constant opacity for simplicity and neglecting radiation viscosity whose effect is simply to damp the instability at small scales. A radiation pressure supported medium in a strong vertical magnetic field is subject to the spontaneous development of arbitrary fluctuations in the vertical distribution of density, while still maintaining hydrostatic equilibrium. This is simply because the equilibrium equations (A.2a)-(A.2c) admit any arbitrary vertical density distribution, which then sets the

distribution of vertical radiation pressure gradient. As a result, the linearized equations of motion (A.3a)-(A.3e) admit an exact, zero-frequency static ($\delta v = 0$) mode provided there are no horizontal variations in the perturbations ($k_x = 0$). However, any horizontal variation in the perturbations, as much be present in a neutron star accretion column with finite horizontal width, will introduce a horizontal diffusive flux. This in turn will cause some time-dependence, but if the diffusion is slow, vertical hydrostatic equilibrium can be maintained because the inertia term in the momentum equation will be small. Let us first consider this case.

Neglecting the radiation viscosity and inertia term in the momentum equation so that hydrostatic equilibrium is maintained in the perturbations, adopting a constant opacity in the energy equation, and applying the WKB approximation, the linearized equations (A.3a), (A.3b), (A.3c), (A.3d) and (A.3e) become

$$-i\omega\delta\rho + \frac{\partial\rho_0}{\partial z}\delta v + \rho_0\frac{\partial\delta v}{\partial z} = 0 \quad , \tag{A.12a}$$

$$-i\omega\rho_0\delta v \simeq 0 = -\frac{\partial\delta P}{\partial z} - \delta\rho g \quad , \tag{A.12b}$$

$$-i\omega\delta P + \delta v\frac{\partial P_0}{\partial z} + \frac{4}{3}P_0\frac{\partial\delta v}{\partial z} = -\frac{i}{3}k_x\delta F_x - \frac{1}{3}\frac{\partial\delta F_z}{\partial z} \quad , \tag{A.12c}$$

$$\delta F_x = -\frac{c}{\rho_0\kappa_0}ik_x\delta P \quad , \tag{A.12d}$$

$$\delta F_z = -\frac{c}{\rho_0\kappa_0}\left(\frac{\partial\delta P}{\partial z} + \delta\rho g\right) = -i\frac{c}{\kappa_0}\omega\delta v \simeq 0 \quad . \tag{A.12e}$$

Note that the perturbed vertical flux naturally vanishes after neglecting the inertia term. We can also eliminate the perturbation in radiation pressure using (A.12a) and (A.12b)

$$-i\omega\delta P + \delta v\frac{\partial P_0}{\partial z} = 0 \quad , \tag{A.13a}$$

So the energy equation (A.12c) becomes

$$\frac{4}{3}P_0\frac{\partial\delta v}{\partial z} = -\frac{i}{3}k_x\delta F_x \quad , \tag{A.13b}$$

indicating an equilibrium between adiabatic work and horizontal heat flow. We can then obtain a dispersion relation using equations (A.2a), (A.12d), (A.13a) and (A.13b)

$$4i\frac{P_0}{g}\frac{\partial}{\partial z}\left(\frac{\delta P}{\rho_0}\right)\omega = \frac{c}{\rho_0\kappa_0}\delta Pk_x^2 \quad . \tag{A.14}$$

This dispersion relation indicates that the time-dependence, which is entirely oscillatory, is determined by horizontal diffusion. To summarize, spontaneous density fluctuations can apparently be maintained in vertical hydrostatic equilibrium with slow oscillatory time-dependence driven by horizontal diffusion, provided fluid inertia is negligible.

However, including that small inertia actually drives this mode unstable. If we include the inertia term and apply the WKB approximation in the z-direction, the perturbed quantities can be solved via equations (A.12a), (A.12b), (A.12c), (A.12d) and (A.12e)

$$\delta\rho = -\frac{1}{g}\frac{\partial\delta P}{\partial z} + \left(1 - i\frac{\omega^2}{gk_z} - i\frac{1}{k_z}\frac{\partial\ln\rho_0}{\partial z}\right)^{-1}\frac{\omega^2}{g^2}\delta P \quad , \tag{A.15a}$$

$$\delta v = -\left(1 - i\frac{1}{k_z}\frac{\partial\ln\rho_0}{\partial z}\right)^{-1}\frac{\omega}{\rho_0 gk_z}\frac{\partial\delta P}{\partial z}$$

$$+ \left[\left(1 - i\frac{1}{k_z}\frac{\partial\ln\rho_0}{\partial z}\right)\left(1 - i\frac{\omega^2}{gk_z} - i\frac{1}{k_z}\frac{\partial\ln\rho_0}{\partial z}\right)\right]^{-1}\frac{\omega^3}{\rho_0 g^2 k_z}\delta P \quad , \tag{A.15b}$$

$$\delta F_x = -\frac{c}{\rho_0\kappa_0}\frac{k_x}{k_z}\frac{\partial\delta P}{\partial z} \quad , \tag{A.15c}$$

$$\delta F_z = -\frac{c}{\rho_0\kappa_0}\left(\frac{\partial\delta P}{\partial z} + \delta\rho g\right) = -i\frac{c}{\kappa_0}\omega\delta v \quad . \tag{A.15d}$$

We already know that the frequency without the inertia term is real (see (A.14)). To explore the instability caused by the inertia term, we first need to define the frequency

and perturbations of the mode without the inertia term

$$\omega^{(0)} = -\left(1 + i\frac{1}{k_z}\frac{\partial \ln \rho_0}{\partial z}\right)^{-1}\frac{cg}{4\kappa_0 P_0}\frac{k_x^2}{k_z} \quad , \tag{A.16a}$$

$$\delta\rho^{(0)} = -\frac{1}{g}\frac{\partial \delta P}{\partial z} \quad , \tag{A.16b}$$

$$\delta v^{(0)} = -\left(1 - i\frac{1}{k_z}\frac{\partial \ln \rho_0}{\partial z}\right)^{-1}\frac{\omega^{(0)}}{\rho_0 g k_z}\frac{\partial \delta P}{\partial z} \quad , \tag{A.16c}$$

$$\delta F_x^{(0)} = -\frac{c}{\rho_0 \kappa_0}\frac{k_x}{k_z}\frac{\partial \delta P}{\partial z} \quad , \tag{A.16d}$$

$$\delta F_z^{(0)} = -\frac{c}{\rho_0 \kappa_0}\left(\frac{\partial \delta P}{\partial z} + \delta\rho^{(0)}g\right) \quad , \tag{A.16e}$$

where the superscript (0) refers to the mode without the inertia term. Next, we need to separate this mode from the full dispersion relation. Let us denote the superscript (1) for the modifications introduced by the inertia term, where $f^{(1)} = f - f^{(0)}$. To simplify the calculation, we apply the following assumptions in advance: 1. the short-wavelength approximation, which allows us to treat $\omega^2/(gk_z)$ and $\partial \ln \rho_0/(k_z \partial z)$ as small quantities. 2. small frequency introduced by the inertia term (i.e. $\omega^{(1)} \ll \omega^{(0)}$).

Thus, we can express the perturbed quantities in terms of δP and keep the leading terms in equations (A.15a)-(A.16b), (A.15b)-(A.16c), (A.15c)-(A.16d) and (A.15d)-(A.16e) as follows

$$\delta\rho^{(1)} \simeq \frac{\left(\omega^{(0)}\right)^2}{g^2}\delta P \quad , \tag{A.17a}$$

$$\delta v^{(1)} \simeq \frac{\omega^{(0)}}{\rho_0 g}\left[\frac{\left(\omega^{(0)}\right)^2}{gk_z} - i\frac{\omega^{(1)}}{\omega^{(0)}}\right]\delta P \quad , \tag{A.17b}$$

$$\delta F_x^{(1)} = 0 \quad , \tag{A.17c}$$

$$\delta F_z^{(1)} \simeq -\frac{c}{\rho_0 \kappa_0 g}\left(\omega^{(0)}\right)^2 \delta P \quad . \tag{A.17d}$$

Specifically, we neglect orders higher than $O(\omega^2/(gk_z))$, $O(\partial \ln \rho_0/(k_z \partial z))$ and $O(\omega^{(1)}/\omega^{(0)})$

for $\delta\rho^{(1)}$ and $\delta F_z^{(1)}$, but keeping the leading terms of order $O(\omega^2/(gk_z))$ and $O(\omega^{(1)}/\omega^{(0)})$ for $\delta v^{(1)}$. The dispersion relation for $\omega^{(1)}$ can be determined by the corresponding linearized heat equation by subtracting the mode without the inertia term from (A.12c)

$$-i\omega^{(1)}\delta P - \rho_0 g \delta v^{(1)} + i\frac{4}{3}k_z P_0 \delta v^{(1)} = -\frac{1}{3}\frac{\partial \delta F_z^{(1)}}{\partial z} \quad . \tag{A.18}$$

We can eliminate $v^{(1)}$ and $\delta F_z^{(1)}$ by using (A.17b) and (A.17d) to obtain the complex frequency introduced by the inertia term

$$\omega^{(1)} = \frac{3\rho_0}{4P_0}\frac{1}{k_z^2}\left(\omega^{(0)}\right)^3 + i\left(\frac{c}{4\kappa_0 P_0} - \frac{\omega^{(0)}}{gk_z}\right)\left(\omega^{(0)}\right)^2 \quad . \tag{A.19}$$

This can also be written in dimensionless form as

$$\frac{\omega^{(1)}}{N_0} \simeq -\frac{1}{27}M_0^3\frac{(k_x h)^6}{(k_z h)^5} + i\frac{1}{27}M_0^3\frac{(kh)^2(k_x h)^4}{(k_z h)^4} \tag{A.20a}$$

$$= -\frac{1}{27}M_0^3(kh)\frac{(1-\mu^2)^3}{\mu^5} + i\frac{1}{27}M_0^3(kh)^2\frac{(1-\mu^2)^2}{\mu^4} \quad . \tag{A.20b}$$

The growth rate of instability comes from the imaginary part of $\omega^{(1)}$, which is consistent with the approximation done by Arons (1992) in his equation (41). The physical reasoning is well explained by Arons (1992). We follow his logic and first compare the phase differences of the perturbed quantities. By applying the short-wavelength approximation, we obtain the phase relation from (A.15a) and (A.15c)

$$\delta\rho \propto -i\delta P \quad , \tag{A.21}$$

$$\delta F_z \propto -\delta P \quad , \tag{A.22}$$

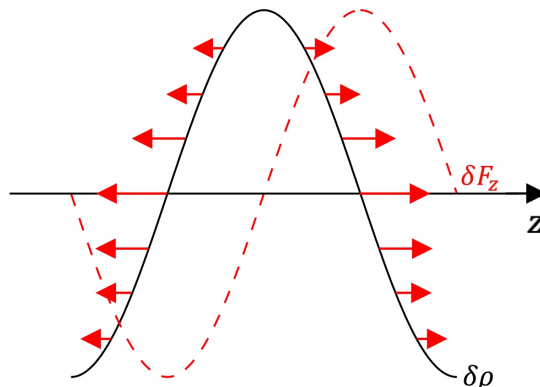which is shown in Figure A.2. Note that for spatially sinusoidal perturbations, $\delta\rho$ and

197

Figure A.2: Phase differences of perturbations.

δP are $90°$ out of phase. This is not an adiabatic perturbation, for which $\delta \rho$ and δP would be in phase. Hence this mode is associated with nonzero entropy perturbations, and is in fact called an entropy mode. In this entropy mode, the perturbed radiation energy density and perturbed horizontal flux are dominated by the negligible inertia terms with the real frequency $\omega^{(0)}$. And the perturbed density is simply determined by the hydrostatic equilibrium. However, the inertia term is small but finite, which is sufficient to destabilize this mode. As shown in the Figure A.2, the perturbed vertical flux transfers photons from high-density regions to the low-density regions due to the $90°$ phase delay. This tendency slowly evacuates the low-density regions with the radiation and leads to the increasing amplitude of perturbed density. Similar analysis can also be found in Arons (1992), where his figure 1 illustrates the same phase relation between the perturbed radiation flux and gas density that leads to the photon bubble instability.

A.4   Instability Driven by Variable Magnetic Opacity

The dispersion relation (A.7) can be affected by incorporating variable Rosseland mean opacities $\kappa(\rho, T)$. The viscous (V) terms generally set the short wavelength cutoff scale when finite gas pressure effects are negligible. Neglecting these terms and taking

the short wavelength $k \to \infty$ limit, we find that there is a mode given by

$$\omega^2 = -igk\mu \left[1 - (1 + \Theta_\rho)\mu^2\right] \quad . \tag{A.23}$$

This agrees exactly with equation (98) of Blaes & Socrates (2003) for a vertical magnetic field, and generalizes the dispersion relation of Gammie (1998) to incorporate the effects of a variable opacity. Temperature fluctuations are smoothed out by rapid diffusion at short wavelengths, which is why Θ_T does not appear in this limit. Indeed, note that in the last three terms of (A.7), the Θ_T term is at one order of k lower than the other two terms.

In chapter 4, the magnetic opacities that we have considered have no density-dependence: $\Theta_\rho = 0$. In addition, the photon bubble instability requires $k_x \neq 0$. If we eliminate photon bubbles by considering purely vertically propagating modes, and adopt $\Theta_\rho = 0$, we find a short wavelength mode with frequency given by

$$\omega^2 + i\frac{3\kappa_0\rho_0 c_r^2}{c}\omega + \frac{g^2}{3c_r^2}\Theta_T = 0 \quad . \tag{A.24}$$

One of the roots of this equation is always unstable if $\Theta_T > 0$. Because it is entirely vertical, the magnetic field plays no role here except in determining the temperature dependence of the opacity, and the instability is fundamentally hydrodynamic in nature.

Appendix B

Derivation of Gravitation in Weak Field Limit

B.1 Conservation Laws in General Relativity

The primary relativistic effect in our simulations of neutron star accretion columns is that the Newtonian Alfvén speed in low density regions can exceed the speed of light, which would then require unreasonably small time steps in the simulation. Even the free-fall speeds in the incoming accretion flow outside the accretion shock are only mildly relativistic.

However, gravity is important in the structure of the accretion column, as well as the dynamics of photon bubbles, and gravity is not defined in special relativity. One could in principle compute using full general relativity, but to do that with radiation would require incorporating the curved trajectories of photon geodesics in our transfer equation, and these effects are tiny over the short mean free paths within the optically thick portions of the column. We therefore need only include weak field gravitational effects in our special relativistic hydrodynamics at lowest, essentially Newtonian, order. We proceed here to

reduce the full general relativistic conservation laws to the weak field limit and neglect all terms that are second order or higher in the corresponding Newtonian potential.

In isotropic coordinates, the weak field spacetime metric can be written as

$$g_{\mu\nu} = \mathrm{diag}(-\mathbb{A}, \mathbb{B}, \mathbb{B}, \mathbb{B}) \quad , \tag{B.1}$$

where $\mathbb{A} = \mathbb{A}(x^j)$ and $\mathbb{B} = \mathbb{B}(x^j)$ only vary in space. The corresponding Christoffel symbols are

$$
\begin{aligned}
&\Gamma^0_{00} = 0 && \Gamma^0_{0j} = \Gamma^0_{j0} = \frac{1}{2\mathbb{A}}\partial_j \mathbb{A} && \Gamma^0_{ij} = 0 \quad , \\
&\Gamma^j_{00} = \frac{1}{2\mathbb{B}}\partial_j \mathbb{A} && \Gamma^j_{ij} = \Gamma^j_{ji} = \frac{1}{2\mathbb{B}}\partial_i \mathbb{B} && \Gamma^j_{0i} = \Gamma^j_{i0} = 0 \quad , \\
& && \Gamma^j_{ii}\big|_{i\neq j} = -\frac{1}{2\mathbb{B}}\partial_j \mathbb{B} && \Gamma^j_{ik}\big|_{i\neq j\neq k} = 0 \quad .
\end{aligned}
\tag{B.2}
$$

The normalization of the four-velocity implies

$$u^0 u^0 = \frac{1}{\mathbb{A} - \mathbb{B}v^2} \quad . \tag{B.3}$$

We now consider the conservation laws of particle number, momentum and energy:

$$\nabla_\mu(\rho u^\mu) = 0 \quad , \tag{B.4a}$$

$$\nabla_\mu \mathrm{T}^{\mu\nu} = 0 \quad , \tag{B.4b}$$

where the stress-energy tensor $\mathrm{T}^{\mu\nu} = w_g u^\mu u^\nu + P_g g^{\mu\nu}$, gas enthalpy $w_g = \rho + \dfrac{\gamma}{\gamma - 1}P_g$ and γ is the gas adiabatic index. For simplicity, we neglect radiation and magnetic fields as that is all that is necessary to derive the form of the gravitational source terms.

Expanding (B.4a) and (B.4b) in the metric (B.1)

$$\partial_0(\rho u^0) + \partial_j(\rho u^j) = -\frac{1}{2}\left(\frac{1}{\mathbb{A}}\partial_j\mathbb{A} + \frac{3}{\mathbb{B}}\partial_j\mathbb{B}\right)\rho u^j \quad , \tag{B.5a}$$

$$\partial_0 \mathrm{T}^{0i} + \partial_j \mathrm{T}^{ij} = -\left(\frac{1}{2\mathbb{A}}\partial_j\mathbb{A} + \frac{2}{\mathbb{B}}\partial_j\mathbb{B}\right)\mathrm{T}^{ij}$$
$$-\frac{1}{2\mathbb{B}}\left(\mathrm{T}^{00}\partial_i\mathbb{A} + \mathrm{T}^{ik}\partial_k\mathbb{B}\Big|_{k\neq i} - \mathrm{T}^{jj}\partial_i\mathbb{B}\Big|_{j\neq i}\right) \quad , \tag{B.5b}$$

$$\partial_0 \mathrm{T}^{00} + \partial_j \mathrm{T}^{j0} = -\left(\frac{1}{\mathbb{A}}\partial_j\mathbb{A} + \frac{3}{2\mathbb{B}}\partial_j\mathbb{B}\right)\mathrm{T}^{j0} - \frac{1}{2\mathbb{A}}\mathrm{T}^{0j}\partial_j\mathbb{A} \quad . \tag{B.5c}$$

B.2   Gravitational Source Terms in Weak Field Limit

In the weak field limit, the metric (B.1) can be specified as

$$\begin{cases} \mathbb{A} = 1 + 2\phi \\ \\ \mathbb{B} = 1 - 2\phi \end{cases} \quad , \text{ where the potential } \phi = -\frac{GM}{c^2 r} \text{ is a small quantity.} \tag{B.6}$$

Then, we expand equations (B.5a), (B.5b) and (B.5c) to first order of ϕ

$$\partial_0(\rho\Gamma) + \partial_j(\rho\Gamma v^j) = S_{\mathrm{gr1}} \quad , \tag{B.7a}$$

$$\partial_0(w_g\Gamma^2 v^i) + \partial_j(w_g\Gamma^2 v^i v^j + P_g\delta^{ij}) = S^i_{\mathrm{gr2}} \quad , \tag{B.7b}$$

$$\partial_0\left(w_g\Gamma^2 - P_g\right) + \partial_j(w_g\Gamma^2 v^j) = S_{\mathrm{gr3}} \quad , \tag{B.7c}$$

where the terms related to the gravitational field are

$$S_{\mathrm{gr1}} = 4\Gamma^2(\partial_0\Gamma + v^j\partial_j\Gamma)\rho\phi + \Gamma(2\Gamma^2 + 1)\rho v^j\partial_j\phi \quad , \tag{B.8a}$$

$$S^i_{\mathrm{gr2}} = 8w_g\Gamma^3\phi v^i(\partial_0\Gamma + v^j\partial_j\Gamma) - 4\phi\Gamma^2\partial_i P_g + 2\Gamma^2(2\Gamma^2 + 1)w_g v^i v^j\partial_j\phi$$
$$- (2\Gamma^2 - 1)w_g\partial_i\phi \quad , \tag{B.8b}$$

$$S_{\mathrm{gr}3} = 8w_g\Gamma^3\phi(\partial_0\Gamma + v^j\partial_j\Gamma) + 4(\Gamma^2 - 1)\phi\partial_0 P_g + 2\Gamma^2(2\Gamma^2 - 1)w_g v^j\partial_j\phi \quad . \tag{B.8c}$$

We can check the consistency with the Newtonian limit by applying approximations on (B.7a), (B.7b) and (B.7c) in different orders of small quantities. Keeping the first order of v and ϕ, we recover the Newtonian continuity equation

$$\partial_0\rho + \partial_j(\rho v^j) = 0 \quad . \tag{B.9a}$$

Define the isothermal sound speed as $c_0^2 = P_g/\rho$. Neglecting the orders higher than $O(c_0^2)$, $O(v^2)$ and $O(\phi)$, we recover the Newtonian momentum conservation

$$\partial_0(\rho v^i) + \partial_j(\rho v^i v^j) = -\partial_i P_g - \rho\partial_i\phi \quad . \tag{B.9b}$$

Neglecting the orders higher than $O(s^3)$, where $c_0 \sim v \sim O(s)$ and $\phi \sim O(s^2)$, we recover the Newtonian energy conservation

$$\partial_0\left(\frac{1}{\gamma - 1}P_g + \frac{1}{2}\rho v^2 + \rho\phi\right) + \partial_j\left[\left(\frac{\gamma}{\gamma - 1}P_g + \frac{1}{2}\rho v^2 + \rho\phi\right)v^j\right] = 0 \quad . \tag{B.9c}$$

Therefore, in order to capture gravitational effects to lowest (Newtonian) order, we can apply the following source terms in the framework of ATHENA++ relativistic MHD module (Beckwith & Stone 2011) to mock up the gravitational effect near the neutron star surface.

$$S_{\mathrm{gr}1} \simeq \Gamma(2\Gamma^2 + 1)\rho v^j\partial_j\phi \quad , \tag{B.10a}$$

$$S_{\mathrm{gr}2}^i \simeq 2\Gamma^2(2\Gamma^2 + 1)w_g v^i v^j\partial_j\phi - (2\Gamma^2 - 1)w_g\partial_i\phi \quad , \tag{B.10b}$$

$$S_{\mathrm{gr}3} \simeq 2\Gamma^2(2\Gamma^2 - 1)w_g v^j\partial_j\phi \quad . \tag{B.10c}$$

Appendix C

Variable Inversion Algorithm with Entropy Equation

C.1 First Law of Thermodynamics in Relativity

In this section, we give a overview of the first law of thermodynamics in general relativity. The governing equations can be concluded as follows in the sequence of gas particle number conservation, gas stress-energy conservation, magnetic induction, and radiative transfer

$$\nabla_\alpha(\rho u^\alpha) = 0 \quad , \tag{C.1a}$$

$$\nabla_\alpha \mathrm{T}^{\alpha\beta} = -G^\beta \quad , \tag{C.1b}$$

$$\nabla_\alpha \mathrm{F}^{\alpha\beta} = 0 \quad , \tag{C.1c}$$

$$\nabla_\alpha \mathrm{R}^{\alpha\beta} = G^\beta \quad , \tag{C.1d}$$

where ρ is the gas density and u^α is the fluid four-velocity. The vector G^α is the coupling term of gas and radiation. The stress-energy tensors of gas, magnetic field, and radiation

are defined as

$$\mathrm{T}^{\alpha\beta} = (w + b_\lambda b^\lambda)u^\alpha u^\beta + (P + \frac{1}{2}b_\lambda b^\lambda)g^{\alpha\beta} - b^\alpha b^\beta \quad , \tag{C.2a}$$

$$\mathrm{F}^{\alpha\beta} = b^\alpha u^\beta - b^\beta u^\alpha \quad , \tag{C.2b}$$

$$\mathrm{R}^{\alpha\beta} = \oint d\bar{\Omega} \int_0^\infty \bar{I}_\nu n^\alpha n^\beta d\bar{\nu} \quad , \tag{C.2c}$$

where $g^{\alpha\beta}$ is the space-time metric and $w = \rho + \rho e + P$ is the total enthalpy of the gas. Note that we adopt velocity unit with $c = 1$ here. The quantities e and P refer to the specific internal energy density and pressure of the gas, respectively. The magnetic field four-vector b^α are defined as

$$b^0 = B^j u_j \quad , \tag{C.3a}$$

$$b^i = \frac{1}{u^0}(B^i + b^0 u^i) \quad , \tag{C.3b}$$

where B^i is the three-vector magnetic field. The radiation stress-energy tensor is defined in the fluid frame with the quantities denoted by overbars, where $\bar{\Omega}$ is the solid angle of the radiation field, $\bar{I}_\nu$ is the radiation intensity field, n^α is the direction of the intensity, and $\bar{\nu}$ is the radiation frequency.

In principle, the energy equation should be equivalent to the first law of thermodynamics. Here, we conduct the sanity check of it. With the gas particle number conservation and the identities of the four-velocity and magnetic field four-vector (i.e. $u^\mu u_\mu = -1$ and $b^\mu u_\mu = 0$), we can reduce and express the gas stress-energy equation by taking the dot product with the four-velocity as $u_\beta \nabla_\alpha \mathrm{T}^{\alpha\beta} = -u_\beta G^\beta$:

$$[(\rho e + P)\nabla_\mu u^\mu + u^\mu \nabla_\mu(\rho e)] + \left[b_\lambda b^\lambda \nabla_\mu u^\mu + b_\lambda u^\mu \nabla_\mu b^\lambda + u_\lambda b^\mu \nabla_\mu b^\lambda\right] = u_\mu G^\mu \quad , \tag{C.4}$$

where the second square bracket contains all the magnetic terms and can be proved to
be zero using the induction equation as follows:

$$\nabla_\mu(b^\mu u^\lambda - b^\lambda u^\mu) = 0$$

$$\implies u^\mu\nabla_\mu b^\lambda = u^\lambda\nabla_\mu b^\mu + b^\mu\nabla_\mu u^\lambda - b^\lambda\nabla_\mu u^\mu$$

$$\implies b_\lambda u^\mu\nabla_\mu b^\lambda = \underbrace{b_\lambda u^\lambda\nabla_\mu b^\mu}_{0} + \underbrace{b^\mu\nabla_\mu(b_\lambda u^\lambda)}_{0} - g^{\lambda\sigma}u_\sigma b^\mu\nabla_\mu b_\lambda - b_\lambda b^\lambda\nabla_\mu u^\mu$$

$$\implies b_\lambda b^\lambda\nabla_\mu u^\mu + b_\lambda u^\mu\nabla_\mu b^\lambda + u_\lambda b^\mu\nabla_\mu b^\lambda = 0 \quad . \tag{C.5}$$

This indicates that the projection of the magnetic tensor onto the gas four-velocity must
be zero because the induction equation is sourced by it (i.e. the magnetic field does
no work onto the gas). Hence, the first law of thermodynamics can be recovered by
substituting the mass conservation as follows:

$$u^\mu\nabla_\mu e + P u^\mu\nabla_\mu\left(\frac{1}{\rho}\right) = \frac{u_\mu G^\mu}{\rho} \quad , \tag{C.6}$$

where the RHS is the radiative source term. Alternatively, if we assume the ideal gas,
i.e. $P = (\gamma - 1)\rho e$, the first law of thermodynamics can be expressed in the conservative
form as:

$$u^\mu\nabla_\mu s = (\gamma - 1)\frac{u_\mu G^\mu}{\rho^\gamma} \qquad \text{or} \qquad \nabla_\mu(\rho s u^\mu) = (\gamma - 1)\frac{u_\mu G^\mu}{\rho^{\gamma-1}} \quad , \tag{C.7}$$

where $s = P/\rho^\gamma$ is the specific entropy (i.e. entropy per unit mass). This can be very
useful as a backup approach to compute the gas temperature if the gas pressure updated
by the total energy conservation fails to be resolved in the strong magnetic field regime.

C.2   Variable Inversion Algorithm

The inversion from conservative variables to primitive variables in relativity is non-trivial and usually involved with solving a nonlinear equation set. In this section, we summarize two schemes of the variable inversion in special relativity. In general relativity, the conservative variables can be transformed into the normal observer frame, where the special relativistic inversion algorithm can be easily generalized.

Given the primitive variable set (ρ, v^i, P, B^i), the conservative variables can be defined as either (D, M^i, E, B^i) or (D, M^i, S, B^i), depending on whether we use the gas energy conservation or the first law of thermodynamics to close the system and update the gas pressure. The conservative gas density D, momentum M^i, energy E and entropy S are defined as follows

$$D = \rho u^0 \quad , \tag{C.8a}$$

$$M^i = (w + b_\lambda b^\lambda) u^0 u^i - b^0 b^i \quad , \tag{C.8b}$$

$$E = (w + b_\lambda b^\lambda) u^0 u^0 - (P + \frac{1}{2} b_\lambda b^\lambda) - b^0 b^0 \quad , \tag{C.8c}$$

$$S = \rho s u^0 \quad . \tag{C.8d}$$

For convenience for the variable inversion, we also define the following auxiliary quantities following the notations in Newman & Hamlin (2014):

$$\mathcal{T} = M_i B^i = w u^0 b^0 \quad , \tag{C.9}$$

$$M^2 = M_i M^i = \mathcal{L}^2 v^2 + (B^2 + 2\mathcal{L}^2) \left[B^2 v^2 - \left(\frac{b^0}{u^0} \right)^2 \right] \quad , \tag{C.10}$$

$$\mathcal{L} = w(u^0)^2 \quad . \tag{C.11}$$

With above auxiliary quantities, the gas velocity can be solved iteratively by the following

equation

$$v^2 = \frac{M^2\mathcal{L}^2 + \mathcal{T}^2(2\mathcal{L} + B^2)}{\mathcal{L}^2(\mathcal{L} + B^2)^2} \quad , \tag{C.12}$$

The details of the variable inversion algorithm with the total gas energy is described in Newman & Hamlin (2014).

For the variable inversion algorithm with the entropy, we can follow Mignone & McKinney (2007) and modify the algorithm by finding the root of the following equation:

$$f(\mathcal{L}) = D\frac{P}{\rho^\gamma} - S \quad , \tag{C.13}$$

To invoke a Newton-Raphson iteration scheme, we analytically compute the below derivatives for the implementation.

$$\frac{df}{d\mathcal{L}} = \frac{D}{\rho^\gamma}\frac{dP}{d\mathcal{L}} - \gamma\frac{DP}{\rho^{\gamma+1}}\frac{d\rho}{d\mathcal{L}} \quad , \tag{C.14a}$$

$$\begin{aligned}\frac{dP}{d\mathcal{L}} &= \frac{\gamma - 1}{\gamma}\left[(1 - v^2) + (\frac{1}{2}Du^0 - \mathcal{L})\frac{dv^2}{d\mathcal{L}}\right] \\ &= \frac{\gamma - 1}{\gamma}\left\{(1 - v^2) - \frac{u^0\left[D + 2(\mathcal{L} - Du^0)(1 - v^2)u^0\right]}{2}\right\} \quad ,\end{aligned} \tag{C.14b}$$

$$\frac{d\rho}{d\mathcal{L}} = -\frac{Du^0}{2}\frac{dv^2}{d\mathcal{L}} \quad , \tag{C.14c}$$

$$\frac{dv^2}{d\mathcal{L}} = -\frac{2}{\mathcal{L}^3(\mathcal{L} + B^2)^3}\{\mathcal{T}^2[3\mathcal{L}(\mathcal{L} + B^2) + B^4] + M^2\mathcal{L}^3\} \quad . \tag{C.14d}$$

These are also described in Beckwith & Stone (2011) but with typos in their equations.

C.3   Numerical Tests

In this section, we conduct the numerical tests on the variable inversion algorithm described above in the strong magnetic field regime of neutron star column accretion. We adopt the primitive variables specified as shown in Figure C.1, with the corresponding

conservative variables as shown in Figure C.2.   In Figure C.1 and Figure C.2, we label
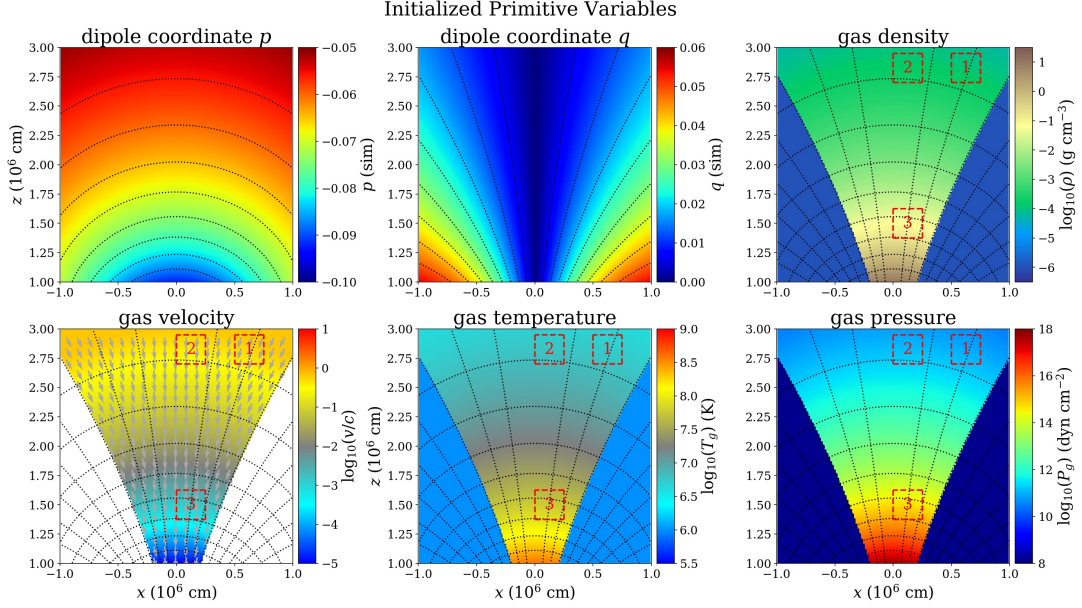

Figure C.1: Profiles in primitive variables for variable inversion test.
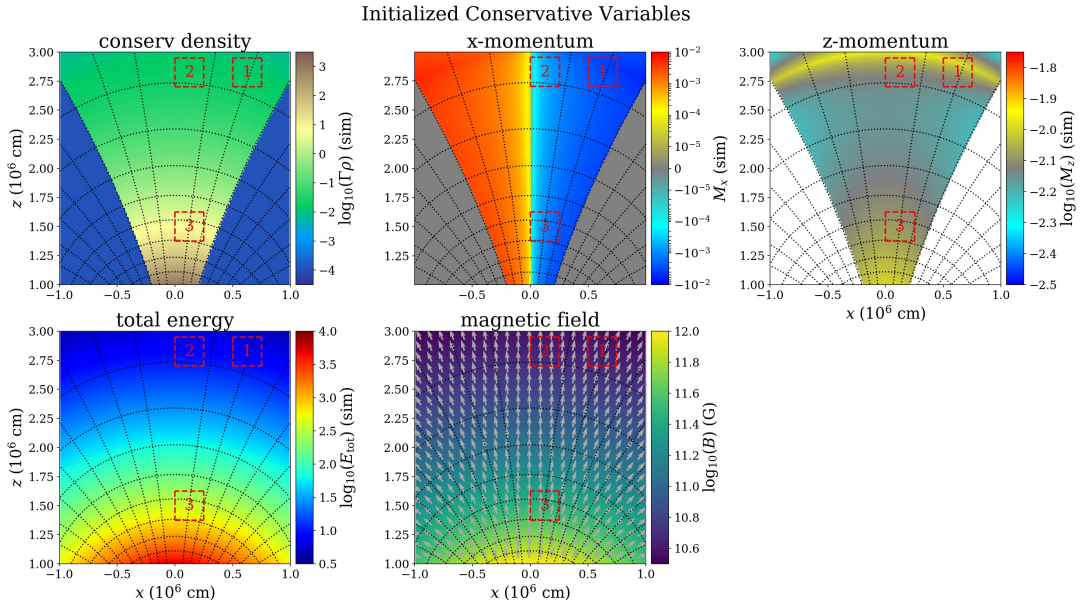
Figure C.2: Profiles in conservative variables for variable inversion test.

three different regions (red dashed box 1, 2, and 3) to quantify how the numerical noise

affects the inversion results.

C.3.1 Newman-Hamllin (N-H) - Energy Scheme

We first test the N-H variable inversion in the total energy scheme, which is used in all of our current neutron star column accretion simulations. Direct N-H inversion results are shown in Despite the unbiased non-convergence issue in few regions (i.e. where the Lipshitz parameter greater than 1), the overall results are highly agree with the initial primitive variables, which indicates the robustness of the N-H algorithm. Figure C.3.

Figure C.3: Variable inversion results in the total energy scheme using N-H method with no random perturbation.

Figure C.4: Variable inversion results in the total energy scheme using N-H method with 10^{-8} random perturbation.

However, if we add a random noise by a factor of 10^{-8} to all the conservative variables (i.e. mocking up the numerical noises, which can come from all sorts of dis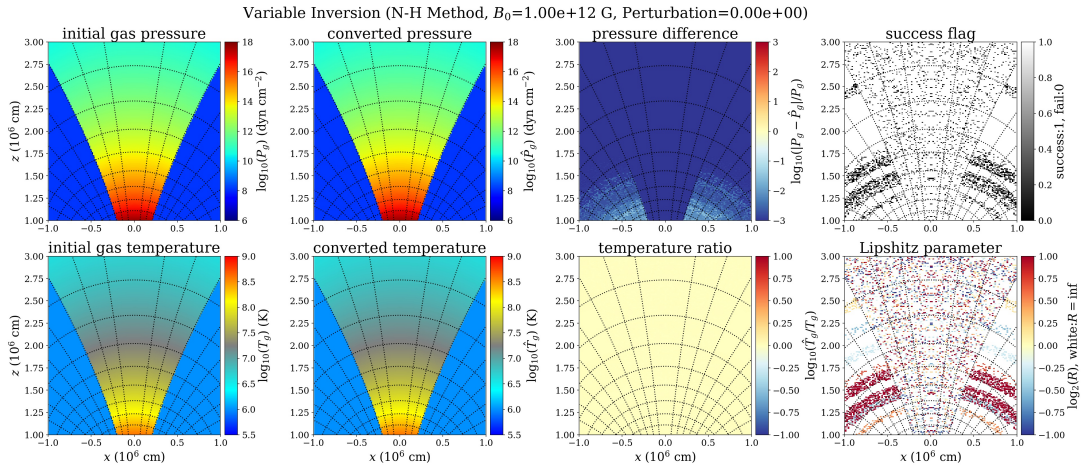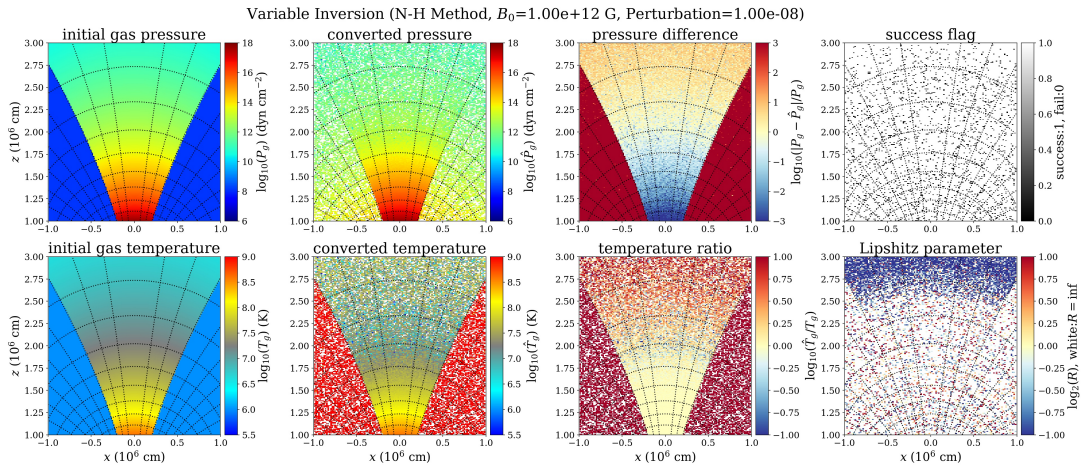cretization in the simulation), the inversion results change dramatically as shown in Figure C.4, especially the failure in the low-density region. In those failed regions, the Lipshitz parameters are in general less than 1, which suggests that the solutions are actually converged numerically but apparently not the physical solutions. This is intrinsically caused by the high sensitivity of one-to-one mapping from the conservative variables to the primitive variables. That is to say, a small perturbation in a conservative variable can lead to a dramatically different inversion result. We can further quantify this effect by varing each conservative variable (i.e. D, M^i, E, and B^i) in region 1, 2, and 3 as indicated by the red dashed boxes in Figure C.1 and Figure C.2. In Figure C.5,

Figure C.5: Quantification of the numerical noise propagation for each conservative variable in region 1, indicated by the red dashed box in Figure C.1 and Figure C.2. The variable inversion is conducted in the total energy scheme using N-H method with 10^{-8} random perturbation.

Figure C.6, and Figure C.7, we measure the factional change of the inversion result caused by the conservative variable perturbation. When the magnetic energy is large

Figure C.6: Quantification of the numerical noise propagation for each conservative variable in region 2, indicated by the red dashed box in Figure C.1 and Figure C.2. The variable inversion is conducted in the total energy scheme using N-H method with 10^{-8} random perturbation.
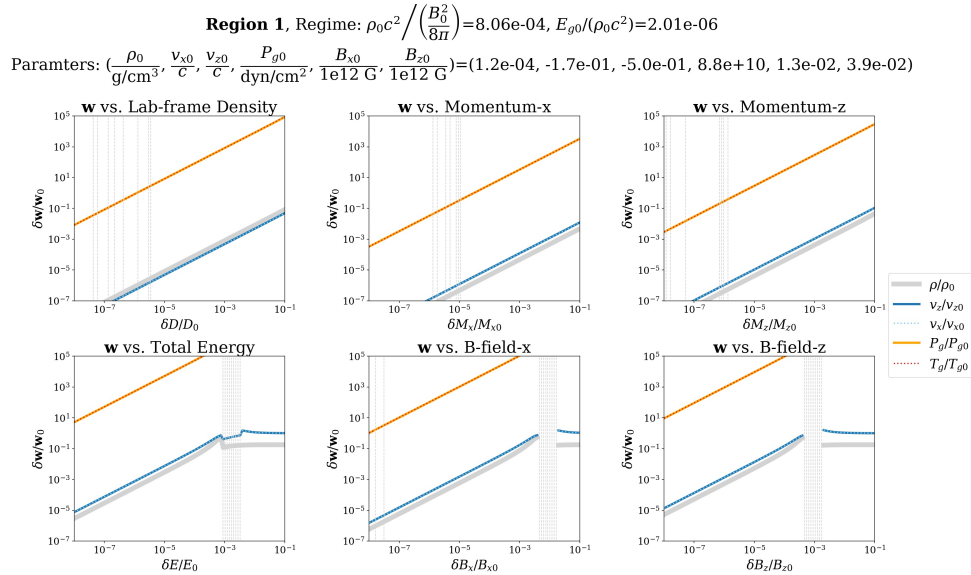

Figure C.7: Quantification of the numerical noise propagation for each conservative variable in region 3, indicated by the red dashed box in Figure C.1 and Figure C.2. The variable inversion is conducted in the total energy scheme using N-H method with 10^{-8} random perturbation.

compared with the rest mass energy and gas internal energy (i.e. strong magentic field regime), the numerical noise from the gas density, total energy or magnetic fields can be easily amplified by a huge factor into the resulting gas pressure, except few cases (last two panels of the first row in Figure C.7).

C.3.2   Mignone-McKinney (M-M) - Entropy Scheme
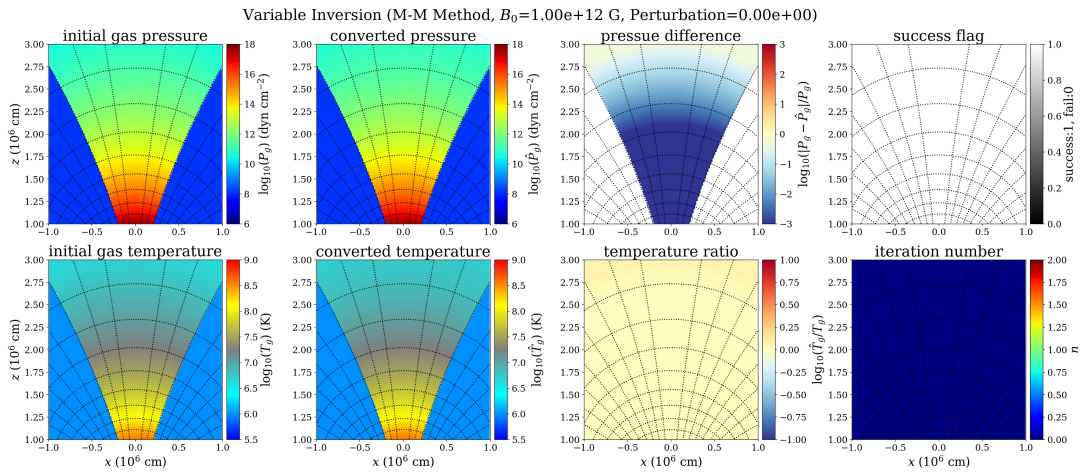
Figure C.8: Variable inversion results in the entropy scheme using M-M method with no random perturbation.
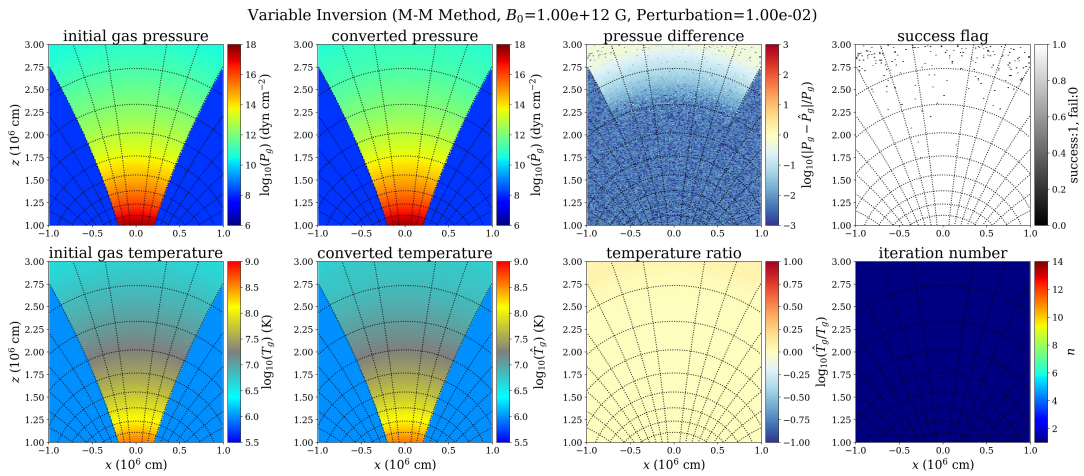
Figure C.9: Variable inversion results in the entropy scheme using M-M method with 1% random perturbation.

We conduct the same numerical tests on the M-M variable inversion in the entropy scheme. The N-H algorithm is numerically more robust than the M-M in terms of the stability and accuracy as shown in Figure C.8. The M-M algorithm relies on a relatively accurate initial guess in the first place. Any wrongly estimated initial guess would lead to the failure of the convergence. However, in the strong magnetic field regime, the variable inversion with total energy is intrinsically troublesome due to the strong coupling between magnetic and gas terms. The similar tests have been done for the entropy scheme. Since the entropy is not coupled with the magnetic field, the variable inversion behaves much better than using the total energy as shown in Figure C.9. The propagated noise in the gas pressure is reduced by a factor of at least 10^{-2}. Note that here the error is not
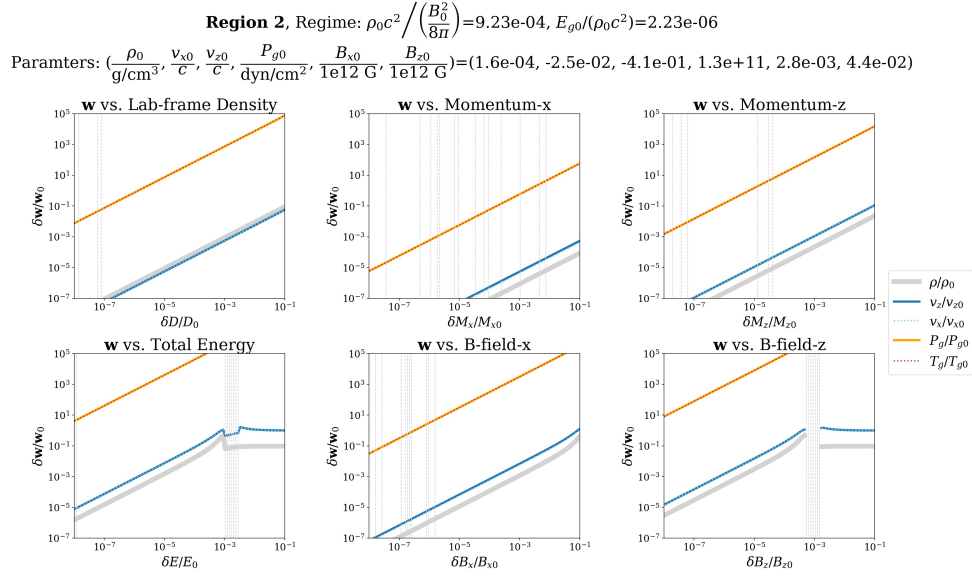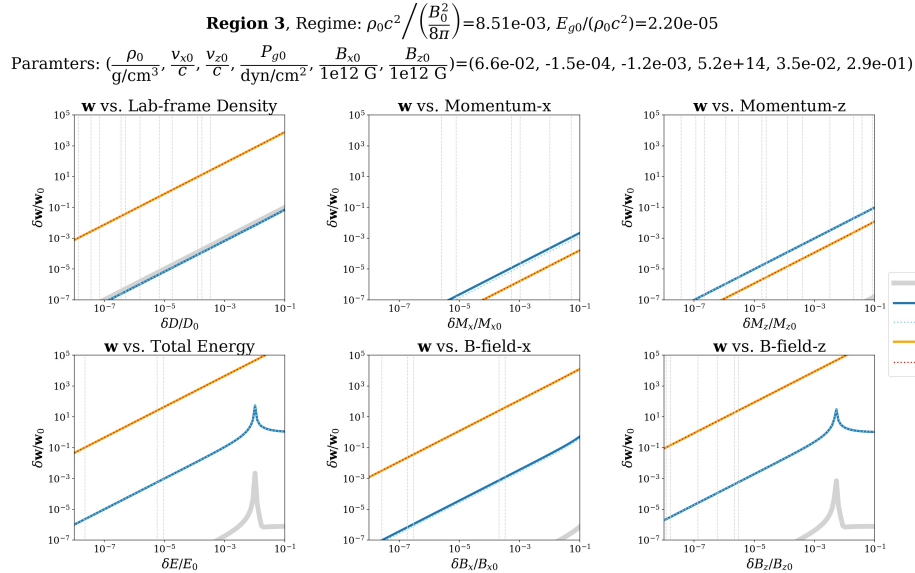

Figure C.10: Quantification of the numerical noise propagation for each conservative variable in region 1, indicated by the red dashed box in Figure C.1 and Figure C.2. The variable inversion is conducted in the entropy scheme using M-M method with 1% random perturbation.

scaled by the input noise as shown in Figure C.10, Figure C.11 and Figure C.12. This indicates the systematic noise of the M-M method is dominated over the noise from the perturbed conservative variables. However, the systematic noise is still small enough and

the physical solution of primitive variables can be obtained by the entropy scheme.
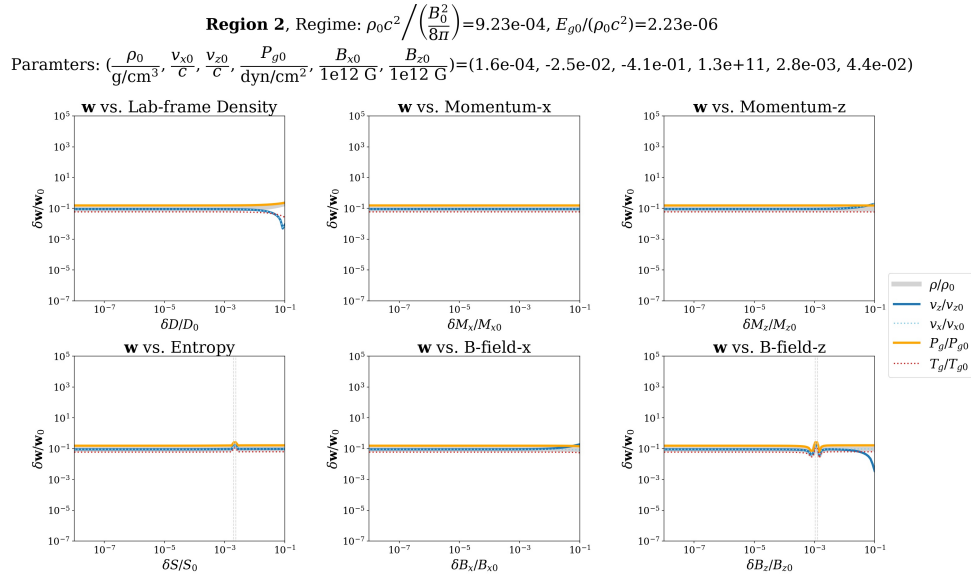
Figure C.11: Quantification of the numerical noise propagation for each conservative variable in region 2, indicated by the red dashed box in Figure C.1 and Figure C.2. The variable inversion is conducted in the entropy scheme using M-M method with 1% random perturbation.

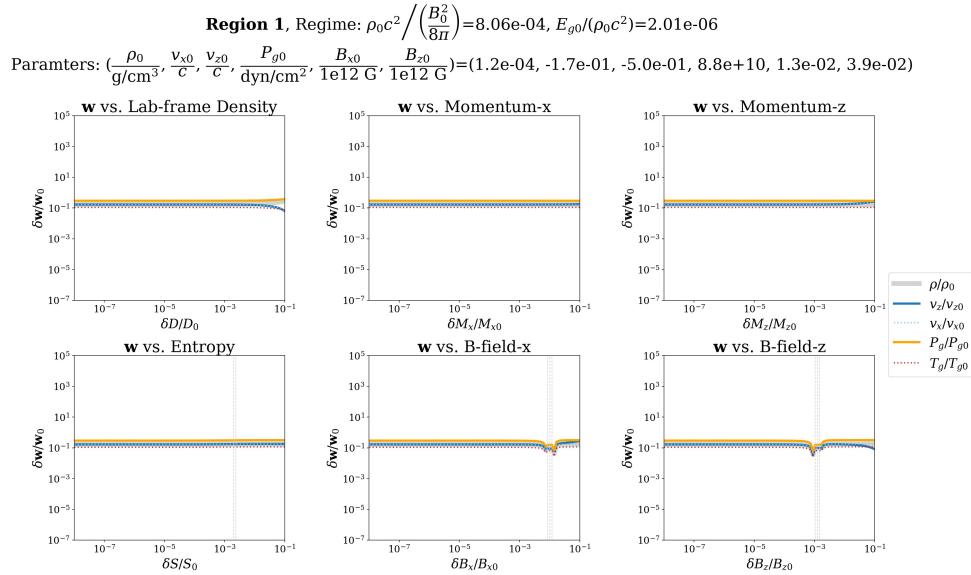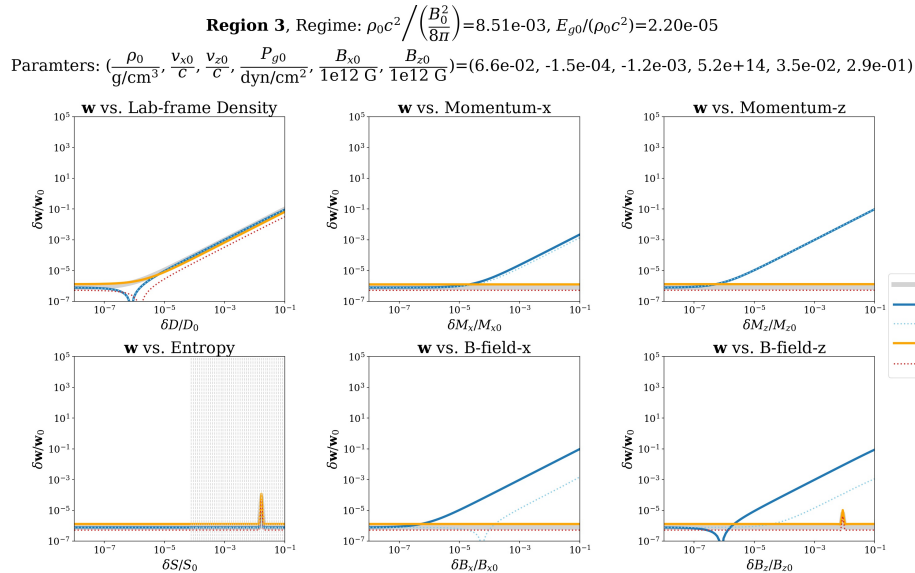Figure C.12: Quantification of the numerical noise propagation for each conservative variable in region 3, indicated by the red dashed box in Figure C.1 and Figure C.2. The variable inversion is conducted in the entropy scheme using M-M method with 1% random perturbation.

Appendix D

Derivation of Dipole Coordinate System

D.1 Dipole Coordinates

D.1.1 Dipole Magnetic Field

In the vicinity of a neutron star with a strong magnetic field, the gas becomes magnetically confined and therefore only move along the field lines. Thus, it is preferable to employ an intrinsic coordinate system that traces the trajectory of the gas as it follows these field lines. Assume a dipole magnetic field

$$\boldsymbol{B}(\boldsymbol{r}) = \frac{m}{r^3} \left[3(\hat{\boldsymbol{m}} \cdot \hat{\boldsymbol{r}})\hat{\boldsymbol{r}} - \hat{\boldsymbol{m}} \right] \quad , \tag{D.1}$$

where r and $\hat{\boldsymbol{r}}$ refer to the radial coordinate and direction, respectively, in the spherical geometry. The quantity $\boldsymbol{m} = m\hat{\boldsymbol{m}}$ is the magnetic dipole moment. We can establish an orthonormal basis in dipole geometry by following the field lines and equipotential lines. Selecting the direction of the dipole moment to be $\hat{\boldsymbol{m}} = \hat{\boldsymbol{z}} = \cos\theta\hat{\boldsymbol{r}} - \sin\theta\hat{\boldsymbol{\theta}}$ and assuming

the surface magnetic field at magnetic pole to be $\boldsymbol{B_0} = B_0\hat{\boldsymbol{z}}$, the magnetic dipole moment can then be expressed as

$$\boldsymbol{m} = \frac{1}{2}B_0 R_\star^3 \hat{\boldsymbol{z}} \quad , \tag{D.2}$$

where $R_\star$ represents the neutron star radius. The dipolar field can also be rewritten in the spherical coordinates as

$$\boldsymbol{B}(\boldsymbol{r}) = \frac{m}{r^3}(2\cos\theta\hat{\boldsymbol{r}} + \sin\theta\hat{\boldsymbol{\theta}}) \quad . \tag{D.3}$$

At any position $\boldsymbol{r} = (x, y, z) = (r, \theta, \phi)$ above the neutron star surface, the magnetic field can be expressed in the following forms

$$\begin{cases} B_x = \dfrac{3mxz}{r^5} = \dfrac{3}{2}B_0 \left(\dfrac{r}{R_\star}\right)^{-3} n_x n_z \\[2mm] B_y = \dfrac{3myz}{r^5} = \dfrac{3}{2}B_0 \left(\dfrac{r}{R_\star}\right)^{-3} n_y n_z \\[2mm] B_z = \dfrac{m(3z^2 - r^2)}{r^5} = \dfrac{3}{2}B_0 \left(\dfrac{r}{R_\star}\right)^{-3} \left(n_z^2 - \dfrac{1}{3}\right) \end{cases} , \tag{D.4a}$$

$$\begin{cases} B_r = B_0 \left(\dfrac{r}{R_\star}\right)^{-3} \cos\theta \\[2mm] B_\theta = \dfrac{1}{2}B_0 \left(\dfrac{r}{R_\star}\right)^{-3} \sin\theta \\[2mm] B_\phi = 0 \end{cases} , \tag{D.4b}$$

where the unit vector in Cartesian coordinates is defined as $(n_x, n_y, n_z) = (x/r, y/r, z/r)$ and $r = \sqrt{x^2 + y^2 + z^2}$.

D.1.2   Constructing Dipole Coordinates

In this section, we construct the dipole coordinates system. Define the unit vectors along and perpendicular to the magnetic field, respectively

$$\hat{\boldsymbol{p}} \equiv \hat{\boldsymbol{n}}_{\parallel} = \hat{p}_r \hat{\boldsymbol{r}} + \hat{p}_\theta \hat{\boldsymbol{\theta}} \quad , \tag{D.5a}$$

$$\hat{\boldsymbol{q}} \equiv \hat{\boldsymbol{n}}_{\perp} = \hat{q}_r \hat{\boldsymbol{r}} + \hat{q}_\theta \hat{\boldsymbol{\theta}} \quad , \tag{D.5b}$$

where $$\begin{cases} \hat{p}_r = \dfrac{2\cos\theta}{\sqrt{3\cos^2\theta + 1}} \\ \hat{p}_\theta = \dfrac{\sin\theta}{\sqrt{3\cos^2\theta + 1}} \end{cases} \quad \text{and} \quad \begin{cases} \hat{q}_r = \dfrac{\sin\theta}{\sqrt{3\cos^2\theta + 1}} \\ \hat{q}_\theta = \dfrac{-2\cos\theta}{\sqrt{3\cos^2\theta + 1}} \end{cases} \tag{D.5c}$$

Here, we use '$\parallel$' and '$\perp$', respectively, to denote the directions parallel and perpendicular to the dipole field. We can then construct the orthogonal basis based on these two directions (D.5). When we differentiate perpendicular to the dipolar field, we preserve a scalar potential μ, where the corresponding vector field $\boldsymbol{U} = \boldsymbol{\nabla}\mu$ is parallel to the field direction. When we differentiate along the dipolar field, we preserve a scalar potential ν, where the corresponding vector field $\boldsymbol{V} = \boldsymbol{\nabla}\nu$ is perpendicular to the field (i.e. $\boldsymbol{U}\cdot\boldsymbol{V} = 0$). The scalar potentials μ and ν can then be employed as an orthogonal coordinate system for the dipolar geometry. To obtain the expressions of μ and ν, we first assume

$$\boldsymbol{U} = k_\mu(r,\theta)(2\cos\theta\hat{\boldsymbol{r}} + \sin\theta\hat{\boldsymbol{\theta}}) \quad , \tag{D.6a}$$

$$\boldsymbol{V} = k_\nu(r,\theta)(\sin\theta\hat{\boldsymbol{r}} - 2\cos\theta\hat{\boldsymbol{\theta}}) \quad . \tag{D.6b}$$

Since $\mu = \mu(r,\theta)$ and $\nu = \nu(r,\theta)$, we have

$$\begin{cases} \dfrac{\partial\mu}{\partial r} = 2k_\mu\cos\theta \\ \dfrac{\partial\mu}{\partial\theta} = rk_\mu\sin\theta \end{cases} \quad \text{and} \quad \begin{cases} \dfrac{\partial\nu}{\partial r} = k_\nu\sin\theta \\ \dfrac{\partial\nu}{\partial\theta} = -2rk_\nu\cos\theta \end{cases} \tag{D.7}$$

Then μ and ν can be solved via the following equations

$$\frac{\partial^2 \mu}{\partial r \partial \theta} = 2\left(\frac{\partial k_\mu}{\partial \theta}\cos\theta - k_\mu \sin\theta\right) = \sin\theta\left(k_\mu + r\frac{\partial k_\mu}{\partial r}\right) \quad , \qquad \text{(D.8a)}$$

$$\frac{\partial^2 \nu}{\partial r \partial \theta} = \frac{\partial k_\nu}{\partial \theta}\sin\theta + k_\nu\cos\theta = -2\cos\theta\left(k_\nu + r\frac{\partial k_\nu}{\partial r}\right) \quad . \qquad \text{(D.8b)}$$

Here, we further assume that $k_\mu(r,\theta) = k_{\mu r}(r)k_{\mu\theta}(\theta)$ and $k_\nu(r,\theta) = k_{\nu r}(r)k_{\nu\theta}(\theta)$ are separable. Hence, above equation sets can be reduced to

$$\frac{d\ln k_{\mu\theta}}{d\theta}\frac{2\cos\theta}{\sin\theta} = 3 + r\frac{d\ln k_{\mu r}}{dr} = c_{\mu 0} \quad , \qquad \text{(D.9a)}$$

$$-\frac{d\ln k_{\nu\theta}}{d\theta}\frac{\sin\theta}{\cos\theta} = 3 + 2r\frac{d\ln k_{\nu r}}{dr} = c_{\nu 0} \quad , \qquad \text{(D.9b)}$$

where $c_{\mu 0}$ and $c_{\nu 0}$ are constants. Solving above equation sets, we obtain

$$k_\mu = c_{\mu 1} r^{c_{\mu 0}-3}(\cos\theta)^{-\frac{c_{\mu 0}}{2}} \quad , \qquad \text{(D.10a)}$$

$$k_\nu = c_{\nu 1} r^{\frac{c_{\nu 0}-3}{2}}(\sin\theta)^{-c_{\nu 0}} \quad , \qquad \text{(D.10b)}$$

where $c_{\mu 1}$ and $c_{\nu 1}$ are also constants. Therefore, the analytical expressions of μ and ν are

$$\mu = \begin{cases} 2c_{\mu 1}\ln r & , \text{ if } c_{\mu 0} = 2 \\ \dfrac{2c_{\mu 1}}{c_{\mu 0}-2}r^{c_{\mu 0}-2}(\cos\theta)^{\frac{2-c_{\mu 0}}{2}} & , \text{ if } c_{\mu 0} \neq 2 \end{cases} \qquad \text{(D.11a)}$$

$$\nu = \begin{cases} 2c_{\nu 1}\ln r & , \text{ if } c_{\nu 0} = 1 \\ \dfrac{2c_{\nu 1}}{c_{\nu 0}-1}r^{\frac{c_{\nu 0}-1}{2}}(\sin\theta)^{1-c_{\nu 0}} & , \text{ if } c_{\nu 0} \neq 1 \end{cases} \qquad \text{(D.11b)}$$

Apparently, μ and ν are only physical to us when $c_{\mu 0} \neq 2$ and $c_{\nu 0} \neq 1$. Note that the selection of (μ,ν) is not unique. We can select $c_{\mu 0}$ and $c_{\nu 0}$ according to different purposes.

Hereafter, we denote the dipolar coordinates as

$$
\begin{cases}
p = -r^{-2n} \cos^n \theta \\[2mm]
q = r^{-\frac{m}{2}} \sin^m \theta \\[2mm]
\phi = \phi
\end{cases}
\tag{D.12}
$$

where $n \neq 0$, $m \neq 0$ and the value of p is selected to increase along $+\hat{\boldsymbol{p}}$ direction. Note that the selection of $n > 0$ and $m > 0$ avoids the singularity at $\theta = 0$, while the selection of $n < 0$ and $m < 0$ avoids the singularity at $r = 0$. Since $0 < \theta < \pi$, we always have q as a real number regardless of the selection of m. However, n needs to be an integer to avoid the complex value of p, unless the domain is constrained above the equator (i.e. $0 < \theta < \pi/2$).

When necessary (e.g. more uniform grid spacing of p or q), the standard dipole coordinates (D.12) can be further generalized as below

$$
\begin{cases}
\tilde{p} = O_p(p) \\[2mm]
\tilde{q} = O_q(q) \\[2mm]
\phi = \phi
\end{cases}
\tag{D.13}
$$

where the orthogonality is still maintained since

$$
\boldsymbol{\nabla}\tilde{p} \cdot \boldsymbol{\nabla}\tilde{q} = \left(\frac{\partial O_p}{\partial p} \boldsymbol{\nabla}p \right) \cdot \left(\frac{\partial O_q}{\partial q} \boldsymbol{\nabla}q \right) = O_p' O_q'(\boldsymbol{\nabla}p \cdot \boldsymbol{\nabla}q) = 0 \quad .
\tag{D.14}
$$

Therefore the operators O_p and O_q merely redistribute the spacing of the coordinates.

D.2   Inverse Transformation

The inverse of dipolar coordinates to spherical coordinates is not trivial. Given (D.12), the coordinate inversion requires solving the quartic equation as follows

$$p^{\frac{2}{n}} r^4 + q^{\frac{2}{m}} r - 1 = 0 \quad . \tag{D.15}$$

When $\theta \in \{0, \pi\}$, we have $r = |p|^{-\frac{1}{2n}}$. Otherwise, (D.15) can be rearranged as

$$\mathbb{C} u^4 + u - 1 = 0 \quad , \tag{D.16a}$$

$$\text{where} \quad \begin{cases} \mathbb{C} = p^{\frac{2}{n}} q^{-\frac{8}{m}} = \dfrac{\cos^2 \theta}{\sin^8 \theta} \geq 0 \\[2mm] u = q^{\frac{2}{m}} r = \sin^2 \theta > 0 \end{cases} \tag{D.16b}$$

This quartic equation has an unique real solution. Note that $\mathbb{C}$ can be very small near the equator (i.e. $\theta = \pi/2$) and very large near the poles (i.e. $\theta \in \{0, \pi\}$). Hence, we need to carefully solve this quartic equation (D.16). Here, we test the solutions using the standard NUMPY routine and both analytical expressions in Kageyama et al. (2006) and Swisdak (2006). In Figure D.1, both the numerical root solver and the analytical expression in Swisdak (2006) have stable numerical behavior near very small and large $\mathbb{C}$. Hence, we summarize the analytical expression in Swisdak (2006) here for the future use

$$u(p, q) = \frac{4\mathbb{U}}{(1 + \mathbb{U})(1 + \sqrt{2\mathbb{U} - 1})} \quad , \tag{D.17a}$$

$$\text{where} \quad \begin{cases} \mathbb{U} = \dfrac{1}{2} \left(\dfrac{\mathbb{A}^2 + \mathbb{A}\mathbb{B} + \mathbb{B}^2}{\mathbb{B}} \right)^{\frac{3}{2}} \\[4mm] \mathbb{A} = \left(\dfrac{256}{27} \mathbb{C} \right)^{\frac{1}{3}} \quad , \quad \mathbb{B} = \left(1 + \sqrt{1 + \dfrac{256}{27} \mathbb{C}} \right)^{\frac{2}{3}} \end{cases} \tag{D.17b}$$
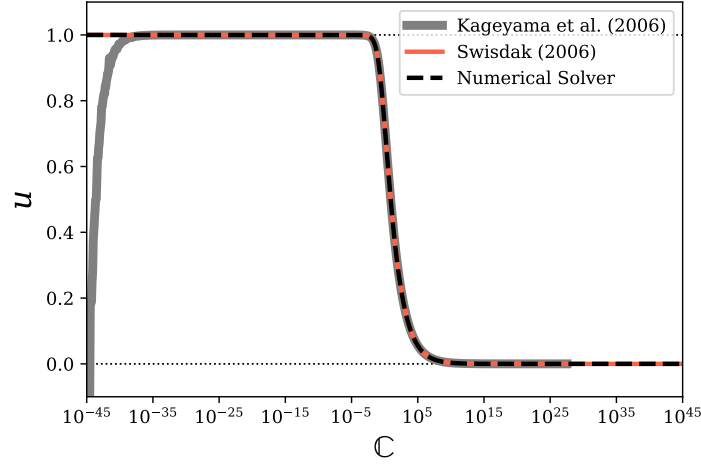
Figure D.1: The solution of quartic equation for the inverse of dipolar coordinates transformation (D.16). Note that the form of analytical expression in Kageyama et al. (2006) fails numerically to resolve the solution when $\mathbb{C}$ is very small or large.

The transformation from the dipole coordinates to the spherical coordinates is then

$$
\begin{cases}
r = u q^{-\frac{2}{m}} \\[2mm]
\theta = \begin{cases} \arcsin u^{\frac{1}{2}} & \text{, if } p < 0 \\[2mm] \pi - \arcsin u^{\frac{1}{2}} & \text{, if } p > 0 \end{cases} & \text{, if } q \neq 0 \\[2mm]
\phi = \phi
\end{cases}
\tag{D.18a}
$$

$$
\begin{cases}
r = |p|^{-\frac{1}{2n}} \\[2mm]
\theta \in \{0, \pi\} & \text{, if } q = 0 \\[2mm]
\phi = \phi
\end{cases}
\tag{D.18b}
$$

For the generalized dipole coordinates (D.13), we need to specify the inverse of O_p and O_q to complete the transformation as

$$
\begin{cases}
p = O_p^{-1}(\tilde{p}) \\[2mm]
q = O_q^{-1}(\tilde{q})
\end{cases}
\tag{D.19}
$$
,

where O_p^{-1} and O_q^{-1} are inverse operators of O_p and O_q.

D.3   Vector and Tensor Operations

Because the inverse of the dipolar coordinates to spherical coordinates is non-trivial, it is more convenient for us to express the geometric factors in its vector and tensor operations in spherical coordinates. Given the dipolar coordinates (D.12), the scale factors can be calculated as

$$\begin{cases} h_p = \dfrac{1}{|n|\sqrt{1+3\cos^2\theta}} \dfrac{r^{2n+1}}{|\cos\theta|^{n-1}} \\[2mm] h_q = \dfrac{2}{|m|\sqrt{1+3\cos^2\theta}} \dfrac{r^{\frac{m+2}{2}}}{(\sin\theta)^{m-1}} \\[2mm] h_\phi = r\sin\theta \end{cases} \tag{D.20}$$

Hence, the grid spacing in dipolar geometry can be tuned via tweaking indices n and m. We can also adopt the appropriate O_p and O_q in the generalized dipolar coordinates (D.13) to adjust the grid spacing (e.g. see section 6.2.2). The scale factors in the generalized dipolar coordinates are

$$h_{\tilde{p}} = \frac{1}{|O_p'|} h_p \quad \text{and} \quad h_{\tilde{q}} = \frac{1}{|O_q'|} \quad . \tag{D.21}$$

The generalized version can be easily adjusted by replacing h_p and h_q with $h_{\tilde{p}}$ and $h_{\tilde{q}}$, respectively. With above scale factors (D.20), we can compute the differential area and volume

$$d\sigma_{pq} = h_p h_q \, dpdq \quad , \qquad d\sigma_{p\phi} = h_p h_\phi \, dpd\phi \quad , \qquad d\sigma_{q\phi} = h_q h_\phi \, dqd\phi \quad , \tag{D.22a}$$

$$d\tau = h_p h_q h_\phi \, dpdqd\phi \quad , \tag{D.22b}$$

223

gradient of a scalar f

$$\boldsymbol{\nabla} f = \frac{1}{h_p}\frac{\partial f}{\partial p}\hat{\boldsymbol{p}} + \frac{1}{h_q}\frac{\partial f}{\partial q}\hat{\boldsymbol{q}} + \frac{1}{h_\phi}\frac{\partial f}{\partial \phi}\hat{\boldsymbol{\phi}} \quad , \tag{D.23}$$

Laplacian of a scalar f

$$\nabla^2 f = \frac{1}{h_p h_q h_\phi}\left[\frac{\partial}{\partial p}\left(\frac{h_q h_\phi}{h_p}\frac{\partial f}{\partial p}\right) + \frac{\partial}{\partial q}\left(\frac{h_p h_\phi}{h_q}\frac{\partial f}{\partial q}\right) + \frac{\partial}{\partial \phi}\left(\frac{h_p h_q}{h_\phi}\frac{\partial f}{\partial \phi}\right)\right] \quad , \tag{D.24}$$

divergence of a vector $\boldsymbol{A}$

$$\boldsymbol{\nabla} \cdot \boldsymbol{A} = \frac{1}{h_p h_q h_\phi}\left[\frac{\partial}{\partial p}(h_q h_\phi A_p) + \frac{\partial}{\partial q}(h_p h_\phi A_q) + \frac{\partial}{\partial \phi}(h_p h_q A_\phi)\right] \quad , \tag{D.25}$$

curl of a vector $\boldsymbol{A}$

$$\begin{aligned}
\boldsymbol{\nabla} \times \boldsymbol{A} = {} & \frac{1}{h_q h_\phi}\left[\frac{\partial}{\partial q}(h_\phi A_\phi) - \frac{\partial}{\partial \phi}(h_q A_q)\right]\hat{\boldsymbol{p}} + \frac{1}{h_p h_\phi}\left[\frac{\partial}{\partial \phi}(h_p A_p) - \frac{\partial}{\partial p}(h_\phi A_\phi)\right]\hat{\boldsymbol{q}} \\
& + \frac{1}{h_p h_q}\left[\frac{\partial}{\partial p}(h_q A_q) - \frac{\partial}{\partial q}(h_p A_p)\right]\hat{\boldsymbol{\phi}} \quad ,
\end{aligned} \tag{D.26}$$

and divergence of a tensor $\mathbf{T}$

$$\boldsymbol{\nabla} \cdot \mathbf{T} = \begin{cases}
\dfrac{1}{h_p h_q h_\phi}\left[\dfrac{\partial}{\partial p}(h_q h_\phi \mathrm{T}_{pp}) + \dfrac{\partial}{\partial q}(h_p h_\phi \mathrm{T}_{qp}) + \dfrac{\partial}{\partial \phi}(h_p h_q \mathrm{T}_{\phi p})\right] \\[2ex]
+\dfrac{\mathrm{T}_{pq}}{h_p h_q}\dfrac{\partial h_p}{\partial q} + \dfrac{\mathrm{T}_{\phi p}}{h_p h_\phi}\dfrac{\partial h_p}{\partial \phi} - \dfrac{\mathrm{T}_{qq}}{h_p h_q}\dfrac{\partial h_q}{\partial p} - \dfrac{\mathrm{T}_{\phi\phi}}{h_p h_\phi}\dfrac{\partial h_\phi}{\partial p}
\end{cases}\hat{\boldsymbol{p}}$$

$$+ \begin{cases}
\dfrac{1}{h_p h_q h_\phi}\left[\dfrac{\partial}{\partial p}(h_q h_\phi \mathrm{T}_{pq}) + \dfrac{\partial}{\partial q}(h_p h_\phi \mathrm{T}_{qq}) + \dfrac{\partial}{\partial \phi}(h_p h_q \mathrm{T}_{\phi q})\right] \\[2ex]
+\dfrac{\mathrm{T}_{qp}}{h_p h_q}\dfrac{\partial h_q}{\partial p} + \dfrac{\mathrm{T}_{q\phi}}{h_q h_\phi}\dfrac{\partial h_q}{\partial \phi} - \dfrac{\mathrm{T}_{pp}}{h_p h_q}\dfrac{\partial h_p}{\partial q} - \dfrac{\mathrm{T}_{\phi\phi}}{h_q h_\phi}\dfrac{\partial h_\phi}{\partial q}
\end{cases}\hat{\boldsymbol{q}} \tag{D.27}$$

$$+ \begin{cases}
\dfrac{1}{h_p h_q h_\phi}\left[\dfrac{\partial}{\partial p}(h_q h_\phi \mathrm{T}_{p\phi}) + \dfrac{\partial}{\partial q}(h_p h_\phi \mathrm{T}_{q\phi}) + \dfrac{\partial}{\partial \phi}(h_p h_q \mathrm{T}_{\phi\phi})\right] \\[2ex]
+\dfrac{\mathrm{T}_{\phi p}}{h_p h_\phi}\dfrac{\partial h_\phi}{\partial p} + \dfrac{\mathrm{T}_{\phi q}}{h_q h_\phi}\dfrac{\partial h_\phi}{\partial q} - \dfrac{\mathrm{T}_{pp}}{h_p h_\phi}\dfrac{\partial h_p}{\partial \phi} - \dfrac{\mathrm{T}_{qq}}{h_q h_\phi}\dfrac{\partial h_q}{\partial \phi}
\end{cases}\hat{\boldsymbol{\phi}} \quad ,$$

where the non-derivative terms of tensor $\mathbf{T}$ in each brace are known as the geometric source terms.

To compute above operations, we first need to prepare some auxiliary derivatives of the dipolar coordinates with respect to the spherical coordinates.

$$
\begin{aligned}
\frac{\partial p}{\partial r} &= \left(\frac{\cos^n \theta}{r^{2n}}\right)(2n)\frac{1}{r} \quad, & \frac{\partial p}{\partial \theta} &= \left(\frac{\cos^n \theta}{r^{2n}}\right)(n)\frac{\sin \theta}{\cos \theta} \quad, \\
\frac{\partial q}{\partial r} &= \left(\frac{\sin^m \theta}{r^{\frac{m}{2}}}\right)\left(-\frac{m}{2}\right)\frac{1}{r} \quad, & \frac{\partial q}{\partial \theta} &= \left(\frac{\sin^m \theta}{r^{\frac{m}{2}}}\right)(m)\frac{\cos \theta}{\sin \theta} \quad.
\end{aligned}
\tag{D.28}
$$

So the Jacobian can be calculated as follows

$$
\begin{aligned}
\frac{\partial(r, \theta)}{\partial(p, q)} &= \begin{pmatrix} \dfrac{\partial r}{\partial p} & \dfrac{\partial r}{\partial q} \\[2ex] \dfrac{\partial \theta}{\partial p} & \dfrac{\partial \theta}{\partial q} \end{pmatrix} = \left(\frac{\partial(p, q)}{\partial(r, \theta)}\right)^{-1} \\[2ex]
&= \begin{pmatrix} \dfrac{\partial p}{\partial r} & \dfrac{\partial p}{\partial \theta} \\[2ex] \dfrac{\partial q}{\partial r} & \dfrac{\partial q}{\partial \theta} \end{pmatrix}^{-1} = \frac{1}{\det\left(\dfrac{\partial(p, q)}{\partial(r, \theta)}\right)} \begin{pmatrix} \dfrac{\partial q}{\partial \theta} & -\dfrac{\partial p}{\partial \theta} \\[2ex] -\dfrac{\partial q}{\partial r} & \dfrac{\partial p}{\partial r} \end{pmatrix} \quad,
\end{aligned}
\tag{D.29a}
$$

where $\det\left(\dfrac{\partial(p, q)}{\partial(r, \theta)}\right) = \dfrac{nm}{2}r^{-2n-\frac{m}{2}-1}(\cos \theta)^{n-1}(\sin \theta)^{m-1}(3\cos^2 \theta + 1) \neq 0$.

Thus, following conditions needs to be satisfied to guarantee a reversible Jacobian

$$
\theta \neq \frac{\pi}{2} \qquad \text{, when } n \neq 1 \quad,
\tag{D.30a}
$$

$$
\theta \notin \{0, \pi\} \quad \text{, when } m \neq 1 \quad.
\tag{D.30b}
$$

Note that there is a possibility that the singularity may be eliminated during these calculations. Therefore, we must conduct a sanity check to ensure its continued existence. But

first, we can temporarily ignore the singularity and proceed with the derivations. Following the inverse of the Jacobian (D.29a), we can obtain the derivatives of the spherical coordinates with respect to the dipolar coordinates

$$
\begin{aligned}
\frac{\partial r}{\partial p} &= \left(\frac{r^{2n}}{\cos^n \theta}\right)\left(\frac{2}{n}\right)\frac{r\cos^2 \theta}{1+3\cos^2 \theta} & \frac{\partial r}{\partial q} &= \left(\frac{r^{\frac{m}{2}}}{\sin^m \theta}\right)\left(-\frac{2}{m}\right)\frac{r\sin^2 \theta}{1+3\cos^2 \theta} \\
\frac{\partial \theta}{\partial p} &= \left(\frac{r^{2n}}{\cos^n \theta}\right)\left(\frac{1}{n}\right)\frac{\sin \theta \cos \theta}{1+3\cos^2 \theta} & \frac{\partial \theta}{\partial q} &= \left(\frac{r^{\frac{m}{2}}}{\sin^m \theta}\right)\left(\frac{4}{m}\right)\frac{\sin \theta \cos \theta}{1+3\cos^2 \theta}
\end{aligned}
\tag{D.31}
$$

Given the scale factors (D.20), the derivatives of them with respect to the spherical coordinates are

$$
\begin{aligned}
\frac{\partial h_p}{\partial r} &= h_p \frac{2n+1}{r} & \frac{\partial h_p}{\partial \theta} &= h_p \left[\frac{3\sin \theta \cos \theta}{1+3\cos^2 \theta} + (n-1)\frac{\sin \theta}{|\cos \theta|}\right] & \frac{\partial h_p}{\partial \phi} &= 0 \\
\frac{\partial h_q}{\partial r} &= h_q \frac{m+2}{2r} & \frac{\partial h_q}{\partial \theta} &= h_q \left[\frac{3\sin \theta \cos \theta}{1+3\cos^2 \theta} - (m-1)\frac{\cos \theta}{\sin \theta}\right] & \frac{\partial h_q}{\partial \phi} &= 0 \\
\frac{\partial h_\phi}{\partial r} &= \sin \theta & \frac{\partial h_\phi}{\partial \theta} &= r\cos \theta & \frac{\partial h_\phi}{\partial \phi} &= 0
\end{aligned}
\tag{D.32}
$$

Applying the chain rules, we can calculate the derivatives of the scale factors with respect to the dipolar coordinates

$$
\frac{\partial h_p}{\partial p} = h_p \left[\left(4+\frac{2}{n}\right)\cos^2 \theta + \left(1-\frac{1}{n}\right)\frac{\cos \theta}{|\cos \theta|}\sin^2 \theta \right.
$$
$$
\left. + \left(\frac{3}{n}\right)\frac{\sin^2 \theta \cos^2 \theta}{1+3\cos^2 \theta}\right]\frac{1}{1+3\cos^2 \theta}\frac{r^{2n}}{\cos^n \theta} \quad , \quad \text{(D.33a)}
$$

$$
\frac{\partial h_p}{\partial q} = h_p \left[\frac{4n}{m}\left(\frac{\cos \theta}{|\cos \theta|}-1\right) - \frac{4}{m}\left(\frac{1}{2}+\frac{\cos \theta}{|\cos \theta|}\right)\right.
$$
$$
\left. + \left(\frac{12}{m}\right)\frac{\cos^2 \theta}{1+3\cos^2 \theta}\right]\frac{\sin^2 \theta}{1+3\cos^2 \theta}\frac{r^{\frac{m}{2}}}{\sin^m \theta} \quad , \quad \text{(D.33b)}
$$

$$
\frac{\partial h_p}{\partial \phi} = 0 \quad , \tag{D.33c}
$$

$$
\frac{\partial h_q}{\partial p} = h_q \left(\frac{6}{n}\right)\frac{\cos^2 \theta(1+\cos^2 \theta)}{(1+3\cos^2 \theta)^2}\frac{r^{2n}}{\cos^n \theta} \quad , \tag{D.33d}
$$

$$
\frac{\partial h_q}{\partial q} = h_q \left\{-1+\left[\frac{2}{m}(1+\cos^2 \theta)+\left(\frac{12}{m}\right)\frac{\sin^2 \theta \cos^2 \theta}{1+3\cos^2 \theta}\right]\frac{1}{1+3\cos^2 \theta}\right\}\frac{r^{\frac{m}{2}}}{\sin^m \theta} \quad , \tag{D.33e}
$$

$$\frac{\partial h_q}{\partial \phi} = 0 \quad , \tag{D.33f}$$

$$\frac{\partial h_\phi}{\partial p} = h_\phi \left(\frac{3}{n}\right) \frac{\cos^2 \theta}{1 + 3\cos^2 \theta} \frac{r^{2n}}{\cos^n \theta} \quad , \tag{D.33g}$$

$$\frac{\partial h_\phi}{\partial q} = h_\phi \left(\frac{2}{m}\right) \frac{3\cos^2 \theta - 1}{1 + 3\cos^2 \theta} \frac{r^{\frac{m}{2}}}{\sin^m \theta} \quad , \tag{D.33h}$$

$$\frac{\partial h_\phi}{\partial \phi} = 0 \quad . \tag{D.33i}$$

With the above auxiliary quantities, we can compute the all the vector and tensor operations in the given dipole coordinate system.

Appendix E

Derivation of Polarized Radiative Transfer in Magnetic Field

E.1 Classical Thomson Scattering in Magnetic Field

E.1.1 Equation of Motion

Consider a planar electromagnetic wave encountering a moving electron with charge $-e$ and mass m_e in the presence of a strong external magnetic field $\boldsymbol{B}_0 = B_0\hat{z}$. The wave vector and the angular frequency of the incident electromagnetic wave are $\boldsymbol{k}_\mathrm{i}$ and ω, respectively. Its corresponding electric field is $\boldsymbol{E}_\mathrm{i} = \hat{\boldsymbol{e}}_\mathrm{i} E_\mathrm{i} \exp[i(\boldsymbol{k}_\mathrm{i} \cdot \boldsymbol{r} - \omega t)]$ and magnetic field is $\boldsymbol{B}_\mathrm{i} = \hat{\boldsymbol{k}}_\mathrm{i} \times \boldsymbol{E}_\mathrm{i}$, where $\hat{\boldsymbol{e}}_\mathrm{i}$ is the unit vector of the incident electric field. The equation of motion in the classical regime is set up by the Newton's second law and Lorentz force as follows:

$$m_e\ddot{\boldsymbol{r}}_e = -e\left[\boldsymbol{E}_\mathrm{i} + \frac{1}{c}\dot{\boldsymbol{r}}_e \times (\boldsymbol{B}_\mathrm{i} + \boldsymbol{B}_0)\right] \quad , \tag{E.1a}$$

where $\boldsymbol{r}_e(t)$ refers to the electron trajectory. In the non-relativistic regime (i.e. $\dot{\boldsymbol{r}}_e \ll c$), the magnetic Lorentz force introduced by $\boldsymbol{B}_\mathrm{i}$ is negligible. For convenience, we choose

the local frame (i.e. $\boldsymbol{r} = \boldsymbol{0}$ for the electric field of the incident radiation) for further evaluation. The equation of motion can be reduced to

$$
\begin{pmatrix} \ddot{r}_{e,x} \\ \ddot{r}_{e,y} \\ \ddot{r}_{e,z} \end{pmatrix} + \omega_{ce} \begin{pmatrix} \dot{r}_{e,y} \\ -\dot{r}_{e,x} \\ 0 \end{pmatrix} = -\frac{e}{m_e} E_{\mathrm{i}} e^{-i\omega t} \begin{pmatrix} \hat{\boldsymbol{e}}_{\mathrm{i}} \cdot \hat{\boldsymbol{x}} \\ \hat{\boldsymbol{e}}_{\mathrm{i}} \cdot \hat{\boldsymbol{y}} \\ \hat{\boldsymbol{e}}_{\mathrm{i}} \cdot \hat{\boldsymbol{z}} \end{pmatrix} \quad , \tag{E.1b}
$$

where $\omega_{ce} = eB_0/(m_e c)$ is the electron cyclotron frequency. The equation (E.1b) can be solved analytically as follows:

$$
\boldsymbol{r}_e = -\frac{e}{m_e} E_{\mathrm{i}} \begin{pmatrix} \dfrac{-(\hat{\boldsymbol{e}}_{\mathrm{i}} \cdot \hat{\boldsymbol{x}}) + i(\omega_{ce}/\omega)(\hat{\boldsymbol{e}}_{\mathrm{i}} \cdot \hat{\boldsymbol{y}})}{\omega^2 - \omega_{ce}^2} \\ \dfrac{-(\hat{\boldsymbol{e}}_{\mathrm{i}} \cdot \hat{\boldsymbol{y}}) - i(\omega_{ce}/\omega)(\hat{\boldsymbol{e}}_{\mathrm{i}} \cdot \hat{\boldsymbol{x}})}{\omega^2 - \omega_{ce}^2} \\ \dfrac{-(\hat{\boldsymbol{e}}_{\mathrm{i}} \cdot \hat{\boldsymbol{z}})}{\omega^2} \end{pmatrix} e^{-i\omega t} + \begin{pmatrix} c_{x1} \\ c_{y1} \\ 0 \end{pmatrix} \cos(\omega_{ce} t) + \begin{pmatrix} c_{x2} \\ c_{y2} \\ 0 \end{pmatrix} \sin(\omega_{ce} t) \quad ,
$$
$$\tag{E.2}$$

where c_{x1}, c_{x2}, c_{y1}, and c_{y2} are constants that can be determined by the initial condition. The solution in z-direction introduces the time-harmonic current density and simply leads to the Thomson scattering cross section, which is expected because the electron can freely move along the magnetic field $\boldsymbol{B}_0$. The solution in x-y plane have three basic modes: $\exp(-i\omega t)$, $\cos(\omega_{ce} t)$, and $\sin(\omega_{ce} t)$. Obviously, we are not interested in the latter two because it merely refers to the helix motion of the electron around the magnetic field. Hence, we only keep the first mode, i.e. $\exp(-i\omega t)$, for the further evaluation.

$$
\boldsymbol{r}_e = -\frac{e}{m_e \omega^2} E_{\mathrm{i}} e^{-i\omega t} \hat{\boldsymbol{r}}_e \quad , \tag{E.3a}
$$

where the direction of the electron trajectory is

$$
\hat{\boldsymbol{r}}_e = -\left[\frac{(\hat{\boldsymbol{e}}_{\mathrm{i}} \cdot \hat{\boldsymbol{x}}) - i\eta(\hat{\boldsymbol{e}}_{\mathrm{i}} \cdot \hat{\boldsymbol{y}})}{1 - \eta^2} \hat{\boldsymbol{x}} + \frac{(\hat{\boldsymbol{e}}_{\mathrm{i}} \cdot \hat{\boldsymbol{y}}) + i\eta(\hat{\boldsymbol{e}}_{\mathrm{i}} \cdot \hat{\boldsymbol{x}})}{1 - \eta^2} \hat{\boldsymbol{y}} + (\hat{\boldsymbol{e}}_{\mathrm{i}} \cdot \hat{\boldsymbol{z}})\hat{\boldsymbol{z}} \right] \quad , \tag{E.3b}
$$

and $\eta \equiv \omega_{ce}/\omega$.

E.1.2   Scattering Cross Section

To describe the scattered radiation, we similarly define the outgoing electromagnetic wave with the wave vector $\boldsymbol{k}_o$, electric field $\boldsymbol{E}_o = \hat{\boldsymbol{e}}_o E_o \exp[i(\boldsymbol{k}_o \cdot \boldsymbol{r} - \omega t)]$, and magnetic field $\boldsymbol{B}_o = \hat{\boldsymbol{k}}_o \times \boldsymbol{E}_o$. For convenience, we adopt the outgoing wave propagation direction as $\hat{\boldsymbol{k}}_o = \hat{\boldsymbol{r}}$ in the local frame. The cross section for scattering is scaled by the ratio of the scattered radiation power to the incident radiation power, e.g. see equation (21.2) of Zangwill (2012).

$$d\sigma = \frac{E_o^2}{E_i^2} r^2 d\Omega \quad , \tag{E.4}$$

where $r^2 d\Omega$ refers to the spherical surface element. The outgoing radiation is essentially sourced by the current density of the moving electron and the electromagnetic wave in vacuum can be entirely determined by the radiation vector potential. The key is to eliminate the charge density using the charge continuity equation (for details see chapter (20.5.3) of Zangwill 2012). Therefore, we can rewrite the electric field of the outgoing radiation as

$$\boldsymbol{E}_o(\boldsymbol{r}, t) = \hat{\boldsymbol{r}} \times \left(\hat{\boldsymbol{r}} \times \frac{1}{c} \frac{\partial \boldsymbol{A}_o(\boldsymbol{r}, t)}{\partial t} \right) \quad , \tag{E.5a}$$

$$\boldsymbol{A}_o(\boldsymbol{r}, t) = \frac{1}{c} \int d^3 r' \frac{\boldsymbol{j}(\boldsymbol{r}', t - |\boldsymbol{r} - \boldsymbol{r}'|/c)}{|\boldsymbol{r} - \boldsymbol{r}'|} \quad , \tag{E.5b}$$

where $\boldsymbol{A}_o$ is the retarded vector potential and $\boldsymbol{j}$ refers to the current density. For convenience of calculation, we can adopt the following expansion:

$$|\boldsymbol{r} - \boldsymbol{r}'| = r \left[1 - (r'/r)(\hat{\boldsymbol{r}}' \cdot \hat{\boldsymbol{r}}) + \frac{1}{2}(r'/r)^2 [1 - (\hat{\boldsymbol{r}}' \cdot \hat{\boldsymbol{r}})^2] + O\left((r'/r)^3\right) \right] \quad , \tag{E.6}$$

where we retain the leading term for the denominator and the first two terms for the current density in the numerator of (E.5b). The general idea of this approximation is to keep the overall variance of $1/r$ while resolve the angular dependence in the current density. The detail reasoning can be found in chapter (20.5.3) of Zangwill (2012). Hence, we can further multipole expand the current density as follows:

$$\boldsymbol{j}(\boldsymbol{r}',t - \frac{|\boldsymbol{r}-\boldsymbol{r}'|}{c}) \simeq \boldsymbol{j}(\boldsymbol{r}',t - \frac{r}{c} + \frac{\boldsymbol{r}'\cdot\hat{\boldsymbol{r}}}{c}) = \boldsymbol{j}(\boldsymbol{r}',t - \frac{r}{c}) + \left(\frac{\boldsymbol{r}'\cdot\hat{\boldsymbol{r}}}{c}\right)\frac{\partial}{\partial t}\boldsymbol{j}(\boldsymbol{r}',t - \frac{r}{c})$$
$$+ \frac{1}{2}\left(\frac{\boldsymbol{r}'\cdot\hat{\boldsymbol{r}}}{c}\right)^2\frac{\partial^2}{\partial t^2}\boldsymbol{j}(\boldsymbol{r}',t - \frac{r}{c}) + O\left(\left(\frac{\boldsymbol{r}'\cdot\hat{\boldsymbol{r}}}{c}\right)^3\right) \quad, \quad \text{(E.7)}$$

where the first term sources the electric dipole radiation, the second term sources the magnetic dipole radiation, and the third term sources the electric quadrupole radiation. The detail proof can be found in chapter (20.7) of Zangwill (2012). In our case of non-relativistic regime, we consider the long radiation wavelength and the small electron oscillation (in terms of amplitude and frequency). Since the oscillating electron produces electric dipole moment, we can only retain and evaluate the electric dipole term of equation (E.7). Given the current density of the moving electron $\boldsymbol{j}(\boldsymbol{r},t) = -e\dot{\boldsymbol{r}}_e\delta(\boldsymbol{r}-\boldsymbol{r}_e)$, the magnetic vector potential for the outgoing radiation can be approximated as:

$$\boldsymbol{A}_{\mathrm{o}}(\boldsymbol{r},t) \simeq \frac{1}{cr}\int \boldsymbol{j}(\boldsymbol{r}',t - \frac{r}{c})d^3r' = \frac{-e}{cr}\frac{d}{dt}\boldsymbol{r}_e(t - \frac{r}{c}) \quad. \quad\quad \text{(E.8)}$$

Therefore, the electric field of the scattered radiation is reduced to

$$\boldsymbol{E}_{\mathrm{o}} \simeq \frac{1}{c^2r}\hat{\boldsymbol{r}} \times \left[\hat{\boldsymbol{r}} \times \frac{d^2}{dt^2}(-e\boldsymbol{r}_e)\right] \quad. \quad\quad \text{(E.9)}$$

Here, $\boldsymbol{r}_e = \boldsymbol{r}_e(t - r/c)$ is retarded. But this does not bother in the cross section calculation, as the power is time averaged. With (E.9), (E.3), and (E.4), we can obtain a

general expression for the scattered electric field and the differential cross section of the magnetic Thomson scattering:

$$\boldsymbol{E}_{\mathrm{o}} \simeq -\frac{r_e}{r} E_i e^{-i\omega t} \left[\hat{\boldsymbol{r}} \times (\hat{\boldsymbol{r}} \times \hat{\boldsymbol{r}}_e) \right] \quad , \tag{E.10}$$

$$\frac{d\sigma}{d\Omega} \simeq r_e^2 \left| \hat{\boldsymbol{r}} \times (\hat{\boldsymbol{r}} \times \hat{\boldsymbol{r}}_e) \right|^2 \quad , \tag{E.11}$$

where $r_e = e^2/(m_e c^2)$ is the classical electron radius. Given the radial direction $\hat{\boldsymbol{r}} = \hat{\boldsymbol{x}} \sin\theta \cos\phi + \hat{\boldsymbol{y}} \sin\theta \sin\phi + \hat{\boldsymbol{z}} \cos\theta$ in Cartesian coordinates, we can prepare the following auxiliary expression for convenience of the further calculation:

$$\hat{\boldsymbol{r}} \times (\hat{\boldsymbol{r}} \times \hat{\boldsymbol{r}}_e) = (\hat{\boldsymbol{r}} \cdot \hat{\boldsymbol{r}}_e)\hat{\boldsymbol{r}} - \hat{\boldsymbol{r}}_e$$

$$= \begin{bmatrix} -(1 - \sin^2\theta\cos^2\phi) & \sin^2\theta\sin\phi\cos\phi & \sin\theta\cos\theta\cos\phi \\ \sin^2\theta\sin\phi\cos\phi & -(1 - \sin^2\theta\sin^2\phi) & \sin\theta\cos\theta\sin\phi \\ \sin\theta\cos\theta\cos\phi & \sin\theta\cos\theta\sin\phi & -\sin^2\theta \end{bmatrix} \hat{\boldsymbol{r}}_e \quad . \tag{E.12}$$

Let us now confirm above derivations with some previous works. In Chou (1986) and Caiazzo & Heyl (2021), the incident radiation is initialized in the x-z plane (i.e. azimuthal angle $\beta = 0$) and have the polar angle α (see the geometric configuration in Fig. 1 of Chou 1986 or Fig. 2 of Caiazzo & Heyl 2021). In this case, the direction of the incident radiation is simply $\hat{\boldsymbol{k}}_i = \hat{\boldsymbol{x}} \sin\alpha + \hat{\boldsymbol{z}} \cos\alpha$. There are two independent linear polarization modes, where the extraordinary mode (X-mode) is polarized along the y-direction (i.e. $\hat{\boldsymbol{e}}_{i,\perp} = \hat{\boldsymbol{y}}$) and the ordinary mode (O-mode) is perpendicular to the radiation propagation direction in the x-z plane (i.e. $\hat{\boldsymbol{e}}_{i,\parallel} = \hat{\boldsymbol{x}} \cos\alpha - \hat{\boldsymbol{z}} \sin\alpha$). We can further compute the cross section of these two polarization modes by substituting the corresponding radiation propagation direction in (E.3) and (E.11). Then the differential scattering cross sections

of X-modes and O- are

$$\frac{d\sigma_X}{d\Omega} = \frac{r_e^2}{(1-\eta^2)^2} \left[(1 - \sin^2\theta \sin^2\phi) + \eta^2(1 - \sin^2\theta \cos^2\phi) \right] \quad , \tag{E.13a}$$

$$\frac{d\sigma_O}{d\Omega} = r_e^2 \left\{ \frac{\cos^2\alpha}{(1-\eta^2)^2}(1 - \sin^2\theta \cos^2\phi) + \frac{\eta^2\cos^2\alpha}{(1-\eta^2)^2}(1 - \sin^2\theta \sin^2\phi) \right.$$
$$\left. + \frac{2\sin\alpha\cos\alpha}{1-\eta^2}\sin\theta\cos\theta\cos\phi + \sin^2\alpha\sin^2\theta \right\} \quad , \tag{E.13b}$$

which can be further integrated to obtain the total cross sections as

$$\sigma_O = \sigma_T \left[\sin^2\alpha + \frac{1+\eta^2}{(1-\eta^2)^2}\cos^2\alpha \right] \quad , \tag{E.14a}$$

$$\sigma_X = \sigma_T \frac{1+\eta^2}{(1-\eta^2)^2} \quad . \tag{E.14b}$$

Here, the constant $\sigma_T = 8\pi r_e^2/3$ is the Thomson cross section. Our results recover the equations (18a)-(18b) of Caiazzo & Heyl (2021) and the average is consistent with the equations (36) of Chou (1986).

E.1.3   Mueller Matrix

In this section, we will construct the Stokes parameters to describe the polarization state and establish the Mueller matrix for the polarized radiation transfer of magnetic Thomson scattering. Consider the incident radiation with arbitrary direction $\hat{\boldsymbol{k}}_i$ and the unit vectors of linearly polarized basis $\hat{\boldsymbol{e}}_{i,\parallel}$ and $\hat{\boldsymbol{e}}_{i,\perp}$, where

$$\hat{\boldsymbol{k}}_i = \hat{\boldsymbol{x}}\sin\alpha\cos\beta + \hat{\boldsymbol{y}}\sin\alpha\sin\beta + \hat{\boldsymbol{z}}\cos\alpha \quad , \tag{E.15a}$$

$$\hat{\boldsymbol{e}}_{i,\parallel} = \hat{\boldsymbol{x}}\cos\alpha\cos\beta + \hat{\boldsymbol{y}}\cos\alpha\sin\beta - \hat{\boldsymbol{z}}\sin\alpha \quad , \tag{E.15b}$$

$$\hat{\boldsymbol{e}}_{i,\perp} = -\hat{\boldsymbol{x}}\sin\beta + \hat{\boldsymbol{y}}\cos\beta \quad . \tag{E.15c}$$

233

Similarly, for the scattered radiation,

$$\hat{\boldsymbol{k}}_{\rm o} = \hat{\boldsymbol{x}} \sin\theta \cos\phi + \hat{\boldsymbol{y}} \sin\theta \sin\phi + \hat{\boldsymbol{z}} \cos\theta \quad , \tag{E.16a}$$

$$\hat{\boldsymbol{e}}_{\rm o,\parallel} = \hat{\boldsymbol{x}} \cos\theta \cos\phi + \hat{\boldsymbol{y}} \cos\theta \sin\phi - \hat{\boldsymbol{z}} \sin\theta \quad , \tag{E.16b}$$

$$\hat{\boldsymbol{e}}_{\rm o,\perp} = -\hat{\boldsymbol{x}} \sin\phi + \hat{\boldsymbol{y}} \cos\phi \quad . \tag{E.16c}$$

Recall that α and β are polar and azimuthal angles of the incident radiation, respectively. The X-mode is polarized perpendicular to both external magnetic field and the radiation propagation direction, i.e. $\hat{\boldsymbol{k}} \cdot \hat{\boldsymbol{e}}_{\perp}=0$ and $\hat{\boldsymbol{z}} \cdot \hat{\boldsymbol{e}}_{\perp}=0$. The O-mode is polarized perpendicular to the radiation propagation direction, i.e. $\hat{\boldsymbol{k}} \cdot \hat{\boldsymbol{e}}_{\parallel}=0$, and in the plane formed by $\hat{\boldsymbol{k}}$ and $\hat{\boldsymbol{z}}$, i.e. $(\hat{\boldsymbol{k}} \times \hat{\boldsymbol{z}}) \cdot \hat{\boldsymbol{e}}_{\parallel} = 0$. The equation (E.10) then gives the direction of the electric field for the scattered radiation $\hat{\boldsymbol{e}}_{\rm o}$ as a function of $\hat{\boldsymbol{e}}_{\rm i}$.

$$\hat{\boldsymbol{e}}_{\rm o} = -\frac{E_{\rm i} r_e}{E_{\rm o} r} \left[(\hat{\boldsymbol{k}}_{\rm o} \cdot \hat{\boldsymbol{r}}_e)\hat{\boldsymbol{k}}_{\rm o} - \hat{\boldsymbol{r}}_e \right] \quad , \tag{E.17}$$

where $\hat{\boldsymbol{r}}_e$ depends on $\hat{\boldsymbol{e}}_{\rm i}$ given by (E.3). This essentially allows us to express the scattered radiation in terms of the incident radiation. Let us start with the Stokes parameters (I, Q, U, V), where

$$I \propto E_{\parallel} E_{\parallel}^* + E_{\perp} E_{\perp}^* \quad , \tag{E.18a}$$

$$Q \propto E_{\parallel} E_{\parallel}^* - E_{\perp} E_{\perp}^* \quad , \tag{E.18b}$$

$$U \propto E_{\parallel} E_{\perp}^* + E_{\parallel}^* E_{\perp} \quad , \tag{E.18c}$$

$$V \propto i(E_{\parallel} E_{\perp}^* - E_{\parallel}^* E_{\perp}) \quad . \tag{E.18d}$$

The scattered radiation can be then given by the Mueller matrix multiplying with the Stokes intensity vector of the incident radiation as

$$
\begin{pmatrix} I_{\mathrm{o}} \\ Q_{\mathrm{o}} \\ U_{\mathrm{o}} \\ V_{\mathrm{o}} \end{pmatrix} \propto \frac{r_e^2}{2r^2} \begin{pmatrix} M_{11} & M_{12} & M_{13} & M_{14} \\ M_{21} & M_{22} & M_{23} & M_{24} \\ M_{31} & M_{32} & M_{33} & M_{34} \\ M_{41} & M_{42} & M_{43} & M_{44} \end{pmatrix} \begin{pmatrix} I_{\mathrm{i}} \\ Q_{\mathrm{i}} \\ U_{\mathrm{i}} \\ V_{\mathrm{i}} \end{pmatrix} .
\tag{E.19}
$$

Apparently, in order to obtain the Mueller matrix, it is necessary to express the system using the orthogonal basis $(\hat{\boldsymbol{k}}_{\mathrm{i}}, \hat{\boldsymbol{e}}_{\mathrm{i},\parallel}, \hat{\boldsymbol{e}}_{\mathrm{i},\perp})$. For any given vector $\boldsymbol{n}$, we have the coordinates transformation as follows:

$$
\begin{pmatrix} \boldsymbol{n} \cdot \hat{\boldsymbol{x}} \\ \boldsymbol{n} \cdot \hat{\boldsymbol{y}} \\ \boldsymbol{n} \cdot \hat{\boldsymbol{z}} \end{pmatrix} = \begin{pmatrix} \sin\alpha\cos\beta & \cos\alpha\cos\beta & -\sin\beta \\ \sin\alpha\sin\beta & \cos\alpha\sin\beta & \cos\beta \\ \cos\alpha & -\sin\alpha & 0 \end{pmatrix} \begin{pmatrix} \boldsymbol{n} \cdot \hat{\boldsymbol{k}}_{\mathrm{i}} \\ \boldsymbol{n} \cdot \hat{\boldsymbol{e}}_{\mathrm{i},\parallel} \\ \boldsymbol{n} \cdot \hat{\boldsymbol{e}}_{\mathrm{i},\perp} \end{pmatrix} .
\tag{E.20}
$$

Following (E.17), we first calculate the parallel and perpendicular components of the scattered electric field as

$$
E_{\mathrm{o},\parallel} = E_{\mathrm{i}}\frac{r_e}{r}(\hat{\boldsymbol{r}}_e \cdot \hat{\boldsymbol{e}}_{\mathrm{o},\parallel}) = E_{\mathrm{i}}\frac{r_e}{r}\left[(\hat{\boldsymbol{r}}_e \cdot \hat{\boldsymbol{x}})\cos\theta\cos\phi + (\hat{\boldsymbol{r}}_e \cdot \hat{\boldsymbol{y}})\cos\theta\sin\phi - (\hat{\boldsymbol{r}}_e \cdot \hat{\boldsymbol{z}})\sin\theta\right],
\tag{E.21a}
$$

$$
E_{\mathrm{o},\perp} = E_{\mathrm{i}}\frac{r_e}{r}(\hat{\boldsymbol{r}}_e \cdot \hat{\boldsymbol{e}}_{\mathrm{o},\perp}) = E_{\mathrm{i}}\frac{r_e}{r}\left[-(\hat{\boldsymbol{r}}_e \cdot \hat{\boldsymbol{x}})\sin\phi + (\hat{\boldsymbol{r}}_e \cdot \hat{\boldsymbol{y}})\cos\phi\right].
\tag{E.21b}
$$

Given the electron trajectory in Cartesian coordinates (E.3) and $\hat{\boldsymbol{e}}_{\mathrm{i}} \cdot \hat{\boldsymbol{k}}_{\mathrm{i}} = 0$, we can use the coordinate transformation (E.20) to obtain the electron position in terms of the components under the basis of $(\hat{\boldsymbol{k}}_{\mathrm{i}}, \hat{\boldsymbol{e}}_{\mathrm{i},\parallel}, \hat{\boldsymbol{e}}_{\mathrm{i},\perp})$:

$$
\hat{\boldsymbol{r}}_e \cdot \hat{\boldsymbol{x}} = \frac{1}{1-\eta^2}\left[(-\cos\alpha\cos\beta + i\eta\cos\alpha\sin\beta)(\hat{\boldsymbol{e}}_{\mathrm{i}} \cdot \hat{\boldsymbol{e}}_{\mathrm{i},\parallel}) + (\sin\beta + i\eta\cos\beta)(\hat{\boldsymbol{e}}_{\mathrm{i}} \cdot \hat{\boldsymbol{e}}_{\mathrm{i},\perp})\right] ,
$$

$$
\hat{\boldsymbol{r}}_e \cdot \hat{\boldsymbol{y}} = \frac{1}{1-\eta^2}\left[(-\cos\alpha\sin\beta - i\eta\cos\alpha\cos\beta)(\hat{\boldsymbol{e}}_{\mathrm{i}} \cdot \hat{\boldsymbol{e}}_{\mathrm{i},\parallel}) - (\cos\beta - i\eta\sin\beta)(\hat{\boldsymbol{e}}_{\mathrm{i}} \cdot \hat{\boldsymbol{e}}_{\mathrm{i},\perp})\right] ,
$$

$$
\hat{\boldsymbol{r}}_e \cdot \hat{\boldsymbol{z}} = (\sin\alpha)(\hat{\boldsymbol{e}}_{\mathrm{i}} \cdot \hat{\boldsymbol{e}}_{\mathrm{i},\parallel}) .
$$

Plug above into (E.21), we can obtain expressions for the scattered electric field in terms of the components under the basis of $(\hat{\boldsymbol{k}}_i, \hat{\boldsymbol{e}}_{i,\parallel}, \hat{\boldsymbol{e}}_{i,\perp})$:

$$E_{o,\parallel} = E_i \frac{r_e}{r} \left[\mathcal{A}_1 (\hat{\boldsymbol{e}}_i \cdot \hat{\boldsymbol{e}}_{i,\parallel}) + \mathcal{A}_2 (\hat{\boldsymbol{e}}_i \cdot \hat{\boldsymbol{e}}_{i,\perp}) \right] \quad ,$$

$$E_{o,\perp} = E_i \frac{r_e}{r} \left[\mathcal{A}_3 (\hat{\boldsymbol{e}}_i \cdot \hat{\boldsymbol{e}}_{i,\parallel}) + \mathcal{A}_4 (\hat{\boldsymbol{e}}_i \cdot \hat{\boldsymbol{e}}_{i,\perp}) \right] \quad .$$

The complex coefficients $\mathcal{A}_1$, $\mathcal{A}_2$, $\mathcal{A}_3$, and $\mathcal{A}_4$ are

$$\mathcal{A}_1 = \mathcal{A}_{1R} + i\mathcal{A}_{1I} = \left(\frac{-1}{1 - \eta^2} \cos\alpha \cos\theta \cos\tilde{\phi} - \sin\alpha \sin\theta \right) + i \left(\frac{-\eta}{1 - \eta^2} \cos\alpha \cos\theta \sin\tilde{\phi} \right) \ ,$$

$$\mathcal{A}_2 = \mathcal{A}_{2R} + i\mathcal{A}_{2I} = \left(\frac{-1}{1 - \eta^2} \cos\theta \sin\tilde{\phi} \right) + i \left(\frac{\eta}{1 - \eta^2} \cos\theta \cos\tilde{\phi} \right) \ ,$$

$$\mathcal{A}_3 = \mathcal{A}_{3R} + i\mathcal{A}_{3I} = \left(\frac{1}{1 - \eta^2} \cos\alpha \sin\tilde{\phi} \right) + i \left(\frac{-\eta}{1 - \eta^2} \cos\alpha \cos\tilde{\phi} \right) \ ,$$

$$\mathcal{A}_4 = \mathcal{A}_{4R} + i\mathcal{A}_{4I} = \left(\frac{-1}{1 - \eta^2} \cos\tilde{\phi} \right) + i \left(\frac{-\eta}{1 - \eta^2} \sin\tilde{\phi} \right) \ ,$$

where $\tilde{\phi} \equiv \phi - \beta$ is the azimuthal angle difference between the incident and scattered radiation. The subscripts 'R' and 'I' refer to the real and imaginary parts of the complex coefficients, respectively. Recall that equations (E.18) allow us to express the incident electric field in terms of the Stokes parameters:

$$E_{i,\parallel} E_{i,\parallel}^* = E_i^2 (\hat{\boldsymbol{e}}_i \cdot \hat{\boldsymbol{e}}_{i,\parallel})(\hat{\boldsymbol{e}}_i \cdot \hat{\boldsymbol{e}}_{i,\parallel})^* \propto \frac{1}{2}(I_i + Q_i) \quad , \tag{E.22a}$$

$$E_{i,\perp} E_{i,\perp}^* = E_i^2 (\hat{\boldsymbol{e}}_i \cdot \hat{\boldsymbol{e}}_{i,\perp})(\hat{\boldsymbol{e}}_i \cdot \hat{\boldsymbol{e}}_{i,\perp})^* \propto \frac{1}{2}(I_i - Q_i) \quad , \tag{E.22b}$$

$$E_{i,\parallel} E_{i,\perp}^* = E_i^2 (\hat{\boldsymbol{e}}_i \cdot \hat{\boldsymbol{e}}_{i,\parallel})(\hat{\boldsymbol{e}}_i \cdot \hat{\boldsymbol{e}}_{i,\perp})^* \propto \frac{1}{2}(U_i - iV_i) \quad , \tag{E.22c}$$

$$E_{i,\parallel}^* E_{i,\perp} = E_i^2 (\hat{\boldsymbol{e}}_i \cdot \hat{\boldsymbol{e}}_{i,\parallel})^*(\hat{\boldsymbol{e}}_i \cdot \hat{\boldsymbol{e}}_{i,\perp}) \propto \frac{1}{2}(U_i + iV_i) \quad . \tag{E.22d}$$

Therefore, we can construct the Mueller matrix as follows:

$$M_{11} = \mathcal{A}_1\mathcal{A}_1^* + \mathcal{A}_2\mathcal{A}_2^* + \mathcal{A}_3\mathcal{A}_3^* + \mathcal{A}_4\mathcal{A}_4^* \ ,$$

$$M_{12} = \mathcal{A}_1\mathcal{A}_1^* - \mathcal{A}_2\mathcal{A}_2^* + \mathcal{A}_3\mathcal{A}_3^* - \mathcal{A}_4\mathcal{A}_4^* \ ,$$

$$M_{13} = \mathcal{A}_1\mathcal{A}_2^* + \mathcal{A}_1^*\mathcal{A}_2 + \mathcal{A}_3\mathcal{A}_4^* + \mathcal{A}_3^*\mathcal{A}_4 = 2(\mathcal{A}_{1R}\mathcal{A}_{2R} + \mathcal{A}_{1I}\mathcal{A}_{2I} + \mathcal{A}_{3R}\mathcal{A}_{4R} + \mathcal{A}_{3I}\mathcal{A}_{4I}) \ ,$$

$$M_{14} = -i(\mathcal{A}_1\mathcal{A}_2^* - \mathcal{A}_1^*\mathcal{A}_2 + \mathcal{A}_3\mathcal{A}_4^* - \mathcal{A}_3^*\mathcal{A}_4) = 2(-\mathcal{A}_{1R}\mathcal{A}_{2I} + \mathcal{A}_{1I}\mathcal{A}_{2R} - \mathcal{A}_{3R}\mathcal{A}_{4I} + \mathcal{A}_{3I}\mathcal{A}_{4R}) \ ,$$

$$M_{21} = \mathcal{A}_1\mathcal{A}_1^* + \mathcal{A}_2\mathcal{A}_2^* - \mathcal{A}_3\mathcal{A}_3^* - \mathcal{A}_4\mathcal{A}_4^* \ ,$$

$$M_{22} = \mathcal{A}_1\mathcal{A}_1^* - \mathcal{A}_2\mathcal{A}_2^* - \mathcal{A}_3\mathcal{A}_3^* + \mathcal{A}_4\mathcal{A}_4^* \ ,$$

$$M_{23} = \mathcal{A}_1\mathcal{A}_2^* + \mathcal{A}_1^*\mathcal{A}_2 - \mathcal{A}_3\mathcal{A}_4^* - \mathcal{A}_3^*\mathcal{A}_4 = 2(\mathcal{A}_{1R}\mathcal{A}_{2R} + \mathcal{A}_{1I}\mathcal{A}_{2I} - \mathcal{A}_{3R}\mathcal{A}_{4R} - \mathcal{A}_{3I}\mathcal{A}_{4I}) \ ,$$

$$M_{24} = -i(\mathcal{A}_1\mathcal{A}_2^* - \mathcal{A}_1^*\mathcal{A}_2 - \mathcal{A}_3\mathcal{A}_4^* + \mathcal{A}_3^*\mathcal{A}_4) = 2(-\mathcal{A}_{1R}\mathcal{A}_{2I} + \mathcal{A}_{1I}\mathcal{A}_{2R} + \mathcal{A}_{3R}\mathcal{A}_{4I} - \mathcal{A}_{3I}\mathcal{A}_{4R}) \ ,$$

$$M_{31} = \mathcal{A}_1\mathcal{A}_3^* + \mathcal{A}_1^*\mathcal{A}_3 + \mathcal{A}_2\mathcal{A}_4^* + \mathcal{A}_2^*\mathcal{A}_4 = 2(\mathcal{A}_{1R}\mathcal{A}_{3R} + \mathcal{A}_{1I}\mathcal{A}_{3I} + \mathcal{A}_{2R}\mathcal{A}_{4R} + \mathcal{A}_{2I}\mathcal{A}_{4I}) \ ,$$

$$M_{32} = \mathcal{A}_1\mathcal{A}_3^* + \mathcal{A}_1^*\mathcal{A}_3 - \mathcal{A}_2\mathcal{A}_4^* - \mathcal{A}_2^*\mathcal{A}_4 = 2(\mathcal{A}_{1R}\mathcal{A}_{3R} + \mathcal{A}_{1I}\mathcal{A}_{3I} - \mathcal{A}_{2R}\mathcal{A}_{4R} - \mathcal{A}_{2I}\mathcal{A}_{4I}) \ ,$$

$$M_{33} = \mathcal{A}_1\mathcal{A}_4^* + \mathcal{A}_1^*\mathcal{A}_4 + \mathcal{A}_2\mathcal{A}_3^* + \mathcal{A}_2^*\mathcal{A}_3 = 2(\mathcal{A}_{1R}\mathcal{A}_{4R} + \mathcal{A}_{1I}\mathcal{A}_{4I} + \mathcal{A}_{2R}\mathcal{A}_{3R} + \mathcal{A}_{2I}\mathcal{A}_{3I}) \ ,$$

$$M_{34} = -i\,(\mathcal{A}_1\mathcal{A}_4^* - \mathcal{A}_1^*\mathcal{A}_4 - \mathcal{A}_2\mathcal{A}_3^* + \mathcal{A}_2^*\mathcal{A}_3) = 2(-\mathcal{A}_{1R}\mathcal{A}_{4I} + \mathcal{A}_{1I}\mathcal{A}_{4R} + \mathcal{A}_{2R}\mathcal{A}_{3I} - \mathcal{A}_{2I}\mathcal{A}_{3R}) \ ,$$

$$M_{41} = i(\mathcal{A}_1\mathcal{A}_3^* - \mathcal{A}_1^*\mathcal{A}_3 + \mathcal{A}_2\mathcal{A}_4^* - \mathcal{A}_2^*\mathcal{A}_4) = 2(\mathcal{A}_{1R}\mathcal{A}_{3I} - \mathcal{A}_{1I}\mathcal{A}_{3R} + \mathcal{A}_{2R}\mathcal{A}_{4I} - \mathcal{A}_{2I}\mathcal{A}_{4R}) \ ,$$

$$M_{42} = i(\mathcal{A}_1\mathcal{A}_3^* - \mathcal{A}_1^*\mathcal{A}_3 - \mathcal{A}_2\mathcal{A}_4^* + \mathcal{A}_2^*\mathcal{A}_4) = 2(\mathcal{A}_{1R}\mathcal{A}_{3I} - \mathcal{A}_{1I}\mathcal{A}_{3R} - \mathcal{A}_{2R}\mathcal{A}_{4I} + \mathcal{A}_{2I}\mathcal{A}_{4R}) \ ,$$

$$M_{43} = i(\mathcal{A}_1\mathcal{A}_4^* - \mathcal{A}_1^*\mathcal{A}_4 + \mathcal{A}_2\mathcal{A}_3^* - \mathcal{A}_2^*\mathcal{A}_3) = 2(\mathcal{A}_{1R}\mathcal{A}_{4I} - \mathcal{A}_{1I}\mathcal{A}_{4R} + \mathcal{A}_{2R}\mathcal{A}_{3I} - \mathcal{A}_{2I}\mathcal{A}_{3R}) \ ,$$

$$M_{44} = \mathcal{A}_1\mathcal{A}_4^* + \mathcal{A}_1^*\mathcal{A}_4 - \mathcal{A}_2\mathcal{A}_3^* - \mathcal{A}_2^*\mathcal{A}_3 = 2(\mathcal{A}_{1R}\mathcal{A}_{4R} + \mathcal{A}_{1I}\mathcal{A}_{4I} - \mathcal{A}_{2R}\mathcal{A}_{3R} - \mathcal{A}_{2I}\mathcal{A}_{3I}) \ .$$

Here, we summarize all the Mueller matrix elements explicitly as follows:

$$M_{11} = \frac{1}{(1-\eta^2)^2}(g_1\cos^2\alpha + g_2) + \frac{\eta^2}{(1-\eta^2)^2}(g_2\cos^2\alpha + g_1) + \Lambda \ , \qquad \text{(E.24a)}$$

$$M_{12} = \frac{1}{(1-\eta^2)^2}(g_1\cos^2\alpha - g_2) + \frac{\eta^2}{(1-\eta^2)^2}(g_2\cos^2\alpha - g_1) + \Lambda \ , \qquad \text{(E.24b)}$$

$$M_{13} = \frac{1}{1-\eta^2}\left(\sin\alpha\sin 2\theta\sin\tilde{\phi} - \cos\alpha\sin^2\theta\sin 2\tilde{\phi}\right) \ , \qquad \text{(E.24c)}$$

$$M_{14} = \frac{\eta}{1-\eta^2} \left[\frac{2}{1-\eta^2} \cos\alpha(1+\cos^2\theta) + \sin\alpha \sin 2\theta \cos\tilde{\phi} \right] \ , \tag{E.24d}$$

$$M_{21} = \frac{1}{(1-\eta^2)^2}(f_1 \cos^2\alpha + f_2) + \frac{\eta^2}{(1-\eta^2)^2}(f_2 \cos^2\alpha + f_1) + \Lambda \ , \tag{E.24e}$$

$$M_{22} = \frac{1}{(1-\eta^2)^2}(f_1 \cos^2\alpha - f_2) + \frac{\eta^2}{(1-\eta^2)^2}(f_2 \cos^2\alpha - f_1) + \Lambda \ , \tag{E.24f}$$

$$M_{23} = \frac{1}{1-\eta^2} \left[\cos\alpha(1+\cos^2\theta)\sin 2\tilde{\phi} + \sin\alpha \sin 2\theta \sin\tilde{\phi} \right] \ , \tag{E.24g}$$

$$M_{24} = \frac{\eta}{1-\eta^2} \left(\sin\alpha \sin 2\theta \cos\tilde{\phi} - \frac{2}{1-\eta^2} \cos\alpha \sin^2\theta \right) \ , \tag{E.24h}$$

$$M_{31} = \frac{1}{1-\eta^2} \left(\sin^2\alpha \cos\theta \sin 2\tilde{\phi} - \sin 2\alpha \sin\theta \sin\tilde{\phi} \right) \ , \tag{E.24i}$$

$$M_{32} = \frac{-1}{1-\eta^2} \left[(1+\cos^2\alpha)\cos\theta \sin 2\tilde{\phi} + \sin 2\alpha \sin\theta \sin\tilde{\phi} \right] \ , \tag{E.24j}$$

$$M_{33} = \frac{2}{1-\eta^2} \left(\cos\alpha \cos\theta \cos 2\tilde{\phi} + \sin\alpha \sin\theta \cos\tilde{\phi} \right) \ , \tag{E.24k}$$

$$M_{34} = \frac{-2\eta}{1-\eta^2} \sin\alpha \sin\theta \sin\tilde{\phi} \ , \tag{E.24l}$$

$$M_{41} = \frac{\eta}{1-\eta^2} \left[\frac{2}{1-\eta^2}(1+\cos^2\alpha)\cos\theta + \sin 2\alpha \sin\theta \cos\tilde{\phi} \right] \ , \tag{E.24m}$$

$$M_{42} = \frac{\eta}{1-\eta^2} \left(\frac{-2}{1-\eta^2} \sin^2\alpha \cos\theta + \sin 2\alpha \sin\theta \cos\tilde{\phi} \right) \ , \tag{E.24n}$$

$$M_{43} = \frac{2\eta}{1-\eta^2} \sin\alpha \sin\theta \sin\tilde{\phi} \ , \tag{E.24o}$$

$$M_{44} = \frac{2}{1-\eta^2} \left(\frac{1+\eta^2}{1-\eta^2} \cos\alpha \cos\theta + \sin\alpha \sin\theta \cos\tilde{\phi} \right) \ , \tag{E.24p}$$

where we define the auxiliary quantities following Chou (1986):

$$g_1 \equiv \cos^2\theta \cos^2\tilde{\phi} + \sin^2\tilde{\phi} \ , \qquad g_2 \equiv \cos^2\theta \sin^2\tilde{\phi} + \cos^2\tilde{\phi} \ ,$$

$$f_1 \equiv \cos^2\theta \cos^2\tilde{\phi} - \sin^2\tilde{\phi} \ , \qquad f_2 \equiv \cos^2\theta \sin^2\tilde{\phi} - \cos^2\tilde{\phi} \ , \tag{E.24q}$$

$$\Lambda \equiv \sin^2\alpha \sin^2\theta + \frac{1}{2(1-\eta^2)} \sin 2\alpha \sin 2\theta \cos\tilde{\phi} \ .$$

E.2   Radiative Transfer Equation in Mueller-Matrix Formalism

In this section, we construct the polarized radiative transfer equation with the Stokes parameters. The radiative transfer can be summarized in form of

$$\frac{1}{c}\frac{\partial \boldsymbol{S}_\nu}{\partial t} + \hat{\boldsymbol{n}} \cdot \nabla \boldsymbol{S}_\nu = j_\nu \begin{pmatrix} 1 \\ 0 \\ 0 \\ 0 \end{pmatrix} - \chi_{\nu,\mathrm{a}}\boldsymbol{S}_\nu + n_e \oint \boldsymbol{S}_{\nu,\mathrm{scat}}(\hat{\boldsymbol{n}}',\hat{\boldsymbol{n}})r^2 d\Omega' - n_e \mathbf{S}_{\mathrm{scat,a}}\boldsymbol{S}_\nu \quad , \quad (E.25)$$

where $\boldsymbol{S}_\nu = (I_\nu, Q_\nu, U_\nu, V_\nu)^T$ is the Stokes parameter vector, $\hat{\boldsymbol{n}}$ is the unit vector of the radiation propagation direction, j_ν represents the unpolarized thermal emission, $\chi_{\nu,\mathrm{a}} = \rho \kappa_{\nu,\mathrm{a}}$ is the thermal absorption coefficient, n_e is the electron number density, $\boldsymbol{S}_{\nu,\mathrm{scat}}$ refers to the emission of the incident radiation due to the Thomson scattering, $\hat{\boldsymbol{n}}'$ is the direction unit vector for the incident radiation, and $\mathbf{S}_{\mathrm{scat,a}}$ is the matrix of the absorption coefficients due to the scattering process.

It would be convenient to integrate the first row of Mueller matrix over the outgoing radiation direction in advance. Define the cross section component corresponding to each Mueller matrix element as

$$\sigma_{ij} = \frac{1}{2}r_e^2 \oint M_{ij}d\Omega \quad . \tag{E.26}$$

Although we only use the first row, we still conclude all the non-zero elements here for the completeness:

$$\sigma_{11} = \frac{1}{2}\sigma_T \left[\frac{1+\eta^2}{(1-\eta^2)^2}(\cos^2 \alpha + 1) + \sin^2 \alpha \right] = \frac{1}{2}(\sigma_O + \sigma_X) \quad , \tag{E.27a}$$

$$\sigma_{12} = \frac{1}{2}\sigma_T \left[\frac{1+\eta^2}{(1-\eta^2)^2}(\cos^2\alpha - 1) + \sin^2\alpha \right] = \frac{1}{2}(\sigma_O - \sigma_X) \quad , \tag{E.27b}$$

$$\sigma_{14} = \sigma_T \frac{2\eta}{(1-\eta^2)^2}\cos\alpha \quad , \tag{E.27c}$$

$$\sigma_{21} = \frac{1}{2}\sigma_T \left[-\frac{1}{2}\frac{1+\eta^2}{(1-\eta^2)^2}(\cos^2\alpha + 1) + \sin^2\alpha \right] \quad , \tag{E.27d}$$

$$\sigma_{22} = \frac{1}{2}\sigma_T \sin^2\alpha \left[\frac{1}{2}\frac{1+\eta^2}{(1-\eta^2)^2} + 1 \right] \quad , \tag{E.27e}$$

$$\sigma_{24} = \sigma_T \frac{-\eta}{(1-\eta^2)^2}\cos\alpha \quad , \tag{E.27f}$$

The rest of integrated elements are all equal to zero (i.e. $\sigma_{13} = \sigma_{23} = \sigma_{31} = \sigma_{32} = \sigma_{33} = \sigma_{34} = \sigma_{41} = \sigma_{42} = \sigma_{43} = \sigma_{44} = 0$). Note that the integration over ϕ and $\tilde{\phi}$ are essentially the same because the integration covers the whole the azimuthal plane.

E.2.1   Absorption Term of Thomson Scattering

We can evaluate the absorption term of Thomson scattering by calculating the attenuation for each pure polarization mode. The cross section can be obtained by integrating equation (E.4) and then expressed in terms of the angle-integrated Mueller matrix elements as

$$\sigma = \frac{1}{2}r_e^2 \oint \frac{I_{\nu,o}}{I_\nu}d\Omega = \sigma_{11} + \frac{Q_\nu}{I_\nu}\sigma_{12} + \frac{U_\nu}{I_\nu}\sigma_{13} + \frac{V_\nu}{I_\nu}\sigma_{14} \quad . \tag{E.28}$$

Therefore, the unpolarized radiation $\boldsymbol{S}_\nu = (I_\nu, 0, 0, 0)^T$ has the cross section $\sigma_I = \sigma_{11}$. The pure O-mode $\boldsymbol{S}_\nu = (I_\nu, I_\nu, 0, 0)^T$ (i.e. $Q_\nu = I_\nu$, $E_\perp = 0$) has the cross section $\sigma_{Q+} = \sigma_{11} + \sigma_{12}$. The pure X-mode $\boldsymbol{S}_\nu = (I_\nu, -I_\nu, 0, 0)^T$ (i.e. $Q_\nu = -I_\nu$, $E_\parallel = 0$) has the cross section $\sigma_{Q-} = \sigma_{11} - \sigma_{12}$. For the linear polarized radiation with the electric field halfway between parallel and perpendicular $\boldsymbol{S}_\nu = (I_\nu, 0, \pm I_\nu, 0)^T$ (i.e. $U_\nu = \pm I_\nu$, $E_\perp = \pm E_\parallel$), the cross section is $\sigma_{U\pm} = \sigma_{11} \pm \sigma_{13}$. The pure circular mode $\boldsymbol{S}_\nu = (I_\nu, 0, 0, \pm I_\nu)^T$ (i.e. $V_\nu = \pm I_\nu$, $E_\perp = \pm iE_\parallel$) has the cross section $\sigma_{V\pm} = \sigma_{11} \pm \sigma_{14}$. Therefore, the Thomson

scattering absorption matrix can be constructed as

$$\mathbf{S}_{\text{scat,a}} = \begin{pmatrix} \sigma_{11} & \sigma_{12} & \sigma_{13} & \sigma_{14} \\ \sigma_{12} & \sigma_{11} & 0 & 0 \\ \sigma_{13} & 0 & \sigma_{11} & 0 \\ \sigma_{14} & 0 & 0 & \sigma_{11} \end{pmatrix} \quad , \tag{E.29}$$

where all above results are guaranteed to be satisfied.

E.2.2 Emission Term of Thomson Scattering

The emission term due to the Thomson scattering can be easily evaluated given the already constructed Mueller matrix $\mathbf{M}$.

$$\boldsymbol{S}_{\nu,\text{scat}}(\hat{\boldsymbol{n}}', \hat{\boldsymbol{n}}) = \frac{r_e^2}{2r^2}\mathbf{M}(\hat{\boldsymbol{n}}' \to \hat{\boldsymbol{n}})\boldsymbol{S}_{\nu}(\hat{\boldsymbol{n}}') \quad , \tag{E.30}$$

where the Mueller matrix element can be found in equation (E.24). Therefore, we have the emission source term due to the Thomson scattering as

$$\oint \boldsymbol{S}_{\nu,\text{scat}}(\hat{\boldsymbol{n}}', \hat{\boldsymbol{n}})r^2 d\Omega' = \frac{3}{4}\sigma_T \left[\frac{1}{4\pi} \oint \mathbf{M}(\hat{\boldsymbol{n}}' \to \hat{\boldsymbol{n}})\boldsymbol{S}_{\nu}(\hat{\boldsymbol{n}}')d\Omega' \right] \quad . \tag{E.31}$$

With these scattering source terms, the polarized radiative transfer can be rewritten as follows:

$$\frac{1}{c}\frac{\partial \boldsymbol{S}_{\nu}}{\partial t} + \hat{\boldsymbol{n}} \cdot \nabla \boldsymbol{S}_{\nu} = j_{\nu} \begin{pmatrix} 1 \\ 0 \\ 0 \\ 0 \end{pmatrix} - \chi_{\nu,\text{a}}\boldsymbol{S}_{\nu}$$

$$+\frac{3}{4}n_e\sigma_T\left[\frac{1}{4\pi}\oint \mathbf{M}(\hat{\boldsymbol{n}}'\to\hat{\boldsymbol{n}})\boldsymbol{S}_\nu(\hat{\boldsymbol{n}}')d\Omega'\right]-n_e\begin{pmatrix}\sigma_{11}I_\nu+\sigma_{12}Q_\nu+\sigma_{14}V_\nu\\[2mm]\sigma_{12}I_\nu+\sigma_{11}Q_\nu\\[2mm]\sigma_{11}U_\nu\\[2mm]\sigma_{14}I_\nu+\sigma_{11}V_\nu\end{pmatrix}\quad . \qquad (E.32)$$

E.2.3   Moment Equations of Polarized Radiation

Mueller Matrix in Terms of Propagation Vectors

In order to obtain the moment equations via integrating the radiative transfer equation (E.32), we prefer to express the Mueller matrix elements in Cartesian unit vectors. Let us adopt the following notations, where the propagation vectors with prime refer to the incident radiation direction and the scattered radiation is denoted without prime:

$$\hat{n}_x=\sin\theta\cos\phi\quad,\qquad\qquad\hat{n}'_x=\sin\alpha\cos\beta\quad, \qquad (E.33a)$$

$$\hat{n}_y=\sin\theta\sin\phi\quad,\qquad\qquad\hat{n}'_y=\sin\alpha\sin\beta\quad, \qquad (E.33b)$$

$$\hat{n}_z=\cos\theta\quad,\qquad\qquad\hat{n}'_z=\cos\alpha\quad. \qquad (E.33c)$$

Here, we also prepare some auxiliary quantities for convenience:

$$\sin\alpha\sin\theta\cos\tilde{\phi}=\hat{n}_x\hat{n}'_x+\hat{n}_y\hat{n}'_y\quad, \qquad (E.34a)$$

$$\sin\alpha\sin\theta\sin\tilde{\phi}=\hat{n}_y\hat{n}'_x-\hat{n}_x\hat{n}'_y\quad, \qquad (E.34b)$$

$$(g_1\cos^2\alpha+g_2)=\cos^2\theta+\cos^2\alpha+\sin^2\alpha\sin^2\theta\cos^2\tilde{\phi}\quad, \qquad (E.34c)$$

$$(g_2\cos^2\alpha+g_1)=\cos^2\theta+\cos^2\alpha+\sin^2\alpha\sin^2\theta\sin^2\tilde{\phi}\quad, \qquad (E.34d)$$

$$(g_1\cos^2\alpha-g_2)=\sin^2\alpha\sin^2\theta\cos^2\tilde{\phi}-\sin^2\alpha-\sin^2\theta\cos2\tilde{\phi}\quad, \qquad (E.34e)$$

$$(g_2\cos^2\alpha-g_1)=\sin^2\alpha\sin^2\theta\sin^2\tilde{\phi}-\sin^2\alpha+\sin^2\theta\cos2\tilde{\phi}\quad, \qquad (E.34f)$$

$$(f_1 \cos^2 \alpha + f_2) = \sin^2 \alpha \sin^2 \theta \cos^2 \tilde{\phi} - \sin^2 \theta - \sin^2 \alpha \cos 2\tilde{\phi} \quad , \tag{E.34g}$$

$$(f_2 \cos^2 \alpha + f_1) = \sin^2 \alpha \sin^2 \theta \sin^2 \tilde{\phi} - \sin^2 \theta + \sin^2 \alpha \cos 2\tilde{\phi} \quad , \tag{E.34h}$$

$$(f_1 \cos^2 \alpha - f_2) = \sin^2 \alpha \sin^2 \theta \cos^2 \tilde{\phi} + (\cos^2 \alpha + \cos^2 \theta) \cos 2\tilde{\phi} \quad , \tag{E.34i}$$

$$(f_2 \cos^2 \alpha - f_1) = \sin^2 \alpha \sin^2 \theta \sin^2 \tilde{\phi} - (\cos^2 \alpha + \cos^2 \theta) \cos 2\tilde{\phi} \quad , \tag{E.34j}$$

$$\Lambda = 1 - \hat{n}_z^2 - (\hat{n}_z')^2 + \hat{n}_z^2(\hat{n}_z')^2 + \frac{2}{1-\eta^2}\hat{n}_x\hat{n}_z\hat{n}_x'\hat{n}_z' + \frac{2}{1-\eta^2}\hat{n}_y\hat{n}_z\hat{n}_y'\hat{n}_z' \quad , \tag{E.34k}$$

Following our previous calculated Mueller matrix elements (E.24), we have

$$
\begin{aligned}
M_{11} = &\ 1 + \left[\frac{1+\eta^2}{(1-\eta^2)^2} - 1\right]\hat{n}_z^2 + \left[\frac{1+\eta^2}{(1-\eta^2)^2} - 1\right](\hat{n}_z')^2 + \left[\frac{1}{(1-\eta^2)^2}\right]\hat{n}_x^2(\hat{n}_x')^2 \\
&+ \left[\frac{1}{(1-\eta^2)^2}\right]\hat{n}_y^2(\hat{n}_y')^2 + \hat{n}_z^2(\hat{n}_z')^2 + \left[\frac{\eta^2}{(1-\eta^2)^2}\right]\hat{n}_y^2(\hat{n}_x')^2 + \left[\frac{\eta^2}{(1-\eta^2)^2}\right]\hat{n}_x^2(\hat{n}_y')^2 \\
&+ \left[\frac{2}{1-\eta^2}\right]\hat{n}_x\hat{n}_y\hat{n}_x'\hat{n}_y' + \left[\frac{2}{1-\eta^2}\right]\hat{n}_x\hat{n}_z\hat{n}_x'\hat{n}_z' + \left[\frac{2}{1-\eta^2}\right]\hat{n}_y\hat{n}_z\hat{n}_y'\hat{n}_z' \ ,
\end{aligned} \tag{E.35a}
$$

$$
\begin{aligned}
M_{12} = &\ \left[1 - \frac{1+\eta^2}{(1-\eta^2)^2}\right] - \hat{n}_z^2 + \left[\frac{1+\eta^2}{(1-\eta^2)^2} - 1\right](\hat{n}_z')^2 + \left[\frac{1}{(1-\eta^2)^2}\right]\hat{n}_x^2(\hat{n}_x')^2 \\
&+ \left[\frac{1}{(1-\eta^2)^2}\right]\hat{n}_y^2(\hat{n}_y')^2 + \hat{n}_z^2(\hat{n}_z')^2 + \left[\frac{\eta^2}{(1-\eta^2)^2}\right]\hat{n}_y^2(\hat{n}_x')^2 + \left[\frac{\eta^2}{(1-\eta^2)^2}\right]\hat{n}_x^2(\hat{n}_y')^2 \\
&+ \left[\frac{2}{1-\eta^2}\right]\hat{n}_x\hat{n}_y\hat{n}_x'\hat{n}_y' + \left[\frac{2}{1-\eta^2}\right]\hat{n}_x\hat{n}_z\hat{n}_x'\hat{n}_z' + \left[\frac{2}{1-\eta^2}\right]\hat{n}_y\hat{n}_z\hat{n}_y'\hat{n}_z' \\
&+ \left[\frac{-1}{1-\eta^2}\right](\hat{n}_x^2 - \hat{n}_y^2)\cos 2\beta + \left[\frac{-1}{1-\eta^2}\right](2\hat{n}_x\hat{n}_y)\sin 2\beta \ ,
\end{aligned} \tag{E.35b}
$$

$$
\begin{aligned}
M_{13} = &\ \left[\frac{2}{1-\eta^2}\right]\hat{n}_y\hat{n}_z\hat{n}_x' + \left[\frac{-2}{1-\eta^2}\right]\hat{n}_x\hat{n}_z\hat{n}_y' + \left[\frac{-1}{1-\eta^2}\right](2\hat{n}_x\hat{n}_y)(\hat{n}_z'\cos 2\beta) \\
&+ \left[\frac{1}{1-\eta^2}\right](\hat{n}_x^2 - \hat{n}_y^2)(\hat{n}_z'\sin 2\beta) \ ,
\end{aligned} \tag{E.35c}
$$

$$M_{14} = \left[\frac{2\eta}{(1-\eta^2)^2}\right]\hat{n}_z' + \left[\frac{2\eta}{(1-\eta^2)^2}\right]\hat{n}_z^2\hat{n}_z' + \left[\frac{2\eta}{1-\eta^2}\right]\hat{n}_x\hat{n}_z\hat{n}_x' + \left[\frac{2\eta}{1-\eta^2}\right]\hat{n}_y\hat{n}_z\hat{n}_y' \ , \tag{E.35d}$$

$$
\begin{aligned}
M_{21} = &\ \left[1 - \frac{1+\eta^2}{(1-\eta^2)^2}\right] + \left[\frac{1+\eta^2}{(1-\eta^2)^2} - 1\right]\hat{n}_z^2 - (\hat{n}_z')^2 + \hat{n}_z^2(\hat{n}_z')^2 + \left[\frac{1}{(1-\eta^2)^2}\right]\hat{n}_x^2(\hat{n}_x')^2 \\
&+ \left[\frac{1}{(1-\eta^2)^2}\right]\hat{n}_y^2(\hat{n}_y')^2 + \left[\frac{\eta^2}{(1-\eta^2)^2}\right]\hat{n}_y^2(\hat{n}_x')^2 + \left[\frac{\eta^2}{(1-\eta^2)^2}\right]\hat{n}_x^2(\hat{n}_y')^2 \\
&+ \left[\frac{2}{1-\eta^2}\right]\hat{n}_x\hat{n}_y\hat{n}_x'\hat{n}_y' + \left[\frac{2}{1-\eta^2}\right]\hat{n}_x\hat{n}_z\hat{n}_x'\hat{n}_z' + \left[\frac{2}{1-\eta^2}\right]\hat{n}_y\hat{n}_z\hat{n}_y'\hat{n}_z' \\
&+ \left[\frac{-1}{1-\eta^2}\right]\cos 2\phi\,(\hat{n}_x'^2 - \hat{n}_y'^2) + \left[\frac{-1}{1-\eta^2}\right]\sin 2\phi(2\hat{n}_x'\hat{n}_y') \ ,
\end{aligned} \tag{E.35e}
$$

$$M_{22} = 1 - \hat{n}_z^2 - (\hat{n}_z')^2 + \hat{n}_z^2(\hat{n}_z')^2 + \left[\frac{1}{(1-\eta^2)^2}\right]\hat{n}_x^2(\hat{n}_x')^2$$

$$+ \left[\frac{1}{(1-\eta^2)^2}\right]\hat{n}_y^2(\hat{n}_y')^2 + \left[\frac{\eta^2}{(1-\eta^2)^2}\right]\hat{n}_y^2(\hat{n}_x')^2 + \left[\frac{\eta^2}{(1-\eta^2)^2}\right]\hat{n}_x^2(\hat{n}_y')^2$$

$$+ \left[\frac{2}{1-\eta^2}\right]\hat{n}_x\hat{n}_y\hat{n}_x'\hat{n}_y' + \left[\frac{2}{1-\eta^2}\right]\hat{n}_x\hat{n}_z\hat{n}_x'\hat{n}_z' + \left[\frac{2}{1-\eta^2}\right]\hat{n}_y\hat{n}_z\hat{n}_y'\hat{n}_z' \qquad \text{(E.35f)}$$

$$+ \left[\frac{1}{1-\eta^2}\right]\left[2\cos 2\phi \cos 2\beta - (\hat{n}_x^2 - \hat{n}_y^2)\cos 2\beta - \cos 2\phi\left((\hat{n}_x')^2 - (\hat{n}_y')^2\right)\right]$$

$$+ \left[\frac{1}{1-\eta^2}\right]\left[2\sin 2\phi \sin 2\beta - (2\hat{n}_x\hat{n}_y)\sin 2\beta - \sin 2\phi(2\hat{n}_x'\hat{n}_y')\right] \;,$$

$$M_{23} = \left[\frac{2}{1-\eta^2}\right]\hat{n}_y\hat{n}_z\hat{n}_x' + \left[\frac{-2}{1-\eta^2}\right]\hat{n}_x\hat{n}_z\hat{n}_y' + \left[\frac{1}{1-\eta^2}\right](2\sin 2\phi - 2\hat{n}_x\hat{n}_y)(\hat{n}_z'\cos 2\beta)$$

$$+ \left[\frac{-1}{1-\eta^2}\right]\left[2\cos 2\phi - (\hat{n}_x^2 - \hat{n}_y^2)\right](\hat{n}_z'\sin 2\beta) \;, \qquad \text{(E.35g)}$$

$$M_{24} = \left[\frac{-2\eta}{(1-\eta^2)^2}\right]\hat{n}_z' + \left[\frac{2\eta}{(1-\eta^2)^2}\right]\hat{n}_z^2\hat{n}_z' + \left[\frac{2\eta}{1-\eta^2}\right]\hat{n}_x\hat{n}_z\hat{n}_x' + \left[\frac{2\eta}{1-\eta^2}\right]\hat{n}_y\hat{n}_z\hat{n}_y' \;, \qquad \text{(E.35h)}$$

$$M_{31} = \left[\frac{-2}{1-\eta^2}\right]\hat{n}_y\hat{n}_x'\hat{n}_z' + \left[\frac{2}{1-\eta^2}\right]\hat{n}_x\hat{n}_y'\hat{n}_z' + \left[\frac{1}{1-\eta^2}\right](\hat{n}_z\sin 2\phi)\left((\hat{n}_x')^2 - (\hat{n}_y')^2\right)$$

$$+ \left[\frac{-1}{1-\eta^2}\right](\hat{n}_z\cos 2\phi)\left(2\hat{n}_x'\hat{n}_y'\right) \;, \qquad \text{(E.35i)}$$

$$M_{32} = \left[\frac{-2}{1-\eta^2}\right]\hat{n}_y\hat{n}_x'\hat{n}_z' + \left[\frac{2}{1-\eta^2}\right]\hat{n}_x\hat{n}_y'\hat{n}_z' + \left[\frac{1}{1-\eta^2}\right](\hat{n}_z\cos 2\phi)\left(2\sin 2\beta - 2\hat{n}_x'\hat{n}_y'\right)$$

$$+ \left[\frac{-1}{1-\eta^2}\right](\hat{n}_z\sin 2\phi)\left[2\cos 2\beta - \left((\hat{n}_x')^2 - (\hat{n}_y')^2\right)\right] \;, \qquad \text{(E.35j)}$$

$$M_{33} = \left[\frac{2}{1-\eta^2}\right]\hat{n}_x\hat{n}_x' + \left[\frac{2}{1-\eta^2}\right]\hat{n}_y\hat{n}_y' + \left[\frac{2}{1-\eta^2}\right](\hat{n}_z\cos 2\phi)(\hat{n}_z'\cos 2\beta)$$

$$+ \left[\frac{2}{1-\eta^2}\right](\hat{n}_z\sin 2\phi)(\hat{n}_z'\sin 2\beta) \;, \qquad \text{(E.35k)}$$

$$M_{34} = \left[\frac{2\eta}{1-\eta^2}\right]\hat{n}_x\hat{n}_y' + \left[\frac{-2\eta}{1-\eta^2}\right]\hat{n}_y\hat{n}_x' \;, \qquad \text{(E.35l)}$$

$$M_{41} = \left[\frac{2\eta}{(1-\eta^2)^2}\right]\hat{n}_z + \left[\frac{2\eta}{(1-\eta^2)^2}\right]\hat{n}_z(\hat{n}_z')^2 + \left[\frac{2\eta}{1-\eta^2}\right]\hat{n}_x\hat{n}_x'\hat{n}_z' + \left[\frac{2\eta}{1-\eta^2}\right]\hat{n}_y\hat{n}_y'\hat{n}_z' \;, \qquad \text{(E.35m)}$$

$$M_{42} = \left[\frac{-2\eta}{(1-\eta^2)^2}\right]\hat{n}_z + \left[\frac{2\eta}{(1-\eta^2)^2}\right]\hat{n}_z(\hat{n}_z')^2 + \left[\frac{2\eta}{1-\eta^2}\right]\hat{n}_x\hat{n}_x'\hat{n}_z' + \left[\frac{2\eta}{1-\eta^2}\right]\hat{n}_y\hat{n}_y'\hat{n}_z' \;, \qquad \text{(E.35n)}$$

$$M_{43} = \left[\frac{2\eta}{1-\eta^2}\right]\hat{n}_y\hat{n}_x' + \left[\frac{-2\eta}{1-\eta^2}\right]\hat{n}_x\hat{n}_y' \;, \qquad \text{(E.35o)}$$

$$M_{44} = \left[\frac{2(1+\eta^2)}{(1-\eta^2)^2}\right]\hat{n}_z\hat{n}_z' + \left[\frac{2}{1-\eta^2}\right]\hat{n}_x\hat{n}_x' + \left[\frac{2}{1-\eta^2}\right]\hat{n}_y\hat{n}_y' \;, \qquad \text{(E.35p)}$$

 Note that those azimuthal angular terms as listed below suggest that we might need to integrate the extra types of the angular moments for the numerical closure.

$$\cos 2\phi = \frac{\hat{n}_x^2 - \hat{n}_y^2}{\hat{n}_x^2 + \hat{n}_y^2} \quad , \qquad \sin 2\phi = \frac{2\hat{n}_x \hat{n}_y}{\hat{n}_x^2 + \hat{n}_y^2} \quad ,$$

$$\cos 2\beta = \frac{(\hat{n}_x')^2 - (\hat{n}_y')^2}{(\hat{n}_x')^2 + (\hat{n}_y')^2} \quad , \quad \sin 2\beta = \frac{2\hat{n}_x' \hat{n}_y'}{(\hat{n}_x')^2 + (\hat{n}_y')^2} \quad . \tag{E.36}$$

With above expressions, we can easily integrate the radiative transfer moment equations, where we define the following angular moments for the Stokes intensity parameters:

$$J_{I,\nu} = \frac{1}{4\pi} \oint I_\nu d\Omega \qquad H_{I,\nu}^i = \frac{1}{4\pi} \oint \hat{n}^i I_\nu d\Omega \qquad K_{I,\nu}^{ij} = \frac{1}{4\pi} \oint \hat{n}^i \hat{n}^j I_\nu d\Omega , \tag{E.37a}$$

$$P_{I,\nu}^c = \frac{1}{4\pi} \oint \cos 2\phi I_\nu d\Omega \quad P_{I,\nu}^{zc} = \frac{1}{4\pi} \oint \hat{n}_z \cos 2\phi I_\nu d\Omega , \tag{E.37b}$$

$$P_{I,\nu}^s = \frac{1}{4\pi} \oint \sin 2\phi I_\nu d\Omega \quad P_{I,\nu}^{zs} = \frac{1}{4\pi} \oint \hat{n}_z \sin 2\phi I_\nu d\Omega . \tag{E.37c}$$

The rest of angular moments for Q_ν, U_ν, and V_ν are defined similarly, where we simply replace the subscript 'I' with 'Q', 'U', and 'V', respectively, to annotate their corresponding moments. Also, it would be convenient to express the polarized cross section components (E.27) in terms of the propagation vectors as follows:

$$\frac{\sigma_{11}(\Omega)}{\sigma_T} = \frac{1}{2} \left[\frac{1+\eta^2}{(1-\eta^2)^2} + 1 \right] + \frac{1}{2} \left[\frac{1+\eta^2}{(1-\eta^2)^2} - 1 \right] \hat{n}_z^2 \quad , \tag{E.38a}$$

$$\frac{\sigma_{12}(\Omega)}{\sigma_T} = \frac{1}{2} \left[1 - \frac{1+\eta^2}{(1-\eta^2)^2} \right] + \frac{1}{2} \left[\frac{1+\eta^2}{(1-\eta^2)^2} - 1 \right] \hat{n}_z^2 \quad , \tag{E.38b}$$

$$\frac{\sigma_{14}(\Omega)}{\sigma_T} = \left[\frac{2\eta}{(1-\eta^2)^2} \right] \hat{n}_z \quad , \tag{E.38c}$$

$$\frac{\sigma_{21}(\Omega)}{\sigma_T} = \left[\frac{1}{2} - \frac{1}{4} \frac{1+\eta^2}{(1-\eta^2)^2} \right] + \left[-\frac{1}{2} - \frac{1}{4} \frac{1+\eta^2}{(1-\eta^2)^2} \right] \hat{n}_z^2 \quad , \tag{E.38d}$$

$$\frac{\sigma_{22}(\Omega)}{\sigma_T} = \left[\frac{1}{2} + \frac{1}{4} \frac{1+\eta^2}{(1-\eta^2)^2} \right] + \left[-\frac{1}{2} - \frac{1}{4} \frac{1+\eta^2}{(1-\eta^2)^2} \right] \hat{n}_z^2 \quad , \tag{E.38e}$$

$$\frac{\sigma_{24}(\Omega)}{\sigma_T} = \left[\frac{-\eta}{(1-\eta^2)^2} \right] \hat{n}_z \quad , \tag{E.38f}$$

Let us also prepare the auxiliary angular integration as follows:

$$\frac{1}{4\pi} \oint \hat{n}_x^2 d\Omega = \frac{1}{4\pi} \oint \hat{n}_y^2 d\Omega = \frac{1}{4\pi} \oint \hat{n}_z^2 d\Omega = \frac{1}{3} \quad , \tag{E.39}$$

$$\frac{1}{4\pi} \oint \hat{n}_x^2 \hat{n}_y^2 d\Omega = \frac{1}{4\pi} \oint \hat{n}_x^2 \hat{n}_z^2 d\Omega = \frac{1}{4\pi} \oint \hat{n}_y^2 \hat{n}_z^2 d\Omega = \frac{1}{15} \quad , \tag{E.40}$$

$$\frac{1}{4\pi} \oint \hat{n}_x^4 d\Omega = \frac{1}{4\pi} \oint \hat{n}_y^4 d\Omega = \frac{1}{4\pi} \oint \hat{n}_z^4 d\Omega = \frac{1}{5} \quad , \tag{E.41}$$

$$\oint \hat{n}_x d\Omega = \oint \hat{n}_y d\Omega = \oint \hat{n}_z d\Omega = \oint \hat{n}_x \hat{n}_y d\Omega = \oint \hat{n}_x \hat{n}_z d\Omega = \oint \hat{n}_y \hat{n}_z d\Omega = 0 \quad , \tag{E.42}$$

$$\oint \hat{n}_x \hat{n}_y^3 d\Omega = \oint \hat{n}_x^3 \hat{n}_y d\Omega = \oint \hat{n}_x \hat{n}_z^3 d\Omega = \oint \hat{n}_x^3 \hat{n}_z d\Omega = \oint \hat{n}_y \hat{n}_z^3 d\Omega = \oint \hat{n}_y^3 \hat{n}_z d\Omega = 0 \quad , \tag{E.43}$$

$$\oint \hat{n}_x^2 \hat{n}_y \hat{n}_z d\Omega = \oint \hat{n}_x \hat{n}_y^2 \hat{n}_z d\Omega = \oint \hat{n}_x \hat{n}_y \hat{n}_z^2 d\Omega = 0 \quad , \tag{E.44}$$

$$\oint \sin 2\phi \, d\Omega = \oint \hat{n}_x \sin 2\phi \, d\Omega = \oint \hat{n}_y \sin 2\phi \, d\Omega = \oint \hat{n}_x^2 \sin 2\phi \, d\Omega = \oint \hat{n}_y^2 \sin 2\phi \, d\Omega = 0 \quad , \tag{E.45}$$

$$\frac{1}{4\pi} \oint \hat{n}_x \hat{n}_y \sin 2\phi \, d\Omega = \frac{1}{6} \quad , \tag{E.46}$$

$$\oint \cos 2\phi \, d\Omega = \oint \hat{n}_x \cos 2\phi \, d\Omega = \oint \hat{n}_y \cos 2\phi \, d\Omega = \oint \hat{n}_x \hat{n}_y \cos 2\phi \, d\Omega = 0 \quad , \tag{E.47}$$

$$\frac{1}{4\pi} \oint \hat{n}_x^2 \cos 2\phi \, d\Omega = \left(-\frac{1}{4\pi}\right) \oint \hat{n}_y^2 \cos 2\phi \, d\Omega = \frac{1}{6} \quad , \tag{E.48}$$

$$\oint \sin 2\phi \cos 2\phi \, d\Omega = 0 \quad , \tag{E.49}$$

$$\frac{1}{4\pi} \oint (\sin 2\phi)^2 d\Omega = \frac{1}{4\pi} \oint (\cos 2\phi)^2 d\Omega = \frac{1}{2} \quad , \tag{E.50}$$

$$\frac{1}{4\pi} \oint \hat{n}_z^2 (\sin 2\phi)^2 d\Omega = \frac{1}{4\pi} \oint \hat{n}_z^2 (\cos 2\phi)^2 d\Omega = \frac{1}{6} \quad , \tag{E.51}$$

Zeroth Moment Equations

Since the Thomson scattering is frequency independent, the emission term should not alter the energy. Therefore, the scattering source terms should disappear in the zeroth

moment equation of total radiation intensity I_ν, which turns out to be a good sanity check. Integrating the radiative transfer equation of I_ν, we can then obtain the zeroth moment equation as follows

$$
\frac{1}{c}\frac{\partial J_{I,\nu}}{\partial t} + \nabla_j H^j_{I,\nu} = j_\nu - \chi_{\nu,a} J_{I,\nu} + n_e \sigma_T \frac{1+\eta^2}{4(1-\eta^2)^2}\left(K^{xx}_{I,\nu} + K^{yy}_{I,\nu} + K^{zz}_{I,\nu} - J_{I,\nu}\right)
$$
$$
+ n_e \sigma_T \frac{1+\eta^2}{4(1-\eta^2)^2}\left(K^{xx}_{Q,\nu} + K^{yy}_{Q,\nu} + K^{zz}_{Q,\nu} - J_{Q,\nu}\right) + n_e \sigma_T \frac{2\eta}{(1-\eta^2)^2}\left(H^z_{V,\nu} - H^z_{V,\nu}\right) \quad . \quad \text{(E.52)}
$$

Recall that

$$
J_{I,\nu} = K^{xx}_{I,\nu} + K^{yy}_{I,\nu} + K^{zz}_{I,\nu} \quad , \tag{E.53a}
$$

$$
J_{Q,\nu} = K^{xx}_{Q,\nu} + K^{yy}_{Q,\nu} + K^{zz}_{Q,\nu} \quad . \tag{E.53b}
$$

Therefore, we recover the zeroth moment equation without any scattering term

$$
\frac{1}{c}\frac{\partial J_{I,\nu}}{\partial t} + \nabla_j H^j_{I,\nu} = j_\nu - \chi_{\nu,a} J_{I,\nu} \quad . \tag{E.54a}
$$

The rest of zeroth moment equations for Q_ν, U_ν, and V_ν are integrated as follows:

$$
\frac{1}{c}\frac{\partial J_{Q,\nu}}{\partial t} + \nabla_j H^j_{Q,\nu} = -\chi_{\nu,a} J_{Q,\nu}
$$
$$
- n_e \sigma_T \left\{ \frac{1+\eta^2}{4(1-\eta^2)^2}\left[(J_{Q,\nu} + 3K^{zz}_{Q,\nu}) - (J_{I,\nu} - 3K^{zz}_{I,\nu})\right] + \frac{\eta}{(1-\eta^2)^2}H^z_{V,\nu}\right\} \quad , \tag{E.54b}
$$

$$
\frac{1}{c}\frac{\partial J_{U,\nu}}{\partial t} + \nabla_j H^j_{U,\nu} = -\chi_{\nu,a} J_{U,\nu}
$$
$$
- n_e \sigma_T \left\{\left[\frac{1}{2}\frac{1+\eta^2}{(1-\eta^2)^2} + \frac{1}{2}\right] J_{U,\nu} + \left[\frac{1}{2}\frac{1+\eta^2}{(1-\eta^2)^2} - \frac{1}{2}\right] K^{zz}_{U,\nu}\right\} \quad , \tag{E.54c}
$$

$$
\frac{1}{c}\frac{\partial J_{V,\nu}}{\partial t} + \nabla_j H^j_{V,\nu} = -\chi_{\nu,a} J_{V,\nu}
$$
$$
- n_e \sigma_T \left\{\frac{2\eta}{(1-\eta^2)^2}H^z_{I,\nu} + \left[\frac{1}{2}\frac{1+\eta^2}{(1-\eta^2)^2} + \frac{1}{2}\right] J_{V,\nu} + \left[\frac{1}{2}\frac{1+\eta^2}{(1-\eta^2)^2} - \frac{1}{2}\right] K^{zz}_{V,\nu}\right\} \quad .
$$
$$
\tag{E.54d}
$$

By taking $\eta = 0$, we can recover the moments equations for non-magnetic Thomson scattering. If we neglect the magnetic effect (i.e. $\eta = 0$) and assuming the isotropic radiation field, we get negative scattering source terms for Q_ν, U_ν, and V_ν, which suggests the scattering process depolarizes the incident light.

First Moment Equations

The scattering emission terms entails the angular integration of the Muller matrix, where the isotropic terms of angular moments vanish in the first moment equations (recall $\int n^i d\Omega = 0$). The attenuation terms of the Thomson scattering mostly contribute to the first moment equations.

$$\frac{1}{c}\frac{\partial H^i_{I,\nu}}{\partial t} + \nabla_j K^{ij}_{I,\nu} = -\chi_{\nu,a} H^i_{I,\nu} - n_e \sigma_T \left\{ \frac{1}{2}\left[\frac{1+\eta^2}{(1-\eta^2)^2}+1\right] H^i_{I,\nu} \right.$$
$$\left. +\frac{1}{2}\left[\frac{1+\eta^2}{(1-\eta^2)^2}-1\right](L^{izz}_{I,\nu} - H^i_{Q,\nu} + L^{izz}_{Q,\nu}) + \left[\frac{2\eta}{(1-\eta^2)^2}\right] K^{iz}_{V,\nu} \right\} , \tag{E.55a}$$

$$\frac{1}{c}\frac{\partial H^i_{Q,\nu}}{\partial t} + \nabla_j K^{ij}_{Q,\nu} = -\chi_{\nu,a} H^i_{Q,\nu} - n_e \sigma_T \left\{ \frac{1}{2}\left[\frac{1+\eta^2}{(1-\eta^2)^2}+1\right] H^i_{Q,\nu} \right.$$
$$\left. +\frac{1}{2}\left[\frac{1+\eta^2}{(1-\eta^2)^2}-1\right](-H^i_{I,\nu} + L^{izz}_{I,\nu} + L^{izz}_{Q,\nu}) \right\} , \tag{E.55b}$$

$$\frac{1}{c}\frac{\partial H^i_{U,\nu}}{\partial t} + \nabla_j K^{ij}_{U,\nu} = -\chi_{\nu,a} H^i_{U,\nu} - n_e \sigma_T \left\{ \frac{1}{2}\left[\frac{1+\eta^2}{(1-\eta^2)^2}+1\right] H^i_{U,\nu} \right.$$
$$+\frac{1}{2}\left[\frac{1+\eta^2}{(1-\eta^2)^2}-1\right] L^{izz}_{U,\nu} + \frac{n_e \sigma_T}{2(1-\eta^2)}\left[-\delta^{iy}K^{xz}_{I,\nu} + \delta^{ix}K^{yz}_{I,\nu}\right.$$
$$\left.\left. -\delta^{iy}K^{xz}_{Q,\nu} + \delta^{ix}K^{yz}_{Q,\nu} + \delta^{ix}H^y_{U,\nu} + \delta^{iy}H^y_{U,\nu} + \eta(\delta^{ix}H^y_{V,\nu} - \delta^{iy}H^x_{V,\nu})\right] \right\} , \tag{E.55c}$$

$$\frac{1}{c}\frac{\partial H^i_{V,\nu}}{\partial t} + \nabla_j K^{ij}_{V,\nu} = -\chi_{\nu,a} H^i_{V,\nu} - n_e \sigma_T \left\{ \left[\frac{2\eta}{(1-\eta^2)^2}\right] K^{iz}_{I,\nu} + \frac{1}{2}\left[\frac{1+\eta^2}{(1-\eta^2)^2}+1\right] H^i_{V,\nu} \right.$$
$$+\frac{1}{2}\left[\frac{1+\eta^2}{(1-\eta^2)^2}-1\right] L^{izz}_{V,\nu} + \frac{1}{2}n_e \sigma_T \left\{\frac{\eta\delta^{iz}}{(1-\eta^2)^2}(J_{I,\nu} + K^{zz}_{I,\nu})\right.$$
$$+\frac{\eta}{1-\eta^2}(\delta^{ix}K^{xz}_{I,\nu} + \delta^{iy}K^{yz}_{I,\nu}) + \frac{\eta\delta^{iz}}{(1-\eta^2)^2}(K^{zz}_{Q,\nu} - J_{Q,\nu})$$
$$+\frac{\eta}{1-\eta^2}(\delta^{ix}K^{xz}_{Q,\nu} + \delta^{iy}K^{yz}_{Q,\nu}) + \frac{\eta}{1-\eta^2}(\delta^{iy}H^x_U - \delta^{ix}H^y_U)$$
$$\left. +\frac{(1+\eta^2)\delta^{iz}}{(1-\eta^2)^2}H^z_V + \frac{1}{1-\eta^2}(\delta^{ix}H^x_V + \delta^{iy}H^y_V)\right\} , \tag{E.55d}$$

where $L^{izz} = (1/4\pi) \oint n_i n_z^2 d\Omega$ refers to the third moments. In the weak magnetic field regime (i.e. $\eta = 0$), the first moment equations reduce to the usual momentum equations, i.e. with radiation forces that arise from both the thermal absorption of gas ($\chi_{\nu,a}$) and the attenuation from Thomson scattering ($n_e \sigma_T$).

E.3   Angle- and Polarization-Averaged Magnetic Scattering Opacities

The scattering opacities in a neutron star accretion column depend strongly on both photon frequency, propagation angle with respect to the magnetic field, and polarization. A multifrequency group method for isotropic absorption and emission has now been implemented in ATHENA++ (Jiang 2022), and generalizing this to include angle-dependence and polarization would be worthwhile in our future work. In the meantime, the simulations in chapter 4 use the implementation of frequency-integrated radiation transfer in ATHENA++ (Jiang et al. 2014; Jiang 2021). Here we describe the frequency-integrated, angle-, and polarization-averaged scattering opacities that we use in chapter 4.

Recall that we neglect quantum effects and treat photon-electron scattering classically, assuming a cold electron-ion plasma with infinite ion inertia and negligible plasma frequencies so that dispersive effects are negligible. The full Mueller matrix for electron scattering in a uniform magnetic field under these conditions has been derived above (for details see section E.1.3), and maps the Stokes parameters of the incoming to the outgoing radiation field. We simplify the problem here by azimuthally averaging around the direction of the magnetic field (Caiazzo & Heyl 2021) and neglecting circular polarization. Switching from Stokes parameters I_ν and Q_ν to O and X mode intensities defined by $I_{O\nu} = (I_\nu + Q_\nu)/2$ and $I_{X\nu} = (I_\nu - Q_\nu)/2$, respectively, we can then derive

the following scattering coefficients for X-modes

$$\chi_{X\nu} = n_{\rm e}\sigma_{\rm T}\frac{\omega^2(\omega^2 + \omega_{\rm ce}^2)}{(\omega^2 - \omega_{\rm ce}^2)^2} \equiv f n_{\rm e}\sigma_{\rm T} \quad , \tag{E.56}$$

O-mode radiation propagating perpendicular to the magnetic field

$$\chi_{O\nu}^{\perp} = n_{\rm e}\sigma_{\rm T}\left(\frac{4 + f}{5}\right) \quad , \tag{E.57a}$$

and O-mode radiation propagating parallel to the magnetic field

$$\chi_{O\nu}^{\parallel} = n_{\rm e}\sigma_{\rm T}\left(\frac{2 + 3f}{5}\right) \quad . \tag{E.57b}$$

Here $\omega = 2\pi\nu$ is the angular photon frequency, and $\omega_{\rm ce} = eB/(m_{\rm e}c)$ is the electron cyclotron angular frequency. These expressions are identical to those in equation (45) of Arons et al. (1987), except that they used an approximation where f is unity for $\omega > \omega_{\rm ce}$ and $\omega^2/\omega_{\rm ce}^2$ for $\omega < \omega_{\rm ce}$. The exact (albeit classical) expression that we use here retains the enhancement of scattering near the cyclotron resonance.

Provided mode exchange is relatively efficient, the angle-averaged mean intensities in both polarization modes will be approximately equal (Arons et al. 1987). The polarization-averaged opacities for diffusion are then

$$\chi_{\nu}^{\perp} = \frac{2\chi_{O\nu}^{\perp}\chi_{X\nu}}{\chi_{O\nu}^{\perp} + \chi_{X\nu}} = \frac{f(4 + f)}{2 + 3f}n_{\rm e}\sigma_{\rm T} \quad , \tag{E.58a}$$

and

$$\chi_{\nu}^{\parallel} = \frac{2\chi_{O\nu}^{\parallel}\chi_{X\nu}}{\chi_{O\nu}^{\parallel} + \chi_{X\nu}} = \frac{f(2 + 3f)}{1 + 4f}n_{\rm e}\sigma_{\rm T} \quad , \tag{E.58b}$$

in agreement with equation (50) of Arons et al. (1987).

We neglect finite photon chemical potential effects, and compute blackbody Rosseland

means:

$$\chi_{\text{R}\perp} = n_{\text{e}}\sigma_{\text{T}}\frac{\displaystyle\int_0^\infty dx\frac{x^4 e^x}{(e^x-1)^2}}{\displaystyle\int_0^\infty dx\frac{x^4 e^x(2+3f)}{f(4+f)(e^x-1)^2}} = n_{\text{e}}\sigma_{\text{T}} \times \begin{cases} 1 & \text{for } x_{\text{ce}} \to 0 \\[2mm] \dfrac{8\pi^2}{5x_{\text{ce}}^2} & \text{for } x_{\text{ce}} \to \infty \end{cases} \tag{E.59a}$$

and

$$\chi_{\text{R}\|} = n_{\text{e}}\sigma_{\text{T}}\frac{\displaystyle\int_0^\infty dx\frac{x^4 e^x}{(e^x-1)^2}}{\displaystyle\int_0^\infty dx\frac{x^4 e^x(1+4f)}{f(2+3f)(e^x-1)^2}} = n_{\text{e}}\sigma_{\text{T}} \times \begin{cases} 1 & \text{for } x_{\text{ce}} \to 0 \\[2mm] \dfrac{8\pi^2}{5x_{\text{ce}}^2} & \text{for } x_{\text{ce}} \to \infty \end{cases} \tag{E.59b}$$

where $x \equiv h\nu/(kT)$ and $x_{\text{ce}} = \hbar\omega_{\text{ce}}/(kT)$.

To see how to implement these opacities, consider for simplicity a static medium. The Rosseland mean opacities can then be incorporated into a frequency-integrated, polarization-averaged transfer equation as follows (cf. equation (6) of Jiang 2021):

$$\begin{aligned} \frac{1}{c}\frac{\partial I}{\partial t} + \hat{\mathbf{n}}\cdot\nabla I = {}& \chi_{\text{Pa}}\left(\frac{acT^4}{4\pi} - J\right) + \chi_{\text{Ra}}(J-I) \\ & + \left[\frac{1}{2}(3\chi_{\text{R}\perp} - \chi_{\text{R}\|}) + \frac{5}{2}(\chi_{\text{R}\|} - \chi_{\text{R}\perp})\cos^2\theta\right](J-I) \quad . \end{aligned} \tag{E.60}$$

Here χ_{Pa} and χ_{Ra} are the Planck and Rosseland mean absorption coefficients for true absorption processes. This equation automatically gives the correct zeroth and first moment equations for radiation energy density and flux, provided we assume nearly isotropic radiation closures on the second and third angular moments: $K_{zz} = J/3$ and $Q_{izz} = (H_i + 2\delta_{iz}H_z)/5$, where J and H_i are the zeroth and first angular moments, respectively. The resulting moment equations are then

$$\frac{1}{c}\frac{\partial J}{\partial t} + \nabla\cdot\boldsymbol{H} = \chi_{\text{Pa}}\left(\frac{acT^4}{4\pi} - J\right) \quad , \tag{E.61a}$$

251

$$\frac{1}{c}\frac{\partial H_i}{\partial t} + \frac{1}{3}\nabla_i J = -(\chi_{\mathrm{Ra}} + \chi_{\mathrm{R}\perp})H_i - (\chi_{\mathrm{R}\parallel} - \chi_{\mathrm{R}\perp})\delta_{iz}H_z \quad , \tag{E.61b}$$

exactly as required. While we have worked in a static medium here, this is sufficient for the numerical radiation MHD scheme used in ATHENA++, which computes the source terms of the transfer equation in the local fluid rest frame and then Lorentz transforms them into the lab frame (see Jiang 2021 for details).

The behaviors of the perpendicular and parallel Rosseland opacities ($\kappa_{\mathrm{s}} = \chi_{\mathrm{R}}/\rho$) from equations (E.59a) and (E.59b) are the same except near $x_{\mathrm{ce}} = 1$, and we therefore simplify our transfer equation still further by neglecting the angle dependence in equation (E.60). We do this by simply replacing $\cos^2\theta$ with unity, as that produces the largest opacity near $x_{\mathrm{ce}} = 1$, in order to partly account for cyclotron resonance which we have neglected in chapter 4. Figure 4.15 compares our prescription with the Rosseland mean opacities computed by Suleimanov et al. (2022), and the agreement is reasonably good below the temperature 3×10^8 K where pair production becomes significant. (We do not reach such temperatures in any of the simulations presented in chapter 4.)

To summarize, in chapter 4, the frequency-integrated, angle- and polarization-averaged magnetic scattering absorption coefficient that we actually use in the fluid rest frame is $2\chi_{\mathrm{R}\parallel} - \chi_{\mathrm{R}\perp}$, where $\chi_{\mathrm{R}\perp}$ and $\chi_{\mathrm{R}\parallel}$ are given by equations (E.59a) and (E.59b), respectively.

Bibliography

Abarca D., Parfrey K., Kluźniak W., 2021, ApJ, 917, L31

Abolmasov P., Lipunova G., 2022, arXiv e-prints, p. arXiv:2207.12312

Arons J., 1992, ApJ, 388, 561

Arons J., Klein R. I., Lea S. M., 1987, ApJ, 312, 666

Bachetti M., et al., 2014, Nature, 514, 202

Basko M. M., Sunyaev R. A., 1975, A&A, 42, 311

Basko M. M., Sunyaev R. A., 1976, MNRAS, 175, 395

Becker P. A., 1998, ApJ, 498, 790

Becker P. A., Wolff M. T., 2007, ApJ, 654, 435

Becker P. A., et al., 2012, A&A, 544, A123

Beckwith K., Stone J. M., 2011, ApJS, 193, 6

Begelman M. C., 2001, ApJ, 551, 897

Begelman M. C., 2006, ApJ, 636, 995

Bellm E. C., et al., 2014, ApJ, 792, 108

Blaes O., Socrates A., 2003, ApJ, 596, 509

Borozdin K., et al., 1990, Soviet Astronomy Letters, 16, 345

Burderi L., Di Salvo T., 2013, Mem. Soc. Astron. Italiana, 84, 117

Caballero I., Wilms J., 2012, Mem. Soc. Astron. Italiana, 83, 230

Caiazzo I., Heyl J., 2021, MNRAS, 501, 109

Chou C. K., 1986, Ap&SS, 121, 333

Dall'Osso S., Perna R., Stella L., 2015, MNRAS, 449, 2144

Davis S. W., Gammie C. F., 2020, ApJ, 888, 94

Doroshenko V., Tsygankov S. S., Mushtukov A. A., Lutovinov A. A., Santangelo A., Suleimanov V. F., Poutanen J., 2017, MNRAS, 466, 2143

Doroshenko V., et al., 2022, Nature Astronomy, 6, 1433

Farinelli R., et al., 2023, MNRAS, 519, 3681

Fernández R., Socrates A., 2013, ApJ, 767, 144

Gammie C. F., 1998, MNRAS, 297, 929

Ghosh P., Lamb F. K., Pethick C. J., 1977, ApJ, 217, 578

Hirose S., Krolik J. H., Blaes O., 2009, ApJ, 691, 16

Hsu J. J. L., Arons J., Klein R. I., 1997, ApJ, 478, 663

Inoue H., 1975, PASJ, 27, 311

Iwakiri W. B., et al., 2019, ApJ, 878, 121

Jaisawal G. K., Naik S., 2016, MNRAS, 461, L97

Jernigan J. G., Klein R. I., Arons J., 2000, ApJ, 530, 875

Ji L., et al., 2020, MNRAS, 493, 5680

Jiang Y.-F., 2021, ApJS, 253, 49

Jiang Y.-F., 2022, ApJS, 263, 4

Jiang Y.-F., Stone J. M., Davis S. W., 2014, ApJS, 213, 7

Kaaret P., Feng H., Roberts T. P., 2017, ARA&A, 55, 303

Kageyama A., Sugiyama T., Watanabe K., Sato T., 2006, Computers and Geosciences, 32, 265

Kawashima T., Ohsuga K., 2020, PASJ, 72, 15

King A., Lasota J.-P., Middleton M., 2023, New Astronomy Reviews, 96, 101672

Klein R. I., Arons J., 1989, in Hunt J., Battrick B., eds, ESA Special Publication Vol. 1, Two Topics in X-Ray Astronomy, Volume 1: X Ray Binaries. Volume 2: AGN and the X Ray Background. p. 89

Klein R. I., Arons J., Jernigan G., Hsu J. J. L., 1996, ApJ, 457, L85

Klochkov D., Santangelo A., Staubert R., Ferrigno C., 2008, A&A, 491, 833

Masaki I., 1971, PASJ, 23, 425

Mignone A., McKinney J. C., 2007, MNRAS, 378, 1118

Mushtukov A., Tsygankov S., 2022, arXiv e-prints, p. arXiv:2204.14185

Mushtukov A. A., Suleimanov V. F., Tsygankov S. S., Poutanen J., 2015, MNRAS, 454, 2539

Mushtukov A. A., Nagirner D. I., Poutanen J., 2016, Phys. Rev. D, 93, 105003

Mushtukov A. A., Suleimanov V. F., Tsygankov S. S., Ingram A., 2017, MNRAS, 467, 1202

Mushtukov A. A., Ognev I. S., Nagirner D. I., 2019, MNRAS, 485, L131

Mushtukov A. A., Portegies Zwart S., Tsygankov S. S., Nagirner D. I., Poutanen J., 2021, MNRAS, 501, 2424

Nagase F., Hayakawa S., Sato N., Masai K., Inoue H., 1986, PASJ, 38, 547

Negele J. W., Vautherin D., 1973, Nucl. Phys. A, 207, 298

Newman W. I., Hamlin N. D., 2014, SIAM Journal on Scientific Computing, 36, B661

Parmar A. N., White N. E., Stella L., 1989, ApJ, 338, 373

Poutanen J., Mushtukov A. A., Suleimanov V. F., Tsygankov S. S., Nagirner D. I., Doroshenko V., Lutovinov A. A., 2013, ApJ, 777, 115

Reig P., Nespoli E., 2013, A&A, 551, A1

Revnivtsev M. G., Molkov S. V., Pavlinsky M. N., 2015, MNRAS, 451, 4253

Rodríguez Castillo G. A., et al., 2020, ApJ, 895, 60

Shaviv N. J., 1998, ApJ, 494, L193

Sheng X., Zhang L., Blaes O., Jiang Y.-F., 2023, MNRAS, 524, 2431

Staubert R., et al., 2019, A&A, 622, A61

Stone J. M., Tomida K., White C. J., Felker K. G., 2020, ApJS, 249, 4

Suleimanov V. F., Mushtukov A. A., Ognev I., Doroshenko V. A., Werner K., 2022, MNRAS, 517, 4022

Swisdak M., 2006, arXiv e-prints, p. physics/0606044

Tananbaum H., Gursky H., Kellogg E. M., Levinson R., Schreier E., Giacconi R., 1972, ApJ, 174, L143

Terrell J., Priedhorsky W. C., 1984, ApJ, 285, L15

Tsygankov S. S., Lutovinov A. A., Churazov E. M., Sunyaev R. A., 2006, MNRAS, 371, 19

Tsygankov S. S., Lutovinov A. A., Serber A. V., 2010, MNRAS, 401, 1628

Tsygankov S. S., Mushtukov A. A., Suleimanov V. F., Poutanen J., 2016, MNRAS, 457, 1101

Tsygankov S. S., Doroshenko V., Lutovinov A. A., Mushtukov A. A., Poutanen J., 2017, A&A, 605, A39

Tsygankov S. S., et al., 2022, ApJ, 941, L14

Turner N. J., Blaes O. M., Socrates A., Begelman M. C., Davis S. W., 2005, ApJ, 624, 267

Walter R., Lutovinov A. A., Bozzo E., Tsygankov S. S., 2015, A&A Rev., 23, 2

West B. F., Wolfram K. D., Becker P. A., 2017a, ApJ, 835, 129

West B. F., Wolfram K. D., Becker P. A., 2017b, ApJ, 835, 130

Whitlock L., Roussel-Dupre D., Priedhorsky W., 1989, ApJ, 338, 381

Wijnands R., van der Klis M., 1998, Nature, 394, 344

Yamamoto T., Mihara T., Sugizaki M., Nakajima M., Makishima K., Sasano M., 2014, PASJ, 66, 59

Zangwill A., 2012, Modern Electrodynamics. Cambridge University Press

Zhang L., Blaes O., Jiang Y.-F., 2021, MNRAS, 508, 617

Zhang L., Blaes O., Jiang Y.-F., 2022, MNRAS, 515, 4371

Zhang L., Blaes O., Jiang Y.-F., 2023, MNRAS, 520, 1421